Study of memory effect in an Atmospheric Pressure Townsend Discharge in the mixture N2-O2 using laser induced fluorescence

Xi Lin

THÈSE

En vue de l'obtention du

DOCTORAT DE L'UNIVERSITÉ DE TOULOUSE

Délivré par l'Université Toulouse 3 - Paul Sabatier

Présentée et soutenue par

Xi LIN

Le 22 février 2019

Study of memory effect in an Atmospheric Pressure Townsend Discharge in the mixture N_2/O_2 using laser induced fluorescence

Ecole doctorale : **GEET - Génie Electrique Electronique et Télécommunications : du système au nanosystème**

Spécialité : **Ingénierie des Plasmas**

Unité de recherche :
LAPLACE - Laboratoire PLAsma et Conversion d'Énergie - CNRS-UPS-INPT

Thèse dirigée par
Simon DAP et Nicolas GHERARDI

Jury

Mme Svetlana Starikovskaia, Rapporteuse
M. Ronny Brandenburg, Rapporteur
Mme Françoise Massines, Examinateur
M. Frédéric Marchal, Examinateur
M. Philippe Teulet, Examinateur
M. Simon DAP, Directeur de thèse

Acknowledgement

I would like to express my deepest thanks to my supervisor, Simon Dap. He has devoted so much time on teaching and leading me into the world of plasma physics. I am very appreciated for his patience and encouragement, also thanks to his support and rich discussion on physics, I finally achieve my thesis.

I would also like to express my thanks to Nicolas Naudé for the fruitful discussions and suggestions on electrical characteristics of discharge, and for his knowledge on electrode fabrication and on OES spectroscopy. Thanks to Nicolas Gherardi for his confidence and support on me.

Thanks to Prof. Svetlana M Starikovskaia and Prof. Ronny Brandenburg, for reviewing my thesis.

I would also like to extend my gratitude to three other jury members, Prof. Françoise Massines, Prof. Feédéric Marchal and Prof. Philippe Teulet, for being the examiners of my work.

I appreciate the assistance and advice from the technicians and engineers of Laplace, Benoît Schlegel, Fédéric Sidor, Vincent Bley, Céline Combettes, Cédric Trupin, and Stéphane Martin. Without your kindly help, I cannot conduct my experiments.

I would also thanks to Richard Clergereaux and Freddy Gaboriau, for their support during the experiments.

I wish to thank my labmates, Rémi Berard, Christophère Laurent, Mathias Rojo, Luice Brès, Inès Martinko, Marvine Soumbo, Jacopo Profili, and Morgane Laurent, for their support and enthusiasm. Especially, thanks to Clémence Tyl, for her valuable information on simulation of discharge characteristics. And thanks to all of MPP group for your kindness and the surprise birthday celebration in 2017.

With a special mention to Shuangshuang, Yuchao, Jingjing in general, it is very delighted to have you in the laboratory. And my two best friends Hui and Shengyue, thanks so much for your company during the nearly four years' life in Toulouse, without you, I would miss much happiness.

Thanks to my boyfriend Yifei. His knowledge of plasma simulation and kinetics helps me a lot, the discussion on plasma is an interesting topic linking us.

Finally, I would like to thank my beloved parents and grandparents for their infinite and firm support and love throughout my life, and especially nearly seven years' life far from home.

Contents

CONTENTS **1**

GENERAL INTRODUCTION **5**

CHAPTER 1. LITERATURE REVIEW AND CONTEXT OF THIS WORK **7**

I. GENERATION OF HOMOGENEOUS DISCHARGES AT ATMOSPHERIC PRESSURE AND BREAKDOWN MECHANISMS **7**

I.1. Two main kinds of breakdown mechanism 8

I.1.1. Townsend breakdown 8

I.1.2. Streamer breakdown 9

II. GENERATION OF A NON-THERMAL PLASMA AT ATMOSPHERIC PRESSURE **10**

II.1. Decreasing the value of $p \times d$ 10

II.2. Generation of a corona discharge 10

II.3. Dielectric barrier discharges 11

III. GENERATION OF A HOMOGENEOUS DBD AT ATMOSPHERIC PRESSURE **12**

III.1. Different kind of homogenous DBD 12

III.2. Atmospheric pressure glow discharge (APGD) 13

III.2.1. Basic features of APGD 13

III.2.2. Memory effect in APGD 14

III.3. Atmospheric pressure Townsend discharge (APTD) 14

III.3.1. Basic features of APTD 14

III.3.2. Memory effect in APTD 16

CHAPTER 2. EXPERIMENTAL SET-UP **25**

I. PLASMA VESSEL AND PUMPING SYSTEM **25**

I.1. Discharge cell and power supply 25

I.1.1. Discharge cell 25

I.1.2. Power supply 27

I.2. Determination of the electrical characteristics of the discharge 27

I.2.1. Calculation of the gas gap voltage and the discharge current 27

I.2.2. Definition and calculation of the discharge power and of the energy dissipated in the discharge 28

II. GENERAL CONSIDERATIONS ABOUT LASER INDUCED FLUORESCENCE **30**

II.1. Principle of laser induced fluorescence 30

II.1.1. Fluorescence spectroscopy with single-photon excitation (LIF) 30

II.1.2. Fluorescence spectroscopy with two-photon excitation (TALIF) 30

II.2. Theoretical approach 31

II.2.1. Measurements at low laser energy 32

II.2.2. Measurements at high laser energy 33

II.2.3. TALIF signal 33

II.2.4. Determination of the LIF/TALIF regime 34

II.2.5. Measuring the LIF/TALIF signal 34

II.3. Calibration method: obtaining absolute densities 36

II.3.1. Calibration of LIF measurements on NO(X) 36

II.3.2. Calibration of TALIF measurements on N(^{4}S) and O(^{3}P) 36
III. LIF/TALIF SETUP 38
III.1. Laser system 38
III.1.1. Configuration for measurement of N ($2p^3\ ^4S_{3/2}$) and Kr ($4p^6\ ^1S_0$) 41
III.1.2. Configuration for measurement of O ($2p^4\ ^3P_J$) and Xe ($5p^6\ ^1S_0$) 42
III.1.3. Configuration for measurement of NO 44
III.2. Acquisition system and boxcar averager 44
III.3. Verification of the operation mode of photomultiplier tube 45
IV. SYNCHRONIZATION OF THE LASER PULSE, DISCHARGE AND BOXCAR 45
V. MEASUREMENT PROCEDURE 46

CHAPTER 3. TALIF MEASUREMENTS OF ATOMIC NITROGEN N ($2P^3\ ^4S_{3/2}$) DENSITY 47

I. VALIDATION OF TALIF MEASUREMENTS, CALIBRATION PROCEDURE AND EXPERIMENTAL ERRORS 47
I.1. Validation of TALIF measurements 47
I.2. Calibration procedure 49
I.3. Influence of the gas temperature 51
I.4. Experimental errors 53
II. N ($2P^3\ ^4S_{3/2}$) DENSITY IN N_2 53
II.1. Evolution of the N ($2p^3\ ^4S_{3/2}$) density during a period of the applied voltage 54
II.2. Evolution of the N ($2p^3\ ^4S_{3/2}$) density along the discharge 54
II.3. N ($2p^3\ ^4S_{3/2}$) density as a function of the discharge power 57
II.4. N ($2p^3\ ^4S_{3/2}$) density as a function of the gas flow rate 60
II.5. Evolution of the N ($2p^3\ ^4S_{3/2}$) density during the post-discharge 61
II.6. Summary 63
III. N ($2P^3\ ^4S_{3/2}$) DENSITY IN THE MIXTURE N_2/O_2 63
III.1. N ($2p^3\ ^4S_{3/2}$) density in the discharge for different oxygen concentration 63
III.2. N ($2p^3\ ^4S_{3/2}$) density in post-discharge for different oxygen concentration 67
IV. CONCLUSION 68

CHAPTER 4. TALIF MEASUREMENTS OF ATOMIC OXYGEN O ($2P^4\ ^3P_J$) DENSITY 69

I. METHODOLOGY EMPLOYED FOR THE TALIF MEASUREMENTS ON O ($2P^4\ ^3P_J$) 69
II. CALIBRATION OF THE TALIF SIGNAL USING XENON 71
III. INFLUENCE OF THE GAS TEMPERATURE ON TALIF MEASUREMENTS 74
IV. ABSOLUTE ATOMIC OXYGEN DENSITY IN THE MIXTURE N_2/O_2 75
IV.1. Absolute density of O ($2p^4\ ^3P_J$) as a function of the position in the discharge for various oxygen concentration 75
IV.2. Absolute density of O ($2p^4\ ^3P_J$) as a function of oxygen concentration 76
IV.3. Absolute density of O ($2p^4\ ^3P_J$) as a function of discharge power 78
IV.4. Evolution of the O ($2p^4\ ^3P_J$) density during a period of the applied voltage 80
IV.5. O ($2p^4\ ^3P_J$) density in post-discharge for different oxygen concentration 81
V. CONCLUSION 82

CHAPTER 5. LIF MEASUREMENTS OF ABSOLUTE NITRIC OXIDE NO($X^2\Pi$) DENSITY 83

I. METHODOLOGY EMPLOYED FOR THE LIF MEASUREMENTS ON NO($X^2\Pi$) 83
II. CALIBRATION OF NO($X^2\Pi$) MEASUREMENTS 85
III. INFLUENCE OF THE GAS TEMPERATURE 86

III.1. Estimation of CT1 88
III.2. Estimation of CT2 88
III.3. Influence of the vibrational temperature 90
IV. OTHER EXPERIMENTAL DRAWBACKS 90
V. ABSOLUTE NITRIC OXYGEN DENSITY IN A MIXTURE OF N_2/O_2 91
V.1. Absolute density of NO($X^2\Pi$) along the discharge for different oxygen concentration 91
V.2. Absolute density of NO($X^2\Pi$) as a function of oxygen concentration 92
V.3. Absolute density of NO($X^2\Pi$) as a function of discharge power 93
V.4. NO($X^2\Pi$) density in post-discharge for different oxygen concentration 94
VI. CONCLUSION 95

CHAPTER 6. DISCUSSION 97

I. SUMMARY OF EXPERIMENTAL RESULTS 97
II. INVESTIGATION OF THE SPECIES DENSITIES DURING THE POST-DISCHARGE 98
II.1. Decay of N(^{4}S) during the post-discharge 101
II.2. Decay of O(^{3}P) during the post-discharge 101
II.3. Decay of NO(X) during the post-discharge 101
III. INVESTIGATION OF THE MEMORY EFFECT RELATED TO THE ASSOCIATIVE IONIZATION PROCESS 103
III.1. Determination of the absolute density of N_2(A) 103
III.2. Determination of absolute density of N(^{2}P) 104
III.3. Determination of electron density and current jump 106
III.4. Estimation of the current jump for different oxygen concentration 107
IV. SUMMARY 109

GENERAL CONCLUSION AND PROSPECTS 111

APPENDIX 1 115

I. GENERAL DESCRIPTION OF THE MODEL 115
II. TYPICAL EXAMPLES OF NUMERICAL RESULTS 117
III. VALIDATION OF THE MODEL 118
III.1. Optical emission over a half-period of electrical excitation 118
III.2. Production and destruction of metastable N_2(A) 119
III.3. Optical emission for different oxygen concentration 120
IV. IDENTIFICATION OF THE MAIN MECHANISMS INVOLVED IN THE PRODUCTION/DESTRUCTION OF SPECIES OF INTEREST 121
IV.1. N(^{4}S) atoms 121
IV.1.1. Main mechanisms of production and destruction 121
IV.1.2. Temporal evolution of N(^{4}S) density 122
IV.2. O(^{3}P) atoms 124
IV.2.1. Main mechanisms of production and destruction 124
IV.2.2. Temporal evolution of O(^{3}P) density 126
IV.3. NO(X) molecules 128
IV.3.1. Production 128
IV.3.2. Destruction 128
IV.4. Summary 128
V. ORDER OF MAGNITUDE OF THE DENSITIES OF THE MAIN SPECIES OF INTEREST FOR DIFFERENT OXYGEN CONCENTRATION 129

VI. ADDITIONAL INVESTIGATIONS AND DISCUSSIONS 131
VI.1. Influence of the reaction $N_2(A) + O(^3P) \rightarrow NO + N(^2D)$ on the formation of NO 131
VI.2. Influence of the rate coefficient of reaction $N(^2P) + N_2 \rightarrow N_2 + N(^4S, ^2D)$ 131
APPENDIX 2 137
REFERENCES 139

General introduction

Dielectric barrier discharges (DBD) are a kind of non-equilibrium discharges, in which at least one electrode is covered by a dielectric. Operating at atmospheric pressure, the value of the product pressure×gas gap distance ($p \times d$) is usually high, which results in a discharge characterized by a large number of independent streamers generated between the two electrodes. It corresponds to the filamentary mode. Nevertheless, under some typical conditions, the discharge can be uniform. These conditions can be related to the power supply, the geometry of the discharge cell, the gas atmosphere, the dielectrics... This kind of homogeneous discharge is suitable for many applications such as thin film deposition or surface treatment. It is thus interesting to understand how to obtain such homogeneous discharges in atmospheres containing complexes molecular precursors and/or oxidizing gases.

Two main kinds of homogeneous DBDs can be obtained. One is obtained in noble gas such as helium or argon. For these discharges, the most luminescent layer is located close to the cathode and their electrical characteristics are very similar to those of a glow discharge obtained at low pressure. These discharges are then called Atmospheric Pressure Glow Discharges (APGD). The other type of homogeneous discharge is usually obtained in a nitrogen atmosphere. In this case, the luminescent layer is located near the anode, and its electrical characteristics are very similar to those of a Townsend discharge generated at low pressure. This kind of discharge is named Atmospheric Pressure Townsend Discharge (APTD) and constitutes the main interest of the present work.

To obtain an APTD, it is necessary to decrease the electric field for the breakdown to occur which is possible if seed electrons are present in the gas volume. In the case of periodic discharges, these seed electrons can originate from the previous discharge: this is the memory effect. It is known from previous studies that several mechanisms arising between two successive discharges can participate in this memory effect, the relative importance of these different mechanisms being strongly related to the experimental conditions. In particular, many experiments put in evidence that a small addition of oxidizing gas into nitrogen can greatly enhance this memory effect thus increasing the working domain of the discharge. It suggests the occurrence of a phenomenon taking place in the discharge volume. A possible candidate is the associative ionization reaction between nitrogen metastable atoms N(^{2}P) and oxygen atoms O(^{3}P): $\mathrm{N(\,^2P) + O(\,^3P) \rightarrow NO^+ + e^-}$. In this reaction, the N(^{2}P) atoms are formed during the excitation of ground state atoms N(^{4}S) by N_2(A) metastable molecules: $\mathrm{N(\,^4S) + N_2(A) \rightarrow N(\,^2P) + N_2(X)}$. The main purpose of the present work is to check the consistency of this hypothesis. In this perspective, the most direct method is to determine the absolute densities of the involved species, namely N(^{4}S) and O(^{3}P) atoms between two discharges. For this purpose, two photon laser induced fluorescence measurements (TALIF) are performed. Moreover, the density of NO molecules, which is an efficient quencher of metastable nitrogen species are also determined by laser induced fluorescence (LIF) measurements. The obtained results together with a modeling of the main chemical mechanisms can then be used to quantify the contribution of the aforementioned associative ionization reaction in the memory effect.

The manuscript is organized as follows:

Chapter 1 presents general considerations about atmospheric pressure discharges. First, the different breakdown mechanisms are described. Then, the more specific case of dielectric barrier discharges is considered. The end of this chapter is dedicated to the APTD and to the different mechanisms involved in the memory effect. Finally, the aim of the present work is described in details.

Chapter 2 starts with the description of the experimental set-up including the vacuum system, the configuration of the discharge cell and the electrical system. Then, the general principle of the laser induced fluorescence technique is presented and the calibration procedure allowing to obtain absolute densities from the measured signals is explained. Finally, the different experimental configurations used for the LIF and TALIF measurements are presented.

Chapters 3, 4 and 5 present the results of the measurements for $N(^4S)$, $O(^3P)$ and NO(X) respectively obtained in different experimental conditions. The effect of the main parameters on the density of the different species is discussed. In particular, a careful attention is paid to the influence of the oxygen concentration. The main mechanisms involved in the production and destruction of the different species are investigated using a model developed in the group. The latter is described in Appendix 1.

Chapter 6 is dedicated to discussions based on the results presented in chapters 3, 4 and 5. In the first part, the evolution of the different species densities in the post-discharge region is discussed. In the second part, the influence of the aforementioned associative ionization reaction on the memory effect is estimated using a model.

Finally, the main results of the present work are summarized and prospects are proposed for further investigations.

Chapter 1. Literature review and context of this work

This chapter starts with a general description of plasmas and of the different breakdown mechanisms. Then a brief review of the different kind of discharges generated at atmospheric pressure, especially dielectric barrier discharges, is provided. After that, the generation of a homogeneous DBD at atmospheric pressure is discussed, including “glow discharge” and “Townsend discharge”. Then, the mechanisms allowing the generation of a Townsend discharge at atmospheric pressure are presented, especially for the necessity of a memory effect between two successive discharges. Finally, the main purposes of the present work are described in this context.

I. Generation of homogeneous discharges at atmospheric pressure and breakdown mechanisms

Plasma is the fourth state of matter, which refers to a quasi-neutral partially or totally ionized gas, primarily composed of electrons, ions, photons, as well as atoms and molecules in their fundamental or excited states with a net neutral charge.

If the plasma is at thermodynamic equilibrium, a single temperature can be used to completely characterize the system (assuming that the density is known). This is typically the case for the so-called “hot plasmas” encountered in fusion and astrophysics where the ionization degree approaches unity. Laboratory plasmas have typically low ionization degrees and two different kinds of plasmas can be distinguished. Usually, at atmospheric pressure, the high electron-neutral collision frequency can result in so-called thermal plasmas where the electron temperature is close to the neutral temperature. This is typically the case of arc discharges. These plasmas are generally close to the local thermodynamic equilibrium (see *e.g.* [1] for more details). It implies that the gas temperature is generally high which can induce several drawbacks regarding specific industrial applications [2]. On the opposite, non-thermal plasmas, often called “cold plasmas”, are out of thermodynamic equilibrium. The kinetic temperature of heavy species (ions, atoms, molecules…) is lower than the electron temperature, and remains sufficiently low to make non-thermal plasmas suitable for industrial applications. This kind of plasma is generally obtained in low-pressure conditions. Nevertheless, it is possible to obtain non-thermal plasmas at elevated pressure (*e.g.* atmospheric pressure) using appropriate conditions and setup as illustrated in section II and III.

In non-thermal plasma, most of the electrical input energy is generally spent to the production of energetic electrons rather than in gas heating. These energetic electrons can, in turn, produce a large number of excited species, free radicals, ions and photons (through excitation and recombination) allowing a large variety of plasma applications such as polymer surface treatment, food decontamination, pollution control applications, etc. [3–9]. In addition, cold plasma technologies have other advantages like high excitation selectivity, high efficiency, low pollution, relatively low maintenance requirements, etc. In this frame, non-thermal plasmas generated at atmospheric pressure are promising. Indeed, the manufacturing costs can be drastically reduced since there is potentially no need to use a vacuum system. Depending on the operating conditions, atmospheric cold plasmas can exhibit a filamentary or a homogeneous structure. Filamentary discharges are adapted and suitable for many applications [4,10]. Nevertheless, homogeneous discharges are more suitable for specific applications such as thin film coatings [3,5,6,11–13]. Consequently, the understanding of the mechanisms involved in the obtaining of a homogeneous discharge at atmospheric pressure is of primary importance and constitutes the purpose of the present work.

To go further, it is necessary to understand the different breakdown mechanisms occurring in electrical discharges, which is the aim of the following section.

I.1. Two main kinds of breakdown mechanism

Electrical breakdown occurs in a gas when the applied voltage across the gas gap exceeds the breakdown voltage. The initially insulating gas then becomes conducting. There are two main mechanisms of breakdown whose occurrence mainly depends on the product $p \times d$ where p is the gas pressure and d represents the gas gap value. For relatively low values of $p \times d$, a Townsend Breakdown is generally observed whereas for higher values of $p \times d$ (typically above few Torr.cm) a streamer breakdown occurs. These two mechanisms are described below [14].

I.1.1. Townsend breakdown

Figure 1-1 shows the mechanism of Townsend breakdown, where the discharge is ignited by a DC power supply between two plane electrodes separated by a gap d. The resulting homogeneous electric field is equal to V/d. Let us consider an initial condition for which some primary electrons present near the cathode are accelerated in the electric field towards the anode. If they have a sufficient kinetic energy these accelerated electrons can ionize the gas, then producing more and more electrons. The multiplication of electrons along the electric field can be expressed by:

$$\frac{dn_e}{dx} = \alpha n_e \tag{1.1}$$

where α is the Townsend ionization coefficient, then the total number of electrons should be:

$$n_e = n_{e0} \exp(\alpha d) = n_{e0} \exp\left(\frac{\alpha}{p} pd\right) \tag{1.2}$$

where n_{e0} is the initial primary density of electron in front of the cathode, and

$$\frac{\alpha}{p} = Aexp\left(-\frac{Bp}{E}\right) \tag{1.3}$$

where E is the electric field, A and B are constants related to nature of the gas.

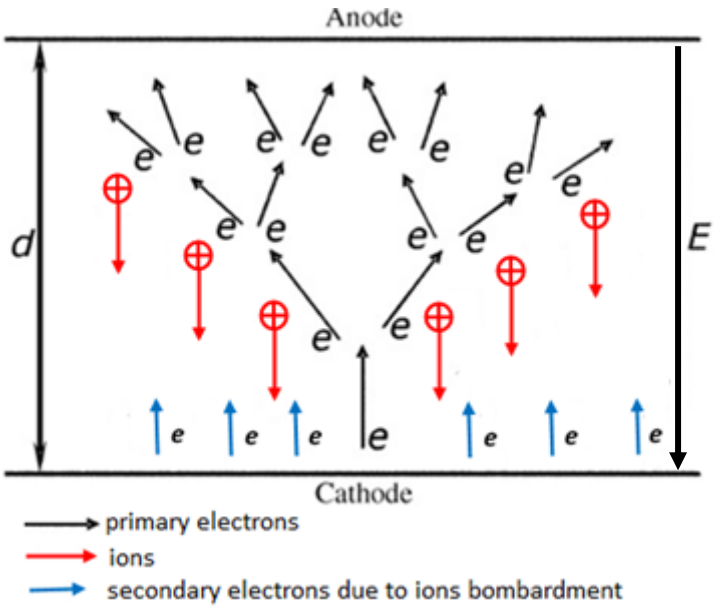

Figure 1-1 Townsend breakdown mechanism (adapted from[2]*)*

Thus, in the gap, each electron would create $[\exp(\alpha d) - 1]$ positive ions, if we consider that there are no losses of electrons due to recombination or attachment onto electronegative species. Then, all these positive ions would arrive at the cathode emitting $\gamma\,(\exp(\alpha d) - 1)$ electrons by secondary electron emission. Here, γ is the secondary emission coefficient.

Hence, to sustain the discharge, positive ions produced during the electron avalanche must generate at least one electron during the bombardment of the cathode to start a new avalanche, which means:

$$\gamma\,(\exp(\alpha d) - 1) = 1 \tag{1.4}$$

Finally, this self-sustained condition is related to the cathode material, the value of $p \times d$ and of E/p *i.e.* the gas pressure, the gap distance and the electric field. The discharge ignited by Townsend breakdown has a uniform appearance.

I.1.2. Streamer breakdown

For higher values of $p \times d$, usually higher than a few dozens of Torr.cm, the breakdown develops much faster than Townsend breakdown [15]: this is the streamer breakdown. This very fast mechanism arises when the multiplication factor $\exp(\alpha d)$ exceeds 10^8. In these conditions, the ion and electron densities resulting from a single avalanche are very high. Moreover, this phenomenon arises at a very small timescale in such a way that only electrons can move towards the anode whereas ions are immobile. This induces space charge electric fields with a magnitude comparable to the applied electric field one.

There exist two different kinds of streamers: the cathode directed streamer (CDS) also called positive streamer and the anode directed streamer (ADS) also known as negative streamer. In the case of a CDS (see Figure 1-2(1)), the ionizing wave moves in the opposite direction of electrons. For a CDS in air, photons originating from the radiative decay of excited species in the primary avalanche create seed electrons between the primary avalanche and the cathode. These seeds electrons then induce the secondary avalanches, which rapidly converge towards the positive space charge of the primary avalanche. Then, new photons are emitted and the process starts again. The photo-ionization process due to the ionization of O_2 molecules dominates the creation of seed electrons for a CDS in air to propagate. Further investigations found that, even in pure nitrogen with very low addition of oxygen (<1ppm), the propagation can be obtained with the same velocity as that in air. The background ionization was then proposed to create free electrons[16,17]. In conclusion, to realize the propagation, the creation of seed electrons is necessary to induce the following avalanche.

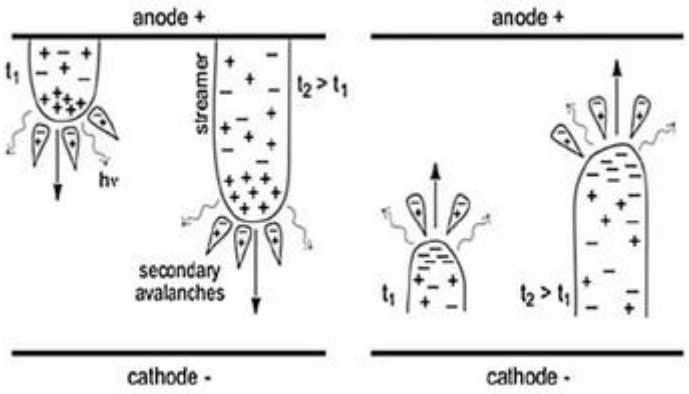

(1) CDS (2) ADS

Figure 1-2 Breakdown mechanism of a streamer breakdown. Propagation of (1) CDS (2) ADS [14]

In the case of an ADS (see Figure 1-2(c)), the streamer propagates in the same direction as the electron motion *i.e.* towards the anode. In this case, the photo-ionization creates seed electrons between the primary avalanche and the anode, which in turn induce secondary avalanches. The photo-ionization phenomenon is not a necessary condition for the negative streamer to propagate but it contributes to accelerating its propagation.

Streamer breakdown leads to the appearance of conducting channels in which the heating of the gas can be important. In the case of metallic electrodes, an arc can develop leading to thermal plasma. If electrodes are covered by a dielectric material, the charge accumulation onto the dielectrics induces a drop of the gas gap voltage leading to the disappearance of the filament, preventing the transition to spark.

II. Generation of a non-thermal plasma at atmospheric pressure

According to the previous discussion, the high value of the product $p \times d$ for atmospheric pressure discharges can easily lead to streamer breakdown and then to the formation of an arc. To avoid the transition to a thermal plasma in such conditions, different approaches can be used. In the following, three different strategies are briefly presented.

II.1. Decreasing the value of $\boldsymbol{p \times d}$

The basic principle of micro-discharges is to reduce the characteristic gas gap in order to recover a low value of the product $p \times d$ for high-pressure conditions. An example of such discharge is the Micro Hollow cathode discharge (MHCD) [18]. It is generated in a metal/dielectric/metal sandwich structure into which a hole is drilled with a typical gas gap ranging from dozens of µm to hundreds of µm. In this configuration, it is possible to obtain different stable regimes depending on the discharge current such as Townsend-like discharges, glow discharges or constricted arcing for higher currents [19].

II.2. Generation of a corona discharge

The corona discharge is usually ignited near sharp points, generally a pin or a thin wire (one electrode) where the electric field is enhanced. Ionization, excitation, and chemical processes mainly occur near the sharp electrode where the electric field is high, defining the active volume of the discharge [2]. The discharge normally does not extend to the counter electrode. The electric current necessary to close the circuit is due to the drift of ions towards the counter electrode in the low electric field.

According to the polarity of the electrode where the high electric field is located, corona discharges can be divided into negative corona discharges (*i.e.* the high electric field is located near the cathode) and positive corona discharges (*i.e*. the high electric field is located near the anode). The ignition mechanisms are actually similar to the Townsend breakdown and positive streamer breakdown respectively [2].

The power of continuous corona discharges is relatively weak which limits many applications. If we increase the amplitude of the high voltage, the transition from corona discharges to sparks or even arcs would occur. To prevent this transition, pulsed corona discharges can be used. Indeed, voltage pulses in the nanosecond range can be short enough to prevent the transition from streamers to sparks and then to maintain a non-thermal plasma. These discharges are used in many practical applications such as generation of ozone, water depollution, removal of NO_x and SO_2 from flue gas, etc.[20–24].

II.3. Dielectric barrier discharges

Besides the narrowing of the gas gap distance and the use of a pulsed corona discharge, another approach to prevent the transition to an arc is to add a dielectric barrier between two electrodes. This kind of discharge is called dielectric barrier discharge (DBD).

Figure 1-3 illustrates typical volume DBD configurations. The planar configuration is mainly used for surface treatment whereas the cylindrical configuration is suitable for gas treatment and UV generation. Other types of DBDs exist such as surface DBD (SDBD) and coplanar discharge, but they are beyond the scope of this thesis.

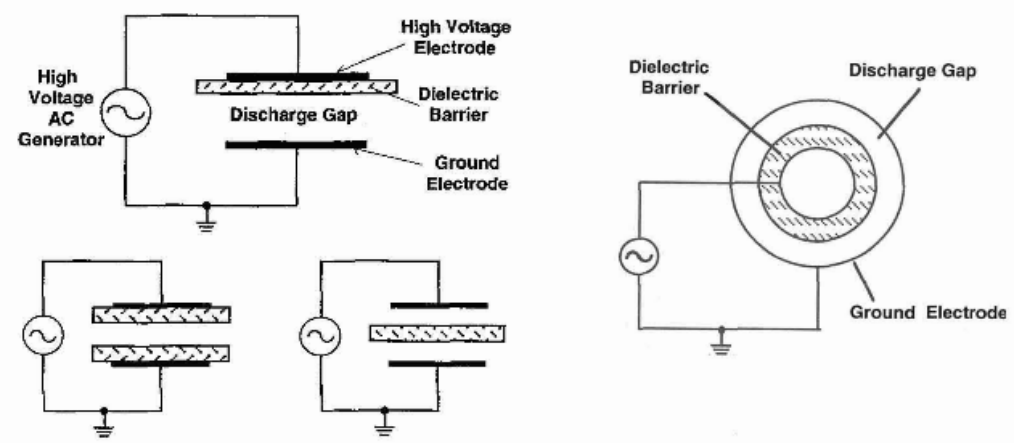

Figure 1-3 Typical DBD configurations [25]

DBDs were first investigated by Siemens in 1857 and used for ozone generation [26]. First observations relate the appearance of amounts of micro-discharges distributed randomly along the electrodes, which could ignite and extinguish independently. The first photographs of these micro-discharges were obtained by K.Buss [27] in 1932. More investigations on the physical nature of DBDs were made by Klemenc [28] in 1937. Figure 1-4 shows a simplified diagram of a single micro-discharge in a DBD with two dielectrics at each electrode and its equivalent circuit. When the streamer breakdown occurs, the discharge current increases dramatically and charges accumulate onto the dielectric surfaces. As a consequence, the electric filed applied on the gas would decrease which induces the extinction of the discharge instead of its transition to an arc.

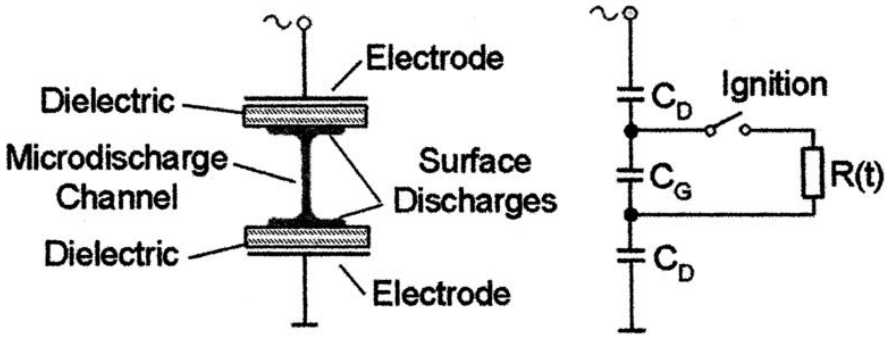

Figure 1-4 Diagram of a single micro-discharge and the equivalent circuit [29]

As explained in section I, homogeneous discharges are suitable for many applications, especially for surface treatment and thin film deposition. The next section is dedicated to the generation of homogeneous DBDs at atmospheric pressure.

III. Generation of a homogeneous DBD at atmospheric pressure

In this section, we present the different homogeneous discharges observed in a DBD configuration. Two main kinds of homogeneous DBDs are presented including their electrical and optical characteristics, and the mechanisms involved in their generation. Then, we focus on the atmospheric pressure Townsend discharge (APTD) and a review of the current knowledge about the memory effect allowing obtaining them is provided. Finally, the main purpose of the present work is presented.

III.1. Different kind of homogenous DBD

The first homogeneous DBD was observed in 1969 by R. Bartnikas in helium [30,31] but the first clear evidence of such discharge regime was brought by the group of S. Okazaki in 1988 [32] and was called “Atmospheric Pressure Glow Discharge” (APGD). Then, by inserting a fine wire mesh between the electrode and the dielectric [33], this group succeed in generating a homogeneous discharge in different gas atmospheres, such as air, nitrogen, argon, and oxygen. After that, more and more teams started to contribute to the understanding of the mechanisms involved in the formation of homogeneous DBD, especially, the team of F.Massine [34,35] and J.R.Roth [36,37]. In parallel to these works, industrial applications were developed taking advantage of their uniform feature for surface treatment and thin film coating [3,5,6,11–13].

APGD takes its name from its similarities with the well-known glow discharge at low pressure. It is obtained for the sufficiently high value of the discharge current. The ion density in this regime is high enough to allow the formation of a cathode fall region characterized by a high space charge electric field.

In nitrogen-based mixtures, another discharge regime was obtained and called “Atmospheric Pressure Townsend Discharge” (APTD) [38]. In this regime, the current is lower than in APGD and the small charged particles density is not sufficient to efficiently affect the electric field. Due to the higher mobility of electrons compared to ions, the electron density is lower than the ion density. Consequently, there is no plasma zone in an APTD.

Both APGD and APTD result from a Townsend breakdown. To obtain a Townsend breakdown at this high value of $p \times d$, it must occur for a low electric field value to avoid streamers formation. This is possible if a small amount of seed electrons is present just before the breakdown.

It is interesting to note that homogenous glow discharges can also be obtained starting from streamer breakdown [39], but only in the presence of seed electrons. In this case, seed electrons are responsible for an increase of the number of primary avalanches and if their density is high enough, it limits the space charge electric field, which becomes uniform thus avoiding the convergence of every avalanche into a single one. This is the streamer coupling breakdown.

The above discussion shows that the presence of seed electrons is a necessary condition to obtain a uniform DBD. These seeds electrons can be provided by an external source such as photo-ionization by a laser [39]. In this case it is called pre-ionization. For periodic discharges, seed electrons can be produced by different mechanisms resulting from the previous discharge. In this case, it is called memory effect.

In the next sections, we describe especially the investigation history in our group on the basic features of APGD and APTD together with the different mechanisms involved in the memory effect which allows a Townsend breakdown to occur.

III.2. Atmospheric pressure glow discharge (APGD)

III.2.1. Basic features of APGD

The APGD was first obtained in helium as a homogeneous discharge [34]. Figure 1-5(a) shows a typical oscillogram of the discharge current and applied voltage of an APGD obtained in helium and (b) a similar oscillogram of a filamentary discharge for comparison. The discharge current is composed of a single pulse suggesting that the discharge is homogenous. On the contrary, the filamentary discharge exhibits several current pulses each one corresponding to one micro-discharge.

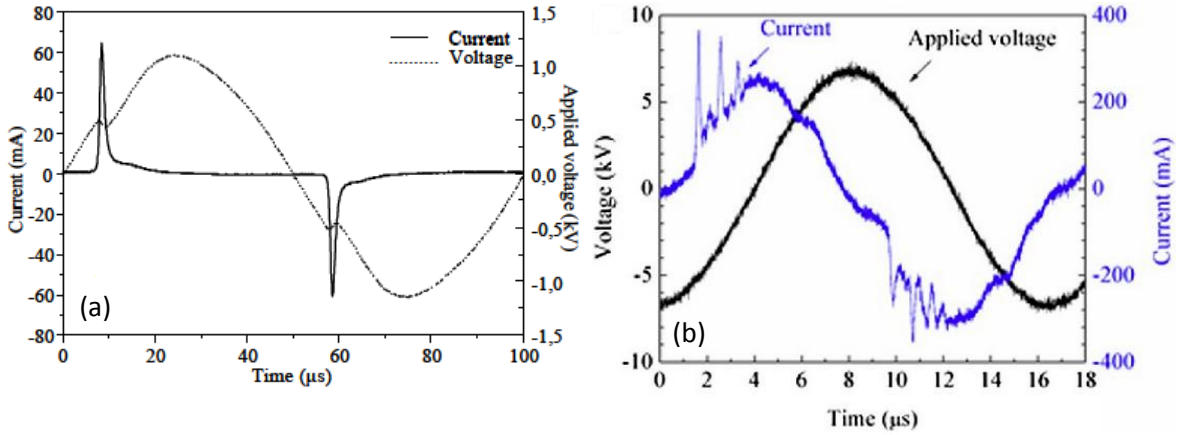

Figure 1-5 Current-voltage oscillogram of (a)a homogeneous DBD [40] *(b) a filamentary DBD* [41]

Figure 1-6(a) shows a picture of the inter-electrode space of an APGD at the maximum of the discharge current. One can clearly see different bright and dark zones corresponding to the typical glow discharge structure. The brighter zone near the cathode corresponds to the cathode fall and to the negative glow, then a dark zone is observed corresponding to the Faraday dark space whereas the bright zone near the anode corresponds to the positive column. This discharge structure can also be observed on the numerical results presented in Figure 1-6(b). The electric field is maximum in the cathode fall, becomes close to zero in the negative glow and keeps a constant and small value in the positive column. The ion density increases dramatically near the cathode to form the cathode fall whereas electrons are efficiently repelled. In the rest of the discharge, electron and ion density are nearly equal defining a quasi-neutral plasma.

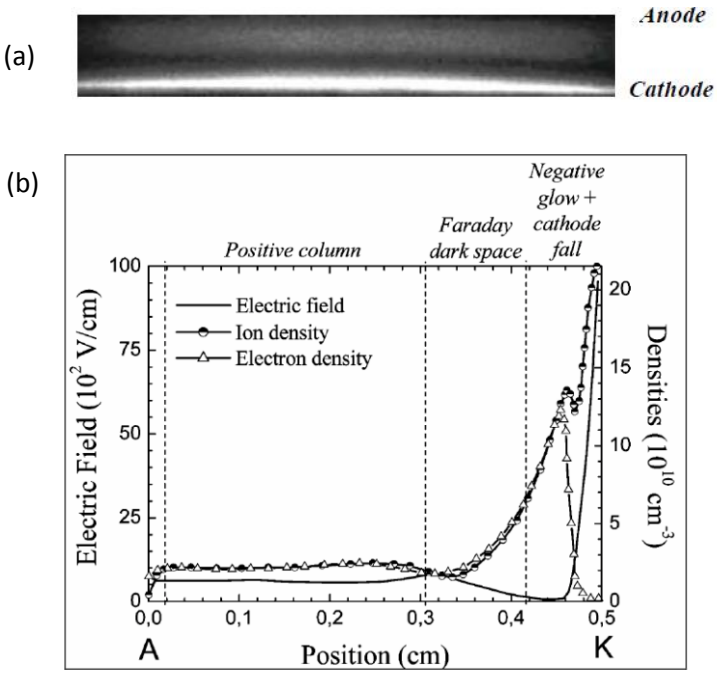

Figure 1-6 (a) Photograph of inter-electrode of an APGD in helium [42] *(b) Spatial evolution of the electric field, the ion, and the electron densities of an APGD in helium at the time when the discharge current is maximum* [42]

III.2.2. Memory effect in APGD

It is now well accepted that the memory effect in APGD is related to Penning ionization process [38]. Penning ionization refers to the interaction between an excited-state atom and a target molecule, resulting in its ionization. Let us consider as an example the case of an APGD in helium in presence of some impurities such as nitrogen molecules. Due to their long lifetime, metastable helium atoms He(2^3S) can remain in the gas phase between two successive discharges. The energy of these metastable atoms (19.8 eV) is higher than the ionization potential of N_2 (15.57 eV), a Penning ionization process can occur. It leads to the production of seed electrons allowing a Townsend breakdown to occur.

This process is not restricted to helium and APGD can be generated in other noble gases such as neon or argon whose respective metastable states have energies of 16.6 and 11.5 eV, in the presence of molecular impurities with lower ionization thresholds (*e.g.* NH_3 for argon and N_2 for neon).

III.3. Atmospheric pressure Townsend discharge (APTD)

III.3.1. Basic features of APTD

Up to now, APTD has been obtained in nitrogen, oxygen, and helium, and in air at atmospheric pressure [38,43–45]. In this work, we will mainly focus on APTD generated in the nitrogen-based atmosphere. Figure 1-7(a) shows an oscillogram of such kind of discharge. The discharge current presents only one current pulse for each half period of the applied voltage, typical of homogenous discharges. The homogeneity of the discharge is confirmed on the picture presented in Figure 1-7(b), which represents a short time exposure photograph of the inter-electrode space at the maximum of the discharge current. One can clearly see a bright zone located near the anode, which is characteristic of the Townsend discharges. To understand this feature, Figure 1-8 represents some results of a fluid simulation of an APTD discharge in nitrogen at the maximum discharge current [46], namely, the reduced electric field, the main ion density (N_4^+), the electron density and the density of

the nitrogen metastable molecule $N_2(A)$ which is the dominant one. The electron density increases exponentially from the cathode to the anode, as predicted by equations (1.1) and (1.2), but remains relatively low with a maximum value about 10^8 cm^{-3}. The density of N_4^+ increases from the anode to the cathode up to 2 10^{10} cm^{-3}, but there is no ion accumulation near the cathode as in APGD. Thus, there is no cathode fall formation and the electric field only slightly varies along the gas gap. Consequently, the maximum excitation rate occurs near the anode where the electron density is maximum explaining the bright zone observed on the photograph presented in Figure 1-7(b). Finally, it is interesting to note that the density of $N_2(A)$ metastable molecules can reach very high values, the maximum density on the order of 10^{13} cm^{-3} being obtained on the anode side. We will come back to this important point in the following section.

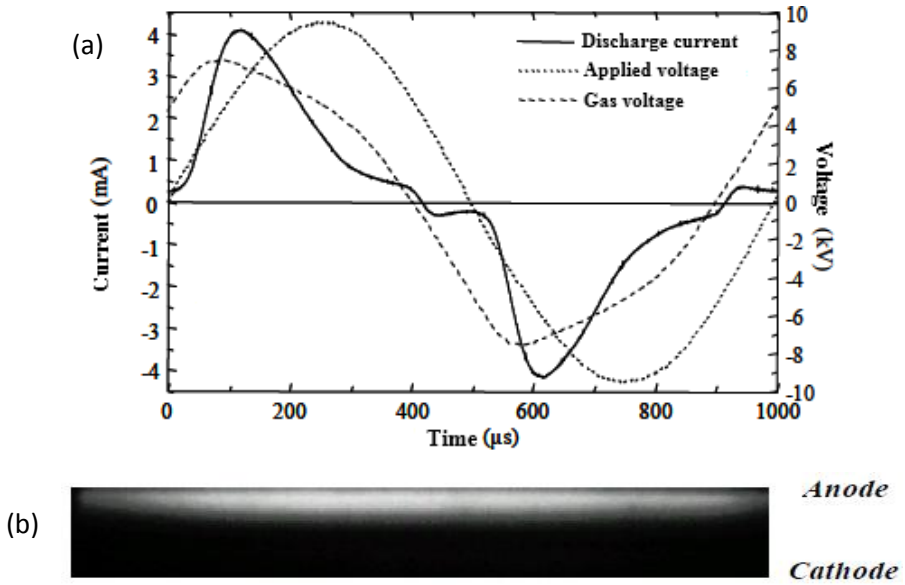

Figure 1-7 (a)Current-voltage oscillogram of a APTD [47]*(b) Photograph of inter-electrode space of an APTD with a time exposure of 10 ns* [42].

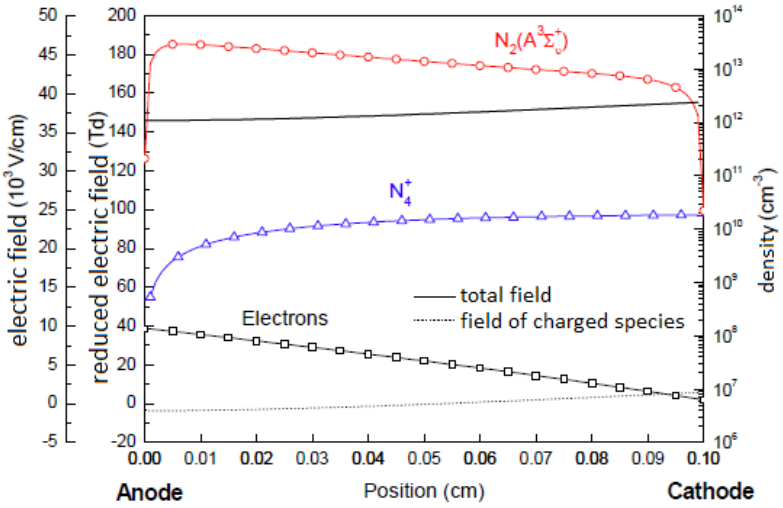

Figure 1-8 Simulations results showing the spatial evolution of density of ions and electrons, the reduced electrical field calculated at the maximum of current in an APTD generated in high purity nitrogen [46]

In section III.1, we discussed the necessary presence of seed electrons to obtain a Townsend breakdown. In the next section, a review of the different mechanisms able to produce seed electrons between two successive discharges is presented.

III.3.2. Memory effect in APTD

Figure 1-9 shows the temporal evolution of the applied voltage and discharge current during the first periods of an APTD generated in high purity nitrogen. One can see that the first two discharges are filamentary as indicated by a large number of micro-discharges visible on the discharge current. On the contrary, the third discharge and the following ones are homogeneous with one single current pulse per half-period of the applied voltage. This clearly indicates the building up of a memory effect during the first discharge period.

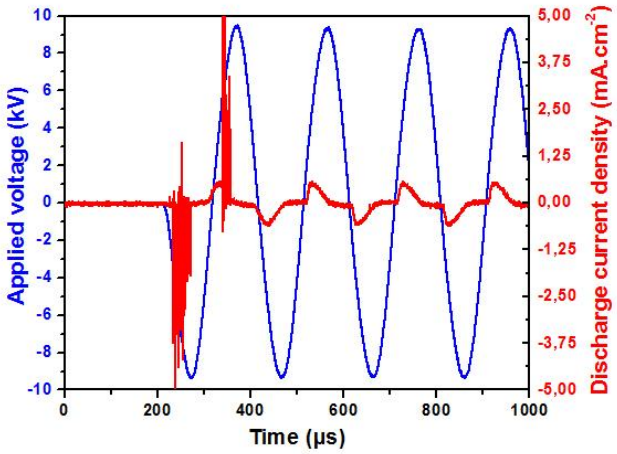

Figure 1-9 Electrical characteristics of the first discharge periods of an APTD in nitrogen [38]

A marker of this memory effect can be seen on the discharge current of Figure 1-10 where the permanent regime is reached. When the gas gap voltage approaches zero, a discharge current is present despite the fact that the discharge is extinguished. Moreover, when the gas gap polarity reverses, the sign of the discharge current rapidly changes suggesting that electrons, which have a high mobility compared to ions, contribute significantly to this current. Consequently, this current jump is related to the presence of seed electrons [48] and its magnitude for a given condition is related to the strength of the memory effect. Thus, the determination of the current jump allows quantifying the memory effect.

A definition of the current jump is proposed in [48]. It can be defined as the mean value of the absolute value of the discharge current when the discharge is turned off, divided by the electrode surface (see equation (1.5)). The analysis interval Δt is defined by the time between the zero passage of the discharge current t_0 and the moment when the time derivative of the discharge current is equal to zero.

$$I_{jump} = \frac{1}{2 \times \Delta t \times surface} \int_{t_0-\Delta t}^{t_0+\Delta t} |I_d(t)| dt \quad (1.5)$$

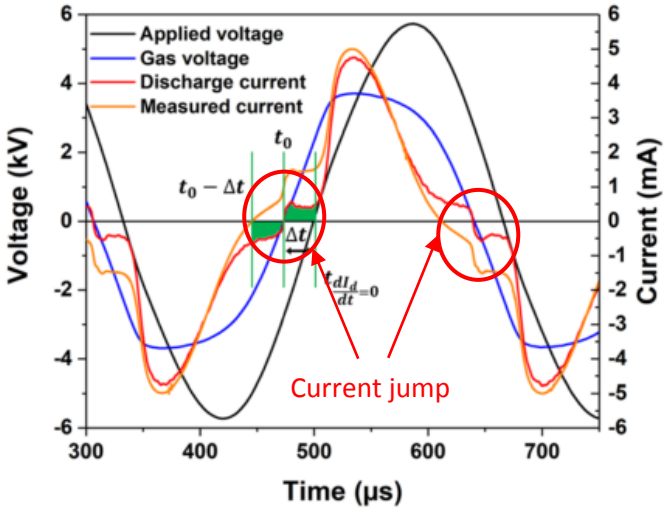

Figure 1-10 Oscillogram of an APTD in nitrogen with 25 ppm O_2 [48]

Many studies were devoted to elucidating the mechanisms involved in the production of these seed electrons between two successive discharges in different experimental conditions. A brief review of these studies is provided in the following.

III.3.2.1. Role of the $N_2(A)$ metastable molecules

Numerous works performed by Massines *et al.* [38,49] showed that a significant amount of $N_2(A)$ metastable molecules is necessary to obtain a Townsend discharge in nitrogen. As shown in Figure 1-8, the density of $N_2(A)$ reaches its maximum value near the anode where the electron density is higher. Indeed, the formation of $N_2(A)$ results from electron excitation of N_2 molecules [50], either directly during the reaction $e^- + N_2 \rightarrow e^- + N_2(A)$ or during the deactivation of $N_2(B)$ state through the reaction $N_2(B) + N_2 \rightarrow N_2(A) + N_2$ where the production of $N_2(B)$ also involves electron excitation. When the polarity of the gas gap voltage reverses *i.e.* when the anode becomes cathode, the latter is submitted to a significant $N_2(A)$ flux by diffusion inducing secondary emission of electrons [51]. This continuous production of seed electrons results in a measurable current corresponding to the current jump. As soon as the voltage becomes sufficient, avalanches develop starting from these seed electrons and the discharge current rises exponentially. This is the breakdown voltage, which diminishes when the amount of seed electrons increases.

Obviously this process is highly related to the secondary emission coefficient γ. The latter can be greatly enhanced by the electron accumulation onto the dielectric surface during the previous discharge *i.e.* when the electrode is the anode. This mechanism is in good agreement with the numerical model developed by Khamphan *et al.* [52]. Indeed, the author showed that a necessary condition to obtain a good description of the discharge behavior was to consider a variable γ coefficient whose value depends on the charge accumulated onto the dielectrics (see Figure 1-11).

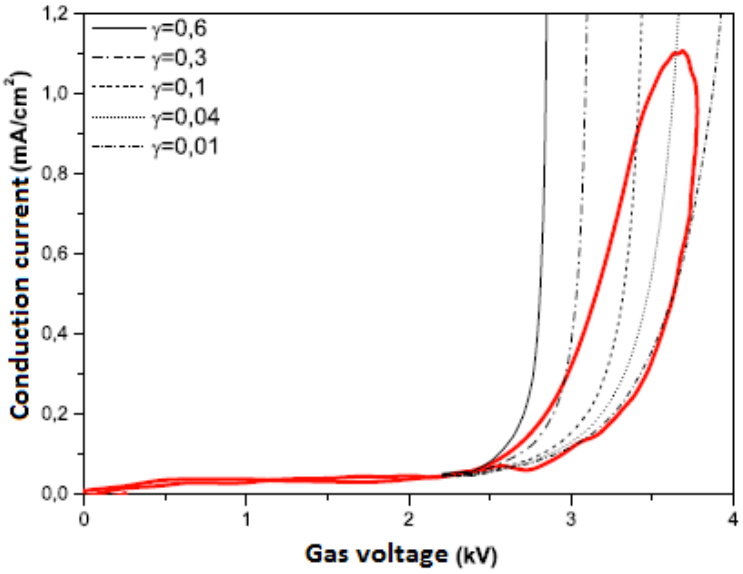

Figure 1-11 The variation of secondary emission coefficient during the whole period of the conduction current [53]

III.3.2.2. Spontaneous electron desorption

The spontaneous electron desorption mechanism was proposed by Golubovskii *et al.* [54] to explain the production of seed electrons leading to the generation of APTD. Nevertheless, this hypothesis was excluded later [55] because it was not able to explain the homogeneous to filamentary transition observed when a significant amount of efficient quenchers of $N_2(A)$ such as NH_3 or O_2 molecules are added into N_2. On the contrary, these experimental observations reinforced the hypothesis of an important role played by $N_2(A)$.

However, more recent experimental works during which homogeneous Townsend discharges were obtained in air or in flowing nitrogen at very low frequency (dozens of Hz), bring a renewed interest on this mechanism [43–45]. In these experiments, the density of $N_2(A)$ metastable molecules is very low or even zero either because of its very high quenching rate by oxygen molecules and their dissociation products, or due to the very long off-time between two successive discharges during which the whole gaseous medium is renewed. In this case, it is clear that only mechanisms arising at the dielectric surfaces can be responsible for the released of seed electrons making spontaneous desorption the most probable mechanism. The very small number of seed electrons released by this mechanism probably explains why APTDs can only be obtained in air for very low frequency *i.e.* for a smooth rising slope of the applied voltage.

III.3.2.3. Gas phase mechanisms in N_2 with small admixture of oxidizing gases

1) Highlight of the special discharge behavior of an APTD generated in N_2 with small addition of oxidizing gases

We saw previously that in high purity nitrogen, the secondary electron emission induced by $N_2(A)$ can play a significant role in the memory effect. In the previous section, we explained that the generation of APTD in air only involves surface mechanism such as the spontaneous desorption of electrons. Nevertheless, the aforementioned mechanisms are unable to explain the experimental behavior observed when a small amount of oxidizing gases is added to nitrogen [48,55,56].

Figure 1-12(a) represents the temporal evolution of the discharge current for an APTD in high purity N_2 and in N_2 with an addition of 50 ppm of O_2, for the same applied voltage. If one compares the case N_2+50 ppm O_2 to the high purity nitrogen case, one can see that: the discharge ignition occurs earlier, the current jump is higher and the amplitude of the discharge current is higher suggesting a higher discharge power. Nevertheless, if the amount of injected oxygen is too high, the obtained discharge becomes filamentary as indicated on Figure 1-12(b) which represents the discharge current for a mixture of N_2 with 500 ppm of O_2 for the same applied voltage. These observations suggest that a mechanism arising in the gas phase enhances the memory effect for small oxygen addition.

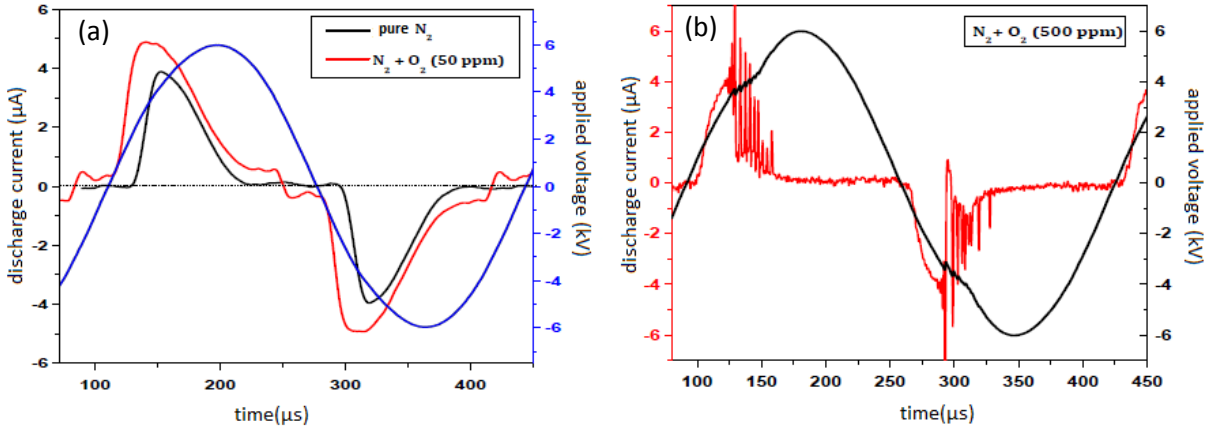

Figure 1-12 Comparison of the discharge current for the same condition (Va=12 kV_{pp}, f=2 kHz) in (a) high purity nitrogen and N_2+50 ppm O_2 and (b) N_2+500 ppm O_2 [56]

To go further in the investigation of this phenomenon, many optical and electrical measurements were performed in our group. The principle of these measurements is described in the following. Then, a small review of the main results obtained in these studies and the corresponding discussions are presented.

2) Investigations on the explanation of this phenomenon

a) Description of the optical emission spectroscopy and electrical measurements

Optical emission spectroscopy (OES) can bring information regarding the relative density of different species of interest. A typical spectrum of APTD in high purity nitrogen is provided in Figure 1-13(a) and a magnification of the spectrum in the range 220-290 nm is provided in Figure 1-13(b). Several emission bands can be identified on this spectrum such as the N_2 second positive system (N_2-SPS) and Hermann Infrared system (N_2-HIR). An interesting point is that the spectrum also exhibits the emission bands of oxidizing species such as the NOγ system or the O(^{1}S)-N_2 green band, despite the high purity of the nitrogen gas used, indicating that the presence of oxidizing species is unavoidable. A possible explanation is that oxygen comes from the interaction between the discharge and the alumina plates used as dielectrics.

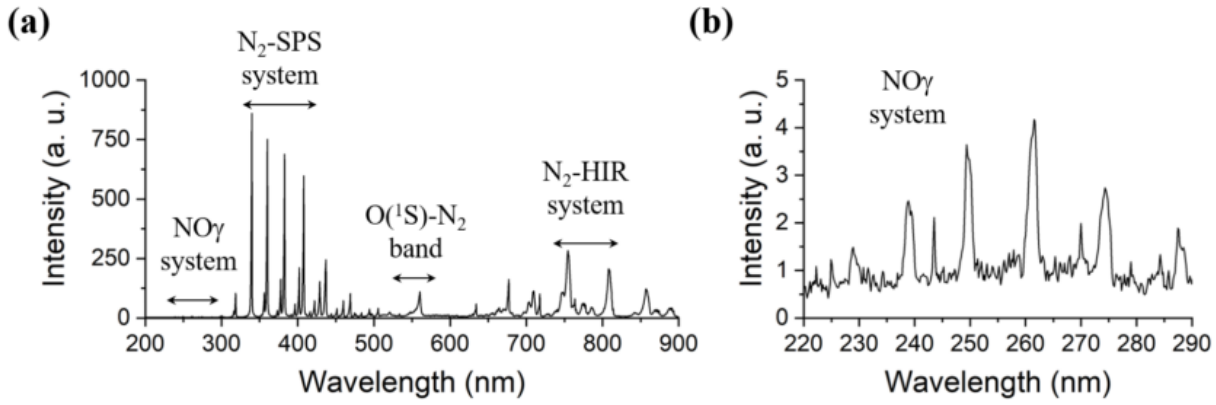

Figure 1-13 (a) Optical emission spectrum of APTD in high purity nitrogen (b) magnification of NO(γ) system [48]

The emission intensity of these bands can be used to estimate the relative densities of the different species involved in the formation of the corresponding excited states [48,55,56]. Table 1-1 summarizes the mechanisms leading to the formation of the different excited states and the relations between the emission intensities and the relative densities.

Table 1-1 Summary of the mechanisms involved in the formation of the excited emitting species

Emission bands	Mechanisms for the production of the excited state
N_2-HIR	$N_2(A) + N_2(A) \rightarrow N_2(C''^5\Pi_u) + N_2$
NO(γ)	$NO(X) + N_2(A) \rightarrow NO(A) + N_2(X)$
ON_2*	$O(^3P) + N_2(A) \rightarrow O(^1S) + N_2$ $O(^1S) + 2N_2 \rightarrow O(^1S)N_2 + N_2$

To study the evolution of the electrical characteristics of the discharge along the gas flow, a dedicated setup was developed during the Ph.D. thesis of Mohamed Cherif Bouzidi [56]. The ground electrode was divided into 8 stripes in the gas flow direction, allowing local current measurements. A simplified schematic description of the device is shown in Figure 1-14(a).

b) Experimental investigations in N_2/NO mixtures

A picture of the discharge in the mixture N_2+30 ppm NO [48] is depicted in Figure 1-14(a). As can be seen, the color of the discharge dramatically changes along the gas flow from violet to green suggesting that significant changes in the gas composition take place along the gas flow. The spatial evolutions of the main emitted intensities between two successive discharges are depicted Figure 1-14(b), together with the evolutions of the current jump and discharge surface power. One can see that the N_2-HIR and $O(^1S)$-N_2 emissions increases from the entrance to the exit of the discharge indicating an increasing density of $N_2(A)$. On the contrary the NOγ system emission decreases which is necessary due to a decrease of the NO concentration since the $N_2(A)$ concentration increases. A probable explanation is that NO molecules are dissociated through the reaction $N(^4S, ^2P, ^2D) + NO \rightarrow N_2 + O(^3P, ^1D)$, thus producing $O(^3P)$ atoms which contributes to the increase of the O^1S-N_2 emission. The increase of the $N_2(A)$ density with the position can be attributed to both the increase of the discharge power and the decrease of its overall quenching rate since the NO dissociation products such as $O(^3P)$ or O_2 are less efficient quenchers of $N_2(A)$ than NO.

The current jump increases along the gas flow indicating an increase of the memory effect. It is interesting to note that it seems to be correlated with the evolution of the N_2-HIR and $O(^1S)$-N_2 emissions.

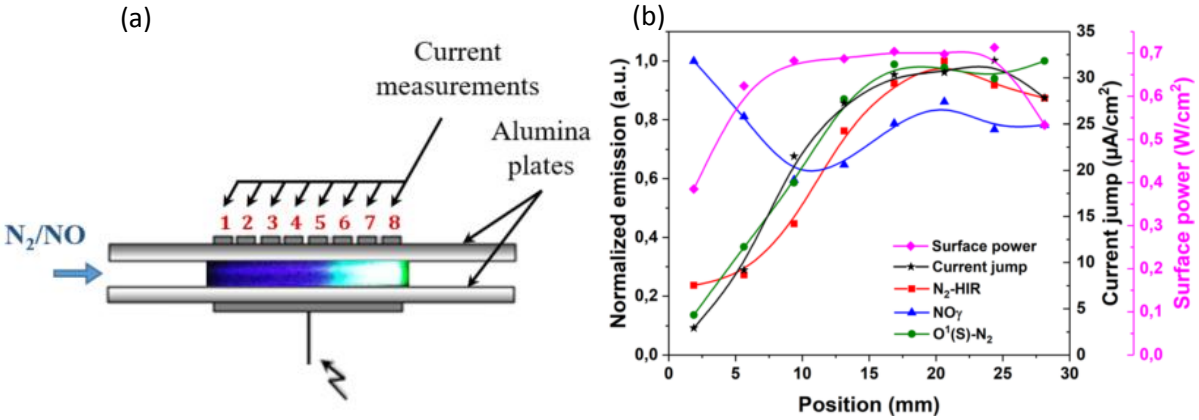

Figure 1-14 (a) Visual aspect of 8 stripes of an APTD; (b) Correlation between the current jump, the surface power and N_2-HIR, NOγ, $O(^1S)$-N_2 emissions as a function of the position of an APTD. Measurement conditions: f=2 kHz, HV=13 kV_{pp}, gap=1 mm, concentration of NO = 30 ppm [48]

c) *Experimental investigations in N_2/O_2 mixtures*

Similar systematic studies were also performed in [48,56] for small oxygen addition into N_2. An example of the results obtained for 50 ppm of O_2 is presented in Figure 1-15(a).

In this case, the intensities of the N_2-HIR, $O(^1S)$-N_2 and NOγ emissions increase along the gas flow together with the current jump. The increase of the N_2-HIR emission suggests an increase of the $N_2(A)$ density, which can be explained by an increase of the discharge power. In a Townsend discharge, $O(^3P)$ atoms are mainly produced during O_2 dissociation through the reaction $N_2(A) + O_2 \rightarrow N_2 + 2O(^3P)$, rather than by electron impact dissociation because of the low electron density compared to the $N_2(A)$ density. Consequently, the increase of the $O(^1S)$-N_2 emission probably results from both the increase of the $N_2(A)$ density and $O(^3P)$ density. Finally, the NO molecules can be produced through the reactions: $N_2(A) + O(^3P) \rightarrow NO + N(^2D)$ and $N(^2D) + O_2 \rightarrow O(^3P) + NO$.

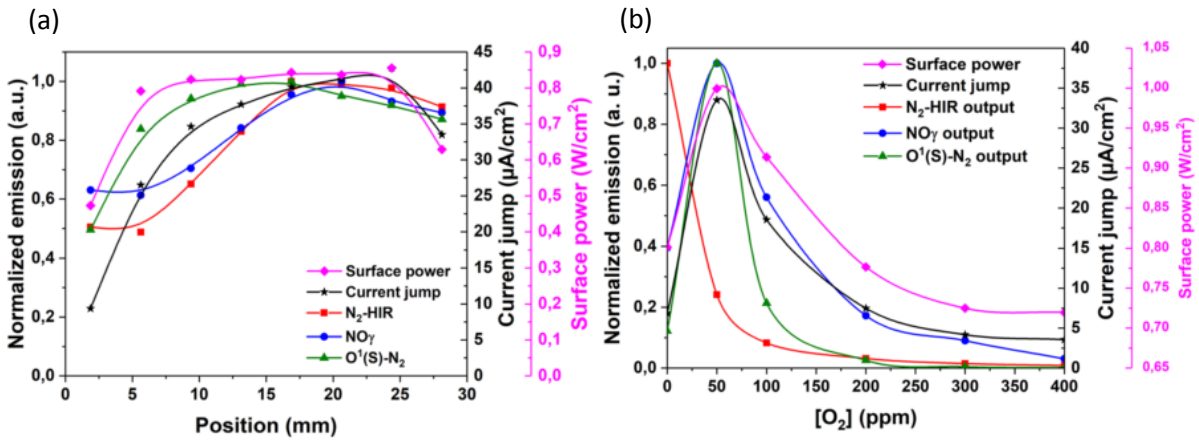

Figure 1-15 Correlation between the current jump, the surface power and N_2-HIR, NOγ, $O(^1S)$-N_2 emissions as a function of (a) position of discharge with an addition of oxygen of 50 ppm; (b) concentration of O_2 at the gas output on the 8th zone. Measurement conditions: f=3 kHz, HV=12 kVpp, gap=1 mm.[48]

Thus, the increase of the NOγ emission intensity is related to the increase of the N_2(A) and NO densities. Note that, as for the case of NO addition into N_2, the spatial evolution of the current jump is strongly correlated to the evolution of the N_2-HIR and O(^{1}S)-N_2 green band emission intensities. To push forward the investigation of these correlations, systematic measurements were performed for different oxygen concentrations. The corresponding results are presented in Figure 1-15(b). Some interesting observations can be made:

- the intensity of the N_2-HIR emission continuously decreases with the injection of O_2 indicating a decreasing N_2(A) density between two successive discharges which can be explained by the increase of the quenching rate of N_2(A) by oxidizing species. The behavior of the current jump and discharge power (described below) is quite different suggesting that the secondary electron emission induced by N_2(A) cannot be the only mechanism responsible for the memory effect.
- Up to 50 ppm of O_2, both the emission intensities of O(^{1}S)-N_2 and NOγ increases indicating an increase of the O(^{3}P) and NO densities since the N_2(A) density decreases. The surface power and current jump also increase suggesting an enhanced memory effect.
- For higher oxygen concentrations, the emission intensities of O(^{1}S)-N_2 and NOγ decrease for increasing oxygen concentrations. It can be explained by the decrease of the N_2(A) density and/or by a decrease of the O(^{3}P) or NO density respectively. Note that the current jump and the surface power also decrease.

These measurements show that the emissions of O(^{1}S)-N_2 and N_2-HIR are strongly correlated to the evolution of the current jump and discharge power. Moreover, this behavior is observed in N_2/O_2 and in N_2/NO mixtures. It suggests that O(^{3}P) atoms and N_2(A) are involved in the memory effect. The mechanism responsible for this phenomenon is likely to occur in the gas phase. A possible candidate able to explain the observed behavior is the associative ionization reaction between N(^{2}P) metastable atoms and O(^{3}P) atoms [57]:

$$\mathrm{N}(\,^2\mathrm{P}) + \mathrm{O}(\,^3\mathrm{P}) \rightarrow \mathrm{NO}^+ + \mathrm{e}^- \qquad \text{(R 1-1)}$$

where N(^{2}P) atoms are produced through excitation of N(^{4}S) atoms by N_2(A) molecules:

$$\mathrm{N_2(A)} + \mathrm{N}(\,^4\mathrm{S}) \rightarrow \mathrm{N_2(X)} + \mathrm{N}(\,^2\mathrm{P}) \qquad \text{(R 1-2)}$$

The addition of a small amount of oxidizing gases brings O(^{3}P) atoms in the discharge volume, which could promote the rate of the associative ionization reaction thus increasing the memory effect. Above a given concentration of oxidizing species, the strong quenching of N_2(A) should result in a decrease of the associative ionization reaction thus decreasing the memory effect.

d) Aim of the study

The aim of the present work is to check the consistency of the previous hypothesis *i.e.* is the associative ionization reaction $\mathrm{N}(\,^2\mathrm{P}) + \mathrm{O}(\,^3\mathrm{P}) \rightarrow \mathrm{NO}^+ + \mathrm{e}^-$ responsible for the increase of the memory effect in APTD when a small amount of oxidizing gas is added to N_2? To answer this question, it is necessary to determine the density of the main species involved in this reaction.

The density of N_2(A) metastable molecules was already determined by Dilecce *et al.* [58] in very similar conditions (APTD in N_2 with ppm of O_2). They found a maximum density during the discharge around 10^{13} cm^{-3} with a corresponding quenching rate in the range 3 10^{-3} – 10^{-4} s^{-1} for oxygen concentration below 400 ppm.

The density of N(^{4}S) and O(^{3}P) can be determined using two photon laser induced fluorescence (TALIF) measurements. Then, knowing the density of N_2(A), it is possible to estimate the production rate of N(^{2}P) atoms due to reaction (R 1-2). To get an accurate estimation of the N(^{2}P) atoms density, it is also necessary to estimate its quenching rate, which in turn requires the knowledge of the density of the main responsible species such as O_2, O(^{3}P) and NO. The density of NO molecules can be obtained from laser induced fluorescence measurements (LIF). Such measurements have been performed in the group during the Ph.D thesis of Et-touhami Es-Sebbar [59]. For this purpose, a dedicated experimental setup was developed and measurements were performed for a wide range of experimental conditions in N_2 [60] and in the mixtures N_2/O_2 [61] and N_2/N_2O [61]. The measured N(^{4}S) density was about few 10^{14} cm^{-3} in pure nitrogen and decreases when oxidizing gas was injected down to few 10^{13} cm^{-3}. The O(^{3}P) density was estimated to be within the range $1 - 3 \times 10^{14}\mathrm{cm}^{-3}$. NO densities as high as 10^{15}cm^{-3} were determined by LIF, which is extremely high. In N_2/O_2, the corresponding conversion efficiency was estimated around 40% and can reach up to 90% in the mixture N_2/N_2O. With this NO density, the metastable N_2(A) would be destructed very efficiently and as a consequence one should not observe the N_2-HIR emissions, in contradiction which is presented on Figure 1-15. Thus, such very high concentrations are poorly probable and need to be confirmed by other measurements. Moreover, the dielectric plates used for the DBD cell were made of quartz whereas other investigations [48,56] were performed with alumina making hazardous the comparison. Indeed, it can have potential consequences since surfaces phenomena related to the memory effect can occur and since the dielectric surfaces are suspected to interact with the discharge leading to the injection of oxidizing species in the discharge volume as explained above.

In this work, we present new measurements of N(^{4}S), O(^{3}P) and NO using the TALIF and LIF technique. For this purpose, the experimental device was improved. The investigation of the main mechanisms responsible for the production and destruction of these species is performed using a 0D model developed in the group and briefly presented in the appendix. The measured densities are then used as input in a simple model to estimate the density of N(^{2}P) atoms following the aforementioned procedure. Then, on the basis of the obtained results, the current jump due to associative ionization reactions is estimated and compared to experimental measurements.

Chapter 2. Experimental set-up

This chapter describes in detail the experimental set-up used to measure the absolute density of N ($2p^3\ ^4S_{3/2}$), O ($2p^4\ 3P_J$) and NO($X\ ^2\Pi$), and the method used to determine the electrical characteristics of the Townsend discharge from electrical measurements.

First, the plasma vessel is described, including the discharge cell and the power supply. Then, we present the method used to determine the electrical characteristics of the discharge. The principle of the laser induced fluorescence diagnostic is then presented and the calibration procedure is detailed. Finally, we describe the system used for laser-induced fluorescence and we detail the measurement procedure.

I. Plasma vessel and pumping system

The plasma vessel is a vertical metallic cylinder equipped with 3 large Brewster angle observation windows dedicated to LIF/TALIF measurements, the volume of the plasma vessel is about 65L.

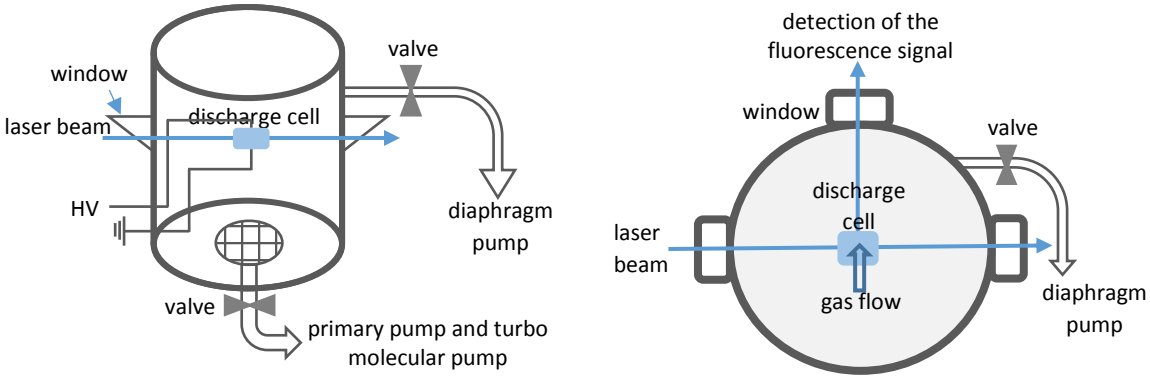

Figure 2-1 (a) General schema of the plasma vessel and pumping system; (b) side view

Figure 2-1 shows the general configuration of the plasma vessel and pumping system. The dielectric barrier discharge apparatus (discharge cell) is positioned at the center of the vessel. Between each experiment, the pressure in the vessel is decreased down to 10^{-6} mbar using a primary pump (Agilent Technologies Rotary Vane Pumps DS602) coupled to a turbo molecular pump (Leybold TURBOVAC 361). During experiments, the gas (provided by AirLiquid) is injected into the chamber up to atmospheric pressure using mass flow controllers (Bronkhorst Hi-TEC). A continuous gas injection is necessary during operation in order to maintain a well-controlled atmosphere and the working pressure is regulated at 1025 mbar using a diaphragm pump (KNF N035.3 AN.18) connected to a microvalve (MKS 0248AC-10000SV).

I.1. Discharge cell and power supply

I.1.1. Discharge cell

Figure 2-2 shows the schema of the discharge cell used for the measurements and photographs are presented in Figure 2-3. The DBD has a plane-to-plane configuration, with a dielectric on each side. The electrodes are made of silver paint directly deposited on the dielectric plates, which consist of 635µm thick alumina plates. The wires used to connect the electrodes to the electrical circuit are pasted using silver epoxy. Finally, the whole metallic surface of the electrodes is coated by a layer of

Araldite in order to avoid arcing. The electrodes have an 18 mm × 22 mm rectangular shape for a corresponding area of S=3.96 cm^2.

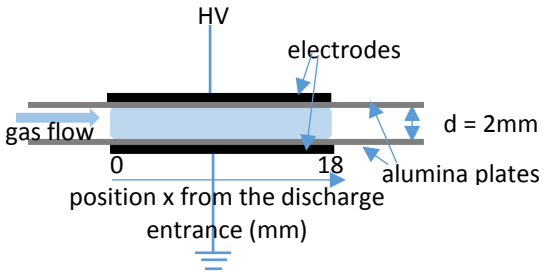

Figure 2-2 Schema of discharge cell and gas flow injection

In order to obtain a laminar and uniform gas flow, a diffuser is placed between the gas inlet and the discharge cell. The gas flow is then guided through the discharge by 4 lateral glass slides. Dielectric plates are inserted onto two slits present on each slide in order to ensure a constant space d=2 mm between the dielectric plates. On each side, the two slides are separated by 2 mm in order to allow the laser beam to cross the discharge.

In this work, many measurements are performed along the gas flow *i.e.* at different x positions from the entrance of the discharge. For this purpose, the whole discharge cell is moved while the laser beam is kept at the same position. More details on the fixation of the discharge cell during the movement could be found in Appendix 2.

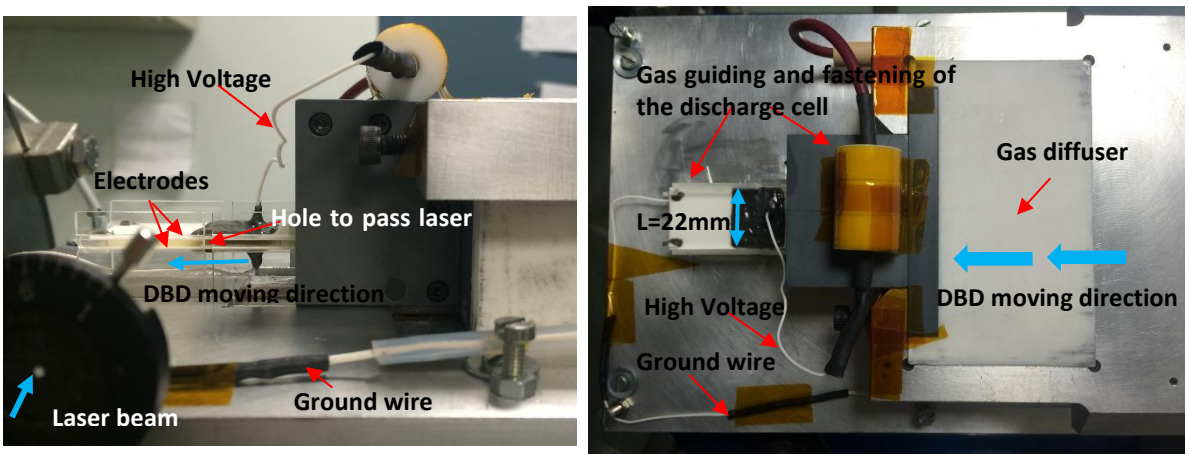

Figure 2-3 Photograph of the plasma reactor presented the discharge cell

At this stage it is important to define τ, the mean residence time of the gas along the discharge:

$$\tau = \frac{x}{v} \tag{2.1}$$

where x is the position from the discharge entrance and v is the mean gas flow velocity. This last parameter can be easily calculated using the following relation:

$$v = \frac{Q}{d \times L} \tag{2.2}$$

where Q is the gas flow rate, d is the distance between the two dielectrics (d =2 mm) and L is the width of the dielectrics perpendicular to the gas flow *i.e.* $d \times L$ represents the area crossed by the gas flow.

I.1.2. Power supply

Figure 2-4 shows the electrical circuit used in the experiment. First, a function generator is used to generate a reference sinusoidal signal. This signal is then amplified by a CREST AUDIO 4801 power amplifier. The output of the amplifier is connected in series to the primary winding of a transformer provided by the Montoux Company through a resistor Ra = 4 Ω. The secondary winding of the transformer is connected in series to the discharge electrodes through a resistor R_m=100 Ω allowing the determination of the measured current I_m.

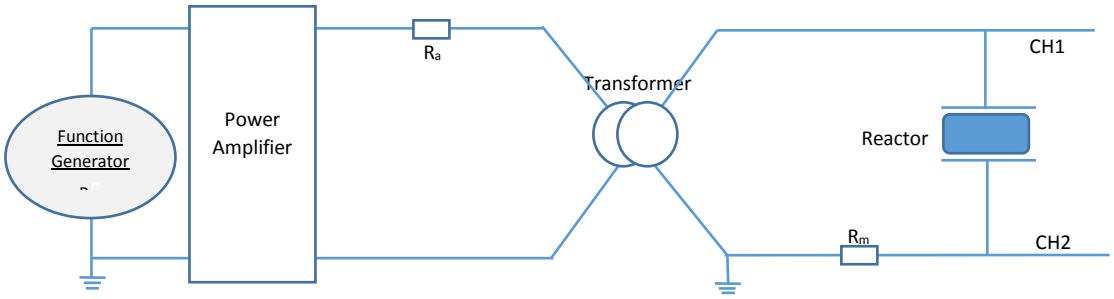

Figure 2-4 Electrical circuit for the power supply of the discharge

I.2. Determination of the electrical characteristics of the discharge

I.2.1. Calculation of the gas gap voltage and the discharge current

To characterize the electrical behavior of the discharge, it is necessary to know the discharge current I_d, which corresponds to the conduction current *i.e.* to the current arising from the motion of the charged particles (ions and electrons) in the electric field, together with the gas gap voltage V_g, which corresponds to the voltage across the gas *i.e.* to the voltage seen by the charged particles in the discharge. These two parameters cannot be measured directly and have to be determined from the measurement of the applied voltage V_a and the measured current I_m using an electrical equivalent circuit of the discharge [62] which is presented in Figure 2-5. The applied voltage V_a is measured using a high voltage probe (Tektronix P6015A) whereas I_m is obtained from the measurement of the voltage across R_m. Both signals are captured by an oscilloscope (LeCroy WAVESURFER 64Xs-A) connected to a computer allowing a direct calculation of the discharge parameters in real time.

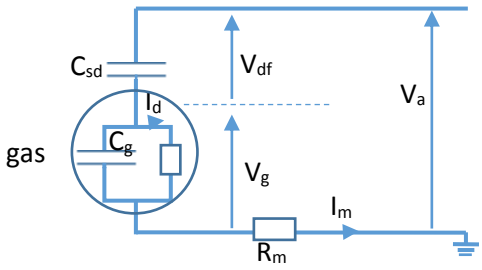

Figure 2-5 Equivalent circuit diagram of discharge cell

The electrical equivalent circuit is presented in Figure 2-5. C_{sd} represents the capacitance of the two alumina plates and C_g represents the capacitance of the gaseous gap before the breakdown. The applied voltage V_a can be separated into two components: V_g and V_{sd}, where V_g is the voltage across the gas gap and V_{sd} is the voltage across the dielectrics. Accordingly, the gas gap voltage V_g is given by:

$$V_g(t) = V_a(t) - V_{sd}(t) \tag{2.3}$$

$V_{sd}(t)$ can be calculated using the following equation:

$$V_{sd}(t) = \frac{1}{C_{sd}} \int_{t_0}^{t_0+t} I_m(t)dt + V_{sd}(t_0) \tag{2.4}$$

where the constant $V_{sd}(t_0)$ is adjusted to ensure that no charge accumulate onto the dielectrics over a period.

The equivalent capacitance of the symmetric dielectrics C_{sd}, is determined by the following equation:

$$C_{sd} = \frac{\varepsilon_0 \varepsilon_r(diel)S}{2e} \tag{2.5}$$

where S is the electrode surface which is equal to the section of the discharge channel in the case of homogeneous discharge S=3.96 cm^2, e is the thickness of an alumina plate (635 µm). The relative dielectric constant $\varepsilon_r(diel)$ is 9.8 and the permittivity of vacuum ε_0 is 8.85 pF/m. Therefore C_{sd} has a typical value around 26.8 pF. Knowing the gas gap voltage V_g, it is possible to separate the discharge current I_d from the current due to the capacitive effect of gas:

$$I_d(t) = I_m(t) - C_g \frac{dV_g(t)}{dt} \tag{2.6}$$

where C_g is the equivalent capacitance of the gas before breakdown which is given by equation (2.7):

$$C_g = \frac{\varepsilon_0 \varepsilon_r(gas)S}{d} \tag{2.7}$$

where $\varepsilon_r(gas) \approx 1$ is the relative permittivity of the gas and d=2 mm is the gas gap. Therefore, we obtain C_g=1.8 pF.

Figure 2-6 shows a typical example of the measured current and applied voltage and the corresponding discharge current and gas gap voltage obtained using the aforementioned procedure.

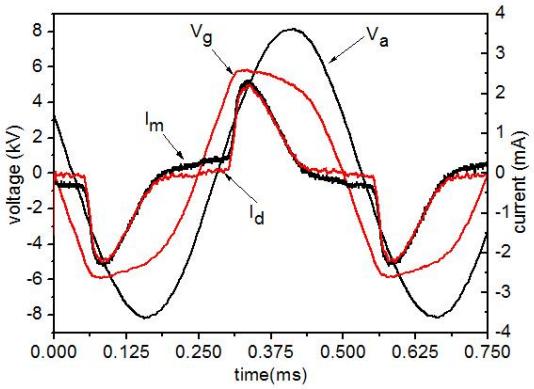

Figure 2-6 Example of electrical characteristics: applied voltage (V_a), gas gap voltage (V_g), measured current (I_m) and discharge current (I_d) in a Townsend discharge. Measurement conditions: HV=17.1 kV_{pp}, f=2 kHz, P=0.9 W/cm^2, flow rate=1.0 L/min, concentration of O_2=0 ppm

I.2.2. Definition and calculation of the discharge power and of the energy dissipated in the discharge

The instantaneous dissipated discharge power, $p(t)$, can be calculated using the following expression:

$$p(t) = I_d(t) \times V_g(t) \tag{2.8}$$

The mean power dissipated in the discharge is the integration of instantaneous power during a period of the excitation voltage:

$$P = \frac{1}{T}\int_0^T p\,(t)dt \tag{2.9}$$

It should be noted that during the experiments, what we used is the surface power density. And in the later chapters that show the experimental results, we take also the surface power density.

$$P_{surface} = P/S \tag{2.10}$$

where S is the electrode surface.

Finally, we define the mean energy E dissipated in the discharge at a given position x from the entrance using equation (2.11). It represents the energy received by a small gas volume a carried out by the gas flow along the time.

$$E = P_{volume} \times \tau = \frac{P}{d \times S} \times \frac{x \times d \times L}{Q} \tag{2.11}$$

where P_{volume}represents the mean volumetric power dissipated in the discharge.

Table 2-1 summarizes the main parameters used in the measurements, the characteristics of the gas and the mass flow controllers used for the injection of each gas.

Table 2-1 Main experimental conditions, gas and mass flow controllers used in the measurements

1.Main experimental conditions		
Electrode surface (cm^2)	3.96	
Gas gap (mm)	2	
Gas flow velocity (L/min)	0.5-2	
Residence time (ms)	0-45(for the gas flow velocity of 1.0 L/min)	
Concentration of O_2 (ppm)	0-200	
Discharge power (W/cm^3)	<6.0	
Pressure (mbar)	1025	
2. Gas used in the experiments		
Type of gas	Purity of gas	
N_2	99.9999%	
Air(N_2/O_2=80/20%)	99.999%	
Mixture of gas(N_2/NO=99.9/0.1%)	99.999%	
Kr	99.998%	
Xe	99.998%	
Ar	99.9999%	
3. Mass flow controller used in the experiments		
Mass flow controller for	Maximum flow	Reference AirLiquid
N_2	10 L/min	ALPHAGAZ 2 AZOTE SMART
Air (used for the injection of O_2)	1 mL/min	ALPHAGAZ 1 AIR AMARTOP
Kr/Xe/NO	4.38/4.22/2.97 mL/min	OTO ST 29 (Mélange SAPHIR)
Ar(used to mix with Xe)	10 L/min	KR-N48(Gaz Pur GAZ RARES)

II. General considerations about laser induced fluorescence

Before the description of the optical system, we present firstly an overview of the laser induced fluorescence diagnostic technique at one (LIF) or two (TALIF) photons. LIF/TALIF is an active spectroscopic method widely used to detect and quantify atomic or molecular species present in a gaseous medium (flames, plasmas…) or even in a liquid [63–67]. Using this technique in a gas discharge offers a mean to detect and quantify species, which do not emit radiations such as atoms or molecules in the ground state or in a metastable state. More details can be found in [58,68,69].

We detail at first the general principle of the LIF/TALIF technique. Then, we describe the calibration method used to determine the absolute densities from the measurements.

II.1. Principle of laser induced fluorescence

In this part, a brief presentation of the principle of LIF/TALIF is provided.

II.1.1. Fluorescence spectroscopy with single-photon excitation (LIF)

A LIF measurement begins with the excitation of an atom or a molecule in state |1> by resonant absorption of a laser photon into a higher state |3>. Subsequently, the excited species de-excite during a transition to a lower state |2> by emitting a photon: this is the fluorescence process. The detection of the fluorescence signal allows, in appropriate conditions, to get information about the population in state |1>. Figure 2-7 represents schematically this process.

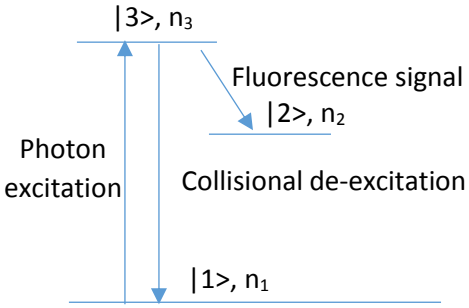

Figure 2-7 Photon excitation schema of principle of LIF

In this study, LIF measurements are performed on NO molecules at atmospheric pressure and consequently other competing de-excitation processes are involved: quenching, vibrational energy transfer (VET) and rotational energy transfer (RET) [68]. They correspond to collisional processes during which the energy of the excited level populated by laser excitation is transferred during a collision to the collision partner. These processes can be of great importance especially in our conditions since measurements are performed at atmospheric pressure. In this description, we neglect other processes such as dissociation and ionization. Note that for sufficiently high laser intensity, the stimulated emission can play a significant role in the transition from level |3> to level |1>.

II.1.2. Fluorescence spectroscopy with two-photon excitation (TALIF)

The excitation wavelength of light atoms is located in the VUV spectral range, which is not convenient from an experimental point of view. Indeed, laser sources in the VUV range are less

available than in the visible range but the most critical point is that oxygen molecules present in the air and possibly in the discharge efficiently absorb VUV radiations. To overcome this limitation, the excitation is realized by the simultaneous absorption of two photons in the UV range and the corresponding technique is called TALIF. Figure 2-8 depicts this principle. Since the two-photon excitation is less efficient than the single-photon excitation, it is necessary to focus the laser beam using a focusing lens, which increases the incoming flux of photons.

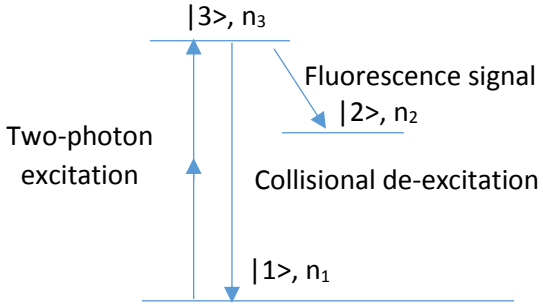

Figure 2-8 Two-photon excitation schema of principle of TALIF

II.2. Theoretical approach

In this section, we use a basic approach of the LIF principle based on a "two-level system". For a sake of clarity, we use the same scheme as presented in Figure 2-7, so that the ground state corresponds to level |1> and the excited state to level |3>. Level |2> is not considered in the subsequent calculations but is used to recall the reader that the final level corresponding to the detected fluorescence can be different from the ground state.

The intensity of LIF signal is directly proportional to the density n_3 of the population in state |3> which is itself populated from state |1>:

$$S_{LIF} \propto A_{3-2} n_3 \tag{2.12}$$

Where A_{3-2} is the Einstein transition probability for spontaneous emission |3>→|2>.

Consequently, one needs to establish the relationship between n_1 and S_{LIF} in order to deduce the density n_1 of the population in state |1> from the measured LIF signal S_{LIF}. It is thus necessary to solve the population balance equation for the level |3>.

The population of level |3> is ruled by the following equation:

$$\frac{dn_3(t)}{dt} = \left(n_1 - \frac{g_1}{g_3} n_3\right) \sigma_{LIF} \left(\frac{I_0(t)}{h\nu_{laser}}\right) - n_3(Q_3 + A_3) \tag{2.13}$$

1 2 3 4

where

- term 1 corresponds to the rise of n_3 by laser excitation from level |1>;
- term 2 corresponds to the stimulated emission from level |3> under laser irradiation;
- terms 3 and 4 correspond to the decrease of n_3 by collisional de-excitation and spontaneous emission respectively;
- n_1 is the ground-state population; g_1 and g_3 are the statistical weights of the levels |1> and |3> respectively; A_3 is the sum of the spontaneous de-excitation probabilities of level |3>

towards all the lower levels; $Q_3 = \sum_i q_i p_i$ denotes the term of collisional depopulation of level|3>, where qi and pi are the quenching rate constant and the concentration of species i respectively; I_0 is the laser irradiance; σ_{LIF} is the one-photon absorption cross section. It can be expressed using the following relation:

$$\sigma_{LIF} = \frac{B_{13} U_\nu}{\frac{I_0}{h\nu_{laser}}} \tag{2.14}$$

where U_ν is the spectral density of laser energy and B_{13} is the Einstein coefficient for stimulated absorption from level |1> to level |3>.

To simplify the resolution of equation (2.13), two limiting cases can be considered depending on the laser energy.

II.2.1. Measurements at low laser energy

For low laser intensity, the stimulated emission corresponding to term 2 in equation (2.13), can be neglected compared to spontaneous emission or collisional de-excitation. Moreover, the population of level |1> remains close to its equilibrium value during the measurement because it is not strongly depopulated: $n_1(t) = n_{10}$. Thus equation (2.13) reduces to:

$$\frac{dn_3(t)}{dt} = n_{10}\sigma_{LIF}\left(\frac{I_0(t)}{h\nu_{laser}}\right) - n_3(Q_3 + A_3) \tag{2.15}$$

To determine the exact solution $n_3(t)$ of this equation, it is necessary to know precisely the temporal behavior of $I_0(t)$. For this reason, many authors considered a simplified solution of this equation, assuming a stationary state, which implies that the laser excitation occurs on a time scale greater than all the other phenomena. This assumption is not easily verified since laser pulses have typical durations lower than 10 nanoseconds.

Nevertheless, for all the measurements performed in the present work, the LIF signal is integrated over the time. Consequently, we are much more interested in the value of $\int_0^\infty n_3(t)dt$ rather than in the instantaneous value of $n_3(t)$.

It is thus possible to avoid the use of the stationary state assumption by integrating equation (2.15) over the whole time measurement, which results in the following relation:

$$\int_0^\infty \frac{dn_3(t)}{dt}\mathrm{dt} = 0 = \int_0^\infty \left(n_{10}\sigma_{LIF}\left(\frac{I_0(t)}{h\nu_{laser}}\right) - n_3(Q_3 + A_3)\right)dt \tag{2.16}$$

Indeed, considering that the density of level |3> before the laser pulse and after the measurement is zero *i.e.* $n_3(0) = n_3(\infty) = 0$, the total variation of n_3 is also zero.

We can thus deduce the integrated density:

$$\int_0^\infty n_3(t)dt = \frac{n_{10}\sigma_{LIF}}{h\nu_{laser}}\frac{1}{Q_3+A_3}\int_0^\infty I_0(t)dt = \frac{n_{10}\sigma_{LIF}}{s}\frac{1}{Q_3+A_3}\left(\frac{E_L}{h\nu_{laser}}\right) \tag{2.17}$$

where $\int_0^\infty I_0(t)dt = E_L/s$

with s is the laser beam section and E_L the energy delivered by the laser during one pulse.

The collected LIF signal intensity S_{LIF} can thus be expressed as:

$$S_{LIF} = \mathrm{K}\sigma_{LIF}\frac{A_{32}}{Q_3+A_3}\left(\frac{E_L}{h\nu_{laser}}\right)n_{10} \quad (2.18)$$

where K is a factor that depends on the geometry of the setup which takes into account the solid angle and the spectral response of the detection system. In principle, it is possible to directly calculate the absolute density n_{10} but in practice, the constant K is often difficult to evaluate. To overcome this problem, it is possible to calibrate the measurement as explained in section II.3.

II.2.2. Measurements at high laser energy

For sufficiently high laser energy, the transition |1> → |3> may saturate during the laser pulse: the de-population of level |1> by laser absorption becomes significant as well as the laser induced emission rate between levels |3> and |1> which dominates the collisional and spontaneous emission rates. Consequently, during the laser pulse levels |1> and |3> are in equilibrium ruled by the laser irradiation and $n_1/g_1 = n_3/g_3$. Since $n_{10} = n_1 + n_3$, the population of level |3> can be expressed by equation (2.19).

$$n_3 = \frac{g_3}{g_3+g_1}n_{10} \quad (2.19)$$

This relation implicitly assumes that a stationary state is reached during laser excitation. In this regime, the population of level |3> does not depend on the quenching rate. The fluorescence signal can be easily approximated in saturated regime considering two limiting cases [70]. If the fluorescence lifetime is short compared to the laser pulse duration τ, the fluorescence signal detected after the end of the laser pulse is negligible and the fluorescence signal can be expressed as:

$$S_{LIF} = KA_{32}\frac{g_3}{g_3+g_1}n_{10}\tau \quad (2.20)$$

If on the other hand, the fluorescence lifetime is greater than τ, then the detected fluorescence signal mainly corresponds to the signal collected after the end of the laser pulse and is then given by:

$$S_{LIF} = K\frac{A_{32}}{Q_3+A_3}\frac{g_3}{g_3+g_1}n_{10} \quad (2.21)$$

In the saturated regime, the LIF signal does not depend on the laser energy anymore.

Working in the saturated regime can be interesting because the LIF signal is directly quantitative: it does not depend on the laser intensity. Nevertheless, it also presents some disadvantages. It requires high laser energy, which can be difficult to obtain and which can induce several drawbacks such as photo-dissociation or ionization of the gas. Moreover, if the laser beam is not homogeneous spatially, the saturation may be incomplete.

II.2.3. TALIF signal

In the case of two photons laser absorption fluorescence (TALIF) spectroscopy, the TALIF signal in the linear regime can be deduced from equation (2.18) under low laser energy by taking the absorption of two photons into account [71]:

$$S_{TALIF} = KG^{(2)}\sigma_{TALIF}\left(\frac{E_L}{h\nu_{laser}}\right)^2\frac{A_{32}}{(Q_3+A_3)}n_{10} \quad (2.22)$$

where σ_{TALIF} is the two-photon excitation cross section(unknown), $G^{(2)}$ is the photon statistic factor (equals to 2 for the absorption of two photons from a chaotic radiation field of a laser with no phase

correlations [71–73]) and K is the experimental factor. As can be seen, the TALIF signal is proportional to the square of the laser energy in the linear regime. As for LIF, it saturates at higher laser energy.

II.2.4. Determination of the LIF/TALIF regime

In this work, measurements are performed in the linear regime. It is thus necessary to determine the laser energy E_{SAT} at which the transition starts to saturate for each species (N, O or NO) and for each experimental condition (discharge power, gas composition, position along the gas flow…). For this purpose, preliminary measurements are performed and the LIF/TALIF signal $S_{LIF/TALIF}$ is measured for different laser energy E_L. $S_{LIF/TALIF}$ is then plotted as a function of E_L in log-log scale, as shown in Figure 2-9. In the non-saturated regime, $S_{LIF/TALIF}$ exhibits a linear variation with respect to E_L with the corresponding slope being 1 for LIF and 2 for TALIF as indicated by equations (2.18) and (2.22).

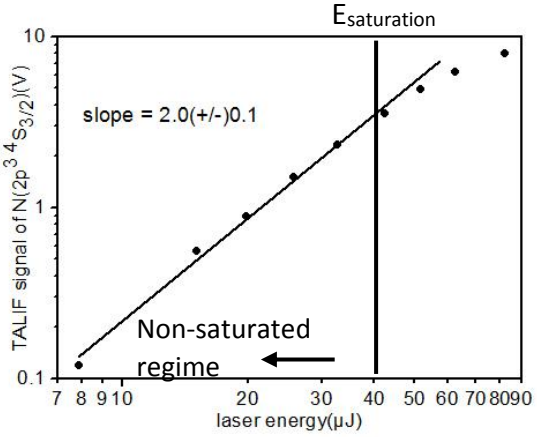

Figure 2-9 Log-log plot of the N atom fluorescence signal as a function of laser energy. Measurement conditions: P=0.6 W/cm², f=2 kHz, HV=15.8 kV_{pp}, position=14 mm, flow rate=1.0 L/min, concentration of O_2=0 ppm

In the subsequent experiments, the laser energy is kept below E_{SAT}.

II.2.5. Measuring the LIF/TALIF signal

Figure 2-10 represents the temporal evolution of a LIF signal after one laser pulse. It corresponds to photons emitted by laser-excited atoms during their radiative de-excitation. The stiff rise of the signal indicates the beginning of laser excitation. After the laser pulse, the LIF signal decreases exponentially. This decrease provides a direct picture of the aforementioned de-excitation processes.

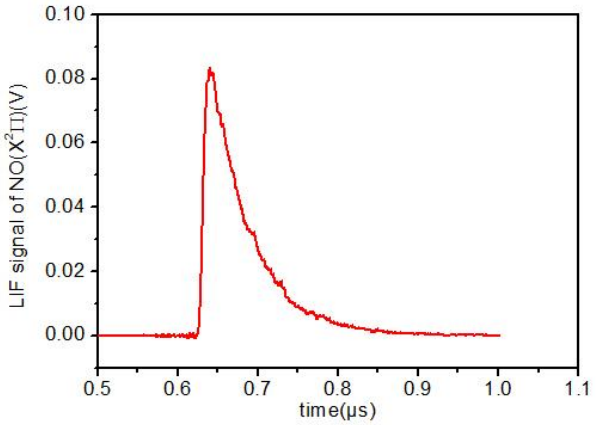

Figure 2-10 LIF signal as a function of time for the transition NO(X $^2\Pi$) -> NO ($A^2\sum$) in a mixture of 1.8 ppm NO in N_2 for a total pressure of 1025 mbar. Measurement conditions: position=14 mm

In this work, the LIF signal at a given wavelength is obtained after time integration. In order to increase the signal to noise ratio, time integrated signals are averaged over typically 500 measurements. To determine the density of a specie, it is recommended to perform an excitation profile of the whole line corresponding to the transition of interest. For this purpose, the laser wavelength λ_{LASER} is tuned and the averaged time integrated signal is recorded for each value of λ_{LASER}. Figure 2-11 represents an example of such an excitation profile.

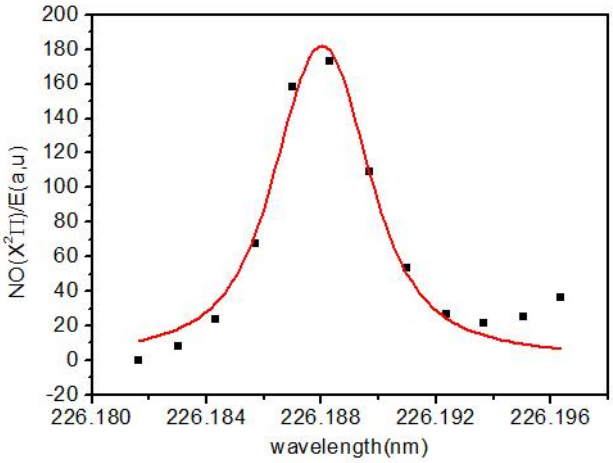

Figure 2-11 Excitation spectrum for the transition NO(X $^2\Pi$) -> NO ($A^2\sum$) in a mixture of 1.8 ppm NO in N_2 for a total pressure of 1025 mbar. Measurement condition: x=14 mm

The shape of the excitation profile strongly depends on the operating conditions. At low pressure, the line profile is essentially Gaussian and results from a convolution of the effective laser line profile and the Doppler broadening profile. In this study, measurements are performed at atmospheric pressure. In these conditions, the line profile corresponds to a Voigt profile resulting from the convolution of Gaussian profiles (laser line profile, Doppler broadening) and Lorentzian profile due to the van der Waals broadening [74].

II.3. Calibration method: obtaining absolute densities

As explained in section II.2.1, a calibration procedure is necessary to obtain absolute values of the density from LIF/TALIF measurements. Several methods have been developed for this purpose [69,75]. For example, absolute densities can be obtained with another diagnostic (*e.g.* absorption or CRDS measurements) in the same conditions as for LIF/TALIF measurements. Rayleigh scattering can also be used to calibrate LIF measurements. In this case, the calibration is based on the comparison between the LIF signal and the Rayleigh scattering signal obtained in similar conditions (laser energy and wavelength, collection system) using a reference gas (usually a noble gas). Nevertheless, this method is not applicable to TALIF due to the non-linearity of the process.

In the present work, the calibration is performed by another method that consists in injecting a known concentration of calibrating gas in the vessel. Then LIF/TALIF measurements are performed which provides a relation between the LIF/TALIF signal and the specie concentration. Two situations are encountered:

- the probed specie is a stable compound such as NO(X). In this case, the calibrating gas injected in the vessel corresponds directly to probed specie.
- The probed specie is not stable such as N(^{4}S) and O(^{3}P). In this case, the calibrating gas corresponds to another specie (generally a noble gas) having an excitation scheme similar to the excitation schema of the probed specie.

II.3.1. Calibration of LIF measurements on NO(X)

In this case, the calibration is straightforward since NO can be directly injected in the vessel at a known concentration. All the details concerning the calibration procedure for NO are reported in chapter 5 section II.

II.3.2. Calibration of TALIF measurements on N(^{4}S) and O(^{3}P)

In this case, the calibration is performed by injecting a known concentration of noble gas in the vessel: the calibrating gas is krypton for N(^{4}S) and xenon for O(^{3}P). This method was proposed by Goehlich *et al*. and Niemi *et al*. [71,76]. Here, we consider the case of N(^{4}S) and krypton as an example to explain the principle of the calibration. Figure 2-12 represents the two excitation schemes used for the measurements of N(^{4}S) atoms and their calibration using krypton. As can be seen, the excitation wavelengths are very similar. It allows to use the same laser for both measurements (dye, optical settings) and then to keep the same experimental arrangement.

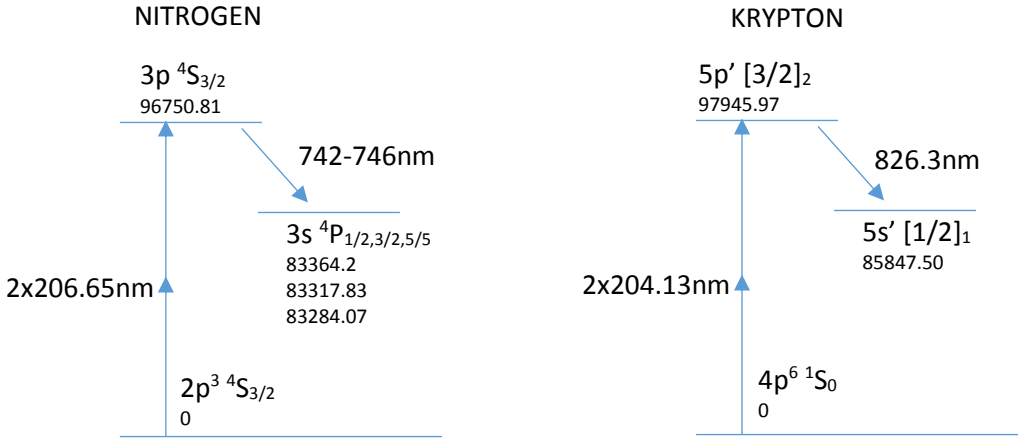

Figure 2-12 Tow-photon excitation schema of nitrogen and krypton. The level energies are given in cm^{-1}

The detected fluorescence wavelengths differ about approximately 80 nm from each other and are located in the red spectral region. Consequently, the same detector (in this case a photomultiplier tube, see section III.1.1) can be used for both measurements but two different interference filters have to be placed in front of the photomultiplier tube.

Using equation (2.22) to express the fluorescence signal for the experiment and the calibration allows to obtain the absolute density of ground state atoms n_{10}:

$$n_{10}(X) = \frac{K(calib)}{K(X)} \frac{\left(\frac{E_L}{h\nu_{laser}}\right)^2(calib)}{\left(\frac{E_L}{h\nu_{laser}}\right)^2(X)} \frac{\frac{A_{32}}{(Q_3+A_3)}(calib)}{\frac{A_{32}}{(Q_3+A_3)}(X)} \frac{S_{TALIF}(X)}{S_{TALIF}(calib)} \frac{\sigma_{TALIF}(calib)}{\sigma_{TALIF}(X)} n_{10}(calib) \quad (2.23)$$

In this equation, the label (X) indicates the parameters involved in the measurement of N(^{4}S) whereas the label $(calib)$ refers to the parameters involved in the calibration. The different Einstein coefficients are available in the literature. The quenching coefficients can be either calculated using the data in the literature or obtained from experimental measurements. The laser energy per pulse E_L and the TALIF signal S_{TALIF} are measured. The ratio of the two excitation cross sections is available in the literature. Consequently, the only remaining unknown is the ratio $K(calib)/K(X)$ but since the setup is the same for both measurements all the geometric considerations such as the solid angle of the detection system or the probed volume cancels each other. Thus this ratio reduces to:

$$\frac{K(calib)}{K(X)} = \frac{\eta_{calib} T_{calib}}{\eta_X T_X} \quad (2.24)$$

where $\eta_{calib/X}$ represents the quantum efficiency of the photomultiplier tube at the detection wavelength and $T_{calib/X}$ represents the transmission of the interference filter at the detection wavelength for the calibration and the measurement respectively.

Note that S_{TALIF} corresponds to the TALIF signal integrated over the whole excitation profile (area under the curve) and not to its maximum value at the central wavelength [74]. Indeed, if the calibration is performed at a different pressure than the measurement itself, which is often the case, the different Van der Waals broadening of the lines could result in wrong density estimation (the laser line broadening can be considered to be the same since the laser setup is identical for both the measurement and the calibration).

III. LIF/TALIF setup

In this section, we describe the optical setup used for the LIF/TALIF measurements.

III.1. Laser system

As explained later, LIF and TALIF measurements on N, O and NO require a tunable laser beam in the UV range. For this purpose, we use a dye laser (Sirah Cobra-Stretch Dye laser) [77] pumped by a Nd:YAG laser (Spectra-Physics Quanta-ray) [77].

The Nd-YAG laser is optically pumped by krypton flash lamps and operates in a pulsed mode, with a frequency of 10Hz. An external function generator is used to trigger the laser pulses. The original 1064 nm laser beam is converted into its second harmonic using a KDP crystal resulting in a 532 nm laser beam used to pump the dye laser. According to the manufacturer, the temporal width of the laser impulsions is around 8 ns.

Figure 2-13 shows a sketch of the internal structure of the dye laser. It is composed of several stages: resonator, pre-amplifier, and amplifier. The resonator is made by an optical arrangement creating a closed beam path *i.e.* a laser cavity. It consists of the output coupler mirror OC, the dye cell DC_{20}, the prim expander PE, the grazing-incidence grating G_1 and the second grating G_2 used to tune the laser wavelength. In our configuration, the grating G_2 is blazed at 2400 grooves/mm for a corresponding resolution of 0.04 cm^{-1}. The DC_{20} cell is filled with the circulating dye and serves as the amplifier media. The 532 nm pump beam is focused by the lens C_1 into the dye cell to excite the dye. The light emitted by the dye during its de-excitation is spectrally filtered by the cavity and the remaining wavelength radiations are trapped in the cavity to produce the new laser beam. In our conditions, the used dye produce a beam in the red spectral region.

The beam created in the laser resonator propagates from the output coupler mirror (OC) to the left side, where it first passes three Brewster plates, which do some additional polarization filtering. The beam then passes a prism arrangement which turns it by 180° and shifts it upward. Then, the dye laser beam passes a second time through the dye cell, which is now used as a pre-amplifier. For the pre-amplification process, the dye is pumped by the 532 nm beam focused by lens C_2. Finally, a larger dye cell (DC_{40}) is used to further increase the laser pulse energy: this is the amplifier.

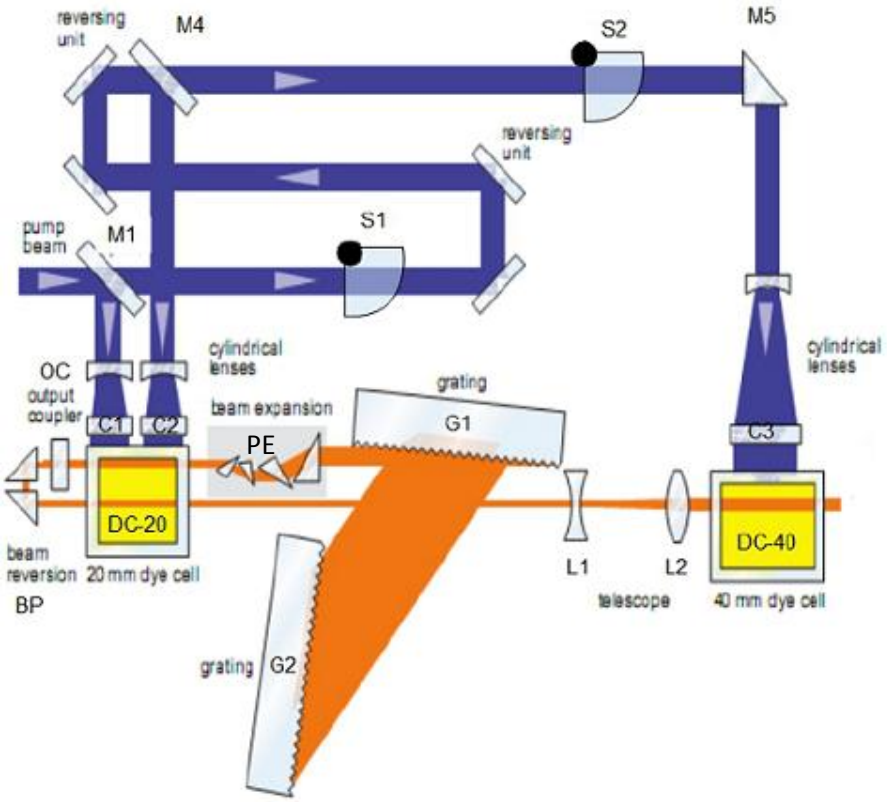

Figure 2-13 Optical set-up of the Cobra-Stretch (G_1-grating; G_2-mirror/grating used for tuning; PE-prism expander; DC_{20}-dye cell 20mm; DC_{40}-dye cell 40mm(optical); OC-output coupler; L_1,L_2-telescopic lenses; BP-polarizing Brewster plates with 180° turning prism; M_i-mirror for pump beam; C_i-cylindrical lenses; S_i-beam shutters) [77]

To obtain a laser beam in the UV range, it is necessary to divide the obtained wavelength by a factor 3. As is shown in Figure 2-14, which summarizes the 2 different steps involved in the production of the UV laser beam. First, the red laser beam passes through the first conversion unit (FCU1) - a doubling crystal made of KDP to generate the second harmonic. At the exit of the FCU1, the remaining fundamental radiation and the second harmonic are combined in the second conversion unit (FCU2) (*i.e.* a BBO crystal) to generate the third harmonic in the UV range. A wavelength separation unit is then used to remove the remaining portion of fundamental and second harmonic.

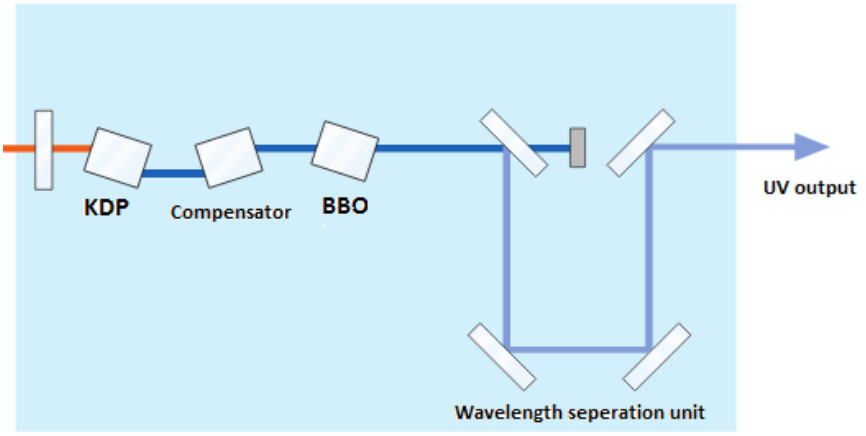

Figure 2-14 Typical configuration of two crystals for the generation of UV laser (adapted from [77]*)*

The laser is turned on at least one hour before each experiment during which the laser energy per pulse increases until it reaches a stationary value indicating that the laser system is in thermal equilibrium. Note that the optimum laser energy in the UV range can be obtained only if the angular position of the FCUs with respect to the incoming laser beam is optimum, this position being temperature dependent. This setting is important because a miss-adjusted FCU can dramatically change the laser beam shape. In the standard configuration of the Sirah dye laser, only the first FCU is equipped with a temperature stabilization unit. Consequently, we observed during early measurements that the position of the second FCU had to be permanently adjusted to compensate for the FCU heating under laser irradiation. To solve this problem, the second FCU was also equipped with a temperature stabilization unit. We also observed that the UV laser beam was continuously shifting during laser operation probably because of the heating of the gratings. For this reason, it is important to probe the whole profile during LIF/TALIF measurements instead of only the maximum. To limit the increase of the room temperature, the air conditioning is running during experiments to maintain a temperature of around 20°C.

The temporal profile of the laser pulse is an important data when doing LIF/TALIF measurements, especially if one wants to determine the temporal decay of the fluorescence signal. One way to determine this profile is to perform Rayleigh scattering measurement of the laser beam. For this purpose, the laser wavelength was tuned to 225 nm and the vessel was filled with high purity nitrogen (see Figure 2-15) up to a pressure of 1013 mbar. The Rayleigh scattering signal was measured using the R928 photomultiplier tube (PMT) biased at 1kV and mounted on the monochromator centered at the laser wavelength. No amplifier was used at the output of the PMT to avoid any distortion of the signal. To ensure that no parasitic reflection is present, a background obtained by doing a similar measurement under vacuum condition was subtracted to the scattering signal. The resulting temporal profile depicted in Figure 2-15. We found that the FWHM of the profile is 10 ns for a base width around 20 ns. The decay rate after the maximum of the laser pulse was estimated considering an exponential fit and a value of 1.9 10^8 s^{-1} has been found.

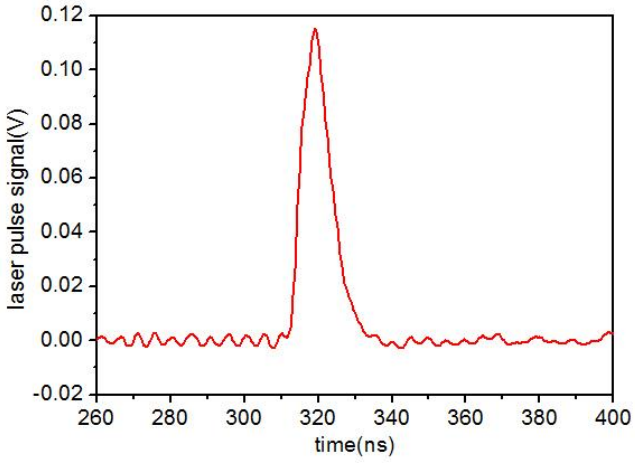

Figure 2-15 Laser pulse as a function of time obtained by Rayleigh scattering. Measurement conditions: total pressure=1013 mbar of nitrogen, laser and detection wavelength: 225 nm.

III.1.1. Configuration for measurement of N ($2p^3\ ^4S_{3/2}$) and Kr ($4p^6\ ^1S_0$)

The optical setup used to measure the absolute density of N ($2p^3\ ^4S_{3/2}$) by TALIF is presented in Figure 2-16. The same setup is used for the measurement of Kr ($4p^6\ ^1S_0$) during the calibration of the TALIF signal. The Nd:YAG laser beam at 532 nm is used to pump the dye composed of a mixture of Rhodamine (Rh B/Rh 101) diluted in ethanol with a maximum efficiency around 615 nm, the corresponding tuning curve of the dye is shown in Figure 2-17. The grating G_2 is adjusted to tune the wavelength around 621 nm for the measurement of N atoms and 613 nm for Kr atoms. After tripling, wavelengths of 207 nm for the excitation of N atom and 204 nm for Kr atoms are obtained. The laser energy per pulse is tuned using a variable attenuator composed of two rotating plates. The first one acts as a filter whose transmission depends on the angle between the plate and the laser beam whereas the second one is used to compensate for the laser beam deviation.

Since the two-photon excitation cross section is small, a focusing lens with a focal length of 50 cm is used to focus the laser beam at the center of the 2 mm gap of the DBD. In front of the laser beam, a laser energy meter (OPHIR P/N 1Z01500) is used to monitor the laser energy in real time. The detection of the fluorescence signal is performed at 90°. A 50 cm focal lens is used to focus the fluorescence light onto a PMT associated with an interference filter. The fluorescence signal at the output of the PMT is then amplified by a homemade 32 dB amplifier and transmitted to a Boxcar averager connected to a computer (more details could be found in section III.2).

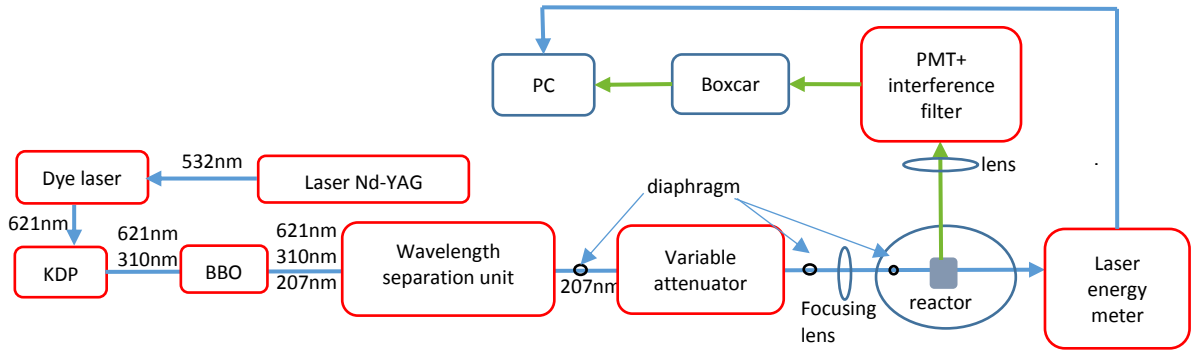

Figure 2-16 Experimental set-up for the measurement of N ($2p^3\ ^4S_{3/2}$)

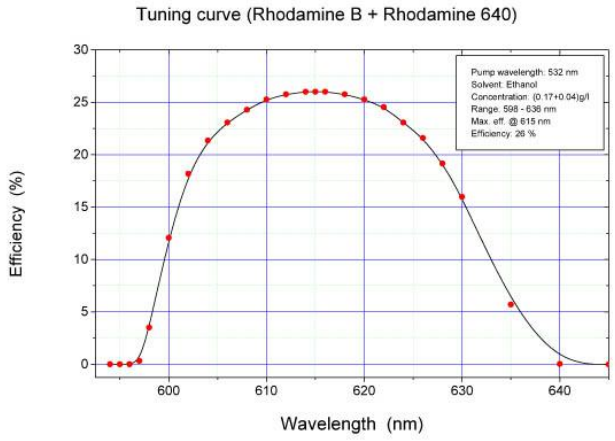

Figure 2-17 Tuning curve of pyridine1 used for a pulsed, 532nm pumped laser [77]

The characteristics of the interference filter (Andover Corporation Optical Filter) used for TALIF on N (P/N: 750FS20-25) and Kr (P/N: 830FS20-25) atoms are given in Table 2-2 and their respective transmission curves are presented in Figure 2-18 (a) and (b).

Table 2-2 Characteristics of the interference filter use for TALIF measurements of N and Kr atom

Interference filter used for TALIF measurement of	Central wavelength (nm)	FWHF (nm)
N	750	20
Kr	830	20

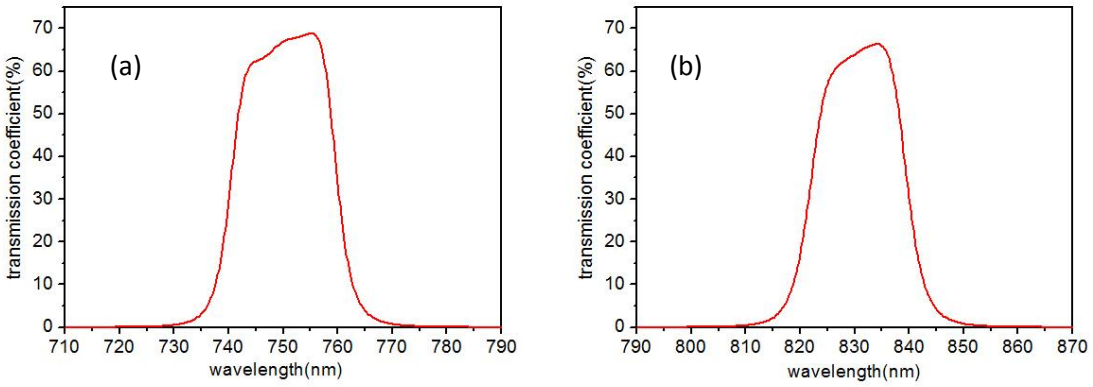

Figure 2-18 Transmission curve of interference filter used for TALIF measurements of N (a) and Kr (b) atom

III.1.2. Configuration for measurement of O ($2p^4\ ^3P_J$) and Xe ($5p^6\ ^1S_0$)

The TALIF system for the measurements of O ($2p^4\ ^3P_J$) and the corresponding calibration using Xe ($5p^6\ ^1S_0$), shown in Figure 2-19, is similar to the one presented in section III.1.1, except for the dye and the interference filter placed in front of the PMT.

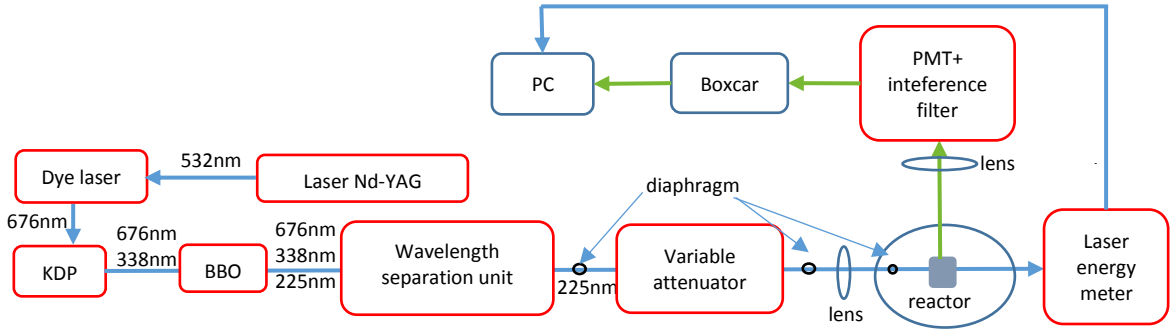

Figure 2-19 Experimental set-up for the measurement of O ($2p^4\ ^3P_J$)

To generate the excitation wavelengths, which are in the range [224-226] nm, we use pyridine 1 (commercialized by Exciton under the name LDS 698) diluted in ethanol with a maximum efficiency around 692 nm, the corresponding tuning curve of dye is shown in Figure 2-20. The red wavelength is then tripled following the same procedure as previously described. It is also possible to use another dye, namely Coumarin 2 with peak efficiency around 450 nm which has the advantage to require only frequency doubling and thus to provide higher laser energy in the UV range. Nevertheless, the lifetime of Coumarin is rather small (generally around a weak). Moreover using Pyridine 1 has the

advantage to require only small adjustments of the dye laser and the FCUs since the dye spectral region remains in the red.

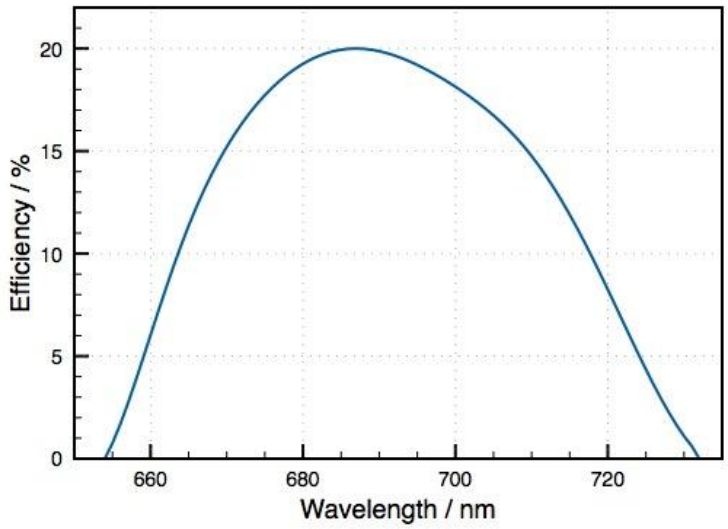

Figure 2-20 Tuning curve of pyridine1 used for a pulsed, 532 nm pumped laser [77]

The characteristics of the interference filter used for TALIF on O (Andover Corporation Optical Filter P/N: 850FS20-25) and Xe (Edmund 65725) atoms are given in Table 2-3 and their respective transmission curves are presented in Figure 2-21.

Table 2-3 Characteristics of the interference filter use for TALIF measurements of O and Xe atom

Interference filter used for TALIF measurement of	Central wavelength (nm)	FWHF (nm)
O	850	20
Xe	830	10

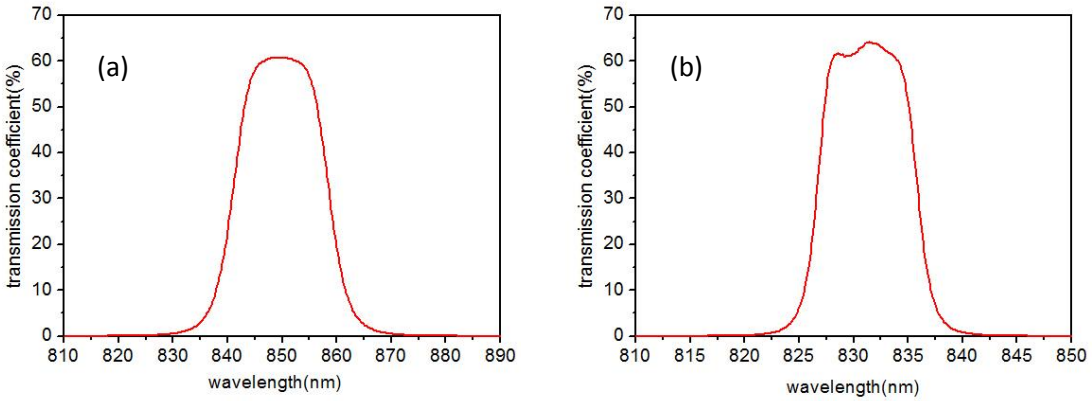

Figure 2-21 Transmission curve of interference filter used for TALIF measurements of O (a) and Xe (b) atom

III.1.3. Configuration for measurement of NO

The NO is excited from the ground state NO(X $^2\Pi$,v=0) to the excited state NO(A $^2\Sigma$,v=0) and the corresponding excitation wavelength is around 226 nm. Consequently, the same dye can be used for measurements on O and NO. For LIF measurements, there is no need to focus the laser beam. On the contrary, it would result in a saturation of the transition. The focusing lens put before entering the discharge is then removed.

The detected fluorescence light corresponds to the transition NO(A $^2\Sigma$,v=0)→NO(X $^2\Pi$,v=1) around 235 nm. It is collected perpendicularly to the laser beam and focused by two quartz lenses on the entrance slit of a monochromator (Jobin Yvon HR 320). Using a monochromator instead of an interference filter allows obtaining a smaller detection bandwidth which is of primary importance for the LIF measurements on NO in our condition. Indeed, during preliminary measurements using a broad interference filter, a parasitic signal was detected. It was attributed to the fluorescence of the alumina plates and/or of the glass slides probably because the laser beam slightly hit them even if it was not visible to the naked eyes. The interference filter was then replaced by the monochromator and a careful attention was paid to ensure that no parasitic signal remains whereas the whole vibrational band of the transition NO(A $^2\Sigma$,v=0)→NO(X $^2\Pi$,v=1) was captured. For this purpose, the detection bandwidth was adjusted by setting the slit widths and the central wavelength was adjusted by moving the monochromator grating.

The rest of the setup is similar to the previous cases. It is depicted in Figure 2-22.

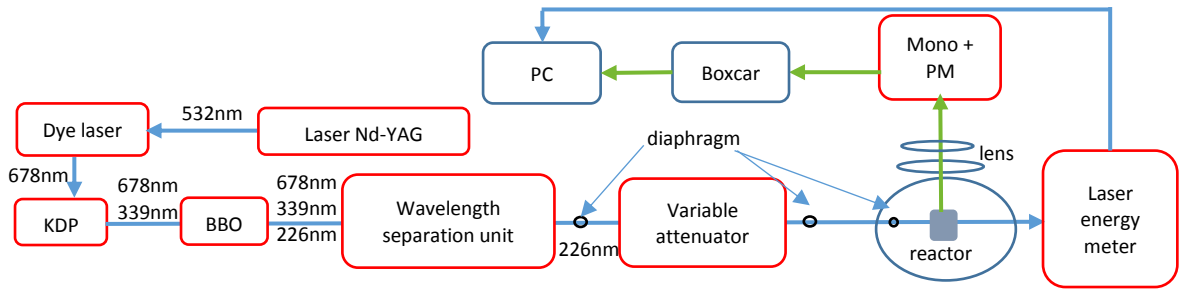

Figure 2-22 Experimental set-up for the measurement of NO(X $^2\Pi$)

III.2. Acquisition system and boxcar averager

As mentioned before, the acquisition of the fluorescence signal is performed using a photomultiplier tube (Hamamastsu R928). The resulting electrical signal is then amplified and transmitted to a Boxcar. The operating principle of a Boxcar is based on the charge of an RC circuit. For each laser shot, the signal is integrated over a time period corresponding to the Boxcar integration gate and then averaged over a large number of measurements. The result is displayed and treated by a computer. Figure 2-23(a) shows an example of the amplified TALIF signal together with the boxcar integration gate (200ns duration), captured by an oscilloscope. The noisy baseline of the TALIF signal, which is due to electrical perturbations induced by the laser firing is perfectly reproducible and can thus be easily removed. Figure 2-23(b) shows the signal delivered by the Boxcar integrated over 500 laser shots.

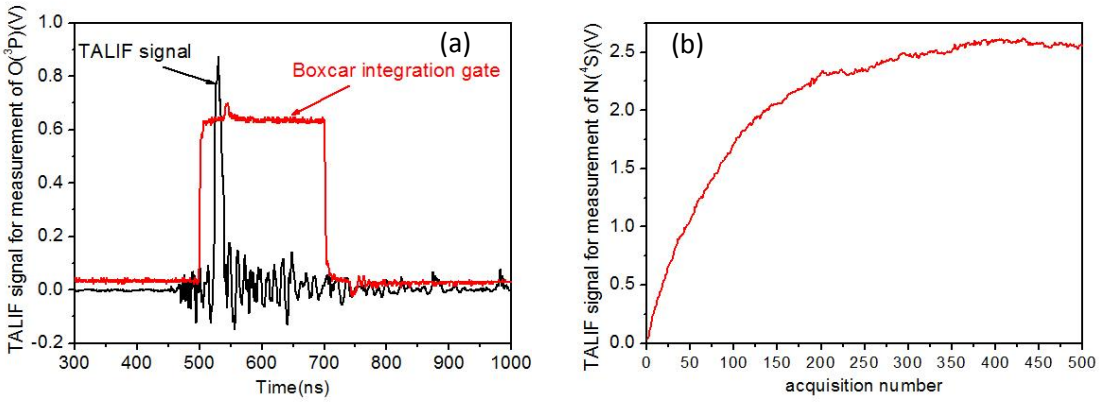

Figure 2-23 (a) Evolution of atomic oxygen fluorescence signal and the Boxcar integration gate (b) Acquisition and treatment of signal delivered by Boxcar

III.3. Verification of the operation mode of photomultiplier tube

When implementing the LIF/TALIF setup, it is necessary to determine the range of supply voltage for which the response of the PMT is linear. This is done by measuring the LIF/TALIF signal in real experimental conditions for different supply HV of the PMT. Figure 2-24 presents an example of such measurements.

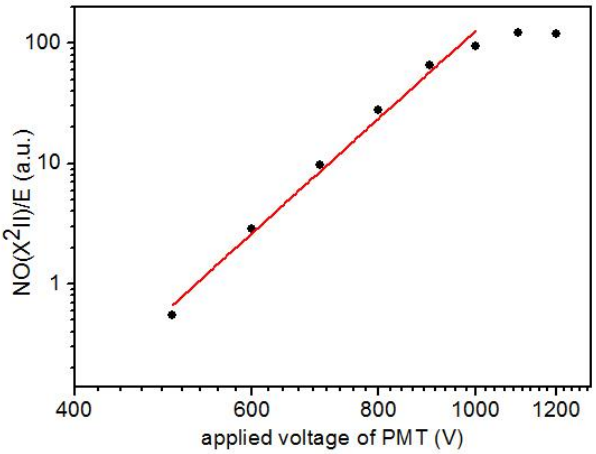

Figure 2-24 LIF signal for the measurement of NO($X^2\Pi$) with discharge as a function of applied voltage of PMT. Measurement conditions: HV=17.1 kV_{pp}, f =2 kHz, P=0.9 W/cm^2, flow rate=1.0 L/min, concentration of O_2=200 ppm

As can be seen, the response of the PMT remains linear below approximately 1000 V and consequently, the working HV supply of the PMT was fixed at 800 V for the present conditions.

IV. Synchronization of the laser pulse, discharge and Boxcar

In this study, we want to perform LIF/TALIF measurements in the discharge for a well-defined time during a period of the applied voltage. It is thus necessary to synchronize the laser pulse and the boxcar integration gate with the applied voltage.

For this purpose two function generators are used as shown in Figure 2-25. The first one generates the sinusoidal signal S1 in the kHz range, which corresponds to the voltage applied to the discharge before amplification. This generator trigs a second one, which generates a square voltage S2 used to control the laser firing. The laser pulses can thus be emitted at different times of the discharge by tuning the phase difference between S1 and S2. This phase difference is represented in the time domain in Figure 2-25 by the time delay τ_d. For each laser shot, a signal is sent from the laser to the boxcar to trig the boxcar acquisition. A time delay τ_{box} can be set on the boxcar to adjust properly the boxcar gate around the laser pulse in time, and the width of the boxcar integration gate can be adjusted to capture the whole fluorescence signal.

In this study, most of the measurements are performed between two successive discharges *i.e.* when the polarity of the discharge reverses and the current jump occurs.

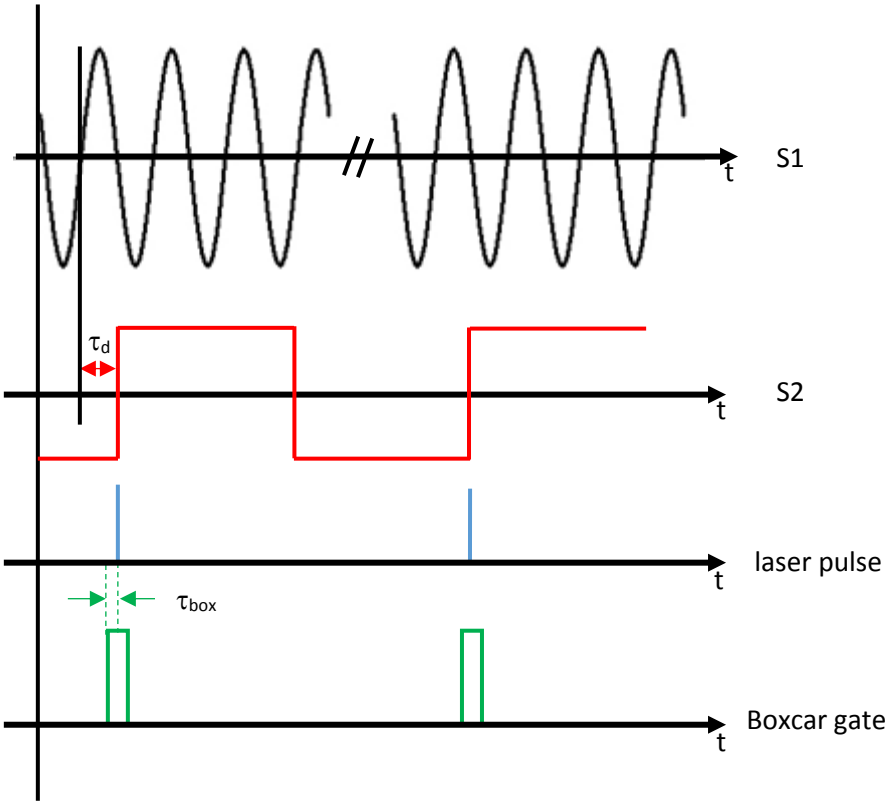

Figure 2-25 Chronogram of synchronization signals

V. Measurement procedure

Each LIF/TALIF measurement is performed in the same way:

- For a given excitation (laser) wavelength λ_L, the time-dependent LIF/TALIF signal $S_{(TA)LIF}(\lambda_L, E_L^{(2)})$ is integrated over time and averaged over typically 500 shots by the boxcar averager.

- The laser wavelength is then changed away from the resonance but sufficiently close to keep similar laser energy to measure the noise signal. The latter takes into account the electrical perturbations, the light emitted by the discharge and potentially the light coming from the interaction of the laser beam with the alumina or with the glass slides. The noise signal is recorded in the same manner as the LIF/TALIF signal *i.e.* it is integrated over 500 laser shots using the boxcar average.

- The corrected LIF/TALIF signal $S^{corr}_{(TA)LIF}(\lambda_L, E_L^{(2)})$ is obtained by subtracting the noise signal to the measured signal. To obtain a quantity representative of the density of the probed species *i.e.* independent of the laser energy, the corrected signal has to be divided by the averaged laser energy per pulse $\langle E_L \rangle$ for LIF measurements or by the averaged of the square of the laser energy per pulse $\langle {E_L}^2 \rangle$ for TALIF measurements. We then obtain $S^{corr}_{(TA)LIF}(\lambda_L)$.

- These measurements are repeated by sweeping the laser wavelength to recover the whole excitation profile. Finally, the LIF/TALIF signal $S^{corr}_{(TA)LIF}$ corresponds to the area under the excitation profile and can be obtained by integration.

- The calibration procedure detailed in this chapter is used to obtain an absolute density from $S^{corr}_{(TA)LIF}$.

Chapter 3. TALIF measurements of atomic nitrogen N ($2p^3\ ^4S_{3/2}$) density

In this chapter, we present the results of TALIF measurements on N ($2p^3\ ^4S_{3/2}$) obtained in homogeneous Townsend discharge either in high purity N_2 or in the mixture N_2/O_2. To simplify the description, in the following chapters, we replace N ($2p^3\ ^4S_{3/2}$) by N(^4S) in most cases, except when we need to detail the ground state. First, we present the necessary validation performed before the TALIF measurements, the calibration procedure using krypton and we discuss the experimental errors. Then, we present the results obtained in high purity N_2 and in the mixture N_2/O_2. Finally, the important points of this chapter are summarized.

I. Validation of TALIF measurements, calibration procedure and experimental errors

Before doing the measurements, some important verifications have to be performed. They are described in this section following the same order. According to the principle of LIF/TALIF explained in chapter 2 section II, one have first to find the optical transition of interest by scanning the laser wavelength. Then one has to tune the laser energy to determine the domain corresponding to the linear fluorescence regime. During the calibration, the same procedure has to be performed. Finally, it is necessary to investigate the different sources of error.

I.1. Validation of TALIF measurements

The excitation schemes of nitrogen and krypton have already been presented in Figure 2-12. We reshow this figure to make the explanation more comprehensive.

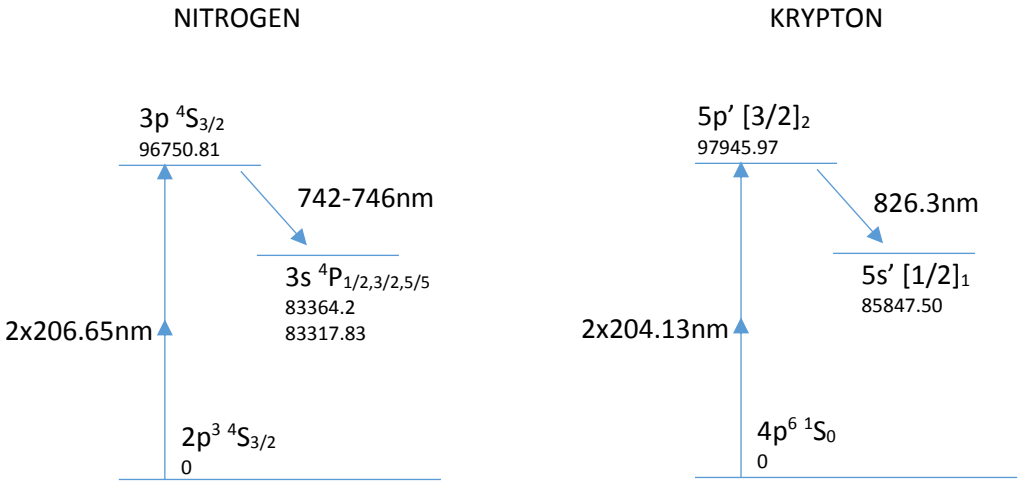

Figure 3-1 Tow-photon excitation schema of nitrogen and krypton. The level energies are given in cm^{-1}

Thus, we start the TALIF measurements with the determination of the excitation wavelengths for the specie of interest. Indeed, a shift always exists between the theoretical wavelength and the experimental one because the laser is never perfectly spectrally calibrated. Figure 3-2 presents a TALIF excitation profile of N(^4S). The optimum two-photon absorption wavelength is 206.875 nm for N(^4S).

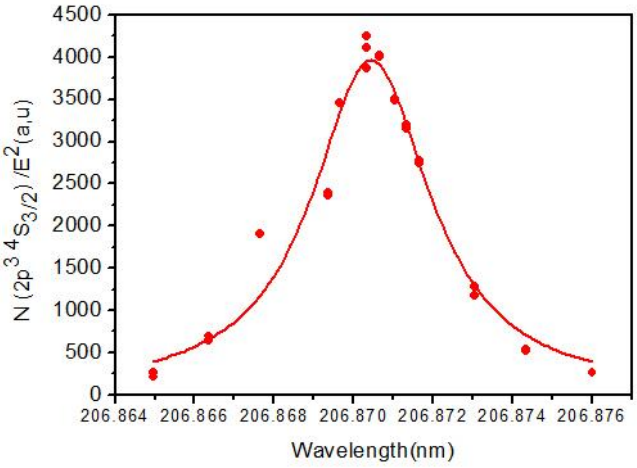

Figure 3-2 Excitation spectrum for the transition N ($2p^3\ ^4S_{3/2}$) -> N ($3p\ ^4S_{3/2}$) obtained in a Townsend discharge for high purity N_2. Measurement conditions: P=0.6 W/cm², f=2 kHz, HV=15.8 kV_{pp}, flow rate=1.0 L/min, x=14 mm

Once the experimental wavelength has been found, it is necessary to determine the laser energy range corresponding to the linear regime. As explained in chapter 2 section II.2.3, the TALIF signal has to be proportional to the square of the laser energy in the unsaturated regime. Figure 3-3 shows the evolution of the TALIF signal as a function of the laser energy per pulse in the logarithmic scale. As can be seen, it remains linear with a corresponding slope of 2 for laser energies below 40 µJ indicating that measurements have to be done under this value. For most of the measurements, we usually keep the laser energy around 27 µJ *i.e.* well below the saturation limit but sufficiently high to have a substantial fluorescence signal.

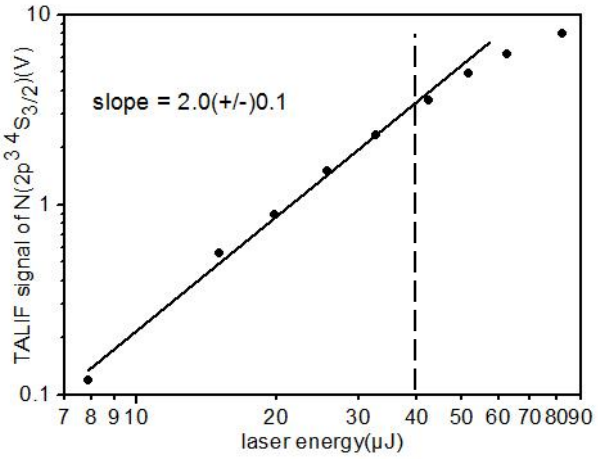

Figure 3-3 Log-log plot of the N atom fluorescence signal as a function of laser energy. Measurement conditions: P=0.6 W/cm², f=2 kHz, HV=15.8 kV_{pp}, position=14 mm, flow rate=1.0 L/min, concentration of O_2=0 ppm

Similar validation is also performed for krypton during the calibration. Since krypton gas is very expensive, the calibration is performed by injecting a small quantity of krypton. In these conditions, the saturation limit is reached for very small laser energy, which is not convenient because of the large uncertainty for the measurement of small laser energies. To overcome this limitation we inject a mixture of krypton and nitrogen in the vessel. It allows to increase the saturation to larger laser

energy thanks to the high quenching rate of krypton by nitrogen. Figure 3-4 shows (a) the excitation profile of krypton, and (b) the log-log plot of the Kr fluorescence signal as a function of the laser energy. The optimum two-photon absorption wavelength is 204.35 nm for Kr. The measurements are performed for a laser energy per pulse around 19 µJ *i.e.* in the linear regime.

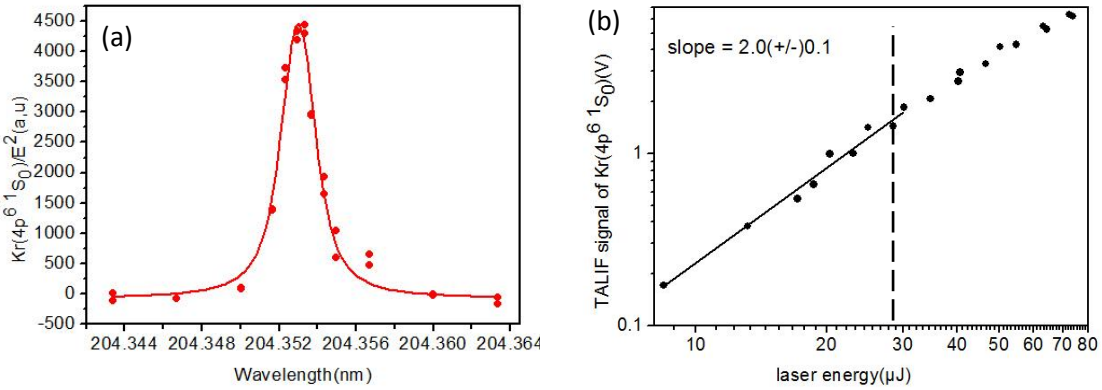

Figure 3-4(a) Excitation spectrum for the transition Kr ($4p^6\ ^1S_0$)-> Kr (5p' [3/2]$_2$) obtained in a mixture of N_2/Kr. Measurement conditions: p(Kr)=0.13 mbar, p(N_2)=195.67 mbar, x=21 mm (b) Log-log plot of the Kr atom fluorescence signal as a function of laser energy. Measurement conditions: p(Kr)=0.013 mbar, p(N_2)=195.9 mbar, x=14 mm

I.2. Calibration procedure

According to equation (2.23) in section II.3.2, the absolute density of N(^{4}S) atoms can be calculated using the following relation:

$$n(N) = \mathrm{CF}_{N/Kr} \times \frac{S_{TALIF}(N)}{\left(\frac{E_L}{h\nu_{laser}}\right)^2(N)} \times \frac{(Q_3+A_3)}{A_{32}}(N) \tag{3.1}$$

where $\mathrm{CF}_{N/Kr}$ is the calibration factor which expression is given by equation (3.2):

$$\mathrm{CF}_{N/Kr} = \frac{\sigma_{TALIF}(Kr)}{\sigma_{TALIF}(N)} \times \frac{T_{Kr}\eta_{Kr}}{T_N\eta_N} \times n\,(Kr) \times \frac{A_{32}}{(Q_3+A_3)}(Kr) \times \frac{\left(\frac{E_L}{h\nu_{laser}}\right)^2(Kr)}{S_{TALIF}(Kr)} \tag{3.2}$$

In this equation, T_X represents the transmission of the interference filters and η_X is the quantum efficiency of the PMT at the fluorescence wavelength. These parameters are given in Table 3-1 for the central fluorescence wavelengths of N and Kr.

Table 3-1 Quantum efficiency of PMT and transmission coefficients of filter for the detection of N and K fluorescence signal

Species	Experimental parameters	
	Quantum efficiency of PMT	Transmission coefficient of filters
N	4.35	0.6
Kr	1.42	0.6

Niemi *et al.* [71] have determined the ratio of two-photon excitation cross section:

$$\frac{\sigma_{TALIF}(Kr)}{\sigma_{TALIF}(N)} = 0.67$$

A_3 represents the overall spontaneous de-excitation probabilities an of the level populated by laser absorption to lower levels whereas A_{32} refers to the transition of interest. Q_3 is the overall quenching rate and can be calculated by $Q_3 = \sum_i n_i k_{q_i}$ where n_i is the density of quencher i and k_{q_i} the corresponding quenching coefficient. All this data are taken from the literature and given in Table 3-2.

Table 3-2 relative parameters involved in the calculation of density of N(^{4}S)

Parameters	N	Kr
A_3(10^7 s^{-1})	4.156 [78]	3.708 [79]
A_{32}(10^7 s^{-1})	3.714[78]	3.53[79]
k_q(N_2) (10^{-10} cm^3/s)	0.41 [71]	3.35[71]
k_q(O_2) (10^{-10} cm^3/s)	6.63 [71]	
k_q(Kr) (10^{-10} cm^3/s)		1.46 [71]

The value of A_{32} for Kr was obtained knowing A_3 and considering the ratio $A_{32}/A_3 = 0.953$ [3].

Note that in principle, it is possible to determine the quenching rates experimentally by measuring the decay rate of the fluorescence signal as explained in chapter 2 section II.2.5. Nevertheless, the fast decay of TALIF signals at atmospheric pressure, the relatively long laser pulse (see Figure 2-15 in section III.1) and the too slow time response of our optical system (PMT and amplifier) make these determinations impossible.

According to the equation (3.2) and knowing the relative parameters, the calibration factor can be calculated as soon as the fluorescence signal of Kr is determined. Figure 3-5 represents the evolution of the TALIF signal during the calibration and the corresponding calibration factor as a function of the position x of the measurement.

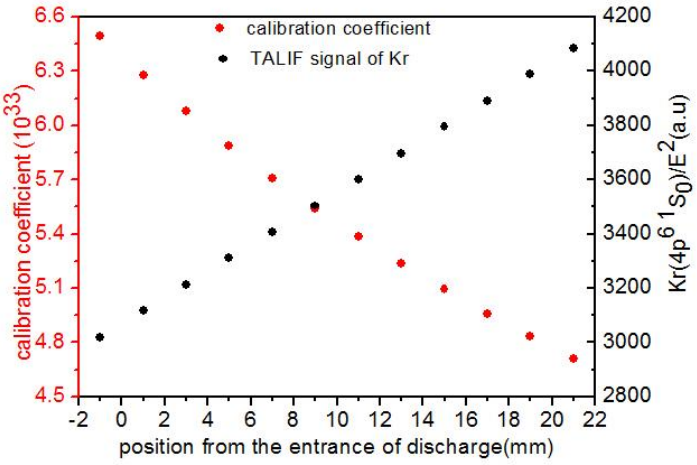

Figure 3-5 TALIF signal and calibration coefficient as a function of position and the corresponding TALIF signal

The measured TALIF signal increases from the entrance to the exit of the discharge cell, which can be explained by the increase of the solid angle of the fluorescence detection. The latter is limited by the dielectrics of the DBD. This effect is schematically described in Figure 3-6. The calibration factor is inversely proportional to the TALIF signal and consequently, it decreases from the entrance to the exit of the discharge cell.

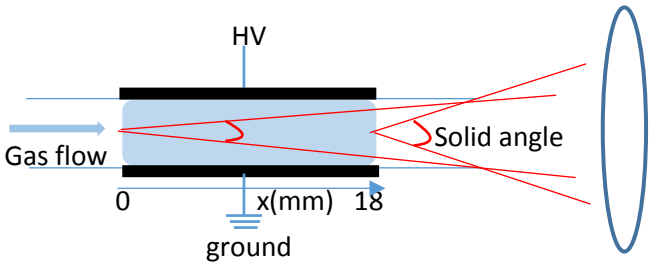

Figure 3-6 The influence of solid angle for the detection of TALIF signal along the discharge

I.3. Influence of the gas temperature

During the calibration, the gas is at thermal equilibrium at the room temperature. But during the experiments, the gas temperature can be higher and a departure from thermal equilibrium is often observed in gas discharges. It implies that molecules can have different rotational (T_{rot}) and vibrational temperatures (T_{vib}). To estimate these temperatures, OES measurements have been performed for some various experimental conditions on the 2nd positive system of nitrogen. The spectra were then fitted using the SPECAIR© software [80] to obtain values of T_{rot} and T_{vib}.

An example of the OES spectrum corresponding to the results obtained for a concentration of 0ppm of O_2 is depicted in Figure 3-7. The temperatures determined in the different conditions are given in Table 3-3.

Table 3-3 Rotational and Vibrational temperature determined by OES

Concentration of O_2 (ppm)	applied voltage (kV_{pp})	Discharge power (W/cm^2)	353nm		377nm	
			T_{rot}=T_{tran}(K)	T_{vib}(K)	T_{rot}=T_{tran}(K)	T_{vib}(K)
0	18.1	0.9[a]	400	1500	394	1500
25	18.1	1.4[a]	443	1500	432	1500
200	18.1	filamentary[a]	355	1500	345	1500

[a] The determination of the temperature was performed with another discharge cell instead of the one used in this work

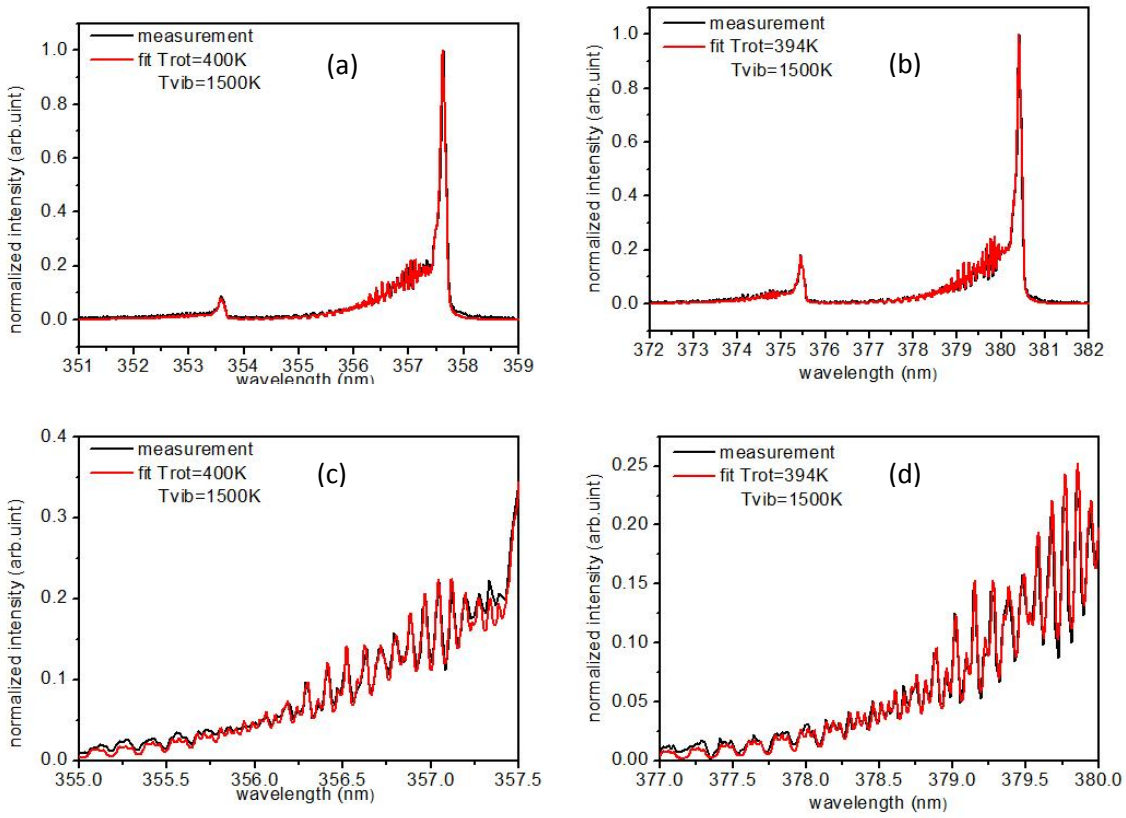

Figure 3-7 OES spectrum of N_2 second positive system, measured at different wavelengths: (a) and (c)-357.5 nm; (b) and (d)-380.5 nm, where (c) and (d) are the zoom of (a) and (b) respectively. Measurement conditions: f=2kHz, HV=18.1k V_{pp}, flow rate=1.0 L/min, concentration of oxygen=0 ppm

The results indicate that the rotational temperature which is generally assumed to be equal to the translational temperature can increase up to T_{rot}=430 K. This is obtained for the measurement performed at the highest input power of 1.4 W/cm^2. Since most of the measurements performed in this work are done for input power lower or equal to this value, T_{rot}=430 K will be considered as an upper limit. The vibrational temperature was found to be T_{vir}=1500 K for every measurement.

A change in the gas temperature is important because the quenching rate depends on the gas temperature T. In most cases, the quenching rate coefficients available in the literature are determined at room temperature and have to be corrected if the temperature of the experiment is different. In the literature, the quenching rate coefficient k is often calculated as the product of the cross section σ by the relative thermal velocity of the colliders (see *e.g.* [81]):

$$k = \sigma \cdot \sqrt{\frac{8k_B T}{\pi \mu}} \tag{3.3}$$

where μ represents the reduced mass of the colliders and T is the translational temperature. σ is generally considered to be poorly temperature dependent.

Then, relation (3.3) can be used to calculate the change in the quenching rate coefficient due to collider q from the room temperature T_0 to a higher temperature T. The corresponding equation writes:

$$k_q(\mathrm{T}) = k_q\ (T_0) \times\ (T/T_0)^{\frac{1}{2}} \tag{3.4}$$

A change in the gas temperature does not only modify the quenching rate coefficient but also the density of the quenchers which can be calculated using the ideal gas low.

Then, the overall quenching coefficient is given by:

$$Q_3(T) = \sum_i \chi_i \cdot \frac{P}{k_B T} \cdot k_{qi}(T_0) \cdot \sqrt{\frac{T}{T_0}} \tag{3.5}$$

where χ_i is the mole fraction of quencher i, P is the working pressure, T is the temperature during the experiment, T_0 is the room temperature (300K), $k_{qi}(T_0)$ is the quenching rate coefficient at room temperature coming from the literature data. Equation (3.5) indicates that the decrease of the quencher's density when the temperature increases, overcomes the increase in the quenching rate coefficient. Thus an increase in the temperature causes the quenching rate to decrease.

Since in the present work the gas temperature is not systematically measured for every experimental condition, the densities determined by LIF/TALIF presented in this work are not corrected for temperature effect. Instead, an estimation of the error if one considers a temperature of 300 K instead of a temperature of 430 K (which corresponds to the maximum gas temperature measured in our conditions) is provided. This error is directly given by the following ratio, where Q_3 is approximated to be only due to nitrogen molecules:

$$\frac{(Q_3 + A_3)_{430K}}{(Q_3 + A_3)_{300K}} = 0.842$$

Thus, considering that the gas temperature is 300K in the experiments results in an overestimation of the N(^{4}S) density of 15.8%.

I.4. Experimental errors

An exact determination of the systematic errors is tricky since a lot of parameters are involved in the TALIF measurements. The main contribution comes from the uncertainty of the ratio of the two-photon absorption cross section $\frac{\sigma_{TALIF}(Kr)}{\sigma_{TALIF}(N)}$, which was estimated by Niemi *et al*. [71] to be 50%. Other errors such as the quenching rates or the radiative lifetimes are neglected because their values result from numerous studies and reliable measurements.

The statistical error was estimated to be ±9.1% based on the reproducibility of the measurements. The error bars indicated on the results presented in the following correspond to the statistical error.

II. N ($2p^3\ ^4S_{3/2}$) density in N_2

In this entire chapter, the N(^{4}S) density is measured between two successive discharges except for some particular measurements presented in section II.1. Indeed, the aim of this thesis is to study the gas phase phenomena related to the memory effect, which takes place between two successive discharges. In the present section, the N(^{4}S) density is investigated in APTD generated in high purity nitrogen. First, the temporal and spatial evolution of the N(^{4}S) density is studied. Then the influence of the discharge power and the gas flow rate are investigated. Finally, the evolution of the N(^{4}S) density during the post-discharge is discussed.

II.1. Evolution of the N ($2p^3\ ^4S_{3/2}$) density during a period of the applied voltage

TALIF measurements were performed at a fixed location (x=14 mm) as a function of different instants during a discharge period in high purity nitrogen. The choice of this location is justified in the next section. The corresponding results are presented in Figure 3-8(a). The measured density varies between 3.5 10^{14} cm^{-3} and 6.5 $10^{14}cm^{-3}$. Nevertheless, no correlation can be made when comparing the N(^{4}S) density during the first negative half-period and the second positive one.

Several experimental errors can disturb the measurements *e.g.* if the laser beam does not pass exactly at the center of the discharge gap. Moreover the measurements performed during the discharge are more subjected to the noise induced by the light emission from the discharge than measurements performed between two discharges.

Nevertheless, since N(^{4}S) atoms are mainly produced by electron impact dissociation on N_2 molecules, one could expect a high N(^{4}S) density near the maximum of the discharge current and a low density between two discharges. This is not observed experimentally which means that if such behavior of the N(^{4}S) density exists, the corresponding density variations remain small compared to experimental errors. Numerical investigations performed using the model presented in appendix show a similar behavior. An example of the time-varying N(^{4}S) density over a discharge period is presented in Figure 3-8(b). As can be seen, the variation of the N(^{4}S) density is on the order of 10^{13} cm^{-3} which corresponds to a variation of 2%. The analysis of the production and destruction rates of N(^{4}S) presented in Appendix 1 indicates that these two rates have very similar evolutions explaining the quasi-constant N(^{4}S) density. Indeed, when the electron density and the electric field are important, the dissociation of N_2 molecules produces a large amount of N(^{4}S) atoms. But at the same time, it causes a large production of N_2(A) metastable molecules which are responsible for a significant excitation of N(^{4}S) towards N(^{2}P) and N(^{2}D) states which compensates for the important N(^{4}S) production by dissociation. The interested reader can refer to section IV.1.2 in Appendix 1 for the detailed analysis.

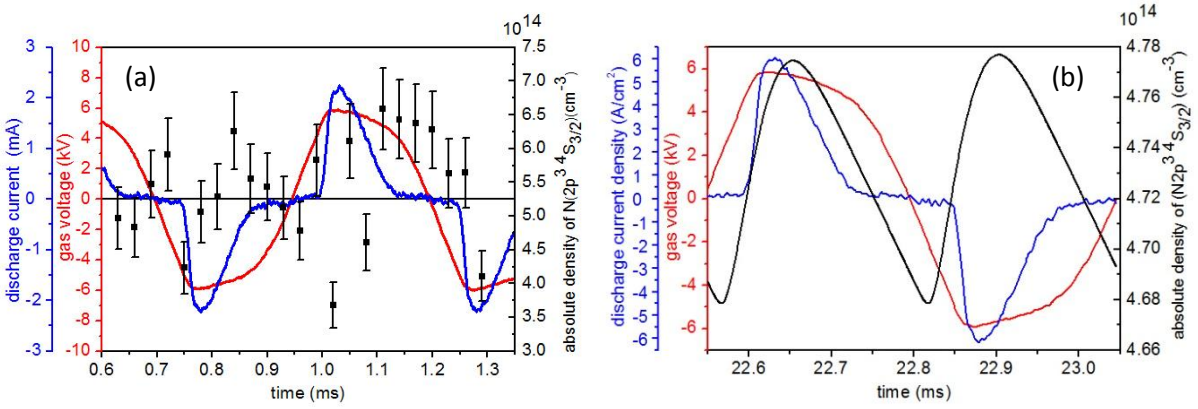

Figure 3-8 Absolute density of N ($2p^3\ ^4S_{3/2}$) as a function of instant of discharge during a whole period, (a) experimental result, (b) simulation result. Measurement conditions: P=0.9 W/cm², f=2 kHz, HV=17.1 kV_{pp}, flow rate=1.0 L/min, position=14 mm

II.2. Evolution of the N ($2p^3\ ^4S_{3/2}$) density along the discharge

In this part, we are interested in the evolution of N(^{4}S) density as a function of the position from the entrance of the discharge. Figure 3-9 shows a typical example of the corresponding results. These measurements are performed at the stationary state *i.e.* electrical characteristics are reproducible

from one discharge period to the other. We can observe an increase of the density along the discharge up to 5 mm followed by a plateau.

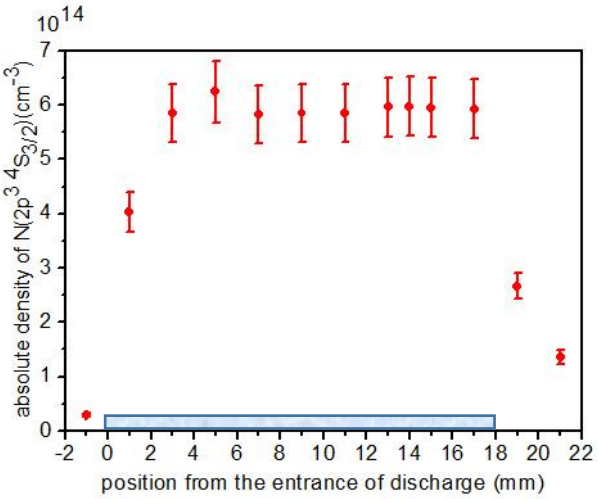

Figure 3-9 Absolute density of N ($2p^3\ ^4S_{3/2}$) as a function of position. Measurement conditions: P=0.9/cm², f=2kHz, HV=17.1 kV_{pp}, flow rate=1.0 L/min

In previous works [48,56], we showed that electrical characteristics change along the discharge in a Townsend DBD even when a stationary state is reached. It is illustrated by Figure 3-10 which reports measurements performed with a segmented electrode [48] to allow independent electrical measurements as a function of the position x.

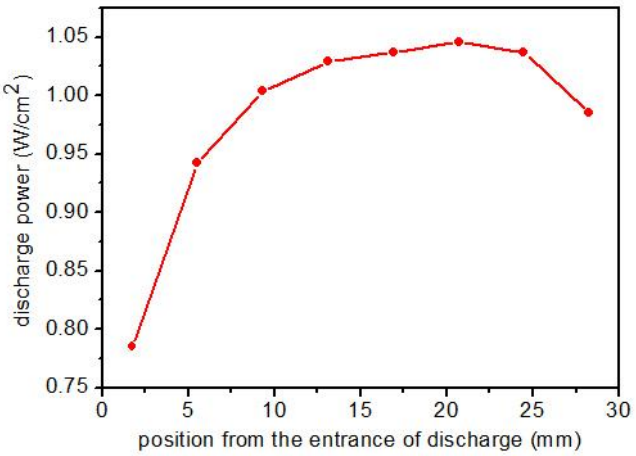

Figure 3-10 Discharge power as a function of the position. Measurement conditions: length of the discharge=3 cm, gas gap=2 mm, HV=16.0 kV_{pp}, f=2 kHz, flow rate=4.0 L/min

As can be seen, the discharge power increases before reaching a constant value. This effect was attributed to the progressive establishment of a memory effect *i.e.* to the production and accumulation of active species directly involved in the operation of the discharge. It can be metastable species such as $N_2(A)$, atoms coming from dissociation of molecules such as atomic oxygen or electrons accumulated onto the dielectrics. Note the decrease of the surface power density at the end of the discharge should be attributed to the spreading of the discharge.

Knowing that, it can be interesting to compare measurements done at different positions in the stationary state to measurements performed at a fixed position as a function of time starting from discharge ignition, for similar experimental conditions. Figure 3-11 presents an example of such comparison in high purity nitrogen. The position/time conversion (black curve) is done knowing the gas flow and using equation (2.1) in section I.1.1 . Time-dependent measurements (red curve) are done at x=14 mm *i.e.* close to the end of the plateau where the discharge is fully established. As can be seen, both results are quite similar in this condition. Note that this is not necessary true when oxygen is introduced in the discharge, as shown and discussed in section III.1.

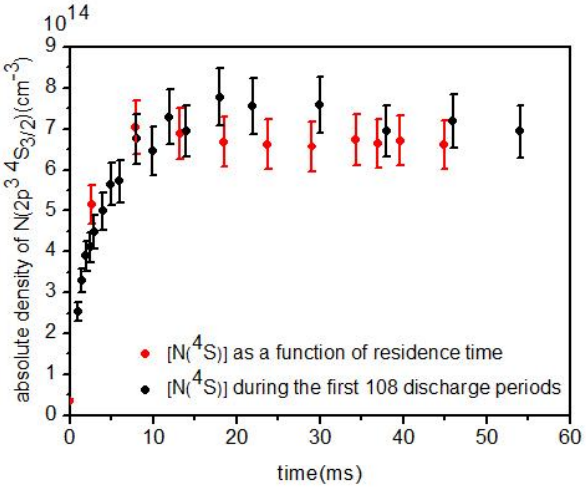

Figure 3-11 Comparison of the absolute density of N ($2p^3\ ^4S_{3/2}$) as a function of residence time (black curve) and at x=14 mm just after the ignition of the discharge for 108 periods (red curve). Measurement conditions: f=2 kHz, HV=18.1 kV_{pp}, flow rate=1.0 L/min

Electrical measurements performed during the first 108 discharges can be used to get a picture of the time evolution of the averaged discharge power. For this purpose, the averaged power dissipated in the gas is calculated for each successive period of the applied voltage. The corresponding results are presented in Figure 3-12. The averaged power increases noticeably during the first 10ms following the discharge ignition and then reaches a stationary value. Note that it does not correspond to the power at the position x=14 mm where TALIF measurements are performed but to an average power over the whole discharge.

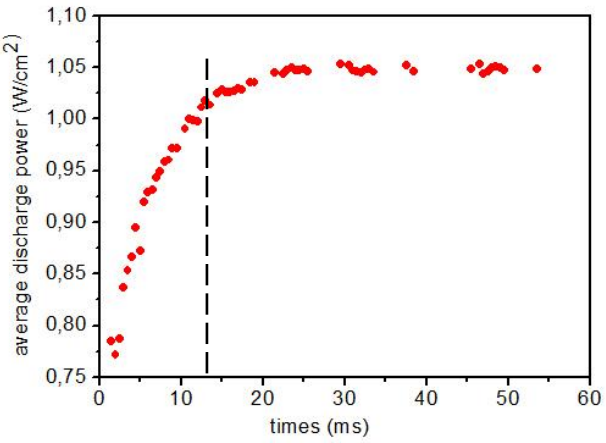

Figure 3-12 Evolution of the average discharge power during the first 108 discharge periods

The evolution of N(^{4}S) density can thus be explained by a combination of two phenomena:

- The power of the discharge increases along the position (time) before reaching a constant value. The production of N(^{4}S) atoms is modulated accordingly, a higher discharge power inducing a higher N(^{4}S) production rate.

- At the beginning (space and time) of the discharge, the production rate is larger than the destruction rate resulting in an increasing N(^{4}S) density. With the increase of N(^{4}S) density, the destruction rate which is directly related to the N(^{4}S) density increases until an equilibrium between the production and destruction mechanisms is reached, resulting in the observed plateau.

To study the mechanism responsible for the production of N(^{4}S), we are interested in the N(^{4}S) production for different discharge powers in the next section.

II.3. N ($2p^3\ ^4S_{3/2}$) density as a function of the discharge power

Measurements are performed for different discharge powers by changing the frequency or the applied voltage. The corresponding results are presented in Figure 3-13. As can be seen, the N(^{4}S) density increases when increasing the input power. Moreover, the higher is the input discharge power, the stiffer is the rise of the N(^{4}S) density at the entrance of the discharge. For the lowest input power, no N(^{4}S) atoms are detected at x=1 mm probably because the discharge is not fully initiated at this position because the applied voltage is too low.

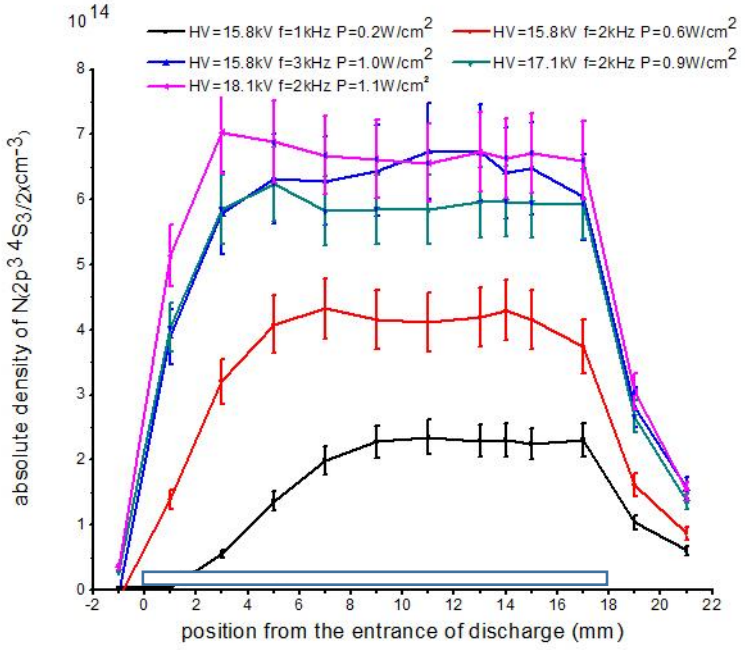

Figure 3-13 Absolute density of N ($2p^3\ ^4S_{3/2}$) as a function discharge power. Measurement conditions: flow rate=1.0 L/min

Figure 3-14(a) presents a summary of the N(^{4}S) density measured for the different discharge powers at x=14 mm. We can see that the N(^{4}S) density is directly proportional to the input power, independently of the applied frequency or voltage. Figure 3-14(b) represents the corresponding simulation results, the density increases slower and slower with the discharge power. And the influence of applied voltage is more considerable than that of frequency, as the two last points show,

even at a lower discharge power with a higher applied voltage, the density is higher than that at a higher discharge power with a higher frequency.

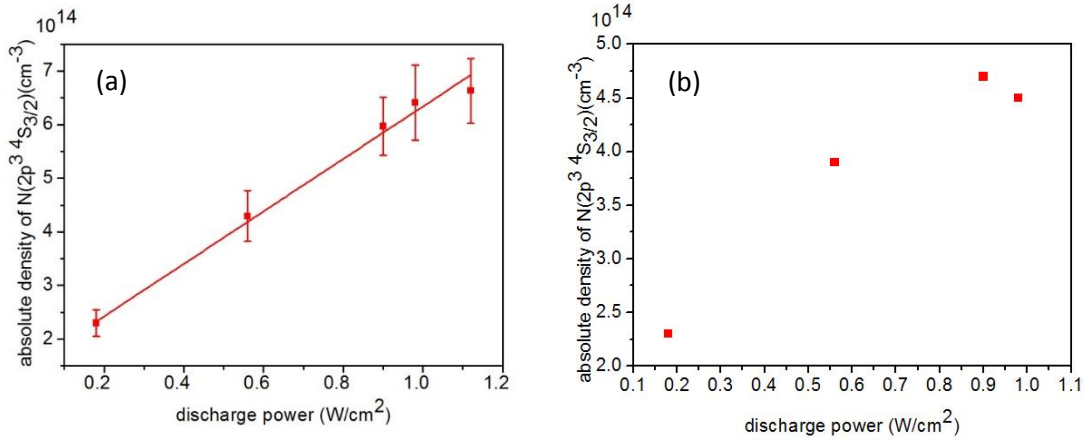

Figure 3-14 Absolute density of N ($2p^3\ ^4S_{3/2}$) as a function of discharge power. (a) experimental result (b) simulation result. Measurement conditions: flow rate=1.0 L/min, position=14 mm

To analyze these results, it is interesting to understand the influence of the applied frequency and applied voltage on the discharge power.

In a Townsend DBD, the gas gap voltage V_g during the discharge is roughly constant in time and is related to the breakdown voltage which mainly depends on fundamental parameters such as the discharge gap, the nature of the gas, the pressure, the temperature. Thus, it does not vary too much when changing the applied frequency or the applied voltage V_a. Now, let us discuss the discharge current I_d on the basis of the equivalent electrical circuit presented in Figure 2-5. Since V_g is roughly constant in time, all the current passes through the resistor (which corresponds to the discharge current itself). This total current is also the current passing through the dielectrics, which can be expressed as $C_{sd}\frac{dV_{sd}(t)}{dt}$. Considering that the variation of the gas voltage is nearly zero, the gradient of V_{sd} can be considered to be the gradient of V_a, then the total current can be expressed as $C_{sd}\frac{dV_a(t)}{dt}$ From this expression, one can deduce that increasing the frequency results in an increase of the discharge current as long as the discharge is ON. The same conclusion can be drawn when increasing the applied voltage. It means that the electron density increases whereas the gas gap voltage (and thus the electric field) which remains approximately the same.

To check the consistency of this hypothesis, the evolutions of the discharge current I_d and of the gas gap voltage V_g are presented in Figure 3-15(a) and (b) respectively.

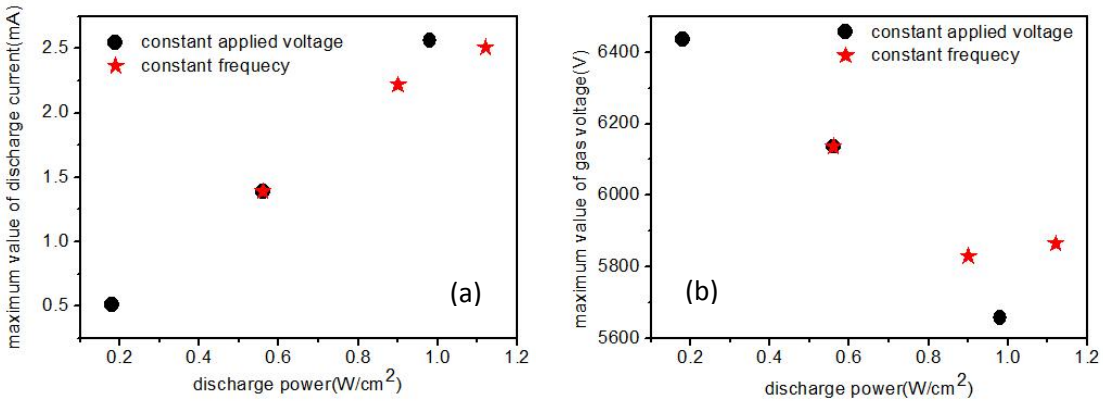

Figure 3-15 The maximum value of (a) discharge current and (b) gas voltage as a function of discharge power

We can see that in the range of investigated parameters the variation of the maximum of V_g is around 15% whereas the maximum of the discharge current changes by a factor 5. These results are in agreement with the previous explanation.

The slight decrease of the gas gap voltage observed in Figure 3-15(b) for increasing powers indicates that the breakdown becomes easier. It can be explained by several phenomena. First of all, the increase of the discharge power results in an increase of the gas temperature, which in turn implies a decrease in the gas density. During his Ph.D., N.Naudé [82] estimated for an APTD operated in N_2 with a gas gap of 1mm that an increase of the gas temperature from 300 K to 400 K results in a decrease of the breakdown voltage of approximately 800V. In our conditions, gas temperatures up to 430 K have been measured for a surface power of 1.4 W/cm^2. Even if the gas gap is 2 mm in our conditions, it is reasonable to assume that gas heating significantly contributes to the decrease of the breakdown voltage. Moreover, increasing the power can also increase the memory effect, which can also contribute to decreasing the breakdown voltage.

To explain the linear increase of the N(^{4}S) density with the discharge power, it is necessary to discuss the production mechanisms of atomic nitrogen. It is well known that N(^{4}S) atoms are mainly produced by electron impact dissociation on N_2 molecules [83–85]. This process can be direct, as described by the following reaction:

$$e^- + N_2 \longrightarrow {N_2}^* \longrightarrow N(^4S) + N(^4S,\ ^2D,\ ^2P) \qquad \text{(R 3)}$$

where ${N_2}^*$ represents a rapidly predissociating state [85], or it can be a two-step process as indicated by Teramoto *et al*. [84]:

$$e^- + N_2 \longrightarrow {N_2}^* + e^- \qquad \text{(R 4)}$$

$${N_2}^* + e \longrightarrow N + N + e^- \qquad \text{(R 5)}$$

Our experimental results show a linear relation between the input power and the N(^{4}S) density at equilibrium (see Figure 3-14(a)), suggesting that, in our conditions, the main nitrogen dissociation channel corresponds to the aforementioned one-step process.

These measurements allow estimating the energy cost of N(^{4}S) atoms production following the method described in [85].

Assuming that N(^{4}S) atoms production is directly related to the discharge power and N(^{4}S) atoms are mainly lost by volume recombination onto nitrogen molecules and during their diffusion to the walls (see section II.5), the equation ruling the N(^{4}S) density in the steady state is:

$$\frac{d[\mathrm{N}(^4\mathrm{S})]}{dt} = \frac{P_{volume}}{\varepsilon_C^N} - 2[\mathrm{N}(^4\mathrm{S})][N_2]k_N - [\mathrm{N}(^4\mathrm{S})]v_{het} = 0 \quad (3.6)$$

where P_{volume} is the power density in ev, ε_C^N is the energy cost of N(^{4}S) production, k_N is the rate coefficient for the volume recombination and v_{het} is the characteristic frequency for heterogeneous recombination of N(^{4}S) atoms. v_{het} can be calculated using the following expression:

$${v_{het}}^{-1} = \left(D_N\left(\frac{\pi}{L}\right)^2\right)^{-1} + \left(\frac{\gamma_N u}{2L}\right)^{-1} \quad (3.7)$$

Here, D_N=0.29 cm^{2}s^{-1} is the diffusion coefficient, L is the gap length, γ_N=3 – 4 10^{-4} is the coefficient for heterogeneous recombination on the alumina surface and u is the thermal speed of N(^{4}S) atoms [85]. With these values, we obtain v_{het}=32.26 s^{-1}.

Considering the previous equations and a gas temperature of 300 K, it is possible to estimate the energy cost for N(^{4}S) atoms production. The corresponding results are presented in Figure 3-16 for the five different input powers presented in this section.

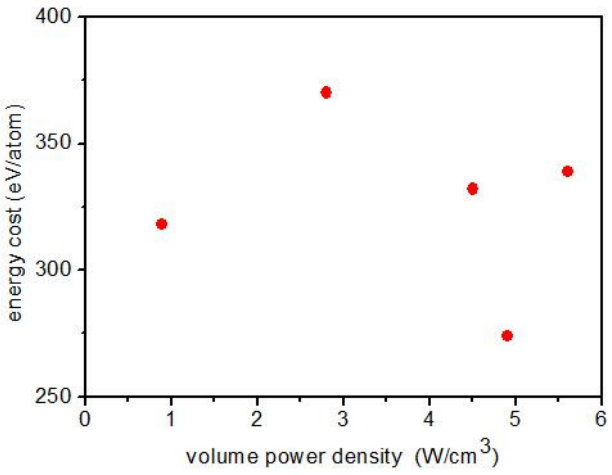

Figure 3-16 Energy cost ε_C^N of electron impact dissociation of N_2 molecule as a function of discharge power

The energy cost for N(^{4}S) atom production is ranging between 274 eV/atom and 370 eV/atom for a corresponding average value of 318 eV/atom, close to the value of 337±35 eV/atom found by N.A. Popov [85] on the basis of experimental results obtained by Es. Sebbar *et al.* [60]. The data obtained in this work are thus in good agreement with the previous studies.

II.4. N ($2p^3\ ^4S_{3/2}$) density as a function of the gas flow rate

Figure 3-17(a) represents the evolution of absolute density of N(^{4}S) as a function of the position for different gas flow rate ranging from 0.5 L/min to 2 L/min while keeping the same discharge power.

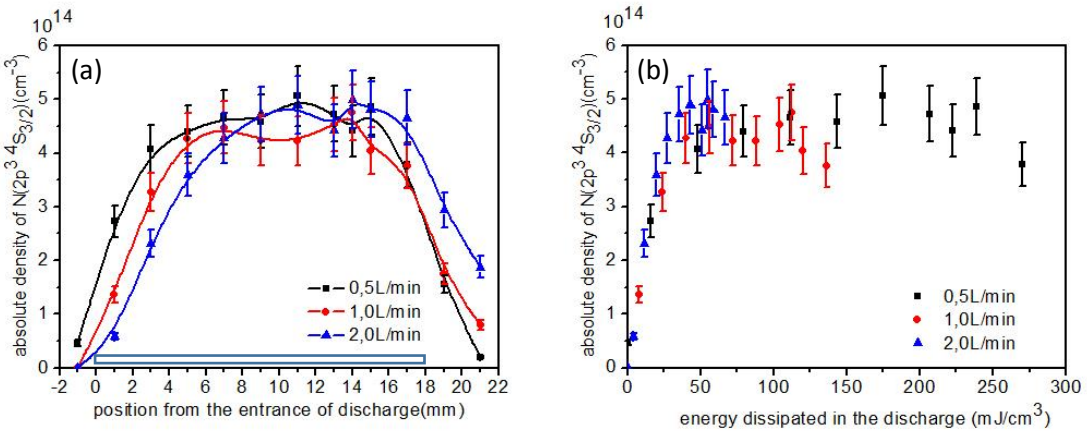

Figure 3-17 Absolute density of N ($2p^3\ ^4S_{3/2}$) as a function of (a) position from the entrance of discharge (b) residence time for different flow rate. Measurement conditions: P=0.6 W/cm² f=2kHz, HV=15.2 kV_{pp} for flow rate=0.5 L/min, HV=15.8 kV_{pp} for flow rate=1.0 L/min, HV=16.2 kV_{pp} for flow rate=2.0 L/min

It indicates that whatever the gas flow, the plateau reached by the N(^{4}S) density is similar, around 4.5 10^{14}cm^{-3}. On the other hand, the higher the gas flow, the slower the increase of the density at the beginning of the discharge, because N(^{4}S) atoms are carried away by the gas flow. To check the consistency of this hypothesis the same results are presented in Figure 3-17(b) as a function of the energy dissipated in the discharge. As can be seen, all the results superimpose with this representation.

Note that in order to keep the discharge power constant, we have to increase the applied voltage when increasing the gas flow rate. Indeed, the higher the gas flow, the more the active species involved in the memory effect such as N_2(A) are blown away, and as a result higher voltage is needed to ensure a similar averaged power value.

II.5. Evolution of the N ($2p^3\ ^4S_{3/2}$) density during the post-discharge

Measuring the density of the different species during the post-discharge is interesting because it offers the possibility to study the main mechanisms involved in their destruction. Figure 3-18 presents an example of such measurements for N(^{4}S) atoms. The discharge is first initiated for 108 periods and then switched off. Measurements are performed at the position x=14 mm as a function of time τ after the discharge extinction. The time τ=0 corresponds to the discharge extinction.

Let us consider that the main loss mechanism for N(^{4}S) atoms are the three-body recombination in volume and the diffusion to the walls:

$$N(^4S) + N(^4S) + N_2 \rightarrow N_2 + N_2(A,B) \quad k = 8.3 \times 10^{-34} \times \exp(500/T)\ [85] \qquad (R\ 6)$$

$$N(^4S) \rightarrow N(^4S)^{wall} \quad k = 32.26\ s^{-1}\ [85] \qquad (R\ 7)$$

Calculations are performed taking into account these two mechanisms and starting from the initial density measured at τ=0 ms. The corresponding results are depicted in Figure 3-18.

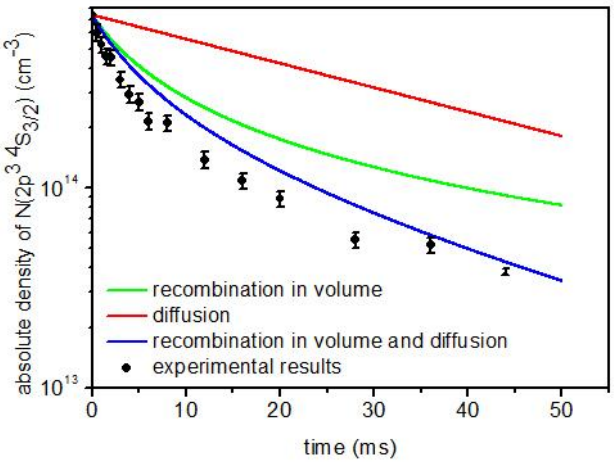

Figure 3-18 Comparison of the decrease of N ($2p^3\ ^4S_{3/2}$) density during the extinction of discharge. Measurement conditions: f=2kHz, HV=18.1kV$_{pp}$, flow rate=1.0l/min, position=14mm

Note that the gas flow is set to 1 L/min during the whole experiment in order to keep a stable discharge and to limit the contamination of the gas. Consequently, the N(^{4}S) density measured at a time τ actually corresponds to the N(^{4}S) density in a small discharge volume initially (*i.e.* at τ=0 ms) located at $\mathrm{x} = 14\mathrm{mm} - \mathrm{v} * \tau$ and transported by the gas flow at a velocity v. It means that experimental and numerical results can be compared only if the initial N(^{4}S) density is the same in both cases. As can be seen in Figure 3-9, for a gas flow of 1.0 L/min, the plateau N(^{4}S) density starts at approximately x=4 mm which means that experimental and numerical results can be compared between τ=0 ms and $\tau \approx 25$ ms.

As can be seen, experimental and numerical results are in good qualitative agreement even if losses are slightly underestimated in the model. It can be due to an underestimation of the N(^{4}S) losses by diffusion or to the unavoidable presence of oxidizing impurities during experiments, which were not accounted for in the model. These results confirm that N(^{4}S) losses in post-discharge in pure nitrogen are dominated by the diffusion to the walls and the three-body volume recombination on N_2 molecules.

Figure 3-19 presents the temporal evolution of the corresponding reaction rates. At the beginning of the post-discharge, the N(^{4}S) density is rather large and losses are dominated by the 3-body recombination, whose reaction rate depends on the square of the N(^{4}S) density. For τ>20 ms when the N(^{4}S) density is lower, losses by diffusion to the walls which are proportional to the N(^{4}S) density dominate.

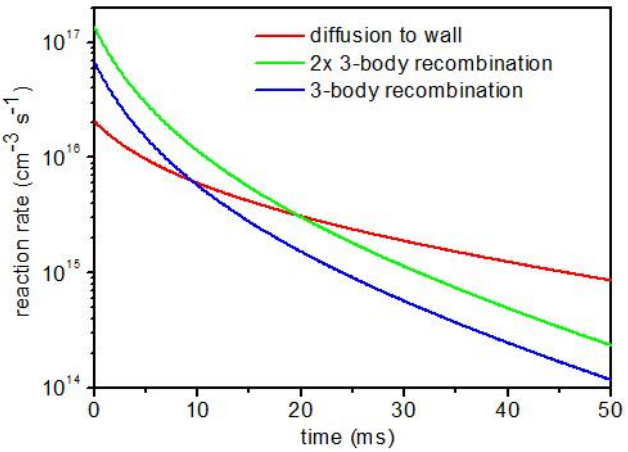

Figure 3-19 Temporal evolution of the reaction rates of the main destruction mechanisms for N(^4S) atoms in high purity nitrogen: three-body recombination and diffusion to the wall

II.6. Summary

In conclusion, the absolute density of N(^4S) atoms was determined in high purity nitrogen. Typical values of few 10^{14} cm^{-3} were found, the maximum measured density being about 7 $10^{14}cm^{-3}$ for a surface discharge power of 1 W/cm^2. The influence of the discharge power and gas flow was studied. The maximum the discharge power, the maximum the N(^4S) density. The averaged energy cost for N(^4S) atoms production was found to be 318 eV/atoms. N(^4S) atoms are produced by direct electron impact dissociation onto N_2 molecules. The main losses mechanisms of N(^4S) were studied during the post-discharge. For a short time scale, the three-body recombination dominates whereas losses to the dielectric surfaces dominate for a longer time scale.

III. N ($2p^3\ ^4S_{3/2}$) density in the mixture N_2/O_2

In this section, the measurements are carried out in a mixture of N_2/O_2 for different oxygen concentrations.

III.1. N ($2p^3\ ^4S_{3/2}$) density in the discharge for different oxygen concentration

Figure 3-20 shows the evolution of the N(^4S) density along the discharge for different concentration of oxygen (a) keeping the same discharge power and (b) keeping the same applied voltage. For a given concentration of oxygen, we can recognize the same trend as for the high purity nitrogen case: it increases, reaches a plateau and then decreases in the post-discharge region. Moreover, for a given position, the higher the oxygen concentration, the lower the N(^4S) density.

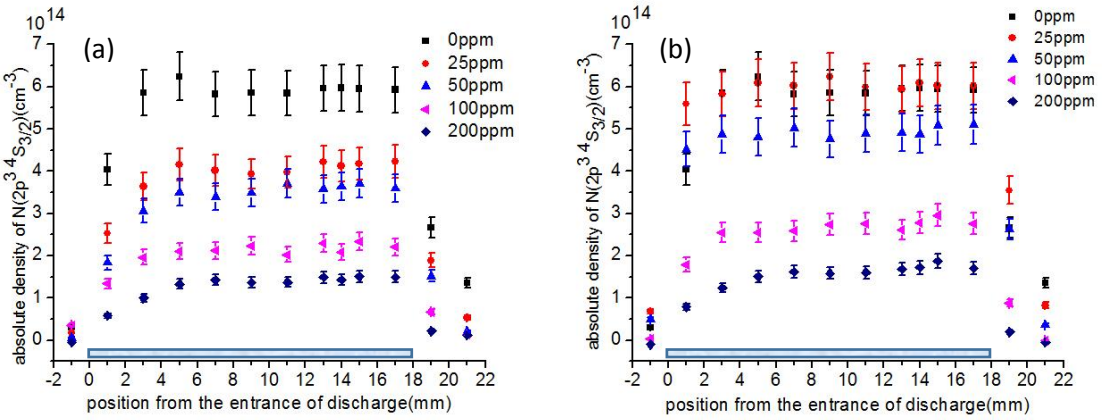

Figure 3-20 Absolute density of N ($2p^3\ ^4S_{3/2}$) as a function of position from the entrance of discharge with different concentration of O_2 (a) in keeping the same discharge power around 0.9 W/cm² by adjusting the applied voltage (b) in keeping the same applied voltage at 17.1 kV_{pp}. Measurement conditions: f=2 kHz, flow rate=1.0 L/min.

A summary of the N(^{4}S) density at x=14mm for both conditions is presented in Figure 3-21, together with the evolution of the current jump and the applied voltage (a) or dissipated power (b).

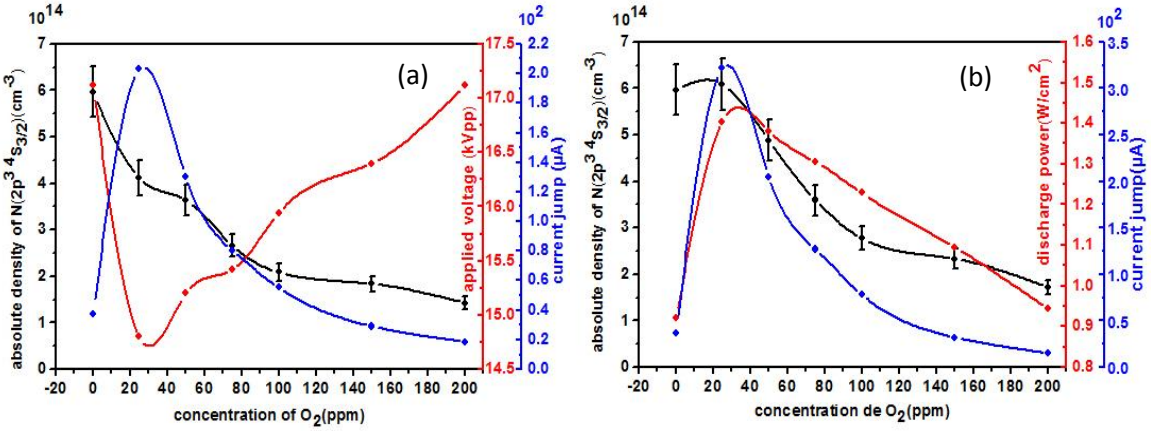

Figure 3-21 (a) Absolute density of N ($2p^3\ ^4S_{3/2}$)(black curve), current jump(blue curve) and applied voltage used to keeping the same discharge power around 0.9 W/cm²(red curve) as a function of concentration of O_2 (b) Absolute density of N ($2p^3\ ^4S_{3/2}$)(black curve), current jump(blue curve) and discharge power correspond to the same applied voltage at 17.1 kV_{pp}(red curve) as a function of concentration of O_2. Measurement conditions: f=2 kHz, flow rate=1.0 L/min

These results clearly indicate that the density of N(^{4}S) at the plateau decreases for increasing oxygen concentration. The calculations performed with the 0D model show a similar behavior. An example of numerical results obtained for a set of simulations performed at a constant voltage for different oxygen concentrations is presented in Figure 3-22.

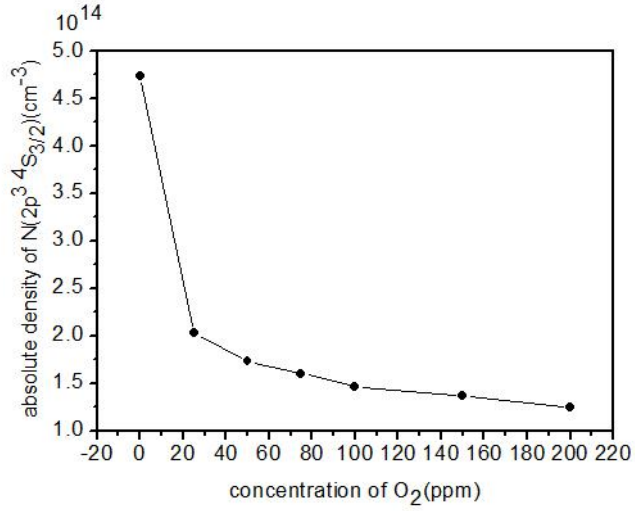

Figure 3-22 numerical results corresponding to simulations performed for the same conditions of Figure 3-21(b): HV=17.1 kVpp, f=2 kHz, flow rate=1.0 L/min

An analysis of the main destruction mechanisms of N(^{4}S) was performed using the model (see Appendix 1 section IV.1.1 for details). When O_2 is introduced in the discharge, the main losses are due to reactions of N(^{4}S) with oxidizing species. According to the model, the dominant reactions are $N(^4S) + NO \rightarrow N_2 + O(^3P,^1D)$ and $N(^4S) + O(^3P) + N_2 \rightarrow NO + N_2$. Thus, the decrease of the N(^{4}S) density for increasing O_2 concentration can be ascribed to a larger consumption of N(^{4}S) by oxidizing species. The careful examination of the N(^{4}S) density decay in post-discharge presented in section III.2 confirms this result.

The results obtained at constant applied voltage or input power exhibit similar trends. And the N(^{4}S) density is always found higher for a given ppm of oxygen when the voltage is kept constant, since the discharge power with a constant applied voltage is always higher than 0.9 W/cm^2 for small oxygen addition. It probably induces a higher production rate of N(^{4}S) atoms.

It is interesting to note that the evolution of the discharge power and the current jump are quite similar. At constant applied voltage, a small addition of oxygen increases the current jump indicating that more seed electrons are produced between two successive discharges. Thus, starting from a higher electron density for the same multiplication factor exp(αd) results in an increase of the discharge current and thus on the dissipated power (see Figure 3-21(b)). Consequently, if one wants to keep the same power when oxygen is introduced in the discharge, it is necessary to decrease the applied voltage (see Figure 3-21(a)).

Another interesting point concerns the profile of the N(^{4}S) density for the different oxygen concentration and especially the density rise at the entrance of the discharge. Whereas the N(^{4}S) density sharply increases for low oxygen concentrations, the density rise is much gradual for a higher concentration of oxygen. It can be due to the higher destruction of N(^{4}S) by oxidizing species or to a stronger decrease of the discharge power at the discharge entrance for increasing oxygen concentration.

Similarly to the high purity nitrogen case, measurements have been done as a function of time after discharge ignition at the position x=14 mm. The corresponding results are depicted in Figure 3-23.

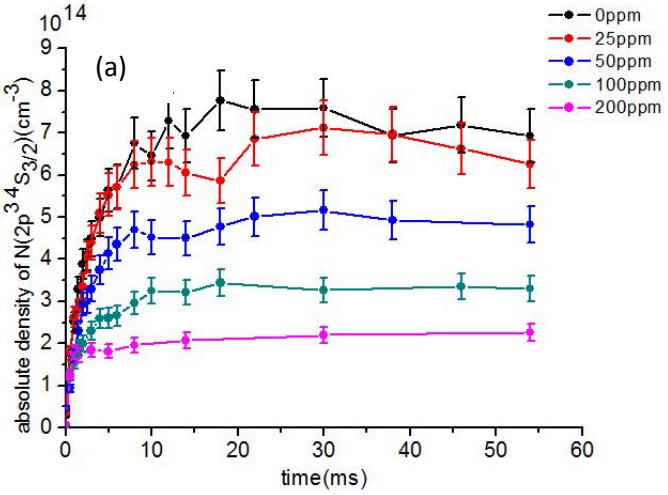

Figure 3-23 Absolute density of N ($2p^3\ ^4S_{3/2}$) as a function of time following the ignition of the discharge for different concentration of O_2. Experimental conditions: HV=18.1 kV_{pp}, f=2 kHz, gas flow=1.0 L/min

For this set of experiments, the increase of the N(^{4}S) density remains stiff even for high oxygen concentrations. Time-dependent measurements performed at x=14 mm imply that the small gas volumes carried by the gas flow previously pass through a well-established discharge along 14 mm before being probed by TALIF. In the frame of these gas volumes, the discharge power increases quickly in time. On the contrary, for measurements performed for different x positions in the stationary state, the probable stronger decrease of the power density at the discharge entrance for high oxygen concentrations results in a more gradual increase of the N(^{4}S) density.

In order to quantify the growth of the N(^{4}S) density, the curves [N(^{4}S)]=f(t) were fitted by a function of form $f(t) = N(\ ^4S)_{ss}\left(1 - \exp(-t/\tau)\right)$, where $N(\ ^4S)_{ss}$ represents the N(^{4}S) density at steady state, and τ represents the characteristic growth time. The corresponding results are presented in Figure 3-24.

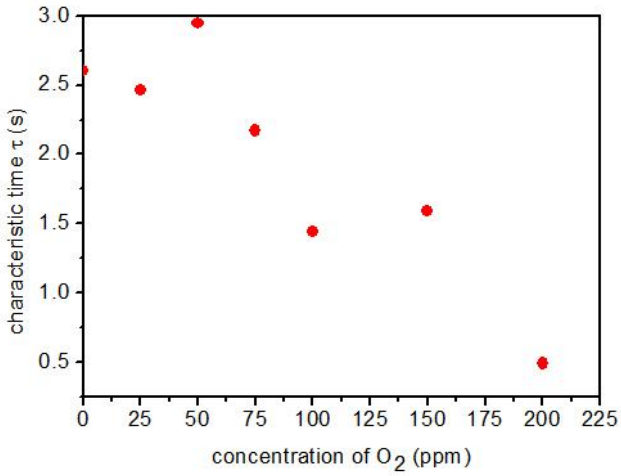

Figure 3-24 Characteristic time for the increase of N ($2p^3\ ^4S_{3/2}$) density as a function of concentration of O_2

It can be seen that the higher the oxygen concentration is; the lower the characteristic time τ is, *i.e.* the steady state is reached faster. To investigate this phenomenon, numerical calculations have been

performed using the model presented in Appendix 1 for different oxygen concentrations and a constant applied voltage. Note that in these simulations the input power is constant, in good agreement with the situation described above for time-dependent measurements. The corresponding results are presented in Figure 3-25.

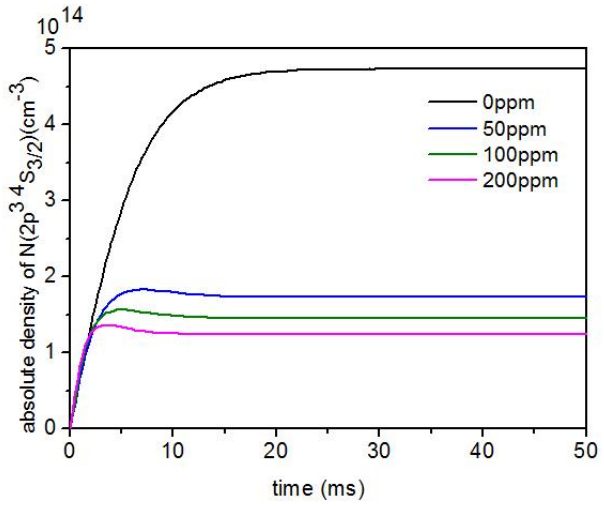

Figure 3-25 Simulation results for the N ($2p^3\ ^4S_{3/2}$) density as a function of time following the ignition of the discharge for different concentration of O_2. Simulation conditions: HV=18.1 kV_{pp}, f=2 kHz, gas flow=1.0 L/min

As can be seen, the model is able to reproduce the experimental behavior: as the amount of oxygen increases, the stationary value of the N(^{4}S) density is reached faster. It can be directly explained by the increase of the N(^{4}S) losses related to oxidizing species: the higher the loss rate, the faster the balance between production and destruction is established and the lower the resulting stationary density is.

III.2. N ($2p^3\ ^4S_{3/2}$) density in post-discharge for different oxygen concentration

The evolution of the N(^{4}S) density in the post-discharge is measured for different oxygen concentrations. The employed method is the same as the one used in high purity nitrogen: measurements are performed at x=14 mm as a function of time after switching off the discharge. The gas flow rate is set to 1.0 L/min and the voltage applied to the discharge before extinction was set to 18.1 kV_{pp}. The results are presented in Figure 3-26.

As the O_2 concentration increases, the shape of the curve [N(^{4}S)]=f(t) changes. Especially, the slope of the curve for short time following discharge extinction is more and more negative. It can be explained by the presence of an increasing density of oxidizing species which efficiently react with N(^{4}S). Among this species, O(^{3}P) atoms and NO(X) molecules are susceptible to play an important role through the reactions $N(^4S) + O(^3P) + N_2 \rightarrow NO + N_2$ and $N(^4S) + NO \rightarrow N_2 + O(^3P, ^1D)$. A deeper investigation of the N(^{4}S) decay in post-discharge is presented in chapter 6 section II.1. Indeed, it requires the knowledge of the O(^{3}P) and NO(X) density to be performed, which are respectively presented in chapter 4 and 5.

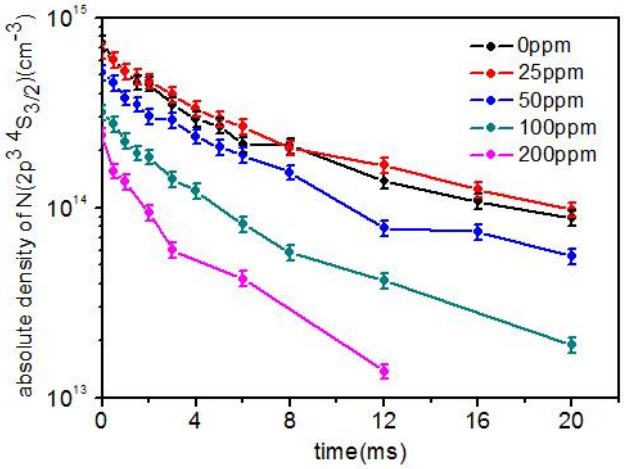

Figure 3-26 Absolute density of N ($2p^3\ ^4S_{3/2}$) as a function of time with different concentration of O_2 from the start of extinction of discharge. Measurement conditions: f=2 kHz, HV=18.1 kV_{pp}, flow rate=1.0 L/min, position=14 mm

IV. Conclusion

In this chapter, we present the results concerning the absolute density of N(^{4}S) in an APTD in N_2 and in the mixture of N_2/O_2. The measurements were performed as a function of the position, the gas flow, and the discharge power, and as a function of time. Moreover, the decrease of the density during the post-discharge was also studied.

In summary, the density of N(^{4}S) obtained is of the order of few 10^{14}cm^{-3}, the higher the oxygen concentration, the lower the N(^{4}S) density. These values are slightly higher than the ones determined by Es. Sebbar [60,61] but remain in the same order of magnitude. The statistical error was estimated about ±9.11%, and the increase of the gas temperature during the discharge operation with respect to the temperature during the calibration can induce an overestimation of the density, which was estimated to be 15.8%.

As a function of the position, the N(^{4}S) increases at the entrance of discharge, then becomes constant, and finally decreases in the post-discharge region.

N(^{4}S) atoms are produced by direct electron impact dissociation of N_2 molecules. In high purity nitrogen, losses are dominated by three-body recombination onto N_2 molecules. Losses by diffusion to the walls also play a role and become dominant for the longer timescale. In the mixture N_2/O_2, the losses of N(^{4}S) atoms are mainly due to reactions with oxidizing species *i.e.* $N(^4S) + O(^3P) + N_2 \rightarrow NO + N_2$ and $N(^4S) + NO \rightarrow N_2 + O(^3P, ^1D)$.

Chapter 4. TALIF measurements of atomic oxygen O ($2p^4\ ^3P_J$) density

This chapter is dedicated to the TALIF measurements on O ($2p^4\ ^3P_J$) in homogeneous Townsend discharges in the mixture N_2/O_2. As is mentioned in chapter 3 for N(^4S), we will use O(^3P) instead of O ($2p^4\ ^3P_J$) in most discussions except in some particular discussions which need to detail the ground state. First, the method used for the TALIF measurements on O ($2p^4\ ^3P_J$) is described. Then, we present the calibration procedure using xenon and we discuss the experimental errors. Finally, the results obtained in the mixture N_2/O_2 are presented and discussed.

I. Methodology employed for the TALIF measurements on O ($2p^4\ ^3P_J$)

The excitation scheme of O ($2p^4\ ^3P_J$) is depicted in Figure 4-1.

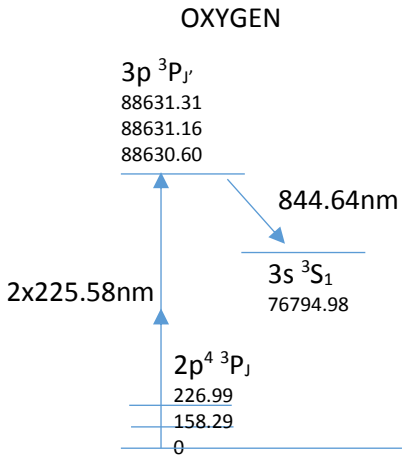

Figure 4-1 Tow-photon excitation schema of oxygen. The level energies are given in cm^{-1}

The ground state O ($2p^4\ ^3P_J$) and the excited state O ($3p\ ^3P_{J'}$) are divided into three levels with different orbital angular momentum quantum numbers, J=2, 1, 0 and J'=1, 2, 0 respectively. Since the energy of the upper three levels are very similar and can't be distinguished during laser excitation and fluorescence detection, we consider these three levels as one level. Nevertheless, this approximation can't be done for the ground state which three levels have very different energies. Consequently, they have to be individually excited with theoretical excitation wavelengths of 2×225.792 nm, 2×226.192 nm, and 2 × 226.375 nm respectively. Figure 4-2(a) and (b) show the excitation spectrums of O for the J=2 and J=1 levels. Unfortunately, for the level characterized by J=0, the corresponding fluorescence intensity is too low to allow a correct and reliable measurement.

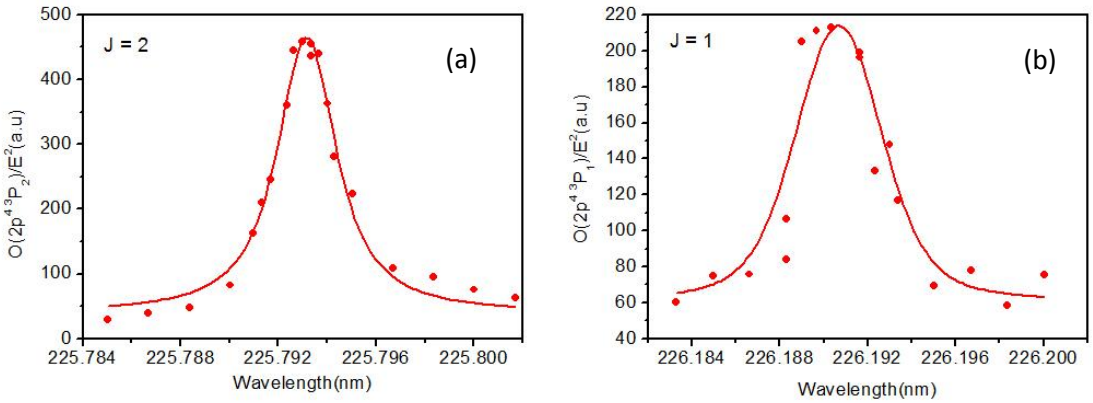

Figure 4-2 (a) and (b) Excitation spectrum for the transition O ($2p^4\ ^3P_2$) -> O ($3p\ ^3P_{J'}$) obtained in a Townsend discharge in a mixture of 200 ppm O_2 Measurement conditions: P=0.9 W/cm², f=2 kHz, flow rate=1.0 L/min, x=14 mm

According to the excitation scheme of O ($2p^4\ ^3P_J$) atom and to the above discussion, the total density of O ($2p^4\ ^3P_J$) is given by the sum of the three sub-levels, which are populated according to the Boltzmann law. Thus, for each level, we can calculate the Boltzmann factor f_J whose expression is:

$$f_J(T) = \frac{(2J+1)e^{\frac{E_J}{k_B T}}}{\sum_{j=2.1.0}(2j+1)e^{\frac{E_j}{k_B T}}} \tag{4.1}$$

Hence, the total density of O ($2p^4\ ^3P_J$) should be given by:

$$n_O = \sum_J n_J = \frac{n_J}{f_J} \tag{4.2}$$

Considering a gas temperature of T=300K, the Boltzmann factors f_J are 0.74, 0.21 and 0.05 for J=2,1,0 respectively. Figure 4-3 represents an example of TALIF measurements in which the absolute densities of the J=2 and J=1 states have been determined as a function of the position in the discharge. The total density of the ground state has also been determined following equation (4.2) using the densities and Boltzmann factors of the J=1 and J=2 states. As can be seen, a good agreement is found between these two different determinations indicating that the considered temperature is close to the gas temperature. Note that due to the small energy difference between these levels, this method is inaccurate to determine the gas temperature [86]. The smaller fluorescence signal of the J=1 level results in a decrease of the signal to noise ratio which in turns results in oscillations in the corresponding curve of the overall density. Consequently, the overall O ($2p^4\ ^3P_J$) ground state density is determined using equation (4.2) and probing only the J=2 level in this work.

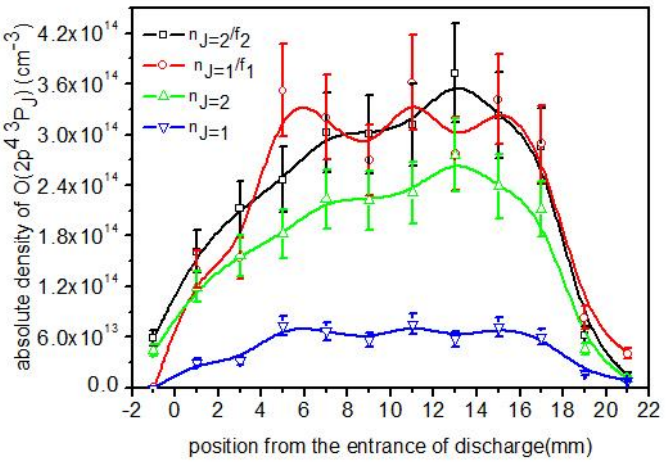

Figure 4-3 Relative density of O ($2p^4\ ^3P_J$) for J=2, 1 respectively, total density calculated by taking the Boltzmann factor f_J into account. Measurement conditions: P=0.9 W/cm², f=2 kHz, HV=17.1 kV_{pp}, position=14 mm, flow rate=1.0 L/min, concentration of O_2=200 ppm

As for the measurements of N (^4S) density, it is necessary to determine the linear working domain in terms of laser energy corresponding to an unsaturated transition. Figure 4-4 shows the TALIF signal of O ($2p^4\ ^3P_2$) as a function of laser energy in logarithmic coordinate.

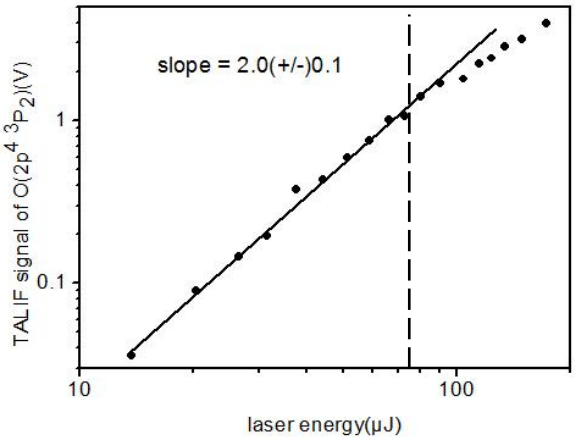

Figure 4-4 Log-log plot of the O atom fluorescence signal as a function of laser energy. Measurement conditions: P=0.9 W/cm², f=2 kHz, HV=17.1 kV_{pp}, position=14 mm, flow rate=1.0 L/min, concentration of O_2=200 ppm

As can be seen, the linear regime characterized by a slope of 2 is obtained for a laser energy below 90µJ. Consequently, the measurements are performed around 75 µJ in order to have a good signal to noise ratio.

II. Calibration of the TALIF signal using xenon

Measurements of O(^3P) are calibrated using xenon which has a very similar excitation scheme. The saturation during excitation of Xe at low pressure occurs at a very low laser energy, which cannot be measured accurately with our energy meter. Thus during calibration, xenon is diluted in argon (with a typical ratio of Xe/Ar about 1:4000) for a typical pressure of 250 mbar. Consequently, the quenching rate of Xe increases thus decreasing the saturation energy level to a measurable value of 6 µJ.

A typical excitation spectrum of Xe is provided in Figure 4-5(a) whereas the evolution of the TALIF signal with respect to the laser energy is presented in Figure 4-5(b).

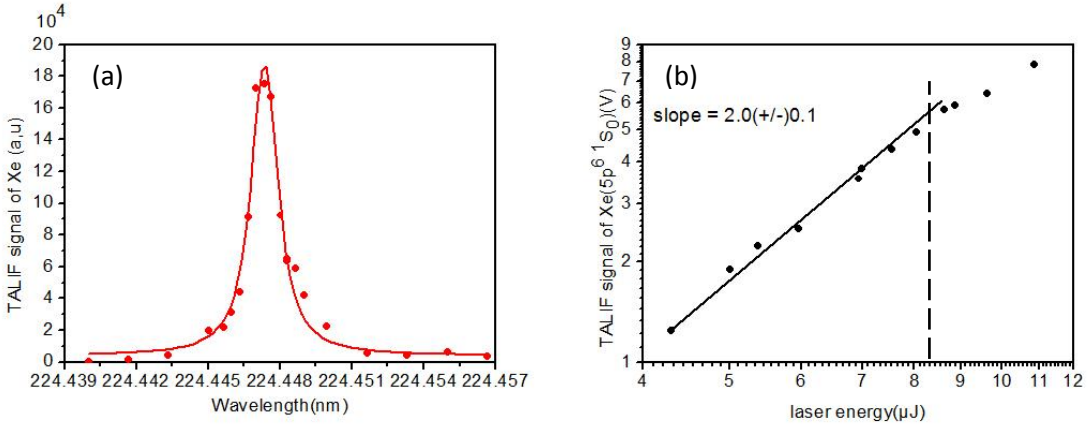

Figure 4-5 (a) Excitation spectrum for the transition Xe($5p^6\ ^1S_0$)) -> Xe(6p' $[3/2]_2$) obtained in a mixture of Ar/Xe. (b) Log-log plot of the Xe atom fluorescence signal as a function of laser energy. Measurement conditions: p(Xe)=0.062 mbar, p(Ar)=249.54 mbar, x=14 mm

Nevertheless, increasing the pressure in the vessel induces a serious drawback regarding the TALIF measurement and especially the fluorescence detection [64,74]. Indeed, after populating the 6p'$[3/2]_2$ state by laser excitation, xenon atoms can decay by emitting photons at 834.68 nm which corresponds to the fluorescence signal of interest. But the 6p'$[3/2]_2$ state can also be quenched to lower levels. Among these levels, the 6p$[3/2]_2$ and 6p$[1/2]_0$ are of primary importance because they can experience a radiative decay to the 6s$[3/2]_2$ or 6s$[3/2]_1$ states respectively with corresponding wavelengths of 823.16 nm and 828 nm. These wavelengths are closed to the fluorescence wavelength of interest and can thus be detected during the measurements. A schematic diagram representing the different levels and transitions of interest is presented in Figure 4-6.

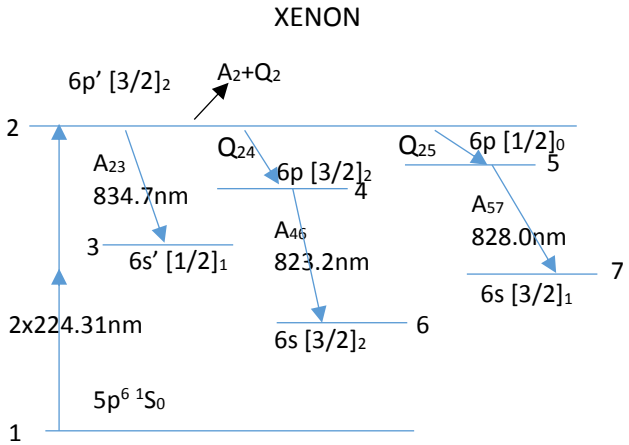

Figure 4-6 Tow-photon excitation schema of xenon.

To avoid this problem, it is recommended to use a very narrow bandpass filter or a monochromator. Unfortunately, when the calibration was performed, we only had one interference filter with a 10 nm bandwidth centered on 830 nm. Consequently, both the emissions at 828 nm and 834.7 nm were collected because the transmission efficiencies *Tr* of the filter are respectively *Tr* =59.9% and *Tr*=55.6%. The emission at 823 nm is more efficiently removed due to the low transmission of the

filter at this wavelength, *Tr=1%*. To overcome this problem, we tried to estimate the relative proportion of the collected signals at 828 nm and 834.7 nm by analyzing the fluorescence signal with a spectrometer. An example of such measurement is depicted in Figure 4-7 together with the spectral transmission of the interference filter used in the experiments for comparison. Nevertheless, this measurement was performed with a high laser energy of 150 µJ which is well above the energy threshold of the saturated regime. Indeed, we did not succeed in measuring the spectrally resolved fluorescence signal for a laser energy below 6µJ. Thus, this measurement cannot be used to estimate the error during the calibration procedure. Another attempt was made using the monochromator used for LIF measurements on NO but again, we did not succeed in measuring the TALIF signal at low laser energy. Consequently, the simultaneous detection of the signals at 828nm and 834.7nm introduces a non-negligible uncertainty regarding the absolute values of the $O(^3P)$ density which is difficult to determine.

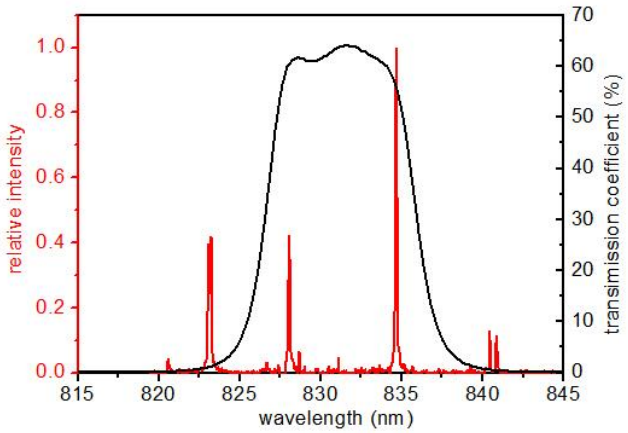

Figure 4-7 Transmission coefficient of the filter (black one) and the TALIF emission spectra of Xe (red one)

The calibration factor is then calculated following the method described in equation (3.2). Table 4-1 summarizes all the parameters taken from literature used in the calculation of the absolute density.

Table 4-1 Parameters used for the calculation of absolute density of O atom

parameters	O	Xe
T	0.54	0.60
η	0.93	1.26
σ_{Xe}/σ_O	1.9 [75]	
$A_{32}(10^7\ s^{-1})$	3.324 [87]	2.09 [88]
$A_3(10^7\ s^{-1})$	3.324 [87]	2.85 [88]
$k_q(O_2)$ (10^{-10} cm^3/s)	9.4 [75]	
$k_q(N_2)$ (10^{-10} cm^3/s)	5.9 [71]	
k_q(Xe) (10^{-10} cm^3/s)		3.6 [75]
k_q(Ar) (10^{-10} cm^3/s)		1.8 [89]

It should be noted that, the two-photon absorption cross section σ is the sum of the excitation from one J ground state to the three J' excited state, and can be considered as equal for all the three J level of the ground state, as well as the ratio of cross section according to [90]. Moreover, the gas temperature was determined experimentally by OES (see section I.3) and was found to be within the

range [300 K;430 K]. Consequently, we consider the quenching coefficients coming from the literature and determined at room temperature. The error introduced by this assumption is discussed in the next section. According to Niemi *et al*. [4], the error concerning the value of the ratio of two-photon absorption cross section of O and Xe atom is around 20%.

To obtain the calibration factor, TALIF measurements on xenon were performed at different locations along the discharge. Using the data provided in Table 4-1, the calibration factor is then obtained within the whole discharge. The corresponding results are presented in Figure 4-8.

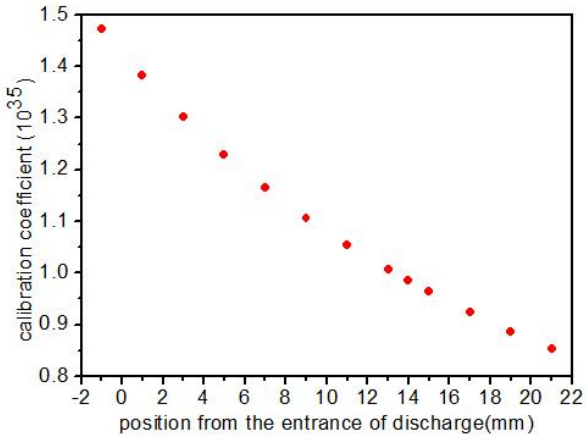

Figure 4-8 Calibration coefficient as a function of position

III. Influence of the gas temperature on TALIF measurements

In chapter 3 section I.3, we show that the gas temperature can increase during the experiments up to 430 K. This can affect the quenching rate and the relative populations of the three J levels of O(^{3}P). In this section, an estimation of the error due to the temperature is provided.

The overall O(^{3}P) density n(O) obtained from TALIF measurements is given by the following relation:

$$n(O) = \mathrm{CF}_{O/Xe} \times \frac{S_{TALIF}(O)}{\left(\frac{E_L}{h\nu_{laser}}\right)^2(O)} \times \frac{(Q_3+A_3)}{A_{32}}(O) \times \frac{1}{f_2} \tag{4.3}$$

Thus if the gas temperature T is different from T_0, the resulting error committed by considering T_0 instead of T is given by the factor

$$\frac{(Q_3+A_3)_T}{(Q_3+A_3)_{T_0}} \times \frac{f_{2_{T_0}}}{f_{2_T}}$$

Assuming that the quenching of excited oxygen atoms is mainly due to nitrogen molecules and considering T_0=300 K and T=430 K, we obtain $\frac{(Q_3+A_3)_{430K}}{(Q_3+A_3)_{300K}} = 0.837$ and $\frac{f_{2_{300K}}}{f_{2_{430K}}}$=1.03 indicating that the main effect of the temperature is related to the quenching rate. Finally, an increase in the temperature up to 430 K during the experiments result in an overestimation of the density of O(^{3}P) by 13.8%.

IV. Absolute atomic oxygen density in the mixture N_2/O_2

In this part, we investigate the evolution of the absolute density of O(^{3}P) with the variation of oxygen concentration, the influence of the discharge power, the creation and the destruction of O(^{3}P) during and after the discharge. The error bars shown in the figures are based on the reproducibility of the measurements, which is ±15.7% on average, it does not take into account the influence of the gas temperature discussed above.

IV.1. Absolute density of O ($2p^4\ ^3P_J$) as a function of the position in the discharge for various oxygen concentration

Figure 4-9(a) and (b) show the evolution of absolute density of O(^{3}P) as a function of the position in the discharge, for different concentrations of O_2 ranging between 25 ppm and 200 ppm for a total flow rate of 1.0 L/min. Measurements are performed in the stationary state. In this set of measurements, the discharge power is kept constant, around 0.9 W/cm^2 by adjusting the applied voltage. The frequency is 2 kHz.

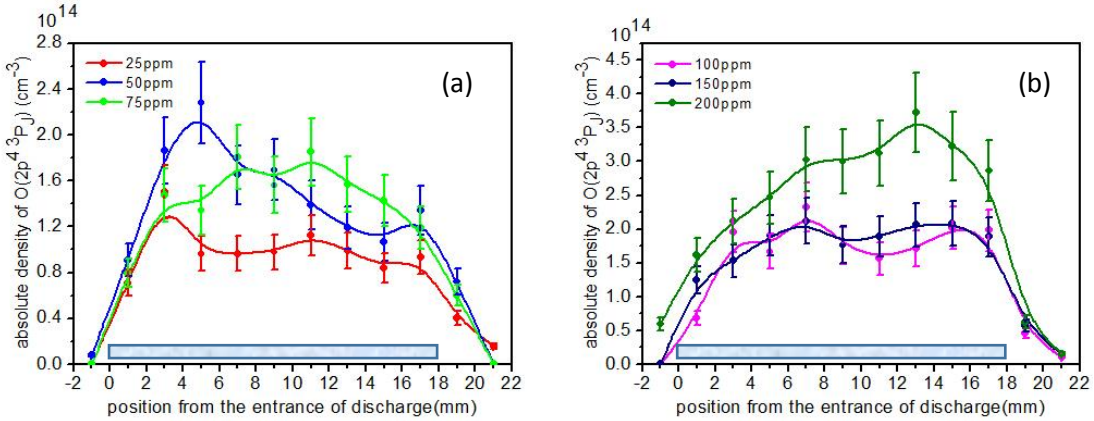

Figure 4-9 Absolute density of O ($2p^4\ ^3P_J$) as a function of position for different concentration of O_2. (a) Concentration of O_2 from 25 ppm to 75 ppm; (b) Concentration of O_2 from 100 ppm to 200 ppm. Measurement condition: P=0.9 W/cm^2, f=2 kHz, flow rate=1.0 L/min.

Similar experiments performed with a constant applied voltage of 17.1kV$_{pp}$ are presented in Figure 4-10.

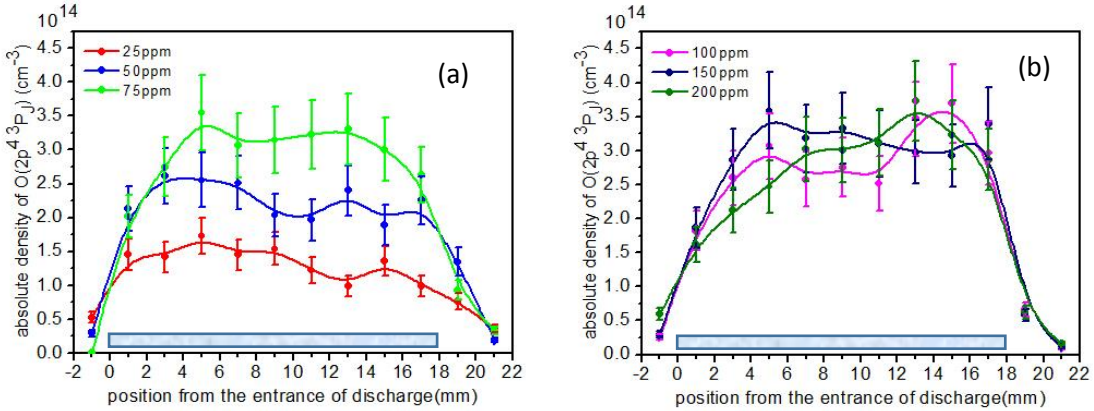

Figure 4-10 Absolute density of O ($2p^4\ ^3P_J$) as a function of position for different concentration of O_2. (a) Concentration of O_2 from 25 ppm to 75 ppm; (b) Concentration of O_2 from 100 ppm to 200 ppm. Measurement condition: HT=17.1 kV_{pp}, f=2 kHz, flow rate=1.0 L/min.

The spatial profiles of the $O(^3P)$ density present similar features compared to the $N(^4S)$ profiles. First $[O(^3P)]$ increases, reach a plateau and then decreases in post-discharge. As previously explained, this behavior can be due to the superimposition of several effects arising in time and space:

- the discharge power increases from the entry of the discharge to the exit,
- the gas flow is responsible for the transport of the produced species,
- the presence of the plateau indicates an equilibrium between the production and the destruction of $O(^3P)$.

The maximum $O(^3P)$ density measured in our conditions is around 3.5 10^{14} cm^{-3}. For some conditions, the $O(^3P)$ profile is different. For example, at 50 ppm and 0.9 W/cm^2, the density increases until x=5 mm and then decreases and no plateau is observed. It can be due to experimental errors during the measurements. For example, a small vertical displacement during the translation of the discharge cell can occur. In this case, the laser beam crosses the discharge at different vertical positions. Nevertheless, this phenomenon should also occur for other measurements performed at different ppm, which is not systematically observed. This particular profile of $O(^3P)$ density can also have a physical origin. Indeed, the composition of the gas changes along the discharge and the production and destruction rates of $O(^3P)$ atoms can vary accordingly.

IV.2. Absolute density of O ($2p^4\ ^3P_J$) as a function of oxygen concentration

A summary of the $O(^3P)$ density measured for the different O_2 concentrations at x=14 mm is presented in Figure 4-11. Figure 4-11(a) corresponds to measurements performed at 0.9 W/cm^2 whereas Figure 4-11(b) presents the results obtained for a constant applied voltage of 17.1kV_{pp}. The measured current jump and applied voltage or discharge power are also presented. To investigate the influence of the O_2 concentration on the $O(^3P)$ density, numerical simulations are performed considering a constant applied voltage of 17.1 kV_{pp} and the corresponding results are presented in Figure 4-11(c) for comparison. Experimental and numerical results are discussed in the following.

For both series of experiments, the $O(^3P)$ concentration increases from 0 to 100 ppm of oxygen whereas for higher O_2 concentrations, the $O(^3P)$ density is roughly constant. At first sight, it seems counterintuitive since $O(^3P)$ atoms directly come from the dissociation of oxygen molecules. To understand this behavior, it is necessary to have a look at the chemical pathways leading to the production of $O(^3P)$. Basically, in low-temperature plasma, the energy necessary for O_2 dissociation is brought either by free electrons or by heavy species in the excited state. In a Townsend discharge for low oxygen concentration, the dissociation of O_2 molecules by electrons is negligible because of the low electron density which maximum value is about 10^7 cm^{-3} for an APTD in pure N_2 [31]. In the same conditions, $N_2(A)$ metastable molecules have densities up to 10^{13} cm^{-3}. Consequently, the O_2 dissociation occurs mainly during their collisions with $N_2(A)$ through the reaction $N_2(A) + O_2 \rightarrow N_2 + O(^3P) + O(^3P)$, as indicated by the results of the model (see Appendix 1 section IV.2.1 for the detailed analysis). In the numerical results presented in Figure 4-11(c), the $O(^3P)$ density shows qualitatively a similar behavior: it increases when increasing the O_2 concentration but this increase is less and less pronounced as the O_2 concentration increases. In the simulations, this behavior is directly related to the decrease of the $N_2(A)$ concentration as indicated in Figure 4-11(c). Indeed when increasing the O_2

concentration, the quenching rate of $N_2(A)$ also increases. Thus it probably limits the dissociation of O_2 and consequently the production of $O(^3P)$.

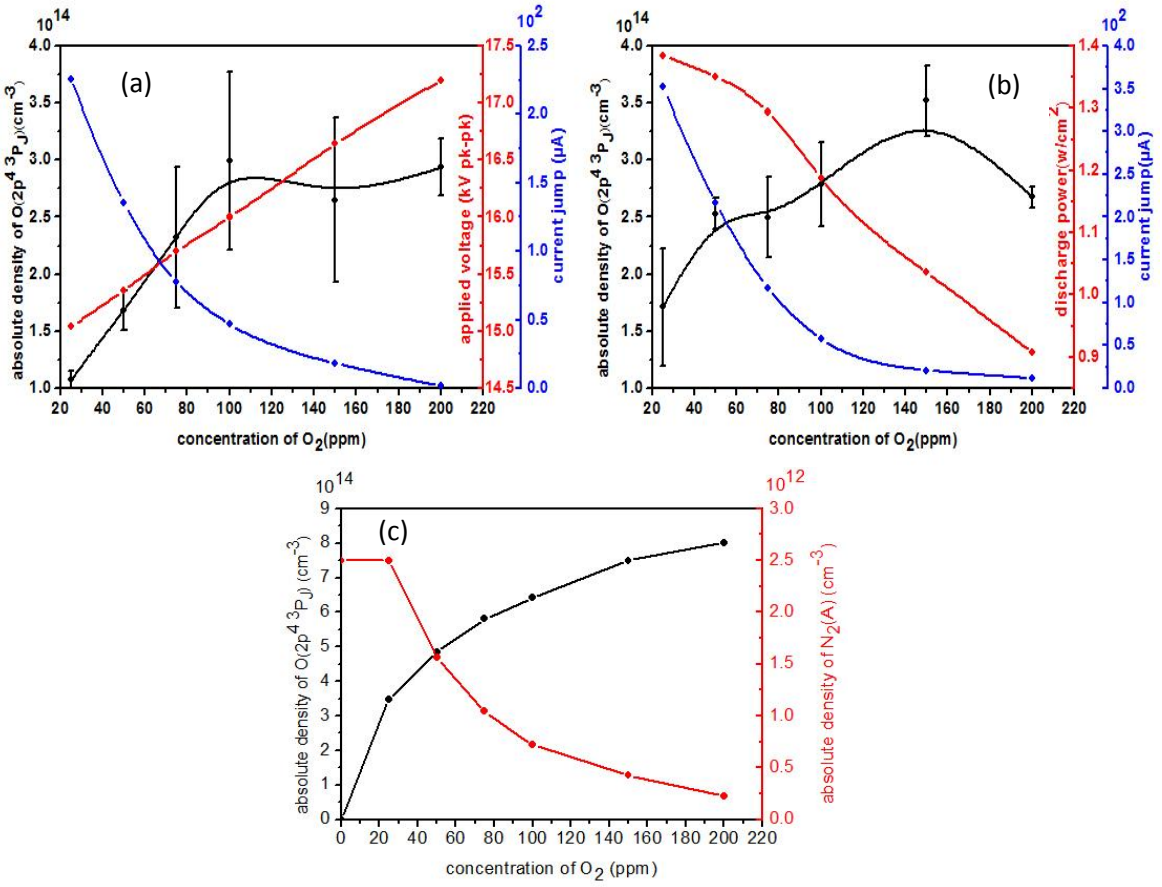

Figure 4-11 Absolute density of O ($2p^4\ ^3P_J$) as a function of concentration of O_2. (a) in keeping the same discharge power around 0.9 W/cm² by regulation the applied voltage; (b) in keeping the same applied voltage at 17.1kV$_{pp}$ (c) simulation results corresponding to the experimental result of (b). Measurement conditions: f=2 kHz, position=14 mm, flow rate=1.0 L/min.

The production of $O(^3P)$ with respect to the input O_2 concentration can be described using the dissociation degree of molecular oxygen which can be defined by the ratio $[O(^3P)]/[O_2]$ [91]. The corresponding results are presented in Figure 4-12(a) for the measurements performed at x=14 mm.

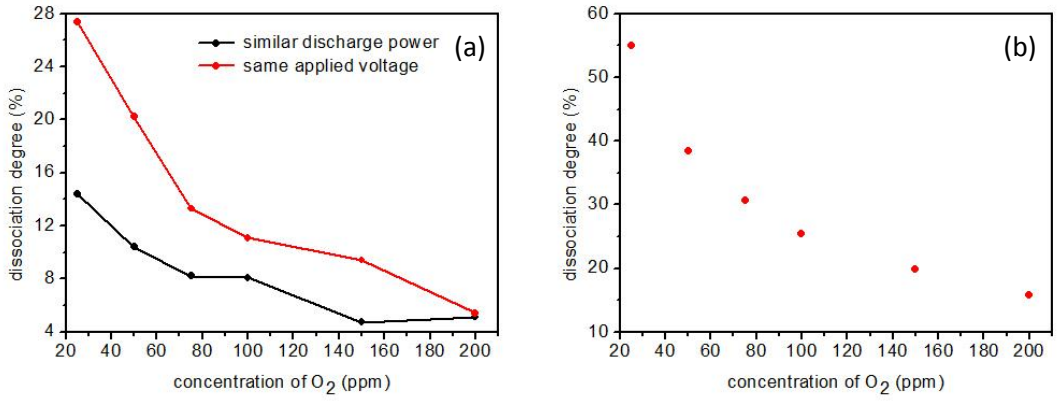

Figure 4-12 Dissociation degree of O atom in a Townsend discharge: (a) experimental results (b) simulation results obtained for a constant applied voltage

As can be seen, the dissociation degree decreases when increasing the O_2 concentration. Numerical results presented in Figure 4-12 (b) present the same trend. This decrease is much pronounced for the set of experiments performed at the constant voltage. A possible explanation is that the discharge power is higher at the constant voltage for low O_2 concentrations as depicted in Figure 4-11(b). To confirm this hypothesis, it is necessary to perform measurements for different discharge powers.

IV.3.Absolute density of O ($2p^4\ ^3P_J$) as a function of discharge power

To investigate the effect of the discharge power on the production of O(^{3}P) atoms, experiments are performed for 200 ppm of O_2 and an applied voltage of 17.1 kV_{pp}. The discharge power is varied from 0.4 W/cm^2 to 2.6 W/cm^2 by changing the frequency of the sinusoidal applied voltage from 1.5 kHz to 4.0 kHz. The corresponding results are presented in Figure 4-13(a). In addition, the evolution of the current jump I_{jump} is also provided. Note that it is not possible to determine I_{jump} for the two lower discharge powers because it is too small. Moreover, at 2.6 W/cm^2 (*i.e.* at 4 kHz), the discharge starts to become filamentary, consequently, the corresponding current jump is not shown. Numerical results corresponding to simulations performed for the same conditions are presented in Figure 4-13(b).

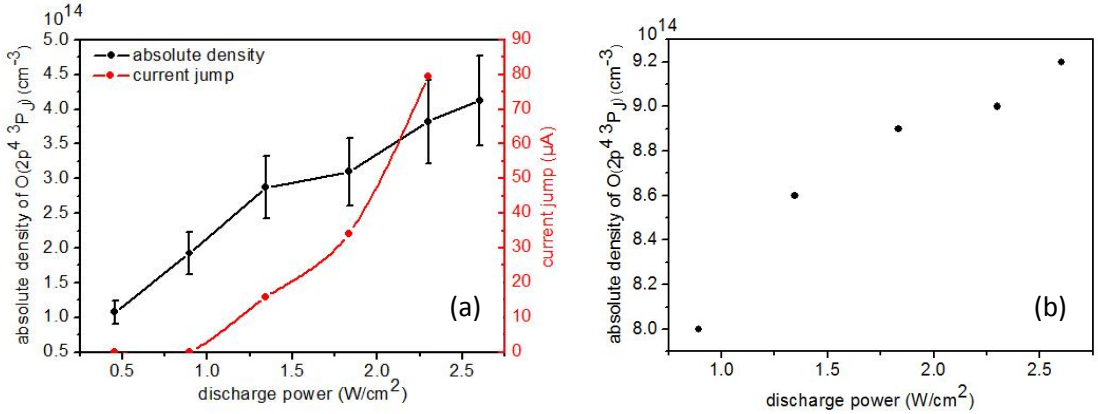

Figure 4-13 Absolute density of O ($2p^4\ ^3P_J$) as a function of discharge power. (a) experimental results (b)simulation results. Measurement condition: HV= 17.1 kV_{pp}, position=14 mm, flow rate=1.0 L/min, concentration of O_2=200 ppm

In the range of investigated power, the density of $O(^3P)$ is directly proportional to the input power. Between 0.4 W/cm^2 and 2.6 W/cm^2, the $O(^3P)$ density increases by a factor 3.8. Numerical results presented in Figure 4-13(b) present a similar trend: the $O(^3P)$ density increases for increasing discharge power. Since in our conditions $O(^3P)$ atoms are mainly produced during dissociation of O_2 by $N_2(A)$ metastable molecules, it is interesting to discuss the effect of the frequency on the production of $N_2(A)$.

The influence of the applied frequency on the discharge parameters was described in chapter 3 section II.3. We saw that increasing the frequency result in an increase of the electron density whereas the gas gap voltage remains roughly the same. Consequently, the production rate of $N_2(A)$ metastable by electron impact increases due to the higher electron density resulting in a higher production of $O(^3P)$ atoms. To check the consistency of this hypothesis the evolutions of the discharge current I_d and of the gas gap voltage V_g are presented in Figure 4-14.

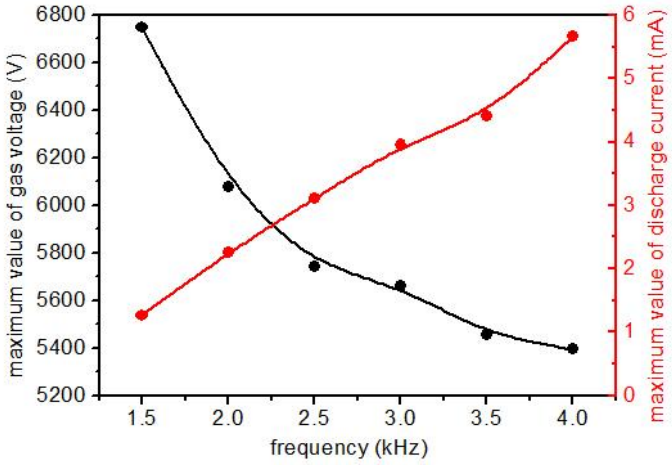

Figure 4-14 The maximum value of gas voltage (black one) and discharge power (red one) as a function of frequency

The gas gap voltage V_g slightly decreases when increasing the frequency from 6748 V at 1.5 kHz to 5394 V at 4 kHz. This evolution means that the breakdown is easier for higher frequencies. As explained in chapter 3 section II.3 , it can be explained by an increase of the gas temperature together with an increase of the memory effect. This last phenomenon is illustrated by the evolution of the current jump presented in Figure 4-13. Contrary to the evolution of V_g, the maximum discharge current $I_d$max increases linearly when increasing the frequency from 1.27 mA at 1.5 kHz to 5.66 mA at 4 kHz in good agreement with the previous discussion. Thus, following the previous discussion, increasing the frequency probably results in an increase of the maximum $N_2(A)$ density, the latter occurring just after the maximum discharge current according to numerical calculations (see *e.g.* Figure A- 3 in Appendix 1). To verify this, the evolution of the maximum $N_2(A)$ density and of the $N_2(A)$ density between two discharges provided by the model are presented in Figure 4-15. One can see that the maximum $N_2(A)$ density increases when increasing the power, from 7 10^{13} cm^{-3} to 9.2 10^{13} cm^{-3} *i.e.* by a factor 1.3.

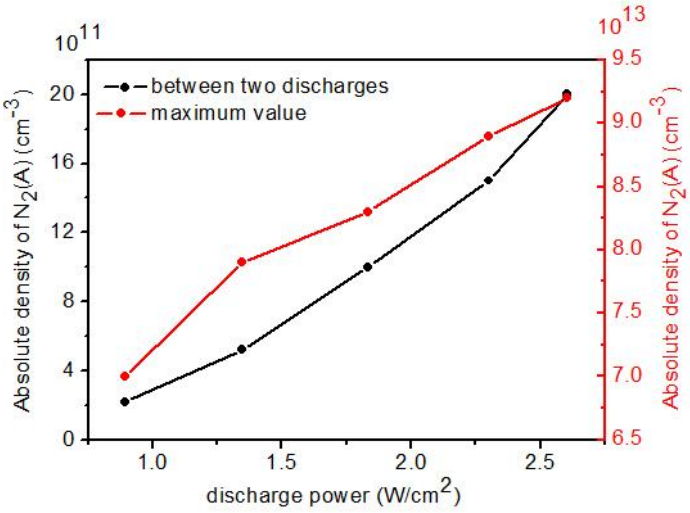

Figure 4-15 Absolute density of $N_2(A)$ as a function of discharge power

Increasing the frequency also decreases the time period during which the discharge is OFF. During this time period, no more $N_2(A)$ are produced by electronic excitation and the $N_2(A)$ density decays due to its quenching by the different species (see *e.g.* Figure A- 4 in Appendix 1). As a consequence, increasing the frequency decreases the time during which $N_2(A)$ are quenched and thus considerably increases the $N_2(A)$ density between two successive discharges. This effect is clearly visible in Figure 4-15. The $N_2(A)$ density between two discharge increases from 2.2 10^{11} cm^{-3} to 2.2 10^{12} cm^{-3} *i.e.* approximately by a factor 10. To conclude, it is important to consider the averaged $N_2(A)$ density, the latter increasing when the applied frequency increases (at a constant applied voltage) resulting in a higher production of $O(^3P)$ atoms.

Note that, the observed increase of the $O(^3P)$ density for increasing discharge power confirms the hypothesis proposed in the previous section to explain the higher $O(^3P)$ density presented in Figure 4-12 for measurements performed at the constant voltage.

IV.4. Evolution of the O ($2p^4\ ^3P_J$) density during a period of the applied voltage

The previous discussion suggests that the role played by $N_2(A)$ metastable molecules is of primary importance. Thus, in this section, we are interested in the evolution of the $O(^3P)$ density during a discharge period to see if $O(^3P)$ density is modulated by the variations of the $N_2(A)$ density. Measurements are performed at x=14 mm for 200 ppm of O_2. The corresponding experimental results are presented in Figure 4-16(a). The results corresponding to numerical simulations performed for the same conditions are presented in Figure 4-16(b) for comparison.

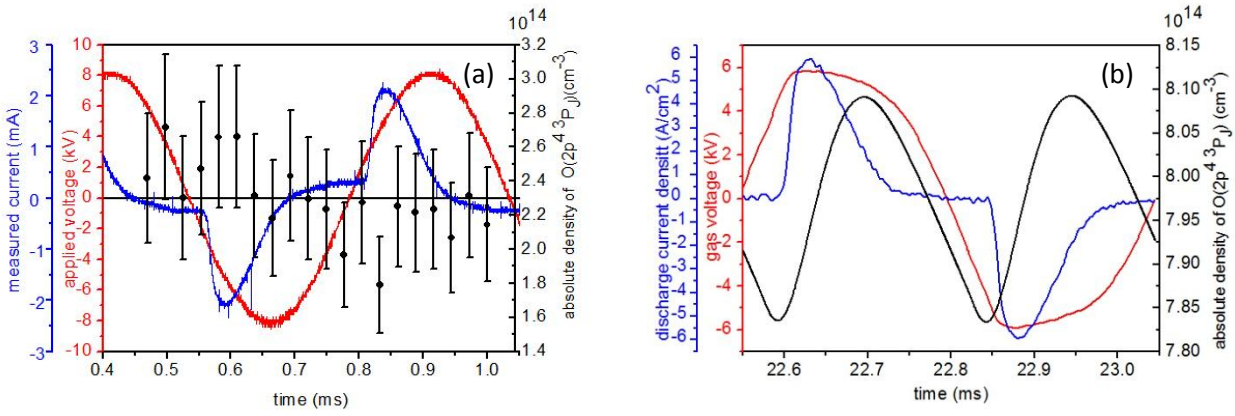

Figure 4-16 Absolute density of O ($2p^4\ ^3P_J$) as a function of instant of discharge.(a) experimental result (b) simulation result. Measurement condition: P=0.9 W/cm², HV= 17.1 kV_{pp}, f=2 kHz, position=14 mm, flow rate=1.0 L/min, concentration of O_2=200 ppm

The experimental O(^{3}P) density presented in Figure 4-16(a) seems to be uncorrelated to the discharge current and exhibits no significant variations. Actually, the measured fluctuations are on the order of the experimental standard error. It means that if the O(^{3}P) density varies, we are not able to measure its fluctuation because the experimental precision is too low. Since O(^{3}P) atoms are mainly produced by O_2 dissociation induced by N_2(A), one should expect a modulation of [O (^{3}P)] related to the variations of the N_2(A) concentration. In [58], Dilecce *et al.* measured the N_2(A) concentration in similar conditions. They found that the maximum N_2(A) concentration is about 1.25 10^{13} cm^{-3} at 200 ppm of O_2 in N_2 with a quenching rate about 3 10^{-4} s^{-1}. If we consider that the maximum N_2(A) concentration is reached just after the maximum of the discharge current, the N_2(A) density between two discharges *i.e.* 0.1 ms later is about 6.2 10^{11} cm^{-3}. It is thus strongly modulated. To understand this behavior, simulations are performed with the 0D model. The same behavior is observed on the numerical results presented in Figure 4-16(b). For sake of clarity, the detailed analysis of this behavior is presented in Appendix 1 section IV.2.2 and we present here the main conclusion of this numerical investigation. The quasi-constant O(^{3}P) density can be attributed to a simultaneous modulation of the production and destruction rate of O(^{3}P) atoms, both connected to the modulation of the N_2(A) density. Indeed, N_2(A) play a major role in the production of O(^{3}P) as discussed previously, but also in its destruction through the reactions $N_2(A) + O(^3P) \rightarrow N_2 + O(^1S)$ and $N_2(A) + O(^3P) \rightarrow NO + N(^2D)$.

IV.5. O ($2p^4\ ^3P_J$) density in post-discharge for different oxygen concentration

The evolution of the O(^{3}P) density in the post-discharge is measured for different oxygen concentrations. For this purpose, measurements are performed at x=14 mm as a function of time after switching off the discharge. The gas flow rate is set to 1.0 L/min and the voltage applied to the discharge before extinction is set to 18.1 kV_{pp}. The results are presented in Figure 4-17.

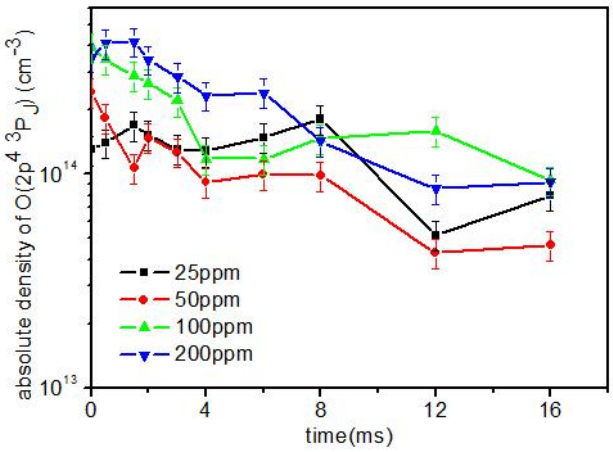

Figure 4-17 Absolute density of N ($2p^3\ ^4S_{3/2}$) as a function of time with different concentration of O_2 from the start of extinction of discharge. Measurement conditions: f=2 kHz, HV=18.1 kV_{pp}, flow rate=1.0 L/min, position=14 mm

The decrease of the O(^{3}P) density depends on the density of other species such as N(^{4}S) and NO(X). Then, a common study of the densities of N(^{4}S), O(^{3}P) and NO(X) in post-discharge is performed in chapter 6 section II.

V. Conclusion

Using the TALIF technique, the density of O(^{3}P) was determined under different experimental conditions. The three sub-levels of the O(^{3}P) ground state required first to check if their respective populations obey the Boltzmann distribution. Then, the experimental errors related to the gas temperature and to the interference filter used for the measurements were investigated.

The measured O(^{3}P) densities were found to be about few 10^{14} cm^{-3}, with a maximum value of 4 10^{14} cm^{-3}. These values are in good qualitative agreement with the ones obtained by Es-Sebbar [59]. O(^{3}P) atoms are mainly produced by O_2 dissociation induced by N_2(A) metastable molecules due to the low electron density in APTD.

The influence of the oxygen concentration on the O(^{3}P) density was studied. For small addition of O_2 (*i.e.* <100 ppm), the O(^{3}P) concentration increases linearly whereas for higher O_2 concentration the increase of the O(^{3}P) density was found to be less and less pronounced as the O_2 concentration increases. The corresponding dissociation degree of O_2 decreases as the O_2 concentration increases. This effect was attributed to the decrease of the N_2(A) density for increasing oxygen concentrations, N_2(A) being efficiently quenched by oxidizing species.

The influence of the discharge power was also investigated by changing the excitation frequency. It was observed that increasing the power results in an increase of the O(^{3}P) density, probably because of a higher averaged N_2(A) density.

The O(^{3}P) density was measured at different times during a discharge period. No significant evolution was observed despite the probable strong variations of the N_2(A) density. Numerical investigations show that it is due to a simultaneous modulation of the production and destruction mechanisms of O(^{3}P) atoms, both mechanisms being strongly related to the N_2(A) concentration.

Chapter 5. LIF measurements of absolute nitric oxide NO($X^2\Pi$) density

In this chapter, we present the results of the NO($X^2\Pi$) density measurements by laser-induced fluorescence. In the following discussions, we will replace NO ($X^2\Pi$) by NO(X) except the discussions which are needed to show the detail of the ground state. First, the excitation and detection schemas are presented and the LIF method is described. Then, the calibration procedure is described and the experimental errors are discussed. Finally, the obtained results are presented.

I. Methodology employed for the LIF measurements on NO($X^2\Pi$)

During LIF measurements, NO molecules are excited from the NO($X^2\Pi$,v=0) state to the NO($A^2\Sigma$,v=0) state where *v* denotes the vibrational number. The corresponding laser wavelength is around 226 nm. The detected fluorescence signal is the full band corresponding to the transition from NO($A^2\Sigma$,v=0) to NO($X^2\Pi$,v=1) around 236.6 nm as is shown in Figure 5-1. Note that the energy levels of the ground state NO($X^2\Pi$) are best described by the Hund's case (a) and consequently, we use the quantum number J to designate the different rotational levels.

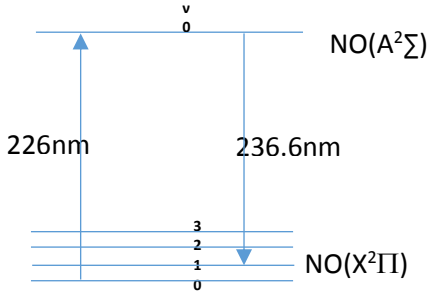

Figure 5-1 Excitation schema of NO($X^2\Pi$)

Choosing an appropriate ro-vibronic transition is important when doing LIF measurements. Ideally, a good choice corresponds to a well-isolated line with a high intensity and poorly dependent on the temperature. Figure 5-2 presents a typical example of an experimental excitation spectrum of the NO-γ (0,0) ro-vibronic band. Note that the excitation spectrum of Figure 5-2(b) is obtained with a higher spectral resolution than the spectrum of Figure 5-2(a). To identify the different lines composing the excitation spectrum, the LIFBASE software is used [92]. Note that the wavelengths indicated in Figure 5-2 correspond the experimental wavelengths. In the following, we will refer to these wavelengths. The additional wavelengths sometimes indicated in parentheses correspond to the theoretical wavelengths provided by the LIFBASE software in vacuum.

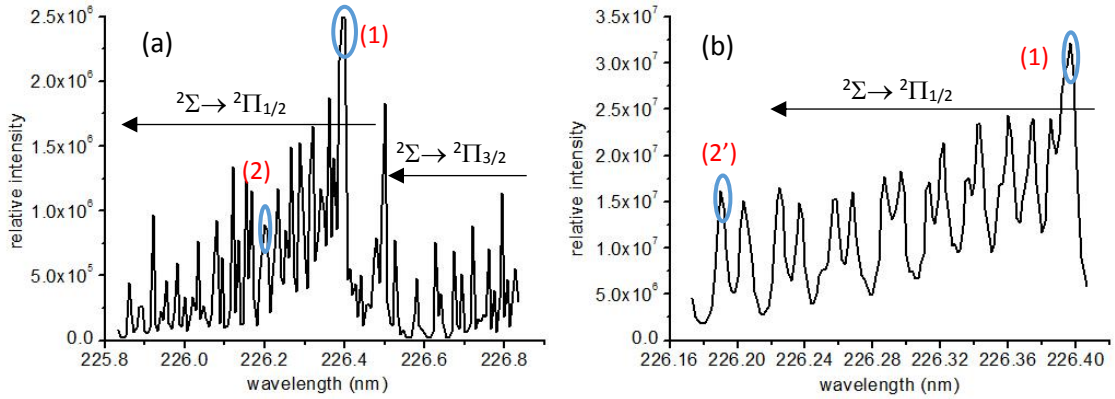

Figure 5-2(a) Excitation spectrum of NO($X^2\Pi$) measured at 14 mm of discharge with 0.9 ppm NO in N_2 for a total pressure of 1025 mbar (b) Excitation spectrum of NO($X^2\Pi$) measured at 14 mm of discharge with 1.8 ppm NO in N_2 for a total pressure of 1025 mbar. Transition for the detection γ(0→1)

Our original choice was to use the $P_{21}+Q_1$ band head of the sub $^2\Sigma \rightarrow {}^2\Pi_{1/2}$ system indicated by label (1) in Figure 5-2(a), because the signal is very high and less sensitive to temperature variations according to [93]. Nevertheless, this line is too close to other lines which makes challenging a good determination of its area. Consequently, we decided to use a line located around 226.188 (226.057) nm and labeled (2') in Figure 5-2(b). Line (2') corresponds to the first line of the doublet indicated by (2) on Figure 5-2(a) and corresponds to the ro-vibronic transitions $Q_{21}(7.5)+Q_{12}(27.5)+P_{12}(36.5)+R_1(7.5)+P_2(27.5)$ where the number in parentheses refers to the rotational quantum number J. It offers the advantage to be sufficiently well isolated from other lines and remains sufficiently populated at moderate rotational temperature by LIF in our conditions. Figure 5-3 presents an example of a LIF excitation profile of this line used for the NO(X) density measurements.

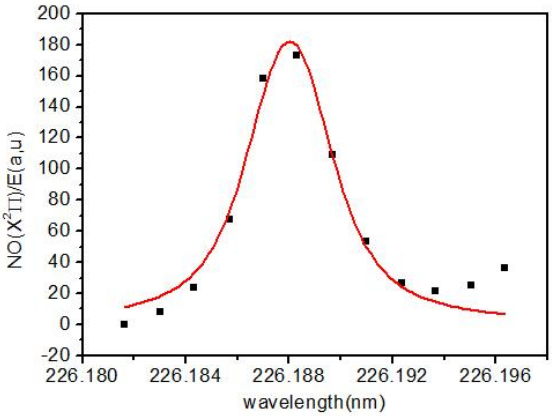

Figure 5-3 Excitation spectrum for the transition NO($X^2\Pi$) -> NO ($A^2\Sigma$) in a mixture of 1.8 ppm NO in N_2 for a total pressure of 1025 mbar. Measurement condition: x=14 mm

Once the rotational line is chosen, it is necessary to determine the laser energy range in which the fluorescence signal remains linear with respect to the laser energy. Figure 5-4 presents an example of such determination.

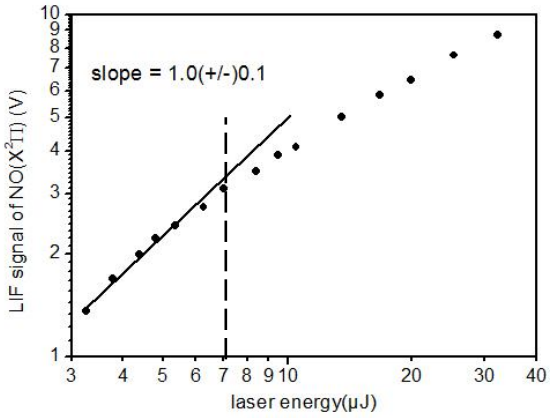

Figure 5-4 Log-log plot of the NO($X^2\Pi$) molecule fluorescence signal as a function of laser energy. Measurement conditions: position=14 mm, 0.9 ppm NO in N_2 for a total pressure of 1025 mbar

As can be seen, the onset of the saturation is located around 7-8 µJ. Consequently, measurements are performed around 4 µJ during experiments.

II. Calibration of NO($X^2\Pi$) measurements

The calibration of LIF measurements is done using experimental conditions as close as possible to the conditions of the experiments with discharge ON. The vessel is filled with a mixture of N_2 and a small amount of NO up to atmospheric pressure. Then measurements are performed using the excitation and detection scheme previously described. During the calibration, the discharge is OFF. This way, the quenching coefficient of NO($A^2\Sigma$,v=0) remains close to the experimental one since it is dominated by N_2.

Calibration measurements are performed for different concentration of NO to check the proportionality between the NO concentration and the LIF signal, keeping the same laser energy. Results are presented in Figure 5-5.

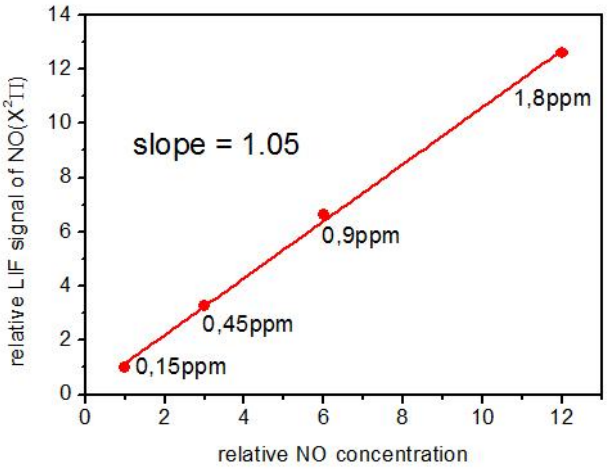

Figure 5-5 Linearity of the normalized fluorescence signal as a function of normalized NO concentration

Measurements are then performed along the discharge cell in order to calculate the calibration factor CF for the different positions x. If one assumes a similar temperature during the calibration and the measurements, the NO(X) density can be calculated using the following relation:

$$[NO] = [NO]_{calib} \cdot \frac{[S_{LIF}/E]}{[S_{LIF}/E]_{calib}} \tag{5.1}$$

where $[\mathrm{NO}]$ represents the experimental NO(X) density, E is the laser energy and $\mathrm{S_{LIF}}$ the LIF signal, during the experiments. The subscript $calib$ indicates the values during the calibration. Then, the calibration factor reduces to $\mathrm{CF} = [\mathrm{NO}]_{\mathrm{calib}}/[\mathrm{S_{LIF}/E}]_{\mathrm{calib}}$.

The evolution of the calibration factor with respect to the position along the discharge cell is presented in Figure 5-6.

This approach is valid only if the gas temperature is the same during the experiments and the calibration. It is thus necessary to estimate the influence of the gas temperature on the calibration factor, which is the purpose of the next section.

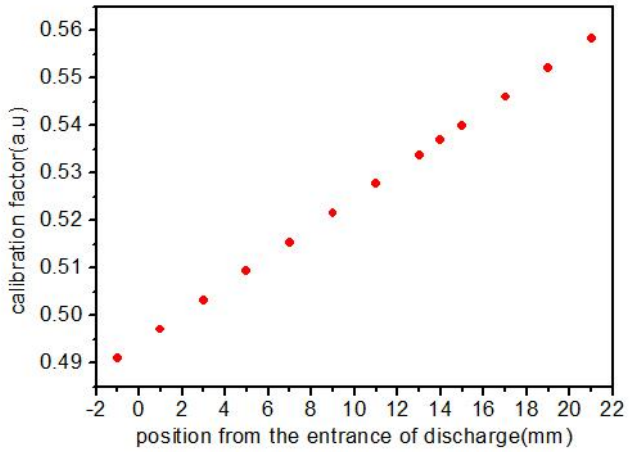

Figure 5-6 Calibration factor as a function of position

III. Influence of the gas temperature

A change in the gas temperature during experiments induces two main drawbacks regarding the estimation of the NO(X) density from LIF measurements. First, the quenching coefficients are modified. Second, the population of the different rotational and vibrational states of the NO molecules can change. The aim of the present section is to estimate the errors relative to these two points.

According to ref [63,94], the LIF signal can be described by equation (5.2):

$$S_{LIF} = \frac{C_{opt}E_p A_{v'=0\rightarrow v''=1}}{[\sum_{v''} A_{v'v''} + Q(P,T_{rot})]} \sum_i (f_{Bi}(T_{rot}) B_i g_i)[NO(X, v=0)] \tag{5.2}$$

where C_{opt} is a constant related to the experimental setup and E_p is the laser energy per pulse. A and B_i are Einstein coefficients for spontaneous emission and stimulated absorption respectively and can be found in ref [95]. $f_{Bi}(T_{rot})$ is the equilibrium Boltzmann fraction and T_{rot} is the rotational temperature. Q is the total quenching rate considering all the processes that depopulate the states

emitting the fluorescence signal. It depends on the translational temperature, which is considered to be equal to the rotational temperature T_{rot}. g_i is the line shape function and corresponds to a convolution between the laser and absorption profile. In our conditions, the pressure is similar in the measurements and during the calibration. Moreover, the gas temperature does not change too much, at most 130 K according to our measurements. As a consequence, the pressure and Doppler broadening of the lines can be assumed to be rather similar and the effect of g_i are assumed to be negligible and are not considered in the following.

The summation in equation (5.2) is performed over all the ro-vibronic transitions probed during the measurement.

The relative populations of the different involved rotational states are taken into account through the Boltzmann factor $f_{Bi}(T_{rot})$ assuming that they are in equilibrium. Let us consider a ro-vibronic transition labeled by i. It corresponds to the absorption of a laser photon from the level NO($X^2\Pi$, J,v=0) to an upper level where J is used to identify the initial rotational level. Consequently, the emitted fluorescence signal directly depends on the population of level J, which in turn directly depends on T_{rot}. The more important the population, the higher the corresponding fluorescence signal. The Boltzmann factor is given by equation (5.3) for the NO($X^2\Pi$) ground state [94].

$$f_B(J, T_{rot}) = \frac{2J+1}{Z_{rot}} e^{-\frac{E_J}{k_B T_{rot}}} \tag{5.3}$$

where Z_{rot} is the rotational partition function and E_J is the energy of the rotational states in the NO($X^2\Pi$,v=0) ground state. E_J is given by:

$$E_J = B_v J(J+1) + K_e \tag{5.4}$$

where B_v=1.705 cm^{-1} [94] is the rotational constant for the vibrational state v =0 and K_e is the electronic energy of the multiple terms that account for the spin-orbit splitting. In our case, we are interested in the $^2\Pi_{1/2}$ state, then K_e0.

The rotational partition function can be calculated using the following equation:

$$Z_{rot} = \sum_J (2J+1) e^{-\frac{E_J}{k_B T_{rot}}} \tag{5.5}$$

Applying equation (5.2) to the LIF measurement during the calibration and during the experiment leads to an improved form of equation (5.1), which takes into account the effect of the rotational temperature:

$$[NO(X, v=0)]_m = [NO(X, v=0)]_{calib} \cdot \frac{[S_{LIF}/E]_m}{[S_{LIF}/E]_{calib}} \cdot \underbrace{\frac{[\sum_i (f_{Bi} B_i)]_{calib}}{[\sum_i (f_{Bi} B_i)]_m}}_{\text{CT1}} \cdot \underbrace{\frac{\tau_{calib}}{\tau_m}}_{\text{CT2}} \tag{5.6}$$

where $\frac{\tau_{calib}}{\tau_m} = \frac{[\sum_{v''} A_{v'v''} + Q(P, T_{rot})]_m}{[\sum_{v''} A_{v'v''} + Q(P, T_{rot})]_{calib}}$

In equation (5.6), two corrections terms involving the rotational temperature appear: CT1, which accounts for the change in the rotational population and CT2, which accounts for the change in the quenching coefficients. In the following, we provide an estimation of CT1 and CT2.

III.1. Estimation of CT1

The rotational temperature was estimated during experiments using the emission of the 2nd positive system of N_2 as reported in chapter 3 section I.3. The maximum temperature measured was about T_{rot}=430 K, for a discharge power of 1.4 W/cm^2. During the calibration, the rotational temperature is equal to the room temperature *i.e.* T_{rot}=300 K.

CT1 can thus be calculated using equations (3.3),(3.4) and (3.5) taking into account all the transitions composing the probed line *i.e.* Q_{21}(7.5), Q_{12}(27.5), P_{12}(36.5), R_1(7.5) and P_2(27.5). Doing this, we find CT1=1.184. It means that neglecting the temperature dependence on the rotational population results can lead to an underestimation of the NO(X) density by 18.4%.

III.2. Estimation of CT2

The quenching of the excited NO(A,v=0) state can be determined experimentally. Figure 5-7 presents an example of the time evolution of the LIF signal during a calibration. In principle, this procedure can also be employed during experimental measurements. In practice, it was not done due to the very low LIF signal in these conditions. Note that to obtain a significant signal, the laser energy was increased beyond the saturation limit but it has no influence on the decay rate after the laser pulse.

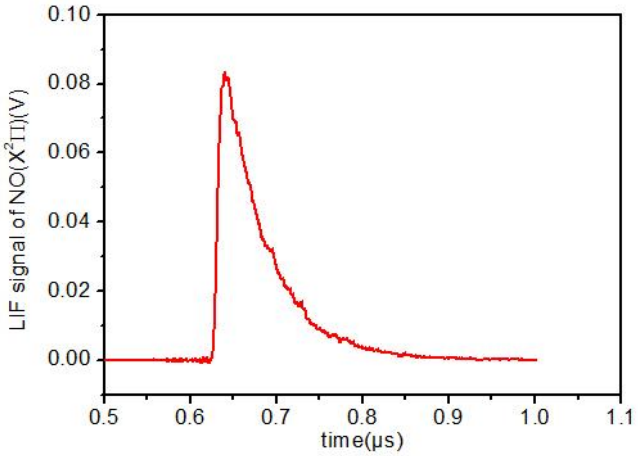

Figure 5-7 LIF signal as a function of time for the transition NO($X^2\Pi$) -> NO ($A^2\Sigma$) in a mixture of 1.8 ppm NO in N_2 for a total pressure of 1025 mbar. Measurement conditions: position=14 mm

The exponential can be fitted to extract the characteristic decay time τ_{calib}. We find τ_{calib}=51 ns, thus the total decay rate should be $A + Q_{calib} = 1/\tau_{calib} = 1.96 \times 10^7 s^{-1}$.

The natural lifetime $\tau_0 = \frac{1}{\sum_{v''} A_{v'v''}} = 205$ ns of the NO(A,v=0) state can be found in the literature [94]. It is used to calculate the quenching coefficient Q using the relation:

$$Q_{calib} = \frac{1}{\tau_{calib}} - \frac{1}{\tau_0} \quad (5.7)$$

Applying this method, we find Q_{calib}= 1.47.10^7 s^{-1}. Some quenching coefficients for NO(A) can be found in the literature. The rate coefficients for electronic quenching (also named electronic energy transfer – EET) and vibrational energy transfer (VET) are provided in Table 5-1 at room temperature and are taken from [94]. Note that the EET corresponds to those of the NO(A,v=0) state whereas the

VET corresponds to those of the NO(X,v=1) state since no data are available for NO(A) according to the authors.

Since during the measurements, the full vibrational band is detected, there is no need to take into account the rotational energy transfers (RET).

The data in Table 5-1 can be used to estimate the relative importance of the different species involved in the quenching. Despite its moderate quenching rate, N_2 molecules are responsible for the dominant quenching contribution because of the high N_2 density. An estimation of this quenching rate using the data provided in Table 5-1 gives Q_{N2}^{300K} = 1.4364 10^7 s^{-1}. Due to the very low oxygen concentration during the experiments the quenching rate by O_2 molecules remains small compared to N_2: Q_{O2}^{300K} = 7.36 10^5 s^{-1}. Assuming a NO(X) concentration of 10^{13} cm^{-3} (see the following results), the self-quenching rate of NO(X) is Q_{NO}^{300K} = 2.58 10^3 s^{-1} which is also negligible. Finally, the LIF decay rate can be estimated. Using the previous calculations and the value of the radiative lifetime of NO(A), we obtain $A + Q_{calib}$=2 10^7 s^{-1}, in good agreement with our experimental measurement.

Table 5-1 Quenching rate coefficient of EET for the NO (A,υ=0) and VET for the NO(X,υ=1)

Species	Quenching rate coefficient k	
	EET ($10^{-16}m^3s^{-1}$)	VET($10^{-18}m^3s^{-1}$)
N_2	0.0037	0.20
O_2	1.51	0.024
NO	2.49	8.8

According to the description in chapter 3 section I.3, the quenching coefficient $Q(T)$ at a temperature T can be expressed by the quenching coefficient $Q(T_0)$ at room temperature T_0, as indicated by equation (3.4). Assuming that all the quenching is due to N_2 and taking into account the variation of the gas density with the temperature through the ideal gas law, the quenching coefficient at temperature T can be written as:

$$Q_{N2}^{T} = k_q(\mathrm{T}) \times [N_2](T) \approx k_q(\mathrm{T}) \times \frac{P}{k_B T} = Q_{N2}^{T_0} \times (T_0/T)^{1/2} \tag{5.8}$$

The correction term CT2 finally writes:

$$\frac{\tau_{calib}}{\tau_m} = \frac{\left[\sum_{v"} A_{v'v"} + Q_{N2}^{T}\right]_m}{\left[\sum_{v"} A_{v'v"} + Q_{N2}^{T_0}\right]_{calib}} = \frac{\frac{1}{\tau_0} + Q_{N2}^{300K} \cdot \left(\frac{T_0}{T}\right)^{1/2}}{\frac{1}{\tau_0} + Q_{N2}^{300K}} \tag{5.9}$$

Considering a maximum temperature of 430 K during the experiments, we obtain $\mathrm{CT2} = \frac{\tau_{\mathrm{calib}}}{\tau_{\mathrm{m}}} = 0.876$ which means that taking into account the increase of the gas temperature during the measurements results in a decrease of the density of $[\mathrm{NO(X, v = 0)}]_{\mathrm{m}}$ of 12.4 %.

Thus, with this approach, the quenching rate decreases when the temperature increases. It is due to the dependence in 1/T of the gas density whereas the quenching rate coefficient has the dependence on $T^{1/2}$. In other words, the decrease of the quencher's density overcomes the increase in the quenching rate coefficient.

III.3. Influence of the vibrational temperature

The NO(X) density determined by LIF measurements corresponds to the density of NO molecules in the ground state *i.e.* in the state NO(X,v=0). Nevertheless, this quantity does not necessarily correspond to the total NO(X). Indeed, if the vibrational temperature is important, a non-negligible fraction of the NO(X) molecules can populate the first vibrational level NO(X,v=1).

The relative population of the vibrational levels can be calculated using the Boltzmann factor. Taking into account the vibrational distribution, the Boltzmann factor presented in equation (5.3) becomes:

$$f_B(J, v, T_{rot}, T_{vib}) = \frac{2J+1}{Z_{rot}Z_{vib}} \cdot e^{-\frac{E_J}{k_B T_{rot}}} \cdot e^{-\frac{E_v}{k_B T_{vib}}} \quad (5.10)$$

with Z_{vib} is the vibrational partition function given by:

$$Z_{vib} = \sum_v e^{-\frac{E_v}{k_B T_{vib}}} \quad (5.11)$$

and E_v the vibrational energy given by:

$$E_v = \omega\left(v + \frac{1}{2}\right) \quad (5.12)$$

where ω=1904 cm^{-1} is the vibrational constant for NO(X) and v is the vibrational quantum number.

The relative population of the NO(X,v=1) level to the ground state NO(X,v=0) can thus be calculated as follows:

$$\frac{[NO(X,v=1)]}{[NO(X,v=0)]} = \frac{e^{-\frac{E_{v=1}}{k_B T_{vib}}}}{e^{-\frac{E_{v=0}}{k_B T_{vib}}}} \quad (5.13)$$

During the calibration, the vibrational temperature is equal to the room temperature, leading to $\frac{[\mathrm{NO(X,v=1)}]}{[\mathrm{NO(X,v=0)}]} = 1.08 \times 10^{-4}$. The population of the vibrational level v=1 is thus negligible and the total NO density thus corresponds to $[\mathrm{NO(X, v = 0)}]$.

During the experiments, T_{vib} can be substantially higher. A vibrational temperature T_{vib}=1500 K has been experimentally determined using the 2nd positive system of N_2. Using this value, we obtain $\frac{[\mathrm{NO(X,v=1)}]}{[\mathrm{NO(X,v=0)}]} = 0.16$. Thus, considering that the measured NO(X) density corresponds to the overall NO(X) density leads to an underestimation of the total NO(X) density of 16%.

IV. Other experimental drawbacks

During experiments, the NOγ system is spontaneously emitted by the discharge, even between two successive discharges because of the presence of N_2(A) metastable molecules which produce NO(A) during the reaction $\mathrm{NO(X) + N_2(A) \rightarrow NO(A) + N_2}$. To limit the interference with LIF measurements, a supplementary measurement is systematically performed by tuning the laser wavelength off resonance but at a wavelength remaining close to the excitation wavelength. The measured signal is then subtracted to the LIF signal. Nevertheless, some small fluctuations of the discharge and/or of the laser are still possible and the accuracy of the measurement is probably affected as well as the detection limit.

V. Absolute nitric oxygen density in a mixture of N_2/O_2

In this part, we present the evolution of the absolute density of NO(X) as a function of the position for different concentration of oxygen. Then the influence of the discharge power is investigated. Note that the error bars shown in the figures are based on the reproducibility of the measurements, which is ±7.1% on average.

V.1. Absolute density of NO($X^2\Pi$) along the discharge for different oxygen concentration

Figure 5-8(a) presents the evolution of the NO(X) density for different oxygen concentration as a function of the position in the discharge. For this set of measurements, the discharge power is kept constant at 0.9 W/cm^2 by adjusting the applied voltage and the flow rate is 1.0 L/min. A similar set of experiments is performed for a constant applied voltage of 17.1 kV_{pp}. The corresponding results are presented in Figure 5-8(b). It should be noted that the electrodes were changed between these two sets of experiments.

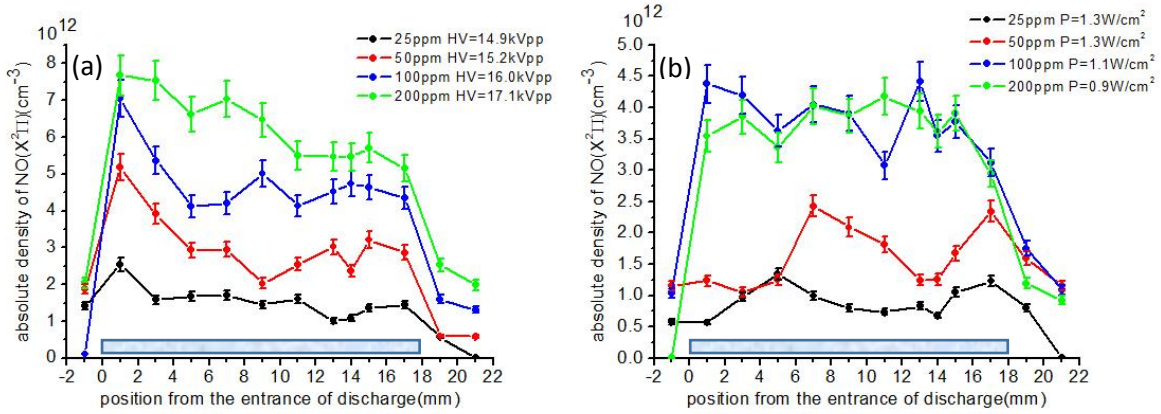

Figure 5-8 Absolute density of NO($X^2\Pi$) as a function of position for different concentration of O_2. (a) in keeping the same discharge power around 0.9 W/cm^2 by adjusting the applied voltage[1] (b) in keeping the same applied voltage at 17.1 kV_{pp}[2]. Measurement conditions: f=2 kHz, flow rate=1.0 L/min
[1]: old electrodes [2]: new electrodes

The NO(X) density rapidly increases at the entrance of the discharge and reach values as high as 7.5 10^{12} cm^{-3}. For the set of experiments performed at 0.9 W/cm^2, the NO(X) density reaches a maximum at x=1 mm and then slowly decreases until the end of the discharge at x=18 mm. Then, the NO(X) concentration decreases in the post-discharge region. The behavior is slightly different for the set of experiments performed at the constant applied voltage and no maximum is observed at the beginning of the discharge zone. Such maximum can have a physical origin. For example, it could be due to the progressive formation of atomic nitrogen along the discharge, which is known to efficiently react with NO molecules. Thus after a rapid increase of the NO(X) density, the later could decrease because of its increasing reduction by N(^{4}S). Nevertheless, since this trend is not observed for the set of experiments performed at constant applied voltage, this maximum is probably due to experimental errors. Among them, a change in the relative position of the laser beam with respect to the discharge gap can occur during the displacement of the discharge cell. Moreover, the important fluctuations of the NO(X) density observed for some experiments (see *e.g.* the series performed at 50 ppm of O_2 in Figure 5-8(b)) together with the non-zero value of the NO(X) density before the

discharge suggest that the measured NO(X) densities are close to the detection limit and that the corresponding signal to noise ratio remains low.

Another interesting point concerns the results obtained for 200 ppm of O_2 in N_2 if one compares both series of experiments. Indeed, the electrical parameters of the discharge are the same in both cases since a voltage of 17.1 kV_{pp} corresponds to a power of 0.9 W/cm^2. Then, one should measure the same NO(X) density, which is not the case. It is probably due to the fact that we change the discharge cell between these two sets of experiments. The new position of the laser beam relative to the discharge gap is thus not exactly the same and can induce the observed discrepancies. Another possible explanation relies on the change in the dielectric surface properties. Indeed, after using it for some hours the color of the alumina plate changes from white to brown thus indicating some modifications of the surfaces. No changes in the electrical properties of the discharge were observed so if changing the surface characteristics modifies the measured NO(X) density, it is probably related to the formation of NO molecules onto the surfaces.

Nevertheless and despite the observed discrepancies, the order of magnitude of the measured NO(X) density is the same in all experiments *i.e.* about few $10^{12}\,cm^{-3}$. These values are significantly lower than those measured during the work of Es-Sebbar [59] who found typical NO(X) densities about $10^{15}cm^{-3}$.

V.2. Absolute density of NO($X^2\Pi$) as a function of oxygen concentration

To study the influence of the O_2 concentration on the NO(X) density, dedicated LIF measurements are performed at x=14 mm for a different input concentration of oxygen at the constant applied power or at the constant applied voltage. The corresponding results are respectively presented in Figure 5-9(a) and (b). In addition, numerical results corresponding to simulations performed at constant applied voltage are presented in Figure 5-9(c).

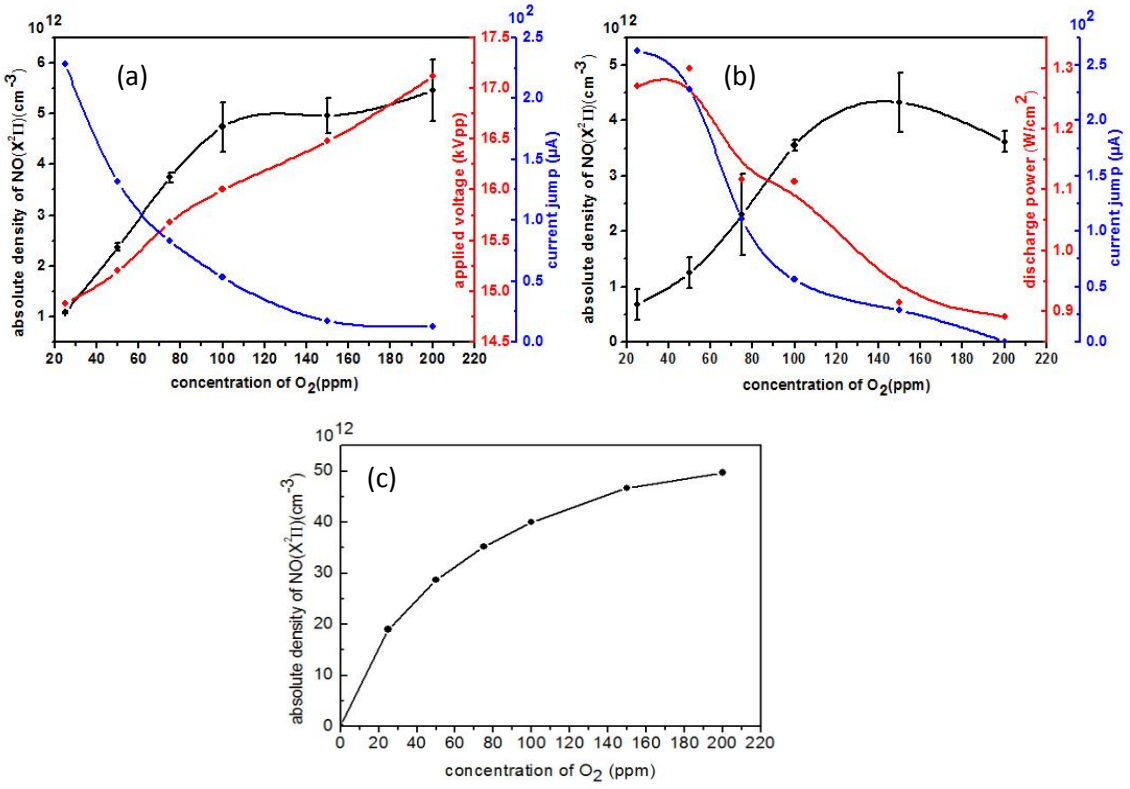

Figure 5-9 Absolute density of NO($X^2\Pi$) as a function of concentration of O_2. (a) in keeping the same discharge power around 0.9 W/cm²by regulation the applied voltage[1]; (b) in keeping the same applied voltage at 17.1 kV_{pp}[2]. (c) simulation results corresponding to the experimental result of (b). Measurement conditions: f=2 kHz, position=14 mm, flow rate=1.0 L/min. [1]: old electrodes [2]: new electrodes

For both series of experiments, the NO(X) density increases with the O_2 concentration up to 100 ppm of O_2. For higher O_2 concentrations, the NO(X) density remains roughly constant. This behavior looks similar to the behavior of the O(^{3}P) density studied in chapter 4 section IV.2. Numerical results show a similar behavior despite the significant overestimation of the NO(X) density.

The main mechanisms involved in the production and destruction of NO(X) have been identified in Appendix 1 section IV.3 using the 0D model. It is found that NO is mainly produced through the reactions $N_2(A) + O(^3P) \rightarrow NO + N(^2D)$ and $N(^4S) + O(^3P) + N_2 \rightarrow NO + N_2$. In the literature [96,97], the reaction $N(^2D,^2P) + O_2 \rightarrow NO + O(^3P,^1D)$ is also pointed out by several authors to be an important source of NO(X) production.

In the previous chapters, we saw that increasing the O_2 concentration results in a monotonous decrease of the N(^{4}S) density, whereas the O(^{3}P) density increases linearly up to 100 ppm and then remains constant. Moreover, we know from the work of Dilecce *et al*. [58] that the averaged N_2(A) concentration in the discharge decreases when increasing the O_2 concentration. Knowing that N(^{2}P) atoms are efficiently produced through the reaction $N_2(A) + N(^4S) \rightarrow N_2 + N(^2P)$, the N(^{2}P) concentration probably also decreases. All these considerations allow us to suggest the following explanation. For O_2 concentration below 100 ppm, increasing the oxygen content favors the production of O(^{3}P) thus promoting the reactions responsible for the creation of NO(X) molecules. For higher O_2 concentrations, the decrease of the N_2(A) and N(^{4}S) density limits the production of O(^{3}P) and as a result the production of NO(X).

Note that for a given O_2 concentration, the NO(X) density measured in the set of experiments performed at constant applied voltage (17.1 kV, Figure 5-9(b)) is systematically lower than the density measured for the set of experiments performed at constant power (0.9 W/cm², Figure 5-9(a)) despite a higher discharge power. It is thus interesting to know if this trend has a physical origin or if it is related to the change of the discharge cell. For this purpose, the influence of the discharge power on the NO(X) density is studied in the following.

V.3. Absolute density of NO($X^2\Pi$) as a function of discharge power

To investigate the effect of the discharge power on the NO(X) production, LIF measurements are performed for different power by changing the frequency of the applied voltage. For this set of experiments, the input oxygen concentration is 200 ppm and measurements are performed at position x=14 mm. The corresponding results are presented in Figure 5-10(a), together with the simulation results presented in Figure 5-10(b). The NO(X) concentration increases when the discharge power increases. As previously discussed, NO(X) molecules are produced by the following reactions:

$$N_2(A) + O(^3P) \rightarrow NO + N(^2D) \quad \text{(R 5-1)}$$

$$N(^4S) + O(^3P) + N_2 \rightarrow NO + N_2 \quad \text{(R 5-2)}$$

$$N(^2D,^2P) + O_2 \rightarrow NO + O(^3P,^1D) \quad \text{(R 5-3)}$$

In the previous chapters, the influence of the discharge power on the production of N(^{4}S), O(^{3}P) and N_2(A) have already been discussed. We saw that increasing the power increases the production of N_2(A) metastable molecules which in turn increases O_2 dissociation resulting in the production of O(^{3}P) atoms. Moreover, a higher discharge power implies a higher dissociation of N_2 molecules by electrons and thus a higher density of N(^{4}S) atoms. Consequently, the rate of reactions *(R 5-2*,3) probably increases when increasing the discharge power. Note that an increased production of N(^{4}S) atoms also means a higher reduction rate of NO(X) but according to the experimental results, it seems that this higher destruction rate is not sufficient to overcome the higher production rate. Consequently, the chemical equilibrium is shifted towards higher density of NO(X) when increasing the discharge power and the resulting NO(X) density increases. Numerical results presented in Figure 5-10(b) are in good agreement with experimental ones despite the larger NO(X) density obtained in the simulations. The higher the input power, the higher the NO(X) density.

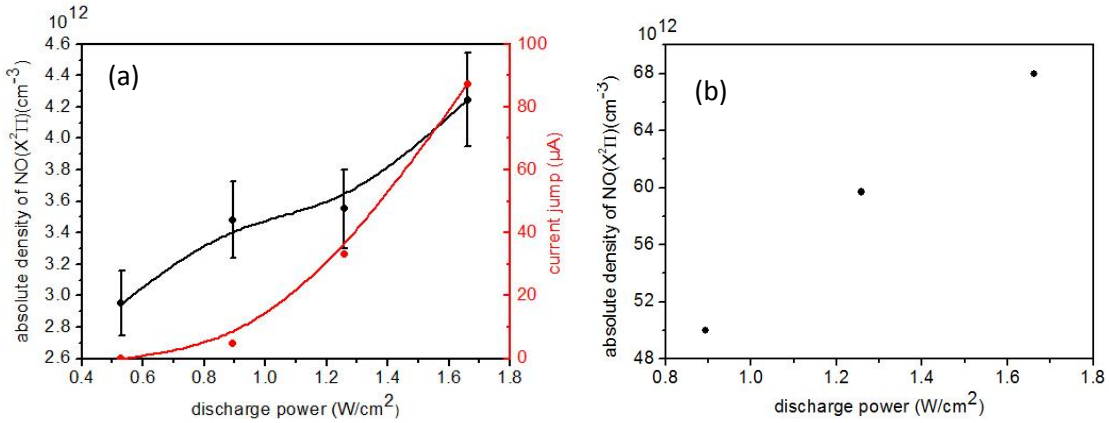

Figure 5-10 Absolute density of NO($X^2\Pi$) as a function of discharge power. (a) experimental results[2] (b) simulation results. Measurement conditions: HV= 17.1 kV_{pp}, position=14 mm, flow rate=1.0 L/min, concentration of O_2=200 ppm
[2]: new electrodes

V.4. NO($X^2\Pi$) density in post-discharge for different oxygen concentration

The evolution of the NO(X) density in the post-discharge is measured for different oxygen concentrations at x=14 mm as a function of time after switching off the discharge. The gas flow rate is set to 1.0 L/min and the voltage applied to the discharge before extinction is set to 18.1 kV_{pp}. The results are presented in Figure 5-11 and are discussed in chapter 6 together with the evolution of the N(^{4}S) and O(^{3}P) density in post-discharge. Note that for the measurements performed at 25 and 50 ppm, the NO(X) density is on the order of the detection limit and thus poorly reliable.

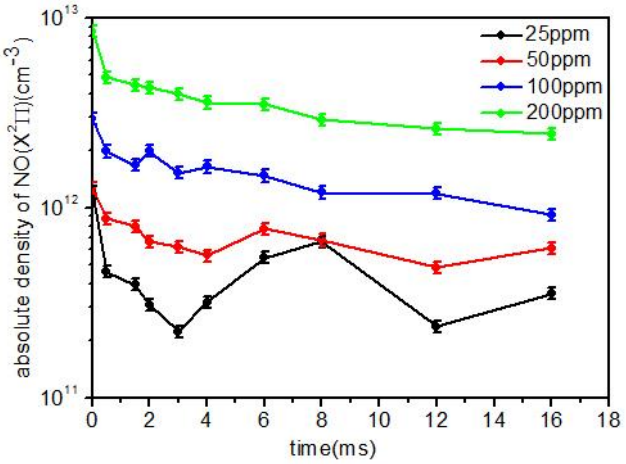

Figure 5-11 Absolute density of NO($X^2\Pi$) as a function of time with 200 ppm O_2 from the start of extinction of discharge. Measurement conditions: f=2 kHz, HV=18.1 kV_{pp}, flow rate=1.0 L/min, position=14 mm

VI. Conclusion

In this chapter, the density of NO(X) was determined by LIF under different experimental conditions.

First, the excitation scheme was defined. The excitation scan was performed over a line around 226.06 nm corresponding to several ro-vibranic transitions from NO($X^2\Pi$,v=0) to NO($A^2\Sigma$,v=0): $Q_{21}(7.5)+Q_{12}(27.5)+P_{12}(36.5)+R_1(7.5)+P_2(27.5)$. The detection of the fluorescence signal was set to collect the whole NO($A^2\Sigma$,v=0) to NO($X^2\Pi$,v=1) vibrational band around 236 nm. The calibration of the LIF signal was then performed by injecting a known concentration of NO(X) in N_2 at atmospheric pressure.

NO(X) densities about few 10^{12} cm^{-3} were measured for a maximum value of around 8 10^{12} cm^{-3}. These values are far below the values determined in rather similar conditions by Es Sebbar [59]. This difference can be explained by the use of an inappropriate bandpass filter. Moreover, measurements were performed by scanning only the maximum of the transition line instead of scanning the whole profile. The influence of the oxygen concentration on the NO(X) density was studied. For small addition of O_2, the NO(X) concentration increases linearly due to the increase of the O(^{3}P) density. For higher O_2 concentration (>100 ppm) the NO(X) density was found to be roughly constant. This effect was ascribed to the noticeable decrease of the N_2(A) and N(^{4}S) densities with increasing O_2 concentration which are both involved in the production of NO(X) molecules.

Measurements performed as a function of the discharge power showed that the higher is the power, the higher is the NO(X) density. It was explained by the simultaneous increase of the N(^{4}S), O(^{3}P) and N_2(A) densities for higher discharge powers.

Chapter 6. Discussion

In the previous chapters, the density of N(^{4}S), O(^{3}P) and NO(X) have been determined by TALIF and LIF measurements in N_2/O_2 mixtures. This chapter begins with a summary of these experimental results. The simultaneous knowledge of these densities in similar experimental conditions allows investigating phenomenon involving these three species. The first investigation presented in this chapter concerns the evolution of the N(^{4}S), O(^{3}P) and NO(X) densities during the post-discharge where each specie is correlated to the others through many chemical reactions. The second study is devoted to the quantification of the memory effect due to the associative ionization $\mathrm{N}(^2\mathrm{P}) + \mathrm{O}(^3\mathrm{P}) \rightarrow \mathrm{NO}^+ + \mathrm{e}^-$ which is the main purpose of the present work. For this purpose, calculations are performed to estimate the density of metastable N(^{2}P) atoms. Then, the associative ionization reaction rate can be assessed and the corresponding current jump can be simulated. The obtained results are compared to experimental measurements.

I. Summary of experimental results

In the previous chapters, the absolute densities of N(^{4}S), O(^{3}P) and NO(X) were determined as a function of the position from the entrance of the discharge and of different concentrations of oxygen. The measured densities are found to strongly increase along the first millimeters of the discharge together with the discharge power whereas only slight density variations attributed to experimental errors are observed near the end of the discharge (17 mm and below) for which the discharge power reaches a constant value. Consequently, to summarize the results as a function of the oxygen concentration, we report the densities measured at x=14 mm. Figure 6-1 shows the corresponding results for measurements performed (a) at a constant discharge power of 0.9 W/cm^2 and (b) at a constant applied voltage of 17.1 kV_{pp}.

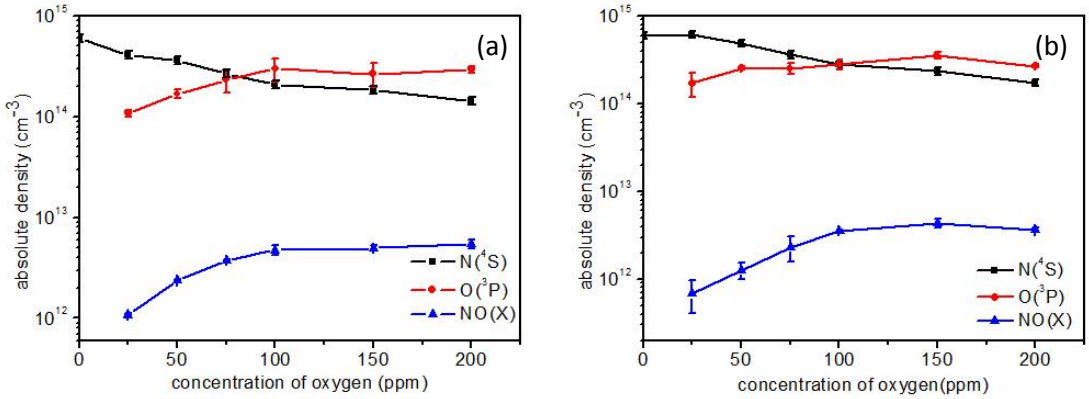

Figure 6-1 Absolute densities of N(^{4}S), O(^{3}P) and NO(X) as a function of concentration of O_2 (a) in keeping the same discharge power around 0.9 W/cm^2 by regulating the applied voltage; (b) in keeping the same applied voltage at 17.1 kV_{pp}. Measurement conditions: f=2 kHz, position=14 mm, flow rate=1.0 L/min.

The evolutions of the different densities were discussed in the corresponding chapters using the model presented in Appendix 1. The main mechanisms involved in the production and destruction of the different species are summarized in Table 6-1.

Table 6-1 Main mechanisms involved in the production and destruction of species

Production	Destruction	
$N(^4S)$	$N(^4S)$	
$e + N_2 \rightarrow e + N(^4S) + N(^2D)$	In pure nitrogen	With the presence of oxygen
	$N(^4S) + N(^4S) + N_2 \rightarrow N_2 + N_2(A, B)$	$N(^4S) + NO \rightarrow N_2 + O(^3P,^1D)$
	$N(^4S) \longrightarrow N(^4S)^{wall}$	$N(^4S) + O(^3P) + N_2 \rightarrow NO + N_2$
$O(^3P)$	$O(^3P)$	
$N_2(A) + O_2 \rightarrow N_2 + 2O(^3P)$	$N_2(A) + O(^3P) \rightarrow N_2 + O(^1S)$	
	$N_2(A) + O(^3P) \rightarrow NO + N(^2D)$	
NO(X)	NO(X)	
$N_2(A) + O(^3P) \rightarrow NO + N(^2D)$	$N(^4S) + NO \rightarrow N_2 + O(^3P,^1D)$	
$N(^4S) + O(^3P) + N_2 \rightarrow NO + N_2$		
$N(^2D,^2P) + O_2 \rightarrow O(^3P,^1D) + NO$		

The $N(^4S)$ density continuously decreases as the concentration of oxygen increases. It was attributed to the increase of its destruction rate by oxidizing species such as NO(X), $O(^3P)$ and O_2.

The $O(^3P)$ density increases significantly for low oxygen concentrations and then remains approximately constant. This effect was attributed to the fact that the increase of the O_2 concentration causes an increase in the quenching rate of $N_2(A)$. Since in our conditions, $O(^3P)$) is mainly produced by O_2 dissociation by $N_2(A)$, it probably limits the production of $O(^3P)$.

The evolution of the NO(X) density is quite similar to the one of $O(^3P)$ indicating that the production of NO(X) is limited for high O_2 concentrations. It can be explained by a decrease of the atomic nitrogen concentration and by a decrease of the $N_2(A)$ density, both species being involved in the production of NO(X) molecules.

The following table gives the maximum density of $N(^4S)$, $O(^3P)$ and NO(X) for information purpose, together with an estimation of the experimental error.

Table 6-2 Summary of absolute densities and the corresponding estimated errors

Species	Maximum density (cm^{-3})	Measured error	Calculated error(related to the gas temperature)	Maximum density corrected with the calculated error (cm^{-3})	Other error
$N(^4S)$	7×10^{14}	±9.1%	Overestimation 15.8%	5.9×10^{14}	
$O(^3P)$	4×10^{14}	±15.7%	Overestimation 13.8%	3.5×10^{14}	Underestimation because of the overestimation of calibration signal
NO(X)	8×10^{12} (old electrode)	±7.1%	Underestimation 20.3%	9.6×10^{12}	

II. Investigation of the species densities during the post-discharge

In this section, we are interested in the temporal evolution of the densities of $N(^4S)$, $O(^3P)$ and NO(X) in the post-discharge. During the post-discharge, no energetic electrons are present which reduces the complexity of the chemistry. Then, it offers a convenient way to identify the dominant mechanisms responsible for the losses of the different species. Moreover, it allows checking the

consistency of the LIF and TALIF measurements because the respective densities of $N(^4S)$, $O(^3P)$ and NO(X) are connected to each other through many chemical reactions.

As reported in the different chapter dedicated to experimental results, measurements were performed for each species at x=14 mm and for different instants after switching off the discharge (this instant corresponds to t=0). As previously explained, due to the presence of the gas flow, numerical and experimental results can only be compared during a small time period (maximum 25 ms) following the discharge extinction. Indeed, for longer times, the gas volume probed by LIF/TALIF was not exposed to the discharge. Measurements presented in this section were performed for 25, 50, 100 and 200 ppm of O_2 at a constant applied voltage of 18.1 kV_{pp} and for a gas flow rate of 1.0 L/min.

Preliminary calculations were performed to identify the main mechanisms involved in the destruction of the different species. The corresponding set of reactions, which is presented in Table 6-3, was found to be sufficient to reproduce the main trend of experimental results.

The numerical results presented in this section are obtained using the following method. Calculations are initialized considering the density of $N(^4S)$, $O(^3P)$ and NO(X) measured at t=0. The density of O_2 in the calculations is considered to be the input density *i.e.* O_2 dissociation is neglected. Then, the set of equations in Table 6-3 is solved.

Table 6-3 Reactions involved in the destruction of species

Reaction	Rate coefficient (s^{-1}, cm^3s^{-1}, cm^6s^{-1})	Reference	Reaction number
$N(^4S) + O(^3P) + N_2 \rightarrow NO + N_2$	$1.76 \times 10^{-31} \times T^{-0.5}$	[98]	(R1)
$O(^3P) + O_2 + N_2 \rightarrow N_2 + O_3$	$6.2 \times 10^{-34} \times (300/T)^2$	[98]	(R2)
$N(^4S) + N(^4S) + N_2 \rightarrow N_2 + N_2(A, B)$	4.1×10^{-33}	[83]	(R3)
$N(^4S) + NO \rightarrow N_2 + O(^3P, ^1D)$	$1.05 \times 10^{-12} \times T^{0.5}$	[57]	(R4)
$O(^3P) + O(^3P) + N_2 \rightarrow N_2 + O_2(X, a, b)$	$2.76 \times 10^{-34} \times \exp(720/T)$	[98]	(R5)
$N(^4S) \rightarrow$ wall	32.26	[85]	(R6)
$O(^3P) \rightarrow$ wall	57.4	This work	(R7)

The value of the rate coefficient concerning $O(^3P)$ losses onto the wall (57.4 s^{-1}) is obtained using equation (3.7) in chapter 3, considering γ=1.8 10^{-3} [99] for the recombination coefficient of $O(^3P)$ onto Al_2O_3.

In this calculation, we use the value of T=430 K for the gas temperature as determined experimentally form OES measurements on the SPS of N_2. Figure 6-2 represents the results obtained for: (a) $N(^4S)$, (b) $O(^3P)$ and (c) NO(X). On each figure, markers indicate the measured values whereas straight lines indicate numerical results. The reaction rates are presented in Figure 6-3(a) and (b) for 25 and 200 ppm respectively.

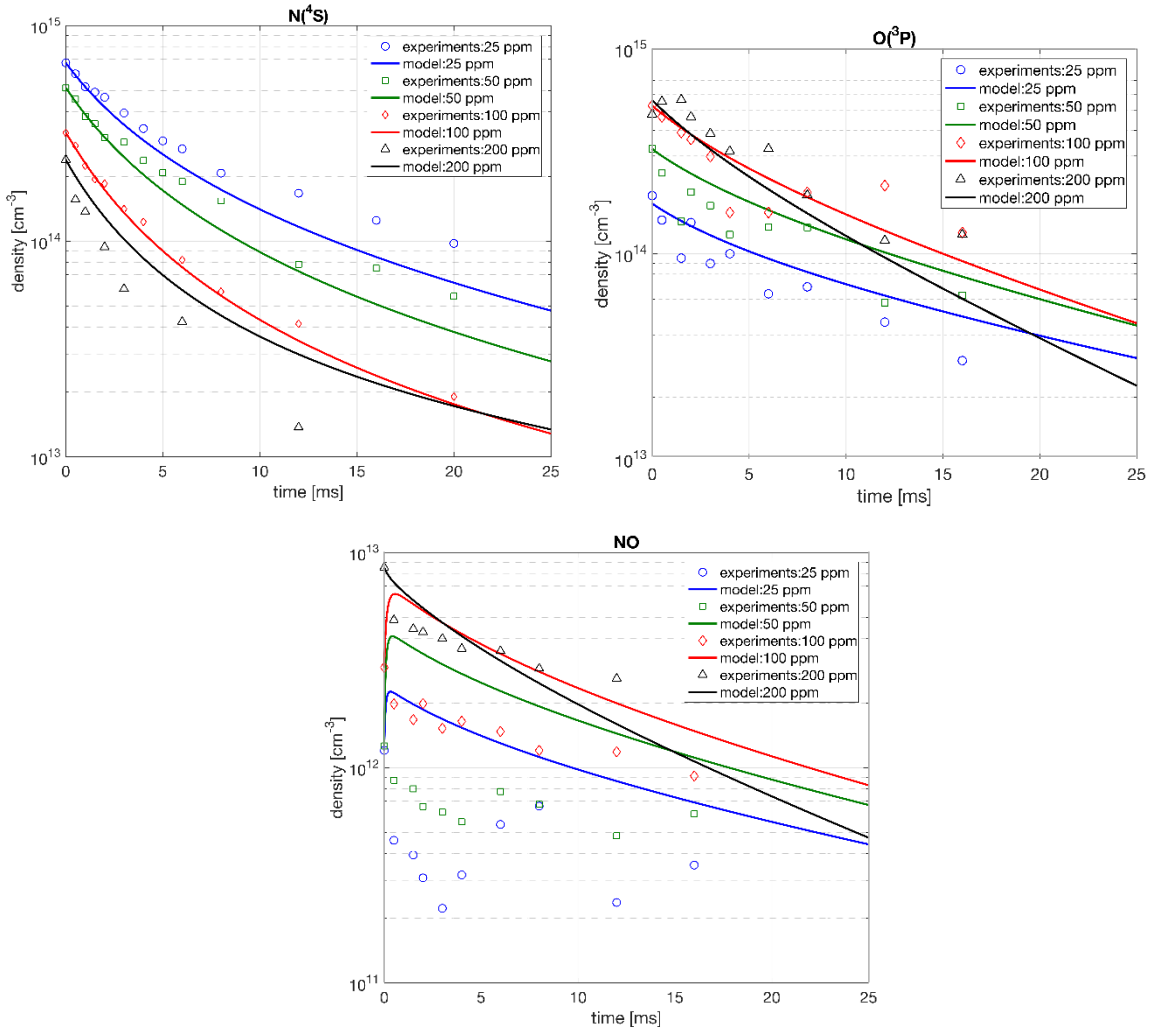

Figure 6-2 Comparison of experimental result and numerical result of the decay of absolute densities

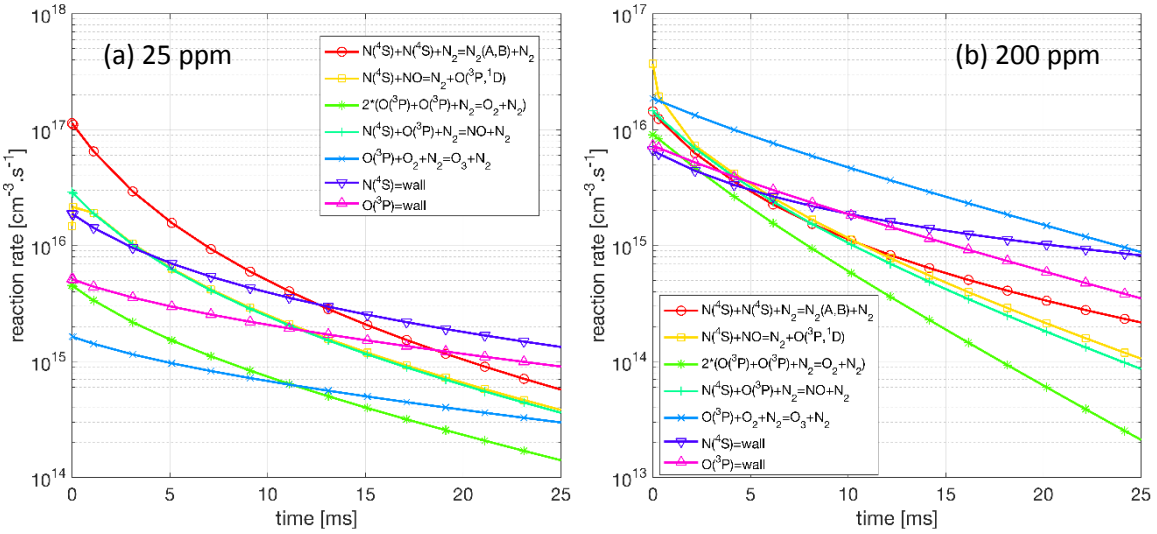

Figure 6-3 Reaction rate with concentration of O_2 (a) 25 ppm and (b) 200 ppm

II.1. Decay of N(^{4}S) during the post-discharge

The model is able to provide a good description of the experimental results except for the case of 200 ppm, the calculation underestimates the decay rate (note that it overestimates the decay rate for O(^{3}P) and NO(X)). For low O_2 concentration, the situation is similar to the high purity nitrogen case. The reaction (R3) continue to play the dominant role at the beginning of the post-discharge. Then, the losses of N(^{4}S) to the wall dominates. The curve [N(^{4}S)]=f(t) is thus first characterized by a pronounced negative slope following the discharge extinction and then by a slightly negative slope for longer durations.

As the input concentration of O_2 is increased, reactions involving oxidizing species become important. In particular, at the beginning of the post-discharge, the reactions (R1) and (R4) dominate. Then, the rapid decrease of [N(^{4}S)], [O(^{3}P)] and [NO(X)] reduces the rate of these reactions and the losses of N(^{4}S) are then dominated by losses by diffusion to the walls. Consequently, the initial decrease of [N(^{4}S)] is more and more pronounced for increasing O_2 concentration whereas the decrease rate for longer durations remains the same independently of the O_2 concentration.

II.2. Decay of O(^{3}P) during the post-discharge

In the case of O(^{3}P), the reactions (R1), (R4) and (R5) are important for short times after discharge extinction and then rapidly decrease due to the fast decrease of [N(^{4}S)], [O(^{3}P)] and [NO(X)]. Note that (R4) is responsible for O(^{3}P) production and then attenuate the decrease of [O(^{3}P)] due to the first two reactions. For longer times and low O_2 concentration, O(^{3}P) loss to the wall is the dominant mechanism. The contribution of the reaction (R2) regarding O(^{3}P) destruction increases with the input O_2 concentration and because of the simultaneous increase of [O_2] and [O(^{3}P)]. For 100 ppm (not shown here) and 200 ppm, it is the main destruction mechanism, followed by the diffusion to the wall.

Note that this simple model overestimates the destruction rate of O(^{3}P) atoms for 200 ppm of O_2. A possible explanation is that other species such as NO_2, which are neglected in this calculation since their densities are unknown, can participate in the formation of O(^{3}P) thus reducing the decay rate. Among the possible reactions there are $\mathrm{N}(^4\mathrm{S}) + \mathrm{NO}_2 \rightarrow \mathrm{N}_2 + \mathrm{O}(^3\mathrm{P}) + \mathrm{O}(^3\mathrm{P})$ and $\mathrm{N}(^4\mathrm{S}) + \mathrm{NO}_2 \rightarrow \mathrm{N}_2\mathrm{O} + \mathrm{O}(^3\mathrm{P})$. Other mechanisms involving N_2(A) metastable for example are poorly probable on this time scale because of their efficient quenching at atmospheric pressure.

II.3. Decay of NO(X) during the post-discharge

For the case of NO(X), the calculations fail to reproduce the experimental behavior. Indeed, even if the slope of the calculated curve seems to be in reasonable agreement with the experimental decay rate indicating that NO destruction is probably mainly due to its reduction by atomic nitrogen, the absolute values of the calculated densities are greater than the measured ones by a factor approximately equal to 2.5. In the calculations, the NO density increases at the beginning of the post-discharge due to the reaction (R1) whereas it is not observed experimentally. It indicates that the measured densities of N(^{4}S), O(^{3}P) and NO(X) are not consistent which can be explained by the experimental uncertainties.

Another possibility is that the set of reactions used in the model is incomplete. Other simulations performed with a much more complete set of reactions provided similar results. Nevertheless, the density of important species such as N_2O or NO_2 being unknown, it makes difficult to conclude about the limitation of the model.

To investigate the overestimation of the calculated NO density, let us assume that the experimental densities were overestimated by a factor 2.5, and perform additional calculations for which the experimental values of [NO] are multiplied by a factor 2.5. The calculations then start from these increased initial densities. The corresponding results are presented in Figure 6-4.

As can be seen, the higher NO(X) density has only a poor influence on the results of N(^{4}S) and O(^{3}P) which remain satisfactory whereas a better agreement is obtained between the corrected experimental data and the numerical results for the case of NO(X). Unfortunately, the model is still unable to provide a satisfactory description of the results obtained for N(^{4}S), O(^{3}P) and NO(X) at 200 ppm suggesting that some important reactions are missing such as $\mathrm{N}(^4\mathrm{S}) + \mathrm{NO}_2 \rightarrow \mathrm{NO} + \mathrm{NO}$.

These results show that experimental uncertainties can explain the observed behavior. Among the possible source of experimental uncertainties, one of the most important is related to the calibration procedure as discussed in chapters 3, 4 and 5. Nevertheless, calculations show that uncertainties regarding the absolute densities remain acceptable. Indeed, changing one of the input densities by one order of magnitude or more makes impossible a correct description of the post-discharge for N(^{4}S), O(^{3}P) and NO(X).

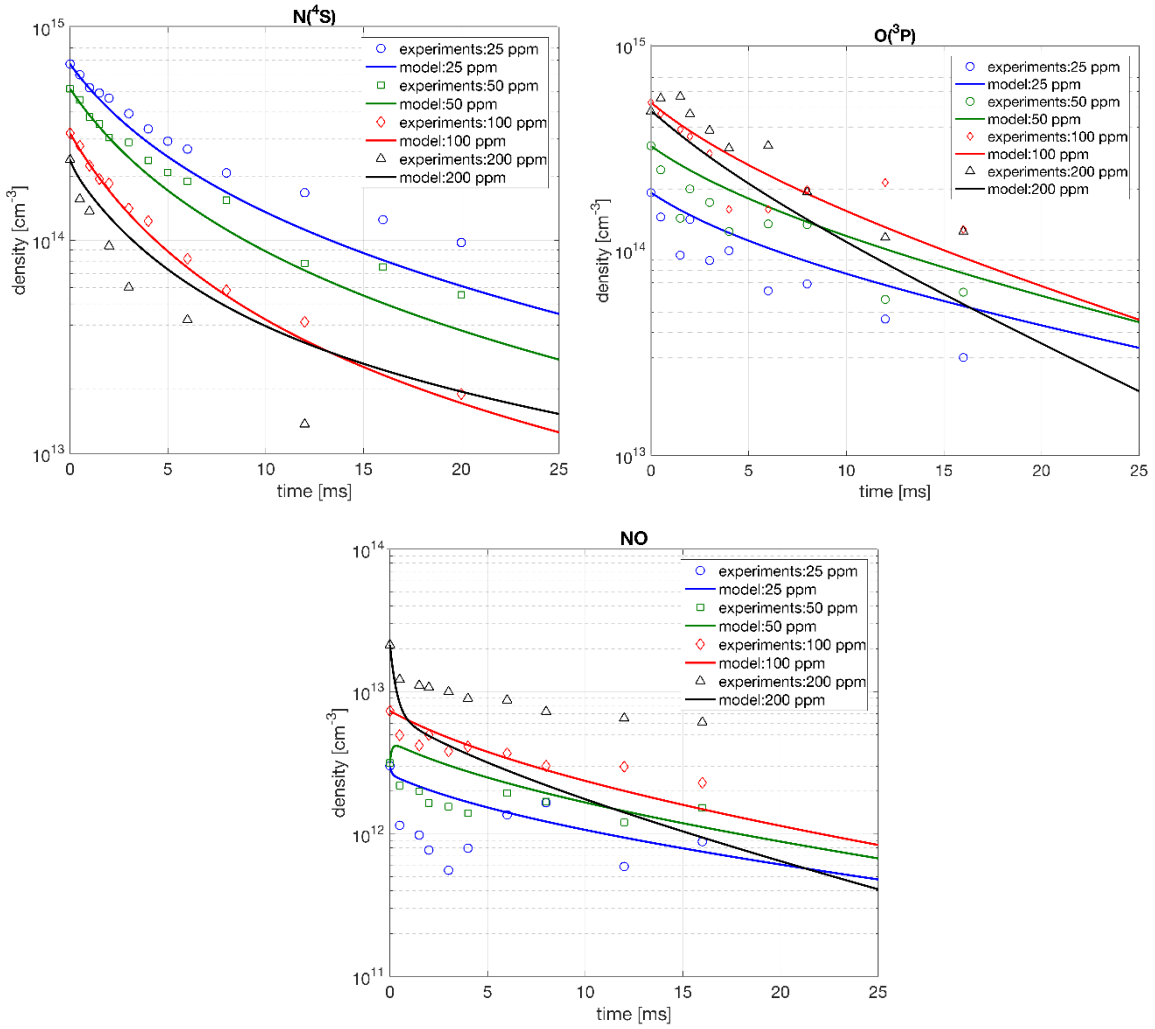

Figure 6-4 Comparison of the experimental result and numerical result of the decay of absolute densities (with a multiplication of 2.5 for the density of NO(X)

III. Investigation of the memory effect related to the associative ionization process

In this section, we discuss the role of the associative ionization reactions in memory effect using the experimental results *i.e.* the density of $N(^4S)$, $O(^3P)$ and NO(X) determined by laser induced fluorescence. A summary of these densities measured at x=14 mm for different O_2 concentrations and under a similar discharge power of 0.9 W/cm^2 has already been provided in Figure 6-1(a).

The possible role played by associative ionization reactions involving $N(^2P)$ metastable atoms (see the following reactions) has been introduced in chapter 1. Following [57], two different reactions involving $N(^2P)$ must be considered:

$$N(^2P) + N(^2P) \rightarrow N_2^+ + e^- \quad \text{(R6-1)}$$

$$N(^2P) + O(^3P) \rightarrow NO^+ + e^- \quad \text{(R6-2)}$$

where $N(^2P)$ is created by the reaction:

$$N_2(A) + N(^4S) \rightarrow N_2 + N(^2P) \quad \text{(R6-3)}$$

The first one is susceptible to occur even in perfectly pure nitrogen discharges whereas the presence of oxygen is required for the second one to occur. Nevertheless, in practice, oxygen impurities are always present in the discharges and both reactions are then likely to occur.

Hence, to verify the role played by associative ionization reactions in the memory effect, it is first necessary to determine the absolute density of $N_2(A)$ between two discharges. Then based on the measured absolute density of $N(^4S)$, $O(^3P)$ and NO(X), we can calculate the density of $N(^2P)$ metastable atoms between two discharges. Finally, the reaction rates can be calculated providing the density of seed electrons generated by the associative ionization reactions, which allows simulating the current jump occurring when the gas gap voltage polarity changes.

III.1. Determination of the absolute density of $N_2(A)$

The absolute density of $N_2(A)$ molecules has not been determined in the present work. Nevertheless, M.C. Bouzidi performed OES measurements of the HIR-system between two discharges during his Ph.D. thesis [56] providing a relative estimation of $[N_2(A)]$ for various O_2 concentrations. The corresponding results are presented in Figure 6-5.

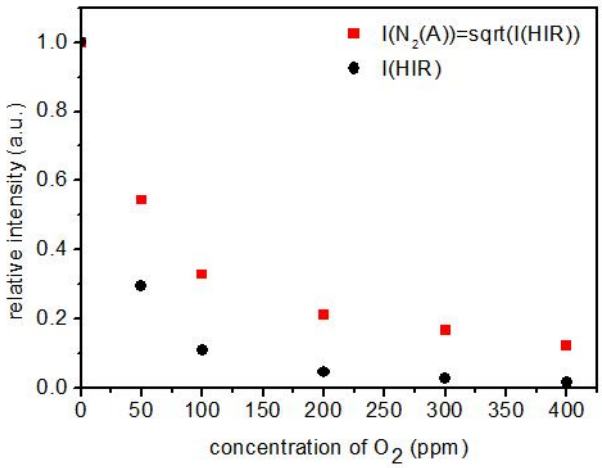

Figure 6-5 Relative concentration of $N_2(A)$ as a function of concentration of O_2 in an APTD

Dilecce *et al.* [58] measured the $N_2(A)$ density and its quenching rate Q for various low O_2 concentrations and for experimental conditions very similar to ours. Thus, the $N_2(A)$ density can be estimated using the following method. The maximum $N_2(A)$ density in pure nitrogen is 1.7 10^{13} cm^{-3} according to Dilecce *et al.* and its quenching rate is 2 10^4 s^{-1}. According to the model presented in Figure A- 3 in Appendix 1, the current jump arises when the gas gap voltage cancels *i.e.* approximately 125 µs after $[N_2(A)]$ reaches its maximum value for a frequency of 2 kHz, which allows to estimate the $[N_2(A)]$ when the polarity reverses. We find $[N_2(A)]$ =1.4 10^{12} cm^{-3}. Then, the relative OES measurements are used to compute the values for the different O_2 concentrations. The obtained results are presented in Figure 6-6.

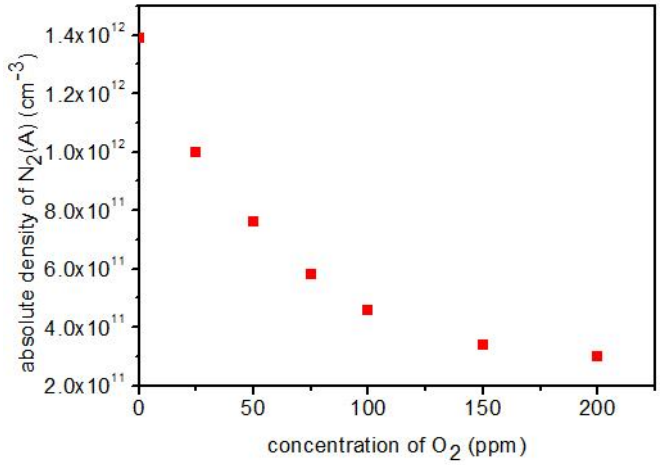

Figure 6-6 Calculated absolute density of $N_2(A)$ as a function of concentration of O_2 in an APTD

Note that Dilecce *et al.* measured a maximum value of $[N_2(A)]$=1.25 10^{13} cm^{-3} and Q=3 10^4 s^{-1} or 200 ppm of O_2 which results in a value of 3 10^{11} cm^{-3} after 125 µs (*i.e.* at the polarity inversion), in very good agreement with the values obtained from OES measurements.

III.2. Determination of absolute density of $N(^2P)$

To estimate the density of $N(^2P)$ atoms between two successive discharges, a simple model is used. The production of $N(^2P)$ atoms is assumed to be due to the reaction between $N(^4S)$ atoms and $N_2(A)$ molecules. The main quenching reactions of $N(^2P)$ atoms are also considered. Note that for the quenching rate by O_2 molecules we consider the O_2 concentration to be equal to the input concentration, which results in a slight overestimation. Finally, the associative ionization reactions are also considered. The whole set of reactions considered in the model are summarized in Table 6-4.

Table 6-4 Reactions considered for the estimation of absolute density of N(²P)

Reactions	Rate constants ($cm^{-3}.s^{-1}$)	References	Reaction number
Formation of N(²P)			
$N_2(A) + N(^4S) \rightarrow N_2 + N(^2P)$	$4.0 \times 10^{-11} \times (300/T)^{2/3}$	[83]	(R8)
Quenching of N(²P)			
$N(^2P) + N_2 \rightarrow N_2 + N(^4S)$	$6 \times 10^{-14}/5 \times 10^{-17}/2 \times 10^{-18}$	[83]/ [96]/[57]	(R9)
$N(^2P) + N(^4S) \rightarrow N(^2D) + N(^4S)$	6.0×10^{-13}	[83]	(R10)
$N(^2P) + N(^4S) \rightarrow N(^4S) + N(^4S)$	1.8×10^{-12}	[57,83]	(R11)
$N(^2P) + O(^3P) \rightarrow N(^2D) + O(^3P)$	1×10^{-12}	[57]	(R12)
$N(^2P) + NO \rightarrow O(^3P,^1D) + N_2$	2.9×10^{-11}	[57]	(R13)
$N(^2P) + O_2 \rightarrow O(^3P,^1D) + NO$	2.5×10^{-12}	[57]	(R14)
Associative ionization reactions			
$N(^2P) + N(^2P) \rightarrow N_2^+ + e^-$	1.5×10^{-11}	[57]	(R15)
$N(^2P) + O(^3P) \rightarrow NO^+ + e^-$	1.5×10^{-11}	[57]	(R16)

For each concentration of O_2, the experimental values of $[N(^4S)]$, $[O(^3P)]$, $[O_2]$ and [NO] are used as input together with the value of $[N_2(A)]$. Then the system corresponding to the set of ordinary differential equations corresponding to the reactions listed in Table 6-4 is solved until a stationary state is reached providing the stationary value of $[N(^2P)]$. The latter is used to estimate the current jump following the method described in the next section.

Note that due to the very high density of nitrogen molecules, a good description of the quenching of $N(^2P)$ by N_2 is of primary importance to obtain reliable results. Nevertheless, 3 very different values of this quenching rate can be found in the literature as indicated in Table 6-4. Thus, 3 different sets of simulations are performed considering the different reaction rates. The resulting densities of $N(^2P)$ atoms are depicted in Figure 6-7. It is interesting to note that the density of $N(^2P)$ atoms is lower than the density of $O(^3P)$ atoms.

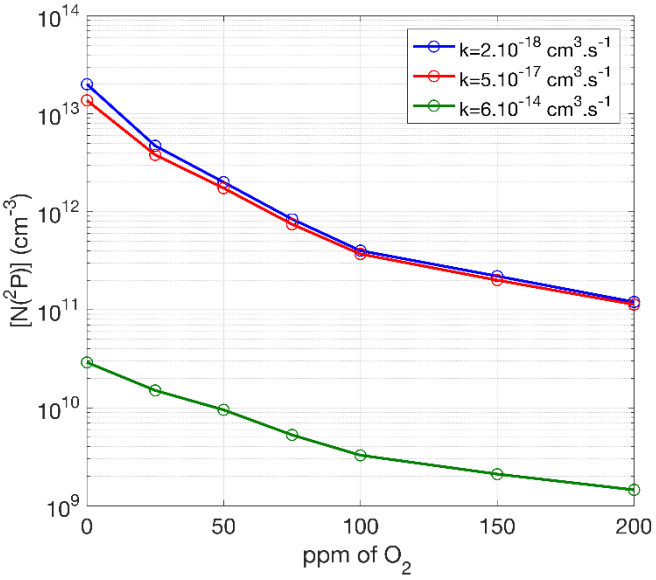

Figure 6-7 Calculated absolute density of N(²P) as a function of concentration of O_2 with different reaction rate of (R9) for a constant discharge power of 0.9 W/cm²

III.3. Determination of electron density and current jump

For a given concentration of O_2 knowing the densities of $N(^2P)$ and $O(^3P)$, it is possible to estimate the reaction rates of the associative ionization reactions. To simplify the calculations, we consider that these densities remain constant in time.

The experimental gas gap voltage $V_g(t)$ is used as input for the modeling. We focus on a small time period surrounding the moment t0 where $V_g(t0)=0$, as is shown in Figure 6-8. Then the electron and ion densities can be calculated assuming that they are continuously produced by the associative ionization reactions and lost due to their drift in the small electric field.

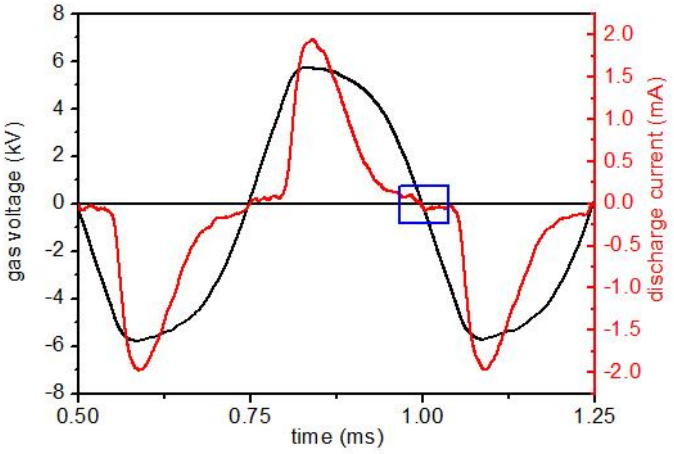

Figure 6-8 The small time period and the corresponding gas voltage used for the calculation of current jump. Simulation conditions: concentration of O_2=100 ppm, HV=15.9 kV_{pp}, f=2 kHz

The equation ruling the electron density n_e is therefore:

$$\frac{dn_e}{dt} = k_9[N(^2P)][O(^3P)] + k_8[N(^2P)]^2 - \mu_e \frac{|V_g(t)|}{d^2} n_e \quad (6.1)$$

where μ_e is the electron mobility taken from[100]. Similarly, the densities of NO^+ and N_2^+ are described by the following equations:

$$\frac{d[NO^+]}{dt} = k_9[N(^2P)][O(^3P)] - \mu_{NO^+} \frac{|V_g(t)|}{d^2} [NO^+] \quad (6.2)$$

$$\frac{d[N_2^+]}{dt} = k_8[N(^2P)][N(^2P)] - \mu_{N_2^+} \frac{|V_g(t)|}{d^2} [N_2^+] \quad (6.3)$$

The ion mobilities are μ_{NO^+}=2.5 $cm^2V^{-1}s^{-1}$ [101] and $\mu_{N_2^+}$=1.85 $cm^2V^{-1}s^{-1}$ [102] . Note that in our conditions, N_2^+ ions are known to be efficiently converted into N_4^+ ions with typical mobility $\mu_{N_4^+}$=2.3 $cm^2V^{-1}s^{-1}$ [101]. Nevertheless, due to the small difference between the ion mobility of both ions, it has only a very poor incidence on the obtained results.

Solving these equations provides the time-varying densities of electrons and ions produced by the associative ionization reactions. The current generated by the drift of ions and electrons can thus be calculated using equation (6.4):

$$I_{jump}(t) = \left(n_e(t) \times \mu_e(t) + [N_2^+](t) \times \mu_{N_2^+} + [NO^+](t) \times \mu_{NO^+}\right) \times \frac{V_g(t)}{d} \times e \times S \quad (6.4)$$

An example of typical results obtained using the aforementioned procedure is presented in Figure 6-9(a). An experimental current jump is also provided Figure 6-9(b) for comparison.

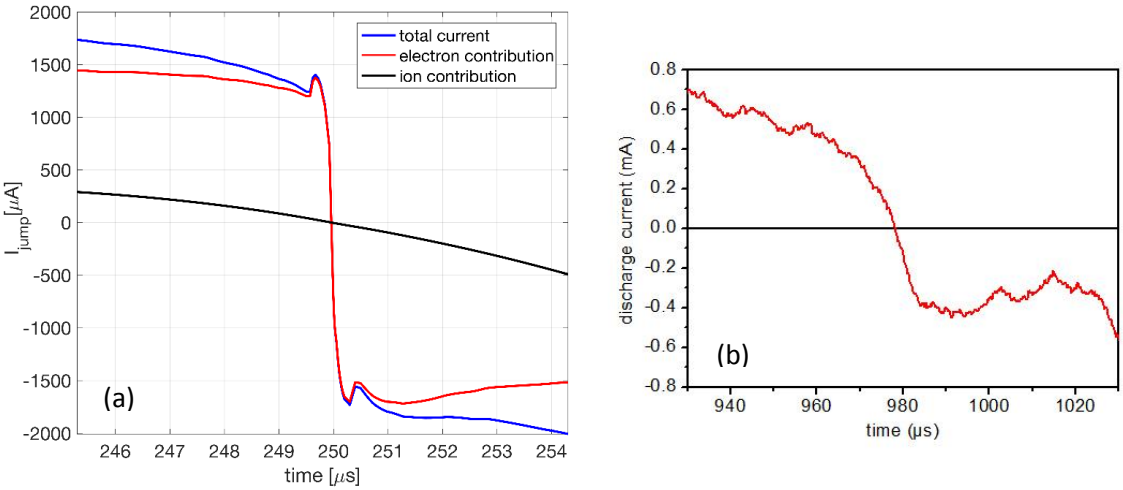

Figure 6-9 (a) Calculated current jump. (b) experimental current jump. Conditions: concentration of O_2=25 ppm, HV = 17.1 kV_{pp}, f=2 kHz, and rate constant of equation (R9) = 2.10^{-18} cm^3s^{-1} for the calculation.

The shape of the calculated current jump is in good agreement with experimental measurements *i.e.* the sign inversion of the current arises very quickly suggesting that it involves charged particles with a high mobility such as electrons. It is confirmed by the detailed contributions to the total current jump presented in Figure 6-9. Nevertheless, ion contribution cannot be neglected because their low mobility results in their accumulation in the gas gap increasing the ion density. The higher ion density then compensates partly the low ion mobility resulting in a non-negligible ion current.

III.4. Estimation of the current jump for different oxygen concentration

Using the aforementioned calculation procedure, the calculated current jump is calculated for different oxygen concentrations under the same discharge power of 0.9 W/cm^2. The corresponding results are presented in Figure 6-10(a), (b) and (c) considering the three different values of the reaction rate of (R9). Figure 6-10(d) shows the experimental results obtained in the same conditions for comparison.

The calculated current jumps show a very similar behavior as a function of concentration of O_2 compared to experimental results. It increases as O_2 is introduced in the discharge; reach a maximum value around 25 ppm of O_2 and then decreases for higher O_2 concentrations. The values of the calculated current jump strongly depend on the quenching rate coefficient used for reaction (R9): the lower the rate coefficient, the higher the $N(^2P)$ concentration and the higher the resulting current jump. Experimentally, the maximum value of the current jump obtained for 25 ppm of O_2 is around 200µA. Then, the better agreement is obtained considering a reaction rate of 5 $10^{-17}cm^3s^{-1}$ for reaction (R9). In this case, the calculated current jump is approximately four times greater than the experimental value.

For 0 ppm O_2, a current jump can be observed experimentally. It was attributed to the secondary electron emission by $N_2(A)$ metastable at the surfaces. But, since impurities are always present experimentally, the associative ionization reactions (R15) and (R16) can also play a role. Numerically, the current jump at 0 ppm when the reaction rate of reaction (R9) is low is found to be greater

compared to experimental results. In this case, it is due to the associative ionization reaction involving two N(^{2}P) atoms which seems to indicate that this reaction rate is overestimated.

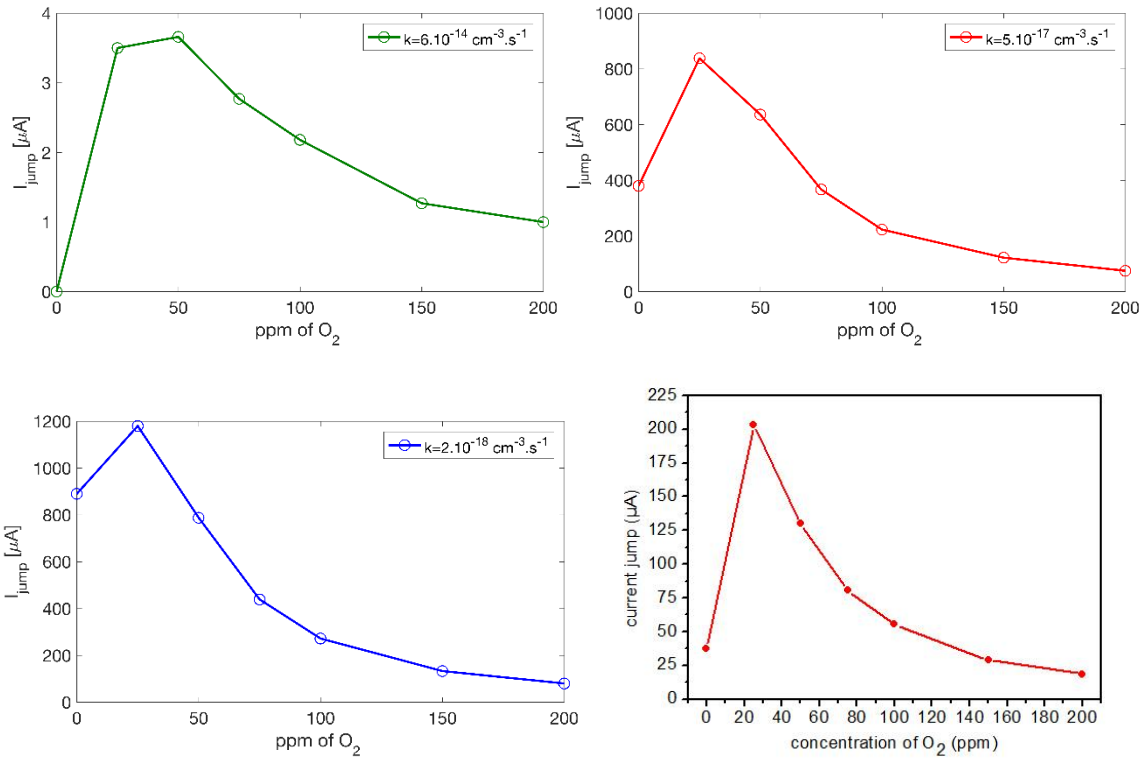

Figure 6-10 Current jump as a function of concentration of O_2 under similar discharge power (0.9 W/cm²), (a), (b) and (c): calculated results with different reaction rate of (R9), (d): experimental result

Finally, supplementary calculations have been performed taking into account electron attachment on O_2 molecules (not shown here). It was found that due to the very low O_2 concentration, it has only a very poor influence on the results. The influence of the electron-ion recombinations in volume was also found negligible.

The uncertainties related to the modeling and especially to the reaction rate of reaction (R9) make difficult to realize an accurate quantitative estimation of the contribution of associative ionization reactions to the current jump. Similarly, it is not possible to conclude that such reactions are the only process involved in the memory effect in these conditions. Nevertheless, recent investigations [103] provide a new estimation of the rate of reaction (R9) which is 3 10^{-17}cm^{3}s^{-1} in good agreement with the value of 5 10^{-17}cm^{3}s^{-1} used in this work (see Figure 6-10(b)). The current jump calculated using this value is on the same order of magnitude than experimental measurements although greater by a factor 4. Note that in experiments, the current jump is not uniform along the discharge; it increases from the entrance to the end of the discharge. Consequently, the experimental values are probably underestimated.

To go further and confirm the role of associative ionization reactions, we need to discuss the less credibility of other mechanisms related to the creation of seed electrons. The creation of seed electrons by secondary electron emission due to the bombardment of N_2(A) onto the dielectrics should be excluded because an oxygen input necessarily leads to a higher destruction of N_2(A). However, the metastable N_2(A) still plays an important role in plasma chemistry, especially for the

formation of O(^{3}P) and N(^{2}P). The mechanisms for the desorption of electrons from the dielectrics have been discussed in [54] in detail. There are three different mechanisms, the first one corresponding to secondary electron emission have been excluded in the previous discussion. The second one called "thermodesorption" is related to the dielectrics' temperature. At thermal equilibrium, the dielectric temperature is equal to the gas temperature. According to our measurements, the maximum temperature is around 450K, *i.e.* an increase of 150K compared to the ambient temperature. This increase is too weak to result in an increase of thermodesorption of electrons from the dielectrics. The third mechanism of electron desorption is caused by the vibrationally excited molecules. However, the vibrational temperature determined by the OES measurements shows that it remains around 1500K whatever the experimental condition. Hence, there is no increase of the vibrational temperature when increasing the injected amount of oxygen, which means that an increase of the electron desorption caused by vibrationally excited molecules is unlikely. Moreover, it seems unrealistic that the very low injected quantity of oxygen can be able to induce a change in the surface characteristics of the dielectrics and thus on its secondary emission coefficient. Based on the above discussion, other mechanisms related to the creation of seed electrons can be excluded, which confirms the important role of associative ionization reactions on the enhanced memory effect in an APTD with low addition of O_2 into N_2.

On the basis of the presented results and following the previous discussion, one can conclude that associative ionization reactions are good candidates to explain the increase of the current jump with very low O_2 admixture in nitrogen and thus the enhancement of the memory effect. These experimental conditions correspond to a compromise. On one hand, the concentration of O_2 is high enough to provide a significant amount of O(^{3}P) atoms whose concentration is found higher than that of N(^{2}P). On the other hand, it remains low enough to limit the concentration of the resulting various oxidizing species, thus to limit the quenching of N_2(A) and N(^{2}P). These conditions are thus suitable to promote the associative ionization $\mathrm{N}(^2\mathrm{P}) + \mathrm{O}(^3\mathrm{P}) \rightarrow \mathrm{NO}^+ + \mathrm{e}^-$ compared to the reaction $\mathrm{N}(^2\mathrm{P}) + \mathrm{N}(^2\mathrm{P}) \rightarrow \mathrm{N}_2^+ + \mathrm{e}^-$. It explains the increase of the memory effect for small additions of O_2 in N_2.

IV. Summary

This chapter starts with a summary of the experimental values obtained for the densities of N(^{4}S), O(^{3}P) and NO(X) as a function of the oxygen concentration.

Then the comparison of the experimental and simulation results for the decay of the species during the post-discharge was performed in order to study the main destruction mechanisms.

The good agreement for N(^{4}S) indicates that the main destruction reactions for N(^{4}S) are validated. For low [O_2], N(^{4}S) losses are dominated by the three-body recombination onto N_2 molecules as for the pure nitrogen case. For higher [O_2], N(^{4}S) atoms are mainly destroyed by oxidizing species through the reactions $\mathrm{N}(^4\mathrm{S}) + \mathrm{O}(^3\mathrm{P}) + \mathrm{N}_2 \rightarrow \mathrm{NO} + \mathrm{N}_2$ and $\mathrm{N}(^4\mathrm{S}) + \mathrm{NO} \rightarrow \mathrm{N}_2 + \mathrm{O}(^3\mathrm{P},^1\mathrm{D})$. Independently of the concentration of O_2, N(^{4}S) losses are dominated by recombination to the wall for long timescale.

A relatively good agreement is also found for O(^{3}P) for low oxygen concentrations. The main reactions responsible for the losses of O(^{3}P) atoms are $\mathrm{N}(^4\mathrm{S}) + \mathrm{O}(^3\mathrm{P}) + \mathrm{N}_2 \rightarrow \mathrm{NO} + \mathrm{N}_2$ and $\mathrm{O}(^3\mathrm{P}) + \mathrm{O}(^3\mathrm{P}) + \mathrm{N}_2 \rightarrow \mathrm{N}_2 + \mathrm{O}_2(\mathrm{X}, \mathrm{a}, \mathrm{b})$ whereas the reduction of NO by N(^{4}S) is responsible for the production of O(^{3}P) atoms. For higher concentration of O_2 (200 ppm), the calculations overestimate the decay of O(^{3}P). A possible explanation is that other species such as NO_2 which are not taken into account can precipitate to the formation of O(^{3}P) thus reducing the decay rate.

The decay of NO molecules during the post-discharge is attributed to its reduction by N(^{4}S) atoms whereas NO(X) is produced by the reaction $\mathrm{N}(^4\mathrm{S}) + \mathrm{O}(^3\mathrm{P}) + \mathrm{N_2} \rightarrow \mathrm{NO} + \mathrm{N_2}$. Nevertheless, the model fails to provide a good description of the experimental behavior. Indeed, the aforementioned reaction is responsible for a significant increase of the NO(X) density at the very beginning of the post-discharge. If one assumes that the main reactions have been taken into account, it suggests a possible incompatibility between the experimental N(^{4}S), O(^{3}P) and NO(X) densities. To investigate this effect, the experimental NO(X) density was increased by a factor 2.5 and new calculations were performed. A better agreement was observed in this last situation, which suggests that experimental uncertainties can partly explain the observed discrepancies. Nevertheless, the model is still unable to provide a good description of the results obtained for the highest O_2 concentration. A possible explanation is a role played by other species such as NO_2 as suggested above.

The last part of this chapter is dedicated to the estimation of the current jump due to associative ionization reactions for different concentration of O_2. For this purpose, the N(^{2}P) metastable atoms density between two discharges was calculated using a model and considering the experimental values of N(^{4}S), O(^{3}P) and NO(X) together with the N_2(A) density determined by Dilecce *et al.* [58]. The results were found to be highly dependent on the value of the quenching rate of N(^{2}P) by N_2. Recent investigations showed that the value of 5 10^{-17} cm^3s^{-1} proposed in [96] is the most realistic. Using this value, the N(^{2}P) concentration was found to decrease monotonously from $\sim 10^{13}$ cm^{-3} at 0 ppm of O_2 to $\sim 10^{11}$ cm^{-3} at 200 ppm of O_2. Knowing the [N(^{2}P)] and [O(^{3}P)], the current jump was estimated as a function of the oxygen concentration. The obtained results reproduce qualitatively the experimental behavior. The current jump increases up to 800 µA at 25 ppm and then decreases. The values of the calculated current jump are four times higher than experimental values. This difference may be explained from two aspects. Firstly with a 0D model, the spatial distribution of the species is not considered, and this limitation can lead to an overestimation of the calculated current jump. Secondly, the experimental values correspond to a current jump averaged over the whole discharge and are consequently underestimated, moreover the uncertainties of the absolute densities will also influence the calculated results.

The experimentally observed increase of the memory effect for small additions of O_2 in N_2 can thus be explained by the associative ionization reaction $\mathrm{N}(^2\mathrm{P}) + \mathrm{O}(^3\mathrm{P}) \rightarrow \mathrm{NO^+} + \mathrm{e^-}$. These experimental conditions correspond to a compromise. The O_2 concentration is high enough to provide a significant amount of O(^{3}P) atoms and low enough to limit the concentration of oxidizing species responsible for the quenching of N_2(A) and N(^{2}P).

General conclusion and prospects

The present work concerns the study of atmospheric pressure Townsend discharges (APTD) generated in a nitrogen atmosphere with the addition of a small oxygen amount (typically lower than 200 ppm). Previous studies have shown that the presence of a memory effect between two successive discharges is a necessary condition to obtain a homogeneous dielectric barrier discharge. In high purity nitrogen in which oxygen is only present as impurities (<10 ppm), the secondary electron emission induced by $N_2(A)$ metastable molecules at the cathode was demonstrated to be an important source of seed electrons between two discharges and thus a major contribution to the memory effect. On the other hand, APTD were obtained in air and in very low-frequency discharges for which $N_2(A)$ is either efficiently quenched by oxidizing species or completely removed between two successive discharge by the gas flow. In these conditions, the mechanism of spontaneous electron desorption is up to now the best candidate to explain experimental observations. In the conditions of the present study *i.e.* in the mixtures of N_2/O_2 with oxygen concentrations about a few dozens of ppm, many studies have pointed out a strong increase of the memory effect. Recent works put in evidence a possible role played by $O(^3P)$ atoms and $N_2(A)$ and suggested that the associative ionization reaction $N(^2P) + O(^3P) \rightarrow NO^+ + e^-$ where $N(^2P)$ atoms are produced by the reaction $N(^4S) + N_2(A) \rightarrow N(^2P) + N_2(X)$, is likely to significantly contribute to the memory effect. The main objective of the present work was to verify this hypothesis.

For this purpose, the density of $N(^4S)$ and $O(^3P)$ was measured by two photon absorption laser induced fluorescence (TALIF). Moreover, the density of NO molecules, which are an efficient quencher of $N_2(A)$, was also measured by laser induced fluorescence (LIF). Most of the measurements were performed between two successive discharges. The influence of several experimental parameters such as the discharge power or the concentration of oxygen on the different species densities was investigated. The observed behaviors were discussed with the help of a 0D-model. The latter was used to identify the main mechanisms involved in the production and destruction of the different species.

The measured density of $N(^4S)$ increases at the entrance of the discharges, then becomes constant and finally decreases in the post-discharge region. Typical values of 10^{14} cm^{-3} were measured with a maximum value of around 7 10^{14} cm^{-3} for the higher discharge power. The higher the discharge power, the higher the $N(^4S)$ density. $N(^4S)$ atoms are produced by direct electron impact dissociation of N_2 molecules. In high purity nitrogen, the losses of $N(^4S)$ are mainly due to three-body recombination onto N_2 molecules. Measurements performed for different times during a discharge period showed that the $N(^4S)$ density present only very small variations. Similar results were obtained numerically, which can be explained by a simultaneous modulation of the production and destruction. In the presence of oxygen, the $N(^4S)$ density decreases due to a higher destruction by oxidizing species. The higher the oxygen concentration, the lower the $N(^4S)$ density. Indeed, for 50 ppm of O_2 and above, $N(^4S)$ losses are dominated by reactions with oxidizing species. Using the model, the main reactions were identified as $N(^4S) + O(^3P) + N_2 \rightarrow NO + N_2$ and $N(^4S) + NO \rightarrow N_2 + O(^3P, ^1D)$.

TALIF measurements on $O(^3P)$ atoms indicated densities about few 10^{14}cm^{-3} with a maximum value of 4 10^{14} cm^{-3}. The evolution of the $O(^3P)$ density along the discharge is quite similar to one of $N(^4S)$: it increases at the entrance of the discharge, reach a plateau and then decreases in the post-discharge. Numerical results indicate that the production of $O(^3P)$ atoms is mainly due to the dissociation of O_2

by $N_2(A)$ metastable molecules. Measurements of the $O(^3P)$ density for different times during a discharge period indicate that the $O(^3P)$ density remains approximately constant. The same behavior was observed numerically and was explained by a simultaneous modulation of the production and destruction rates of $O(^3P)$, both being strongly related to the $N_2(A)$ concentration. Increasing the power results in an increase of the $O(^3P)$ density which was attributed to a higher production rate of $N_2(A)$, as confirmed by the model. The influence of the O_2 concentration on the $O(^3P)$ density was also studied. The higher the O_2 concentration, the higher the $O(^3P)$ density. Nevertheless, the increase of the $O(^3P)$ density with respect to the O_2 concentration was found to be less pronounced for O_2 concentration higher than 100 ppm. This was confirmed by the calculation of the O_2 dissociation degree, which continuously decreases for increasing O_2 concentration. This effect was explained by a higher destruction of $N_2(A)$ by oxidizing species.

The density of NO measured by LIF is about few 10^{12} cm^{-3} with a maximum value of 8 10^{12} cm^{-3}. These values are well below the ones measured previously in our group *i.e.* about 10^{15} cm^{-3}. Some uncertainties remain regarding the mechanisms leading to NO production in our conditions. According to the numerical investigations, the main production mechanisms of NO are $N_2(A) + O(^3P) \rightarrow NO + N(^2D)$ and $N(^4S) + O(^3P) + N_2 \rightarrow NO + N_2$. Nevertheless, according to the literature, the contribution of the first reaction is probably overestimated. Moreover, as pointed out by several authors, another important channel for NO production should be the reaction $N(^2D,^2P) + O_2 \rightarrow NO + O(^3P,^1D)$. Finally, the contribution of the associative ionization reaction $N(^2P) + O(^3P) \rightarrow NO^+ + e^-$ where NO^+ can recombine at the walls to form NO requires further investigations. The NO concentration increases when increasing the discharge power. It was explained by the simultaneous increase of the $N(^4S)$, $O(^3P)$ and $N_2(A)$ densities. The influence of the oxygen concentration on the NO density was investigated. For small addition of O_2, the NO concentration increases linearly due to the increase of the $O(^3P)$ density. For higher O_2 concentration (> 100 ppm) the NO density is roughly constant. This effect was ascribed to the noticeable decrease of the $N_2(A)$ and $N(^4S)$ densities with increasing O_2 concentration which are both involved in the production of NO molecules.

To verify if the associative ionization reaction $N(^2P) + O(^3P) \rightarrow NO^+ + e^-$ can be responsible for the increase of the memory effect in our conditions, the $N(^2P)$ density between two successive discharges was estimated using a 0D model. The production rate through the reaction $N(^4S) + N_2(A) \rightarrow N(^2P) + N_2(X)$ was calculated using the experimental values of the $N(^4S)$ density. The density of $N_2(A)$ was taken from the literature and from OES measurements previously performed in the group. The destruction rate of $N(^2P)$ was calculated considering the main quenching reactions involving N_2, O_2, $O(^3P)$ and NO, the densities of the two last species being known from the TALIF and LIF measurements. Calculations were performed for different oxygen concentrations. The resulting $N(^2P)$ densities were found to be highly dependent on the reaction rate coefficient of the reaction $N(^2P) + N_2 \rightarrow N_2 + N(^4S)$. Considering a value of 5 10^{-17} cm^{3}s^{-1}, which order of magnitude was recently confirmed in the literature, the $N(^2P)$ concentration was found to decrease monotonously from $\sim 10^{13}$ cm^{-3} at 0 ppm of O_2 to $\sim 10^{11}$ cm^{-3} at 200 ppm of O_2 for the set of experiments performed at a constant applied voltage of 17.1 kV. Knowing the $N(^2P)$ and $O(^3P)$ densities, the current jump was estimated as a function of the oxygen concentration. The obtained results reproduce qualitatively the experimental behavior. The current jump increases up to 800 µA at 25 ppm and then decreases thus confirming the important role of associative ionization reactions in the memory effect. The calculated values are approximately four times higher than experimental values. This difference can be explained from the limitation of both 0D model and the experimental uncertainties.

The experimentally observed increase of the memory effect for small additions of O_2 in N_2 can thus be explained by the associative ionization reactions. These experimental conditions correspond to a

compromise. The O_2 concentration is high enough to provide a significant amount of $O(^3P)$ atoms and low enough to limit the concentration of oxidizing species responsible for the quenching of $N_2(A)$ and $N(^2P)$.

For the future investigations, several prospects can be proposed and a few examples are provided in the following.

First, it is necessary to quantify the uncertainty regarding TALIF measurements on $O(^3P)$ atoms due to the interference filter used during the calibration. New measurements performed using a monochromator to precisely select the detected wavelengths will allow estimating the relative error due to the parasitic fluorescence signal and to correct the obtained values.

Measurements of the $N_2(A)$ density using the cavity ring down spectroscopy (CRDS) diagnostic can bring more information regarding the kinetics of this key specie in our conditions. It will allow extending this kind of study to other gas mixtures (*e.g.* N_2/NO, N_2/N_2O…) for which no values of the $N_2(A)$ density have been published in the literature.

As pointed out by this study, the production of NO molecules in our conditions is not fully understood and requires more investigations.

The possibility to generate homogeneous discharges in air, as reported in the review presented in chapter 1 is also of great interest. Even if it is currently admitted that the dominant memory effect in these conditions is due to spontaneous electron desorption at the surfaces, measurements of important species such as $N_2(A)$ or oxidizing species can be interesting.

One of the main limitations of the 0D model used in this study is its incapability to provide a self-consistent calculation of the discharge current and thus of the current jump. Indeed the current (and thus the electron density) and gas gap voltage are imposed from the experimental measurements. Thus, the development of a 1D-model which considers the external electrical circuit and in which the only input is the applied voltage could be of great interest and should be performed. The direct comparison of experimental measurements such as the time-varying gas gap voltage and discharge current and their numerical values should provide more accurate estimations of the different contributions to the memory effect (secondary electron emission, associative ionization reaction…).

APPENDIX 1

In this appendix we describe the 0D model, which was developed in order to identify the main mechanisms responsible for the creation and destruction of the measured species, namely N(^{4}S), O(^{3}P) and NO(X).

I. General description of the model

The general principle of the model is similar to the one proposed by Tsyganov *et al.* [83] . Since it is a 0D model, it is not self-consistent. To overcome this limitation we use electrical experimental measurements of the applied voltage and total current to calculate the gas gap voltage V_g and the discharge current I_d, following the method detailed in [62]. These measurements are performed in conditions similar to those studied in the simulation (applied voltage, power, and concentration of oxygen). Then, the time-varying electron density and the electric field between the dielectric surfaces are deduced using equations ((A 1) and ((A 2), assuming that all the discharge current is due to electrons. This is a rough approximation since it is well known that in atmospheric pressure Townsend discharge (APTD) the ion density can significantly exceeds the electron density [42]. The electron mobility used for the calculations are taken from [100,104].

$$E(t) = \frac{|V_g(t)|}{d} \tag{A 1}$$

$$n_e(t) = \frac{|j_d(t)|}{e\mu_e(E)E(t)} \tag{A 2}$$

An example showing the electrical characteristics and the calculated reduced electric field and electron density is presented in Figure A- 1.

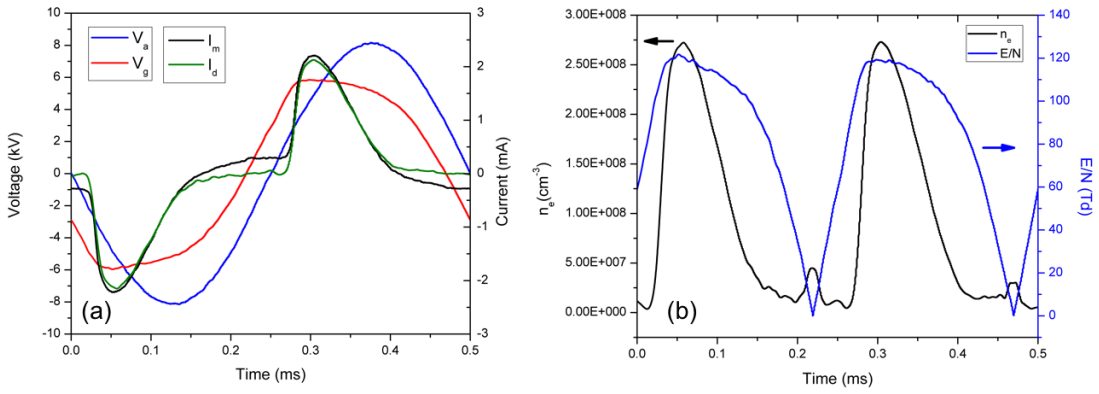

Figure A- 1(a) electrical characteristics of the discharge: applied voltage V_a, gas gap voltage V_g, measured current I_m and discharge current I_d. Experimental conditions are: HV=17.1 kV_{PP}, f=2 kHz, flow rate=1.0 L/min, concentration of O_2=200 ppm. (b) Corresponding calculated reduced electric field and electron density n_e

Another limitation concerns the electron density between two successive discharges, which cannot be accurately described because of the singularity in equation (*(A 1*) when the electric field approaches zero. At this moment, the electric field is very low, thus the electrons, which are considered in equilibrium with the electric field, have very small energy. Consequently, one can expect that it have only a small influence on the reaction rates involving energetic electrons such as nitrogen molecular dissociation. But in turns it implies that reactions involving electrons with small

energies cannot be accurately described. It is especially the case for attachment reactions on oxidizing species. Then, they are not included in the model.

For each specie X_i considered in the model, its time varying density $[X_i]$ is described by the following equation:

$$\frac{d[X_i]}{dt} = \sum_j S_j - \sum_k L_k \quad \text{(A 3)}$$

where S_j correspond to the source terms and L_k to the loss terms. The summations are performed over all the reactions leading to the formation or destruction of specie X_i.

Considering a typical reaction with label j which results in the formation of specie X_i:

$$aA + bB = cC + \alpha_j X_i \quad \text{(A 4)}$$

where a, b, c and α_j are the stoechiometric coefficients. The corresponding source term S_j (production rate) for specie X_i writes:

$$S_j = \alpha_j [A]^a [B]^b \quad \text{(A 5)}$$

Considering a typical reaction with label k which results in the destruction of specie X_i:

$$aA + \alpha_k X_i = cC + dD \quad \text{(A 6)}$$

The corresponding loss term L_k (destruction rate) for specie X_i writes:

$$L_k = \alpha_k [A]^a [X_i]^{\alpha_k} \quad \text{(A 7)}$$

The system is then described by a set of N ordinary differential equations, where N represents the number of considered species.

The reactions considered in the model are given in Table A- 6 for nitrogen-based species, in Table A-7 for oxygen-based species and in Table A- 8 for reactions involving both oxygen and nitrogen species. Since the discharge atmosphere is mainly composed of nitrogen, the set of reactions for nitrogen species including neutral particles in the ground states – N_2, $N(^4S)$ - and excited states – N_2(A,B,a',C), $N(^2P,^2D)$ - and ions – N^+, N_2^+, N_3^+, N_4^+ - is quite complete. Due to the low oxygen concentration, we only focused on neutral oxygen species in the ground states – O_2 and $O(^3P)$, and excited states – O_2(a,b), except for the NO^+ ion which has to be considered because of its production by the associative ionization reaction $\mathrm{N}(^2\mathrm{P}) + \mathrm{O}(^3\mathrm{P}) \rightarrow \mathrm{NO}^+ + \mathrm{e}^-$. Note that negative ions are neglected. Other molecules are only considered in the ground state. Moreover, the different vibrational levels of nitrogen molecules are not considered.

Reaction rates involving the EEDF are obtained using the BOLSIG+ solver [105] using the IST-Lisbon database for nitrogen species [104], the Biagi database [106] for molecular oxygen and the Morgan database for atomic oxygen [107]. Inverse reactions are also considered for reactions (1-5) in Table A- 6 and (43-45) in Table A- 7. Due to the very low concentration of oxygen, the calculations in BOLSIG+ are performed in pure nitrogen. The validity of this approximation was checked by comparing calculations performed in pure N_2 and in N_2 with 200 ppm of O_2. The resulting EEDF was found to be very similar in both cases. Reaction rates related to reactions involving both ions and neutrals were calculated considering the effective temperature of the ion-neutral system [83] in order to take into account the effect of the ion acceleration in the electric field. The effective temperature T_{eff} is then given by:

$$T_{eff} = T_{gas} + \frac{\pi}{k_B}\frac{m_i m_n}{m_i + m_n}\langle v\rangle^2 \quad \text{(A 8)}$$

with T_{gas} the gas temperature, m_i and m_n are the mass of ions and neutral respectively, k_B is the Boltzmann constant and $\langle v\rangle = \langle \mu_i E\rangle$ is the averaged value of the ion velocity in the electric field.

For a sake of simplicity, neutral losses by diffusion to the walls are neglected in the model.

Ions are mainly lost onto the walls due to their motion in the electric field. The corresponding evolution of the ion density $[X_i^+]$ is described by equation (A 9):

$$\frac{d[X_i^+](t)}{dt} = -\frac{[X_i^+]\mu_i E(t)}{L_{gap}} \quad \text{(A 9)}$$

where μ_i is the ion mobility of ion *i*, and $E(t)$ the electric field value. Since ions mobilities are only slightly varying with respect to the reduced electric field, we considered averaged values over an excitation period. Data have been taken from [102]. Reaching the wall, ions are considered to neutralize instantaneously. These processes are then included in the overall set of reactions considering the following reactions in Table A- 1.

Table A- 1 Reactions of ions involved in the neutralization

$N_2^+ \rightarrow N_{2\,wall}^+ \rightarrow N_2$	(R1)
$N^+ \rightarrow N^+_{wall} \rightarrow N(^4S)$	(R2)
$N_3^+ \rightarrow N_{3\,wall}^+ \rightarrow N_2 + N(^4S)$	(R3)
$N_4^+ \rightarrow N_{4\,wall}^+ \rightarrow N_2 + N_2$	(R4)
$NO^+ \rightarrow NO^+_{wall} \rightarrow NO$	(R5)

with their corresponding constant rate equal to $\mu_i E(t)/L_{gap}$.

The model is based on a large number of hypotheses and considers a large number of reactions. Moreover, it does not take into account the effect of surfaces, which are of great importance for the physics and chemistry of DBD (emission and desorption of electrons, chemical reactions, recombination…). For all these reasons, it is unable to give accurate estimations of the species densities but rather to provide order of magnitudes. Assuming that reaction rates coming from the literature are corrects, it can be used to identify the main chemical mechanisms by calculating the averaged reaction rates of all reactions over a period.

II. Typical examples of numerical results

The model returns the time varying evolution of the species densities. Figure A- 2 presents the results for $N(^4S)$, $O(^3P)$ and NO for a simulation performed with 25 ppm of O_2. The whole results are depicted in Figure A- 2(a), whereas Figure A- 2(b) shows the densities between two successive discharges *i.e.* when the gas gap voltage is zero. Note that the post-discharge is not simulated.

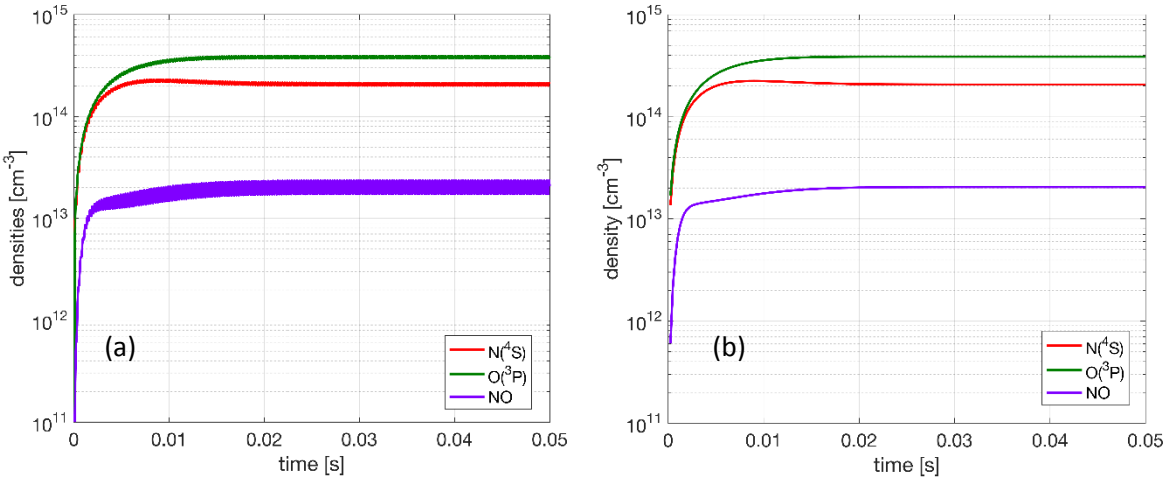

Figure A- 2 Temporal evolution of absolute density of N(^{4}S), O(^{3}P) and NO(X). (a) during the whole period (b) between two discharges. Conditions: HV=17.1 kV$_{PP}$, f=2 kHz, flow rate=1.0 L/min, concentration of O$_2$=25 ppm

The density of each species exhibits the same behavior: it increases after the discharge ignition and after a sufficiently long period, reaches a stationary state. An interesting point is that, even in the stationary state, the time varying density of N(^{4}S) and O(^{3}P) present only very small variations. This point is discussed in more details in chapter 3 section II.1 and chapter 4 section IV.4

It the following sections, several comparisons are made with experimental results. Nevertheless, a direct comparison between experimental results obtained as a function of time or position along the discharge and time resolved numerical results is hazardous. Indeed, the power input in the discharge is constant in the simulation whereas experimentally, the power is lower at the entrance of the discharge as explained in chapter 3 section II.2. Thus, most of the comparisons between numerical and experimental results are performed in the stationary state and between two successive discharges, unless otherwise specified.

III. Validation of the model

The results of the model have been compared to various experimental data obtained in the group (including the present work) or taken from the literature in order to check its consistency.

III.1. Optical emission over a half-period of electrical excitation

One of the most direct ways to validate the temporal dynamic of the model is to compare the optical emission of emitting species to those experimentally observed. In the PhD thesis of Mohamed Cherif Bouzidi [56] several characteristic emissions have been measured along a period of the applied signal, mainly:

- the second positive system (SPS) of nitrogen
- the emission of the Herman infrared system of nitrogen (N_2-HIR)
- the emission of the NOγ system
- the emission of the O(^{1}S)N_2 system

Experimental conditions were slightly different compared to those used in this work: the inter-electrode space was 1mm, the gas flow rate was 4 L/min, the applied voltage was 12 kV$_{PP}$ and the frequency was 3 kHz.

The main mechanism involved in the production and destruction of these emitting species are summarized in Table A- 9. They have been used in the model to recover the temporal evolution of the emitted intensities and to compare them to the experimental ones.

The obtained results are presented in Figure A- 3 together with the discharge current. Because the frequency was fixed to 3 kHz during experiments and 2 kHz for the simulation, the x-axis corresponds to a « normalized time » corresponding to the product of the real time by the applied frequency.

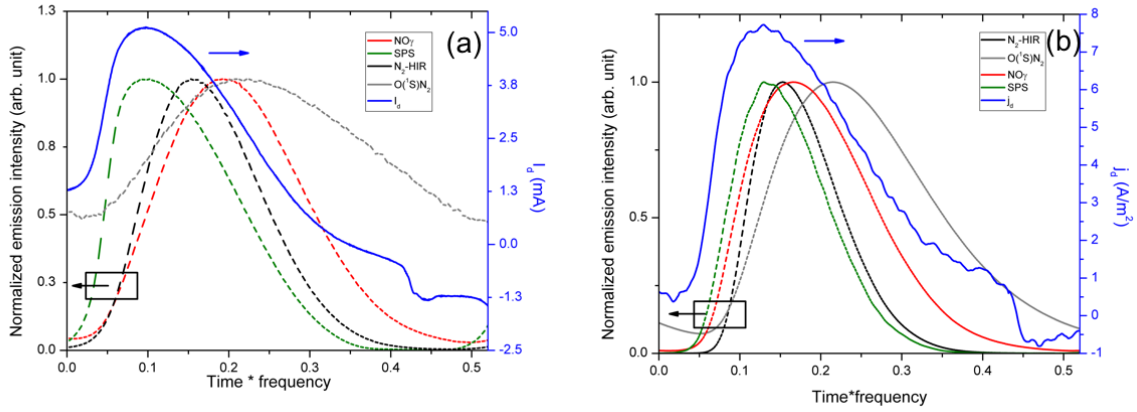

Figure A- 3 Temporal evolution of the second positive system (SPS), the NOγ system, the N_2-HIR system and the $O(^1S)N_2$ system for a discharge in N_2 with 50 ppm of oxygen. (a) Experimental data and (b) numerical results.

As can be seen in both cases the SPS intensity follows the evolution of the discharge current, which is in agreement with the fact that $N_2(C)$ is directly produced by electron impact excitation. The other systems are less direct to generate and then reach their maximum emission after the maximum discharge current. These maximum appears in the same order for both the experiment and the simulation: first the HIR system, which originates from the collision between two metastable $N_2(A)$, then the NO_γ system produced by a collision between a NO(X) molecule and a $N_2(A)$ metastable [55,108] and finally the $O(^1S)N_2$ system. This last one require first to produce $O(^1S)$ which then react with two N_2 molecules to form $O(^1S)N_2$.

Despite the fact that the time delays between these maximum and the maximum of the current are found lower in the simulation than in the experiments which indicates that the dynamic is not perfectly reproduced, we consider these results to be qualitatively acceptable.

III.2. Production and destruction of metastable $N_2(A)$

It is well known that $N_2(A)$ metastable play a crucial role in the physics and chemistry of APTD (see *e.g.*[38]). The results of the model concerning the $N_2(A)$ density thus requires a careful attention. Figure A- 4 represents the time evolution of the $N_2(A)$ density during a half period of the applied voltage for 0 ppm and 200 ppm of oxygen in N_2. From this figure, two important observations can be made. First, the maximum value reached by the $N_2(A)$ density is quite similar for both oxygen concentrations: 6.4 10^{13} cm^{-3} at 0 ppm and 5 10^{13} cm^{-3} at 200 ppm. Second, the quenching rate of $N_2(A)$ is 2.96 10^4 s^{-1} at 0 ppm, mainly due to the quenching by $N(^4S)$ atoms, N_2 molecules and self-quenching, and increases up to 4 10^4 s^{-1} at 200 ppm. Consequently, the minimum density of $N_2(A)$ between two successive discharges is more than ten times smaller at 200 ppm compared to 0 ppm of oxygen. The increase of the $N_2(A)$ quenching rate can be explained by the appearance of efficient

quenchers as soon as O_2 is introduced in the discharge. The main oxidizing species responsible for the enhanced quenching of $N_2(A)$ are, in order of importance, $O(^3P)$, O_2 and NO whereas N_2O and NO_2 have only a poor influence.

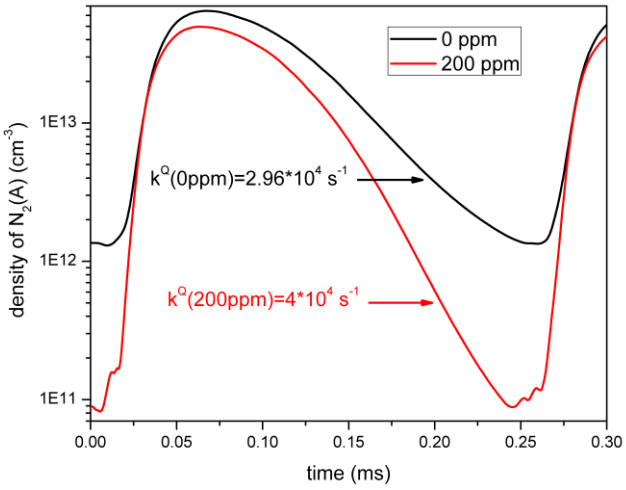

Figure A- 4 Temporal evolution during a half electrical period of the $N_2(A)$ density provided by the model for 0 ppm and 200 ppm of oxygen in N_2. HV=17.12 kV_{PP}, f= 2 kHz, flow rate =1.0 L/min.

Dilecce *et al.* have measured the absolute concentration of $N_2(A)$ in rather similar conditions than those exposed here [58]. The maximum $N_2(A)$ concentration they found is around 1.7 10^{13} cm^{-3} at 0 ppm and 1.2 10^{13} cm^{-3} at 200 ppm of oxygen in N_2. Moreover, the quenching rate they determined is 2 10^4 s^{-1} at 0 ppm and around 3 10^4 s^{-1} at 200 ppm. We can thus conclude that experimental results of Dilecce *et al.* are in the same order of magnitude in comparison with the results of the model. Thus, the latter seems to provide good estimations of the $N_2(A)$ dynamics.

III.3. Optical emission for different oxygen concentration

Optical emission spectroscopy measurements have been performed in the PhD thesis of Mohamed Cherif Bouzidi [56] for various oxygen concentrations ranging from 0 to 400 ppm. We focus here on the intensities of the systems $O(^1S)N_2$, N_2-HIR and NO_γ emitted between two successive discharges. Measurements were performed just before the end of the discharge, where the discharge characteristics (current, optical emission intensities…) reach constant values. The experimental results are presented in Figure A- 5(a). Simulations based on the reactions presented in Table A- 1 have been performed for oxygen concentrations from 0 to 200 ppm and the corresponding results are presented in Figure A- 5(b). All correspond to results obtained in the stationary state and between two successive discharges. Numerical results have been normalized to the value at 0 ppm for N_2-HIR and to the value at 50 ppm for $O(^1S)N_2$ and NO_γ in order to allow a direct comparison with experimental results.

As can be seen, the model is able to reproduce the experimental behavior. The emissions of the NO_γ and $O(^1S)N_2$ systems provided by the model increase from 0 to 25 ppm and then decreases for higher oxygen concentrations. Note that experimentally the maximum is found at 50 ppm because no measurements were performed at 25 ppm. Moreover, the appearance of the NO_γ and $O(^1S)N_2$

systems at 0ppm indicate that impurities are always present experimentally, even when only high purity nitrogen is injected.

The emission of the N_2-HIR system from the model is slightly higher at 25 ppm than at 0 ppm and then decreases with increasing oxygen concentration. This can be explained by the higher discharge power at 25 ppm. Experimentally, since no measurements have been performed at 25 ppm, the intensity of the N_2-HIR system is found to decrease continuously with increasing oxygen concentration.

These evolutions are the results of two competing phenomena. As we will see later, increasing the oxygen concentration results in an increase of the $O(^3P)$ and NO(X) concentration. But at the same time, the quenching rate of $N_2(A)$ continuously increases because of the higher density of oxidizing species (see section III.2). Since the emissions of these three systems are strongly related to the $N_2(A)$ concentration, the quenching of $N_2(A)$ seems to be the dominant effect and consequently the emitted intensities decrease. Similar conclusions have been drawn in [55].

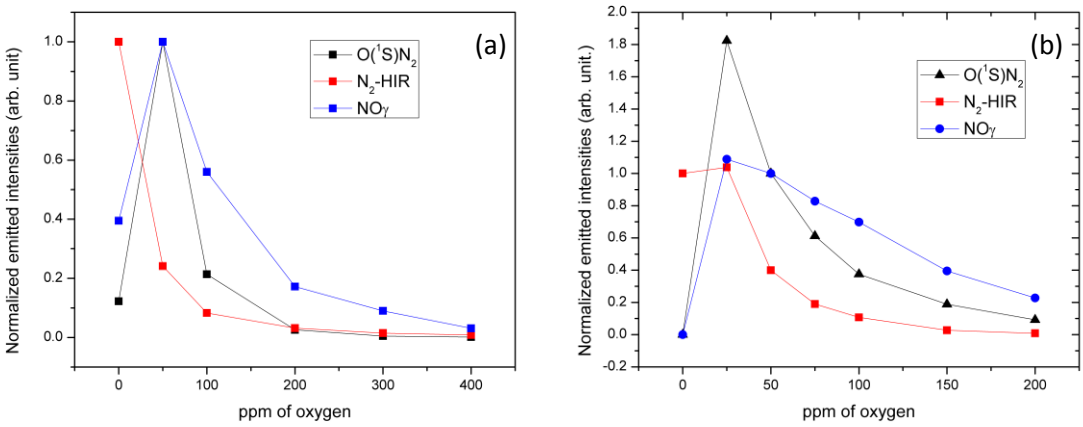

Figure A- 5 Intensity of $O(^1S)N_2$, N_2-HIR and NOγ measured between two successive discharges for various oxygen concentrations. (a) Experimental results with conditions: HV=12 kV_{PP}, f=3 kHz, flow rate=4.0 L/min, gas gap=1 mm (b) numerical results with conditions: HV=17.1 kV_{PP}, f=2 kHz, flow rate=1.0 L/min, gas gap=2 mm

IV. Identification of the main mechanisms involved in the production/destruction of species of interest

In this section we are interested in the production and destruction mechanisms of $N(^4S)$, $O(^3P)$ and NO(X) by looking at their respective production and destruction rates averaged over a discharge period in the stationary state. The production/destruction rates correspond to the reaction rate multiplied by the stoichiometric coefficient referring to the species of interest.

IV.1.N(^{4}S) atoms

IV.1.1. Main mechanisms of production and destruction

IV.1.1.1. Production:

$N(^4S)$ atoms are produced by dissociation of N_2 molecules through direct electron impact following the reaction: $e^- + N_2 \rightarrow e^- + N(^4S) + N(^4S,^2D,^2P)$

Cosby [109] indicates that N(^{4}S)+N(^{2}D) is the dominant channel of this reaction which can also leads to N(^{4}S)+N(^{2}P) as a minor contribution whereas the channel N(^{4}S)+ N(^{4}S) is considered negligible. Thus, only the reaction $e^- + N_2 \rightarrow e^- + N(^4S) + N(^2D)$ is considered in the model. Note that even if the electron density is quite low in this kind of discharge, the large density of N_2 molecules compensates this and results in a significant reaction rate.

Another noticeable source of N(^{4}S) comes from the quenching of N(^{2}P) and N(^{2}D) atoms by nitrogen molecules: $N_2 + N(^2P,^2D) \rightarrow N_2 + N(^4S)$ where N(^{2}P) atoms are mainly produced during the excitation of N(^{4}S) by N_2(A): $N_2(A) + N(^4S) \rightarrow N_2 + N(^2P)$. These two reactions always have a very similar reaction rate indicating that they drive the equilibrium between N(^{4}S) and N(^{2}P) densities. The case of N(^{2}D) atoms is more complex since they are produced either by the reaction $N_2(A) + O(^3P) \rightarrow NO + N(^2D)$ or during N_2 dissociation by electrons.

IV.1.1.2. Destruction:

As explained previously, in post-discharge in pure nitrogen N(^{4}S) atoms are mainly lost by three-body recombination on N_2 molecules and by diffusion towards the dielectrics. Inside the discharge, N(^{4}S) is efficiently excited by N_2(A) to form N(^{2}P).

As soon as oxygen is introduced into the discharge, N(^{4}S) is mainly destroyed by NO molecules and O(^{3}P) atoms. Table A- 2 presents the different destruction rates for 200 ppm of O_2 in N_2.

Table A- 2 averaged destruction rates over a period of the applied voltage for the main reactions involved in the destruction of N(^{4}S) atoms for 200 ppm of oxygen

Reaction	Destruction rate $(cm^{-3}s^{-1})$
$N(^4S) + NO \rightarrow N_2 + O(^3P,^1D)$	1.19×10^{17}
$N_2(A) + N(^4S) \rightarrow N_2 + N(^2P)$	9.87×10^{16}
$N(^4S) + O(^3P) + N_2 \rightarrow NO + N_2$	2.48×10^{16}
$N(^4S) + NO_2 \rightarrow N_2O + O(^3P)$	2.98×10^{15}
$N(^4S) + N(^4S) + N_2 \rightarrow N_2 + N_2(A,B)$	2.54×10^{15}
$N(^4S) + NO_2 \rightarrow NO + NO$	2.29×10^{15}

IV.1.2. Temporal evolution of N(^{4}S) density

The evolutions of the density of atomic nitrogen in the ground and excited states together with the density of N_2(A) metastable are depicted in Figure A- 6 for a simulation performed in pure nitrogen. As can be seen, the density of N(^{4}S) remains constant. The same behavior is observed experimentally. It is surprising because as a first approach, one attempt to observe a fluctuating density with higher values when the discharge is one *i.e.* when electrons efficiently dissociates N_2 molecules.

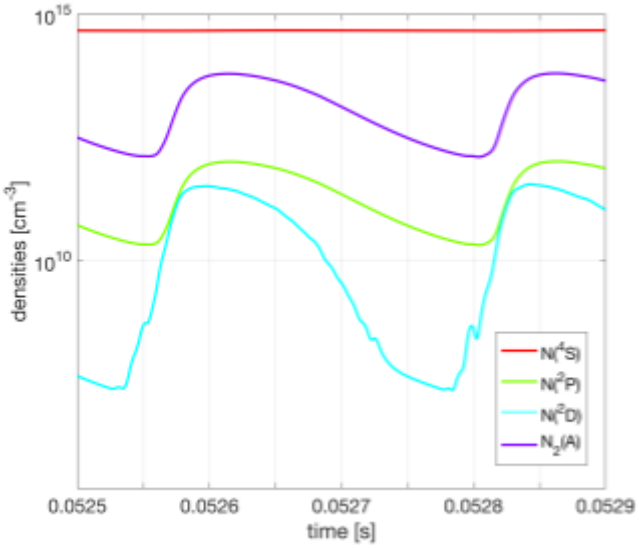

Figure A- 6 Temporal evolution of the densities of N(^{4}S), N(^{2}P), N(^{2}D) and N_2(A) provided by the model. Conditions: HV=17.1 kV_{pp}, f=2 kHz

To explain this trend, the rates of the main reactions involved in the production and destruction of N(^{4}S) atoms are depicted in Figure A- 7(a) and (b) respectively. The dissociation of N_2 molecules by electron impact is efficient only when the discharge is on *i.e.* when the electron density and the accelerating electric field are high enough. But the major part of N(^{4}S) atoms come from the quenching of excited N(^{2}P) (and N(^{2}D)) atoms. This channel is especially important just after the extinction of the discharge and then decreases until the next discharge. Concerning the destruction mechanisms, the excitation of N(^{4}S) atoms by N_2(A) metastable to produce N(^{2}P) (and N(^{2}D)) clearly dominates. One important point is that these two dominant channels of creation and destruction are strongly related to N_2(A) metastable and their rates are directly related to the N_2(A) density presented in Figure A- 6: they are maximum at $t \approx 0.0526\,s$ and minimum at $t \approx 0.0528\,s$. Consequently, when the density of N_2(A) is high, both the production and the destruction of N(^{4}S) are important. On the contrary for low N_2(A) concentrations, the production and destruction rates of N(^{4}S) are weak. The overall creation and destruction rates of N(^{4}S) are summarized in Figure A- 8. The small variations of N(^{4}S) density can thus be attributed to the quasi-equilibrium between the production and destruction of N(^{4}S) at each time.

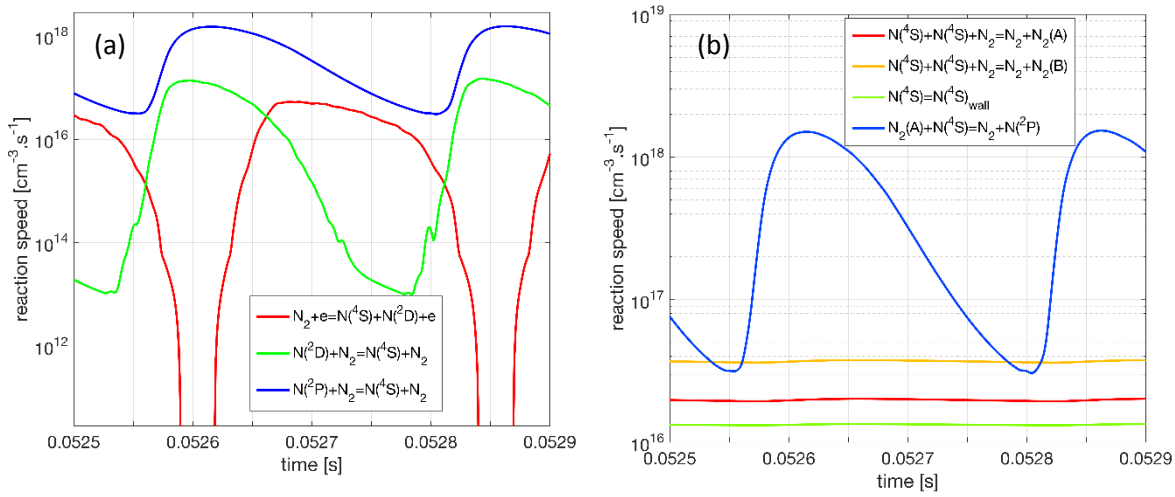

Figure A- 7 Main reactions rates involved in (a) the creation of N(^{4}S) (b) the destruction of N(^{4}S)

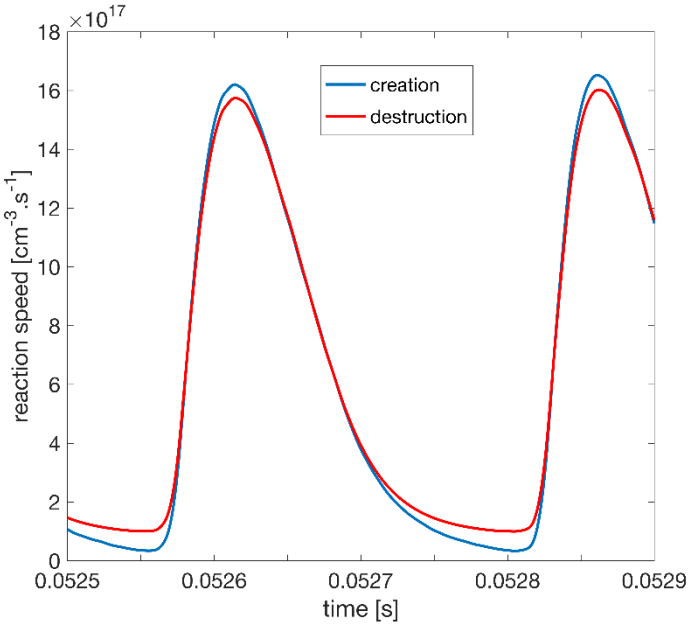

Figure A- 8 Overall creation and destruction rates of N(^{4}S)

IV.2.O(^{3}P) atoms

IV.2.1. Main mechanisms of production and destruction

IV.2.1.1. Production:

When O_2 is introduced in the discharge, the neutral oxygen chemistry starts with the dissociation of molecular oxygen to produce atomic oxygen, which then reacts to form other products such as NO for example. O_2 dissociation can be induced by direct electron impact or through collision with a metastable N_2(A) as indicated in Table A- 8. In our conditions, the electron-induced dissociation is found negligible compared to the dissociation induced by N_2(A). It can be explained by the very low mean electron density which is comprised between a few 10^7 and a few 10^8 cm^{-3} in the simulations depending on the conditions, compared to the averaged N_2(A) density which is around 10^{12}-10^{13} cm^{-3}.

With the appearance of NO molecules, their reduction by $N(^4S)$ becomes an important channel of $O(^3P)$ production.

Another important source of $O(^3P)$ comes from the quenching of metastable $O(^1D)$ atoms by N_2. Note that $O(^1D)$ mainly comes from the quenching of $O(^1S)$ which is itself produced by energy exchange between $N_2(A)$ and $O(^3P)$. $O(^1S)$ can also directly lead to a noticeable production of $O(^3P)$ through its reaction with excited molecular oxygen $O_2(a)$ or during its quenching by NO. The main reaction rates are given in Table A- 3.

Table A- 3 Main creation mechanisms for $O(^3P)$ atoms at 25 and 200 ppm

25 ppm		200 ppm	
Reaction	Production rate ($cm^{-3}.s^{-1}$)	Reaction	Production rate ($cm^{-3}.s^{-1}$)
$O(^1D) + N_2 \rightarrow O(^3P) + N_2$	1.95×10^{17}	$O(^1D) + N_2 \rightarrow O(^3P) + N_2$	3.06×10^{17}
$N(^4S) + NO \rightarrow N_2 + O(^3P)$	3.55×10^{16}	$N_2(A) + O_2 \rightarrow N_2 + O(^3P) + O(^3P)$	2.24×10^{17}
$N_2(A) + O_2 \rightarrow N_2 + O(^3P) + O(^3P)$	3×10^{16}	$N(^4S) + NO \rightarrow N_2 + O(^3P)$	5.93×10^{16}
$O(^1S) + O_2(a) \rightarrow O(^3P) + O_2(A)$	2.02×10^{16}	$O(^1S) + NO \rightarrow O(^3P) + NO$	5.56×10^{16}
$O(^1S) + O_2(a) \rightarrow 3\ O(^3P)$	1.58×10^{16}	$O(^1S) + O_2(a) \rightarrow O(^3P) + O_2(A)$	3.97×10^{16}

IV.2.1.2. Destruction:

Whatever the concentration of oxygen, the dominant mechanism responsible for the destruction of $O(^3P)$ is the reaction $N_2(A) + O(^3P) \rightarrow N_2 + O(^1S)$. The reaction $N_2(A) + O(^3P) \rightarrow NO + N(^2D)$ also plays an important role. The other mechanisms involved in the destruction of $O(^3P)$ are different depending on the oxygen concentration. Higher oxygen concentrations lead to higher concentration of NO and NO_2 which can react efficiently with oxygen atoms. Other oxidizing species such as O_3, NO_3, N_2O_4 and N_2O_5 are produced in too small amount at these low oxygen concentrations (maximum 200 ppm) to play a significant role in the overall chemistry. The dominant reactions and their corresponding destruction rates are given in Table A- 4 for 25 and 200 ppm.

Table A- 4 Main destruction mechanisms of $O(^3P)$ atoms for 25 and 200 ppm

25 ppm		200 ppm	
Reaction	Destruction rate($cm^{-3}.s^{-1}$)	Reaction	Destruction rate($cm^{-3}.s^{-1}$)
$N_2(A) + O(^3P) \rightarrow N_2 + O(^1S)$	2.28×10^{17}	$N_2(A) + O(^3P) \rightarrow N_2 + O(^1S)$	3.65×10^{17}
$N_2(A) + O(^3P) \rightarrow NO + N(^2D)$	5.31×10^{16}	$O(^3P) + O(^3P) + N_2 \rightarrow O_2(X, a, b) + N_2$	9.34×10^{16}
$N(^4S) + O(^3P) + N_2 \rightarrow NO + N_2$	1.7×10^{16}	$N_2(A) + O(^3P) \rightarrow NO + N(^2D)$	8.52×10^{16}
$O(^3P) + O(^3P) + N_2 \rightarrow O_2(X, a, b) + N_2$	1.7×10^{16}	$O(^3P) + NO + N_2 \rightarrow NO_2 + N_2$	6.42×10^{16}

$O(^3P) + NO + N_2 \rightarrow NO_2 + N_2$	1.02×10^{16}	$O(^3P) + NO_2 \rightarrow NO + O_2$	5.7×10^{16}
$O(^3P) + NO_2 \rightarrow NO + O_2$	6.69×10^{15}	$O(^3P) + O_2 + N_2 \rightarrow N_2 + O_3$	5.1×10^{16}
$O(^3P) + O_2 + N_2 \rightarrow N_2 + O_3$	2.01×10^{15}	$N(^4S) + O(^3P) + N_2 \rightarrow NO + N_2$	2.48×10^{16}

IV.2.2. Temporal evolution of $O(^3P)$ density

The evolution of the $O(^3P)$ density obtained for a simulation performed at 200 ppm of O_2 is depicted in Figure A- 9. As for the case of $N(^4S)$, the density of $O(^3P)$ appears to be rather constant in time. The same behavior is observed experimentally. To understand this, the same approach has been used. The main reaction rates for the creation and destruction mechanism of $O(^3P)$ are depicted in Figure A- 10(a) and (b) respectively. $O(^3P)$ atoms are mostly produced through O_2 dissociation by $N_2(A)$ or by the quenching of $O(^1D)$ or $O(^1S)$ atoms which are themselves produced by $N_2(A)$. Thus the creation of $O(^3P)$ is strongly related to the $N_2(A)$ density. Concerning the destruction of $O(^3P)$, it mainly arises during collisions between $O(^3P)$ and $N_2(A)$ to produce $O(^1S)$ or $O(^1D)$. Thus, as for the case of $N(^4S)$, the creation and destruction of $O(^3P)$ atoms are mainly ruled by the $N_2(A)$ density and consequently their rate are close to the equilibrium at each time resulting in a quasi-constant $O(^3P)$ density. Figure A- 11 represents the temporal evolution of the overall creation and destruction rates of $O(^3P)$.

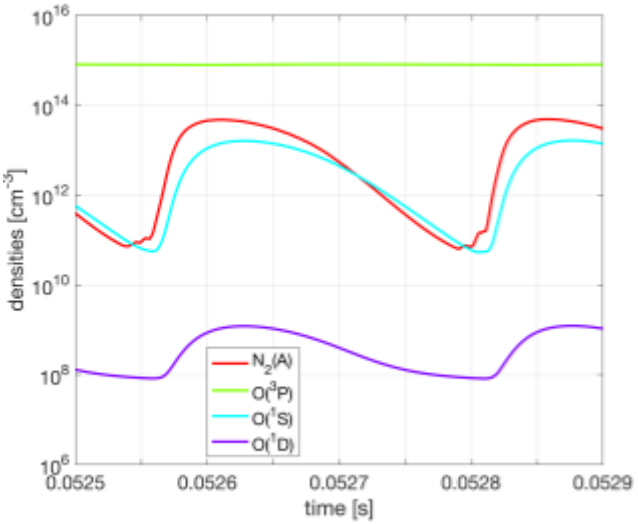

Figure A- 9 Temporal evolution of the density of $O(^3P)$, $O(^1S)$, $O(^1D)$ and $N_2(A)$ obtained from a simulation. Conditions: HV=17.1 kV_{PP}, f=2 kHz, concentration of O_2=200 ppm

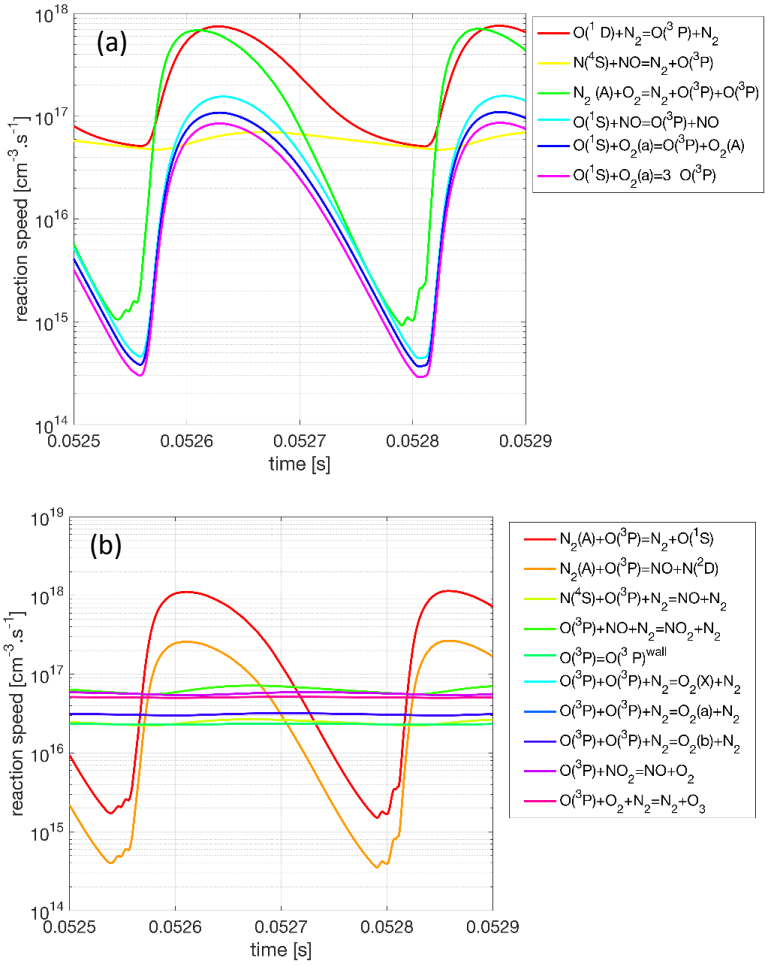

Figure A- 10 Main reactions rates involved in (a) the creation of O(^{3}P) atoms and (b) the destruction of O(^{3}P) atoms

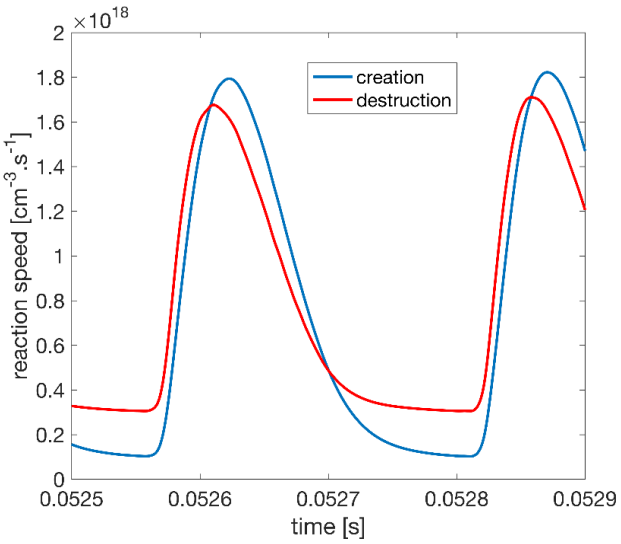

Figure A- 11 Overall creation and destruction rates of O(^{3}P) atoms

IV.3.NO(X) molecules

IV.3.1. Production

It is well known (see *e.g.* [63]) that NO can be very efficiently produced by the so called Zel'dovich reactions given by :

$N_2 + O(^3P) \rightarrow NO + N(^4S)$	(R6)
$N(^4S) + O_2 \rightarrow NO + O(^3P)$	(R7)

Since reaction (R6) has a large activation energy of 3.27 eV, it requires highly energetic particles or N_2 molecules in a highly excited vibrational state $N_2(X,v>12)$ to be effective. This can be obtained in high temperature medium *e.g.* in combustion systems or in low-pressure plasmas where N_2 molecules can be vibrationally excited by electrons without experiencing a high quenching [94]. Nevertheless, in our conditions the temperature remains close to 300K and the quenching rate is large so that reaction (R6) is unlikely. Moreover the population of the vibrationnally excited levels of nitrogen is not considered in the model, so that this reaction is not taken into account. Finally, only electronically excited nitrogen molecules are able to overcome the activation barrier making the reaction $N_2(A) + O(^3P) \rightarrow NO + N(^2D)$ dominant in our conditions.

Reaction (R7) requires a lower activation energy (0.27 eV) and is considered to be significant in DBD discharges [63]. Nevertheless, it is found negligible in our conditions due to the very low gas temperature. The activation energy can be brought by electronically excited atoms ($N(^2D)$ and $N(^2P)$) or by electronically excited $O_2(a)$ molecules. Herron *et al.* [110] found that NO is primary formed by the reaction $N(^2D) + O_2 \rightarrow NO + O(^3P)$. Nevertheless, the results of the model clearly indicate that the corresponding rates remain small in our conditions.

To summarize, in our conditions, the main production mechanism of NO molecules is $N_2(A) + O(^3P) \rightarrow NO + N(^2D)$. For low oxygen concentration (25ppm), the second dominant reaction is the three-body recombination $N(^4S) + O(^3P) + N_2 \rightarrow NO + N_2$ whereas it is $O(^3P) + NO_2 \rightarrow NO + O_2$ for 200 ppm. Their respective reaction rates are given in Table A- 4.

IV.3.2. Destruction

NO molecules are mainly destroyed during their reduction by $N(^4S)$ atoms through the reaction $N(^4S) + NO \rightarrow N_2 + O(^3P,^1D)$. At high oxygen concentration, the reaction $O(^3P) + NO + N_2 \rightarrow NO_2 + N_2$ becomes significant but remains slower than NO reduction.

IV.4.Summary

Based on the previous analysis, a summary of the main reactions related to the production and destruction of $N(^4S)$, $O(^3P)$ and NO(X) is proposed by Figure A- 12.

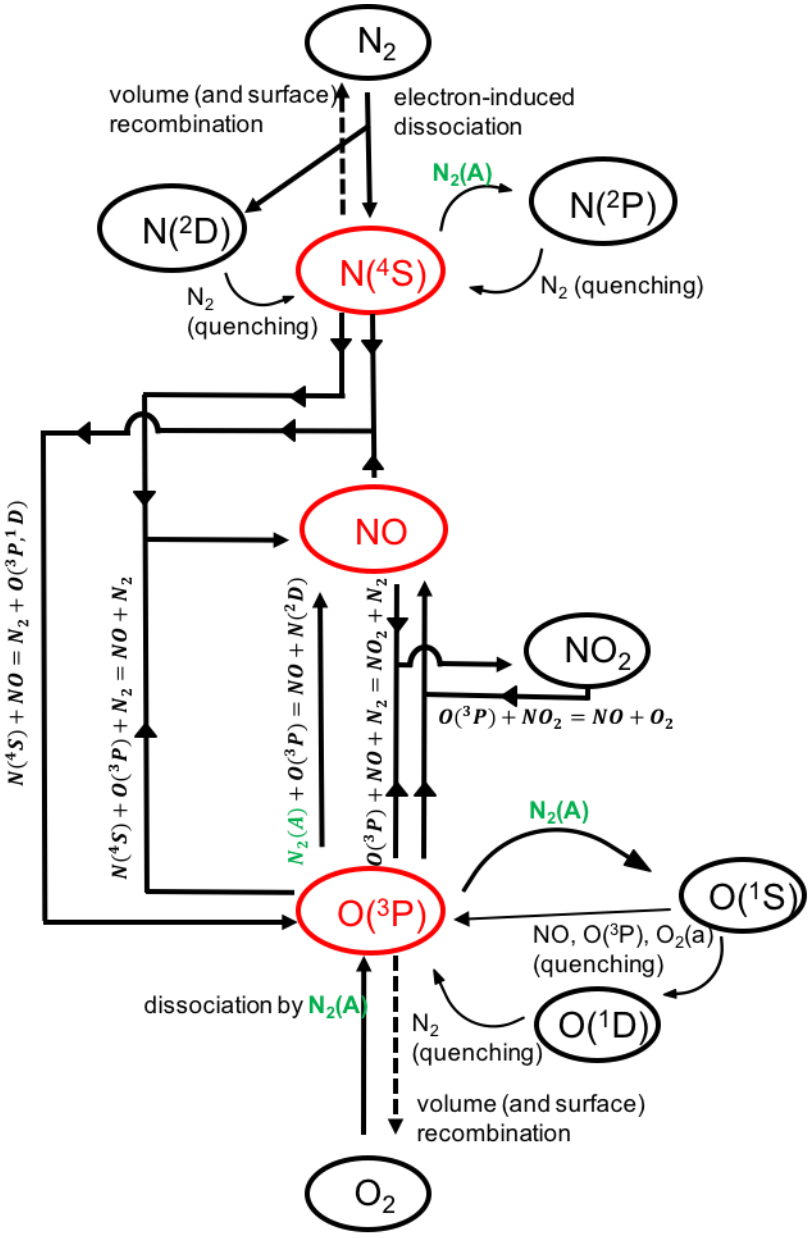

Figure A- 12 Main reactions involved in the production and destruction of N(⁴S), O(³P) and NO(X)

V. Order of magnitude of the densities of the main species of interest for different oxygen concentration

The aim of this part is to provide order of magnitudes for the density of some species of interest: N(^{4}S), O(^{3}P) and NO since they are measured by laser spectroscopy in the present work, O(^{1}S) because it is directly related to the O(^{1}S)N_2 green band emission measured by OES, N_2(A) and N(^{2}P) because of their important role in the associative ionization reaction. Figure A- 13 present the results provided by the model for different oxygen concentration at a constant applied voltage of 17.1 kV_{PP}. Note that the densities presented here correspond to the values obtained at the stationary state and between two successive discharges *i.e.* when the polarity of the gas gap voltage Vg reverses.

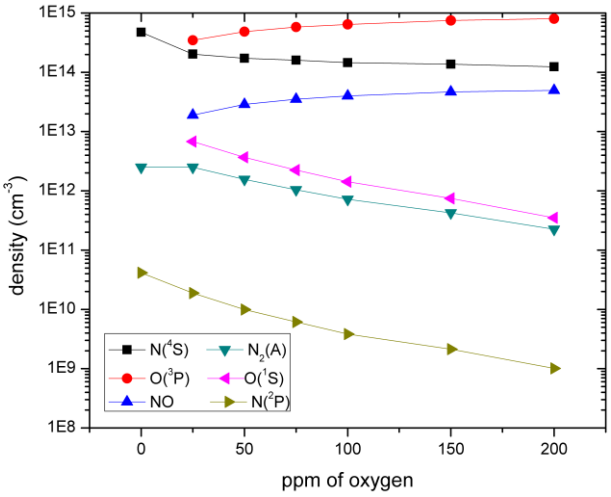

Figure A- 13 Densities between two successive discharges obtained from the model for different oxygen concentrations. Conditions: HV=17.1 kV_{PP}, f=2 kHz

The density of $N(^4S)$ is 4.7 10^{14} cm^{-3} in pure nitrogen. It continuously decreases as the oxygen concentration increases to reach 1.24 10^{14} at 200 ppm of O_2. It can be explained by a higher consumption of $N(^4S)$ by NO molecules (see section IV.1). On the other hand, the densities of $O(^3P)$ and NO increases from 3.5 10^{14} cm^{-3} and 1.9 10^{13} cm^{-3} at 25 ppm to 8 10^{14} cm^{-3} and 5 10^{13} cm^{-3} at 200 ppm respectively.

It is interesting to note that these evolutions are not directly correlated to the evolution of the $O(^1S)N_2$ green band and NOγ system emissions. Indeed, they decrease when the concentration of O_2 increases as indicated in Figure A- 5(a) and (b). It can be explained by the fact that these emissions are not only related to the density of species in the ground state but also to the $N_2(A)$ concentration which is responsible for their excitation. Moreover, these emitting species can also be quenched before they emit radiations. Thus one has to be careful when interpreting the data of OES and all the aforementioned processes have to be considered [111]. The density of $N_2(A)$ decreases from 2.5 10^{12} cm^{-3} at 0 and 25 ppm to 2.2 10^{11} cm^{-3} at 200 ppm. Indeed, $N_2(A)$ is efficiently destroyed by $O(^3P)$ atoms, O_2, and NO molecules. Consequently, the density of $O(^1S)$ also decreases from 6.8 10^{12} cm^{-3} to 3.5 10^{11} cm^{-3}. Thus in our conditions, it seems that the decrease of the $N_2(A)$ density overcomes the increase of $O(^3P)$ density resulting in a decreasing $O(^1S)$ density for higher oxygen concentrations. The same conclusions stand for NO(A) and NO(X). Finally, since both the $N_2(A)$ and $N(^4S)$ densities decrease, the density of $N(^2P)$ also decreases from 4.2 10^{10} cm^{-3} to 1 10^{9} cm^{-3} between 0 and 200 ppm.

The calculated densities of $N(^4S)$, $O(^3P)$ and NO have similar evolution with respect the input O_2 concentration compared to experimental measurements presented in chapter 3,4 and 5. The $N(^4S)$ density continuously decreases as the concentration of O_2 increases whereas the densities of $O(^3P)$ and NO increase. Moreover, this increase is more important for low oxygen concentration than for high concentration. Following the results of the model, it can be ascribed to the decrease of the $N_2(A)$ concentration as the O_2 concentration increases. Indeed, it appears that nitrogen metastable species play a very important role in the chemistry of oxidizing species since it is directly involved in the formation of $O(^3P)$ and NO.

Concerning the absolute values of the densities, numerical and experimental results are in good agreement for N(^{4}S). Nevertheless, the model overestimate the density of O(^{3}P) by a factor 2-3. The discrepancy is even more important concerning the NO densities. The calculated densities are 10 times higher than experimental values.

VI. Additional investigations and discussions

VI.1. Influence of the reaction $\mathbf{N_2(A) + O(^3P) \rightarrow NO + N(^2D)}$ on the formation of NO

In [50,112] the quenching of N_2(A) by O(^{3}P) for low vibrational levels of N_2(A) was found to lead essentially to the formation of O(^{1}S). NO production by this reaction becomes significant only for vibrational levels of N_2(A) greater than v=3. At atmospheric pressure, the redistribution of N_2(A) occurs very quickly due to collisions and one can assume that only the vibrational levels v=0,1 are significantly populated. To investigate this effect onto the production of NO, calculations were performed without the reaction $\mathrm{N_2(A) + O(^3P) \rightarrow NO + N(^2D)}$. Let us consider a simulation performed at 25 ppm of O_2 for an applied voltage of 17.1 kV_{pp}. For this example, suppressing this reaction results in a decrease of the NO density between two successive discharges from 1.7 10^{13} cm^{-3} to 5.5 10^{12} cm^{-3}. This is closer to the experimental value of 6 10^{11} cm^{-3} but the NO density remains greatly overestimated by the model. It shows that the consideration of the reaction $\mathrm{N_2(A) + O(^3P) \rightarrow NO + N(^2D)}$ alone is not able to fully explain the discrepancies between simulations and experiments.

VI.2. Influence of the rate coefficient of reaction $\mathbf{N(^2P) + N_2 \rightarrow N_2 + N(^4S,^2D)}$

All the simulation results presented in this appendix were obtained considering the reaction $\mathrm{N(^2P) + N_2 \rightarrow N_2 + N(^4S)}$ with the rate 6 10^{-14} cm^3s^{-1} (see *e.g.* [83,113]). Nevertheless, this reaction is not present in the set of reactions used by many authors. For example, Kossyi *et al.* [98] or N.A.Popov [57] consider that N(^{2}P) atoms are quenched by the following reaction $\mathrm{N(^2P) + N_2 \rightarrow N_2 + N(^2D)}$ with the small rate 2 10^{-18} cm^3s^{-1}. J. T. Herron [96] consider the same reaction $\mathrm{N(^2P) + N_2 \rightarrow N_2 + N(^4S)}$ but with a very different rate of 5 10^{-17} cm^3s^{-1}. In recent investigations [103] a rate of 3 10^{-17} cm^3s^{-1} was found, in good agreement with the value proposed by J. T. Herron. Thus, to investigate the effect of such reactions, calculations were performed considering these smaller reaction rates and the obtained results were found to be substantially different from the present ones. Table A- 5 provides a comparison of the results obtained with 25 ppm of O_2 and HV=17.1 kV_{PP}, f=2 kHz, considering to different rates for the quenching reaction of N(^{2}P).

Table A- 5 Comparison of the densities obtained between two successive discharges from simulations with different reaction rate for the quenching of N($_2$P) by N_2. Conditions: 25 ppm of O_2, 17.1 kV_{pp}

Species	$k = 6.0 \times 10^{-14}$ cm^3s^{-1}	$k = 5.0 \times 10^{-17}$ cm^3s^{-1}
N(^{4}S)	$2 \times 10^{14}\ cm^{-3}$	$3.5 \times 10^{13}\ cm^{-3}$
O(^{3}P)	$3.8 \times 10^{14}\ cm^{-3}$	$2.1 \times 10^{14}\ cm^{-3}$
NO(X)	$2 \times 10^{13}\ cm^{-3}$	$7.5 \times 10^{13}\ cm^{-3}$
N(^{2}P)	$1.7 \times 10^{10}\ cm^{-3}$	$6 \times 10^{12}\ cm^{-3}$

As can be seen, the N(^{2}P) density is approximately two orders of magnitude higher for the lower quenching rate. Moreover, lowering the rate of this reaction induces a drop of the N(^{4}S) density, whereas the NO and O(^{3}P) density increase.

Deeper investigations revealed what happened. The first consequence is direct: lowering the quenching of N(^{2}P) considerably reduces the amount of N(^{4}S) atoms produced by the quenching of

N(^{2}P). Second, the rate of the associative ionization reaction $N(^2P) + O(^3P) \rightarrow NO^+ + e^-$ increases because of the higher N(^{2}P) density. The neutralization of NO^+ ions to the wall produces a large amount of NO molecules. Consequently, the reduction of NO by N(^{2}P), $N(^2P) + NO \rightarrow O(^3P,^1D) + N_2$, becomes very large which results in a higher production of O(^{3}P). As a conclusion, the equilibrium between N, O and NO density is shifted towards lower density of N(^{4}S) and higher densities of O and NO. Note that these results are in worse agreement with experimental results. The strong dependence of the results with the reaction rate for the quenching of N(^{2}P) by N_2 is of primary importance because the rate of the associative ionization reactions is considerably dependent on the amount of N(^{2}P) in the discharge. This point is discussed in details in chapter 6 section III.4.

Another important consequence of the lowering of the quenching rate of N(^{2}P) by N_2 concerns the ion density. Indeed, the strong increase of the rates of the associative ionization reactions produces a large amount of ions. As a consequence, the total ion density provided by the model increases reaching non-realistic values around 10^{11} cm^{-3}. The maximum of the ion density is reached between two successive discharges, *i.e.* when the electric field is too low to evacuate the ions, contrary to the previous situation. This is illustrated in Figure A- 14, which represents the time varying ion density for the two sets of simulations presented above.

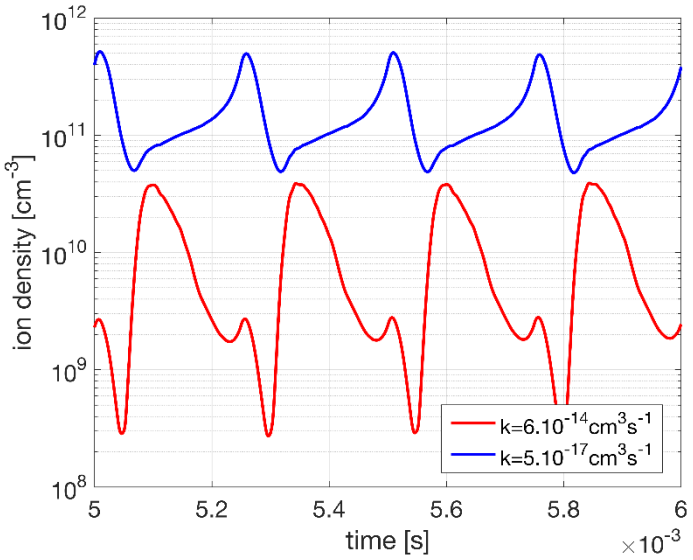

Figure A- 14 ion density obtained for two different values of the quenching rate of N(^{2}P). Conditions: concentration of O_2=25 ppm, HV=17.1 kV_{pp}

It is worthwhile to mention that it is not possible to conclude from these results that the value of 5 10^{-17}cm^{3}s^{-1} for the quenching of N(^{2}P) by N_2 is incorrect. Indeed, the present model is based on the assumption that all the current is due to electrons, which is used to calculate the electron density from the experimental value of the discharge current. Taking into account the ion contribution to the current in a self-consistent way would considerably reduce the electron density especially in the case of high ion densities. A lower electron density would imply a lower excitation and ionization rate thus producing more consistent results.

Table A- 6 Reactions involving nitrogen species

Reaction		Rate constant (s^{-1}, cm^3s^{-1}, cm^6s^{-1})	Reference
Ionization, excitation and dissociation by electron impact			
$\mathbf{e^- + N_2 \rightarrow e^- + N_2(A, B, C, a')}$ +inverse	(1)	from EEDF	[83]
$\mathbf{e^- + N_2 \rightarrow e^- + e^- + N_2^+}$ +inverse	(2)	from EEDF	[83]
$\mathbf{e^- + N_2 \rightarrow e^- + e + N^+ + N}$ +inverse	(3)	from EEDF	[83]
$\mathbf{e^- + N_2 \rightarrow e^- + N(^4S) + N(^2D)}$ +inverse	(4)	from EEDF	[83]
$\mathbf{e^- + N(^4S) \rightarrow N(^2P,\ ^2D) + e^-}$ +inverse	(5)	from EEDF	[21]
Associative ionization			
$\mathbf{N_2(A) + N_2(a') \rightarrow N_4^+ + e^-}$	(6)	4.0×10^{-12}	[83]
$\mathbf{N_2(a') + N_2(a') \rightarrow N_4^+ + e^-}$	(7)	1.0×10^{-11}	[83]
$\mathbf{N(^2P) + N(^2P) \rightarrow N_2^+ + e^-}$	(8)	1.5×10^{-11}	[57,98]
Electron-ion recombination			
$\mathbf{e^- + A^+ + N_2 \rightarrow A + N_2}$ where A^+=N^+,N_2^+	(9)	$6.0 \times 10^{-27} \times (300/T_e)^{1.5}$	[98]
$\mathbf{{N_2}^+ + e^- \rightarrow N(^4S) + N(^4S)}$	(10)	$9.0 \times 10^{-8} \times (300/T_e)^{0.39}$	[83]
$\mathbf{{N_2}^+ + e^- \rightarrow N(^4S) + N(^2D)}$	(11)	$8.1 \times 10^{-8} \times (300/T_e)^{0.39}$	[83]
$\mathbf{{N_2}^+ + e^- \rightarrow N(^4S) + N(^2P)}$	(12)	$9.0 \times 10^{-9} \times (300/T_e)^{0.39}$	[83]
$\mathbf{{N_3}^+ + e^- \rightarrow N_2 + N(^4S)}$	(13)	$2.0 \times 10^{-7} \times (300/T_e)^{0.5}$	[83]
$\mathbf{{N_4}^+ + e^- \rightarrow N_2 + N_2}$	(14)	$2.3 \times 10^{-6} \times (300/T_e)^{0.53}$	[83]
Ion conversion			
$\mathbf{N^+ + N_2 + N(^4S) \rightarrow N_2^+ + N_2}$	(15)	1.7×10^{-29}	[83]
$\mathbf{N^+ + N_2 + N_2 \rightarrow N_3^+ + N_2}$	(16)	$1.7 \times 10^{-29} \times (300/T_{eff})^{2.1}$	[83]
$\mathbf{{N_2}^+ + N(^4S) \rightarrow N^+ + N_2}$	(17)	$7.2 \times 10^{-13} \times (T_{eff}/300)$	[83]
$\mathbf{{N_2}^+ + N_2\,(A) \rightarrow {N_3}^+ + N(^4S)}$	(18)	3.0×10^{-10}	[83]
$\mathbf{{N_2}^+ + N_2 + N(^4S) \rightarrow {N_3}^+ + N_2}$	(19)	$9.0 \times 10^{-30} \times \exp(400/T_{eff})$	[83]
$\mathbf{{N_2}^+ + N_2 + N_2 \rightarrow {N_4}^+ + N_2}$	(20)	$5.2 \times 10^{-29} \times (300/T_{eff})^{2.2}$	[83]
$\mathbf{{N_3}^+ + N(^4S) \rightarrow {N_2}^+ + N_2}$	(21)	6.6×10^{-11}	[83]
$\mathbf{{N_4}^+ + N(^4S) \rightarrow N^+ + N_2 + N_2}$	(22)	1.0×10^{-11}	[83]
$\mathbf{{N_4}^+ + N_2 \rightarrow {N_2}^+ + N_2 + N_2}$	(23)	$2.1 \times 10^{-16} \times \exp(T_{eff}/121)$	[83]
Excited species conversion			
$\mathbf{N_2(B) \rightarrow N_2(A) + h\nu}$	(24)	1.3×10^5	[83]
$\mathbf{N_2(C) \rightarrow N_2(B) + h\nu}$	(25)	2.5×10^7	[83]
$\mathbf{N_2(a') \rightarrow N_2 + h\nu}$	(26)	1.0×10^2	[83]
$\mathbf{N_2(A) + N(^4S) \rightarrow N_2 + N(^4S)}$	(27)	2.0×10^{-12}	[83]
$\mathbf{N_2(A) + N(^4S) \rightarrow N_2 + N(^2P)}$	(28)	$4.0 \times 10^{-11} \times (300/T)^{2/3}$	[83]
$\mathbf{N_2(A) + N_2 \rightarrow N_2 + N_2}$	(29)	3.0×10^{-16}	[83]
$\mathbf{N_2(A) + N_2(A) \rightarrow N_2 + N_2(B)}$	(30)	3.0×10^{-10}	[83]
$\mathbf{N_2(A) + N_2(A) \rightarrow N_2 + N_2(C)}$	(31)	1.5×10^{-10}	[83]
$\mathbf{N_2(B) + N_2 \rightarrow N_2 + N_2}$	(32)	2.0×10^{-12}	[83]
$\mathbf{N_2(B) + N_2 \rightarrow N_2(A) + N_2}$	(33)	3.0×10^{-11}	[83]
$\mathbf{N_2(C) + N_2 \rightarrow N_2(a') + N_2}$	(34)	1.0×10^{-11}	[83]
$\mathbf{N_2(a') + N_2 \rightarrow N_2(B) + N_2}$	(35)	1.9×10^{-13}	[83]]
$\mathbf{N(^2D) + N_2 \rightarrow N_2 + N(^4S)}$	(36)	$2.3 \times 10^{-14} \times \exp(-510/T)$	[83]
$\mathbf{N(^2P) + N_2 \rightarrow N_2 + N(^2D)}$	(37)	2.0×10^{-18}	[83]
$\mathbf{N(^2P) + N_2 \rightarrow N_2 + N(^4S)}$	(38)	6.0×10^{-14}	[83]
$\mathbf{N(^2P) + N(^4S) \rightarrow N(^2D) + N(^4S)}$	(39)	6.0×10^{-13}	[83]
$\mathbf{N(^2P) + N(^4S) \rightarrow N(^4S) + N(^4S)}$	(40)	1.8×10^{-12}	[83]
$\mathbf{N(^4S) + N(^4S) + N_2 \rightarrow N_2 + N_2(A)}$	(41)	1.7×10^{-33}	[83]
$\mathbf{N(^4S) + N(^4S) + N_2 \rightarrow N_2 + N_2(B)}$	(42)	2.4×10^{-33}	[83]

Table A- 7 Reactions involving oxygen species

Reaction		Rate constant (s^{-1}, cm^3s^{-1}, cm^6s^{-1})	Reference
Excitation and dissociation by electron impact			
$\mathbf{O_2 + e^- \rightarrow O(^3P) + O(^3P,\ ^1D) + e^-}$ +inverse	(43)	from EEDF	[108]
$\mathbf{O_2 + e^- \rightarrow O_2(a,b) + e^-}$ +inverse	(44)	from EEDF	[98]
$\mathbf{O(^3P) + e^- \rightarrow O(^1D,\ ^1S) + e^-}$ +inverse	(45)	from EEDF	[98]
Neutral reactions involving ground state particles			
$\mathbf{O(^3P) + O(^3P) + O_2 \rightarrow O_2(X,a,b) + O_2}$	(46)	$2.45 \times 10^{-31} \times T^{-0.63}$	[98]
$\mathbf{O(^3P) + O_2 + O_2 \rightarrow O_3 + O_2}$	(47)	$6.9 \times 10^{-34} \times (300/T)^{1.25}$	[98]
$\mathbf{O(^3P) + O_3 \rightarrow O_2 + O_2}$	(48)	$2.0 \times 10^{-11} \times \exp(-2300/T)$	[98]
Neutral reactions involving electronically excited particles			
$\mathbf{O(^1S) + O(^3P) \rightarrow O(^1D) + O(^3P)}$	(49)	$5.0 \times 10^{-11} \times \exp(-301/T)$	[98]
$\mathbf{O(^1S) + O_2(a) \rightarrow 3\ O(^3P)}$	(50)	3.4×10^{-11}	[98]
$\mathbf{O(^1S) + O_3 \rightarrow O_2 + O_2}$	(51)	2.9×10^{-10}	[98]
$\mathbf{O(^1S) + O_2(a) \rightarrow O(^3P) + O_2(A)}$	(52)	1.3×10^{-10}	[98]
$\mathbf{O(^1S) + O_3 \rightarrow O(^1D) + O(^3P) + O_2}$	(53)	2.9×10^{-10}	[98]
$\mathbf{O(^1S) + O_2 \rightarrow O(^3P) + O_2}$	(54)	$3.0 \times 10^{-12} \times \exp(-850/T)$	[98]
$\mathbf{O(^1S) + O_2(a) \rightarrow O(^1D) + O_2(b)}$	(55)	3.6×10^{-11}	[98]
$\mathbf{O(^1S) + O_2 \rightarrow O(^1D) + O_2}$	(56)	$1.3 \times 10^{-12} \times \exp(-850/T)$	[57]
$\mathbf{O(^1D) + O_2 \rightarrow O(^3P) + O_2}$	(57)	$6.4 \times 10^{-12} \times \exp(67/T)$	[98]
$\mathbf{O(^1D) + O_3 \rightarrow O_2 + O_2}$	(58)	1.2×10^{-10}	[[98]
$\mathbf{O(^1D) + O_3 \rightarrow O(^3P) + O(^3P) + O_2}$	(59)	1.2×10^{-10}	[98]
$\mathbf{O(^1D) + O(^3P) \rightarrow O(^3P) + O(^3P)}$	(60)	8×10^{-12}	[57,98]
$\mathbf{O(^1D) + O_2 \rightarrow O(^3P) + O_2(b)}$	(61)	$3.2 \times 10^{-11} \times \exp(67/T)$	[57,98]
$\mathbf{O_2(a) + O_3 \rightarrow O_2 + O_2 + O(^3P)}$	(62)	$9.7 \times 10^{-13} \times \exp(-1564/T)$	[98]
$\mathbf{O_2(a) + O_2 \rightarrow O_2 + O_2}$	(63)	$2.2 \times 10^{-18} \times (T/300)^{0.8}$	[98]
$\mathbf{O_2(a) + O(^3P) \rightarrow O_2 + O(^3P)}$	(64)	7×10^{-16}	[98]
$\mathbf{O_2(b) + O_2 \rightarrow O_2(a) + O_2}$	(65)	$4.3 \times 10^{-22} \times T^{2.4} \times \exp(-241/T)$	[98]
$\mathbf{O_2(b) + O(^3P) \rightarrow O_2(a) + O(^3P)}$	(66)	8×10^{-14}	[98]
$\mathbf{O_2(b) + O(^3P) \rightarrow O_2 + O(^1D)}$	(67)	$3.39 \times 10^{-11} \times (300/T)^{0.1} \times \exp(-4201/T)$	[98]
$\mathbf{O_2(b) + O_3 \rightarrow O_2 + O_2 + O(^3P)}$	(68)	1.8×10^{-11}	[98]
$\mathbf{O_2(A) + O_2 \rightarrow O_2(b) + O_2(b)}$	(69)	2.9×10^{-13}	[98]
$\mathbf{O_2(A) + O(^3P) \rightarrow O_2(b) + O(^1D)}$	(70)	9×10^{-12}	[98]

Table A- 8 Reactions involving both nitrogen and oxygen species

Reaction		Rate constant (s^{-1}, cm^3s^{-1}, cm^6s^{-1})	Reference
Neutral reactions involving ground state particles			
$\mathbf{N(^4S) + O(^3P) + N_2 \rightarrow NO + N_2}$	(71)	$1.76 \times 10^{-31} \times T^{-0.5}$	[98]
$\mathbf{N(^4S) + NO \rightarrow N_2 + O(^3P,^1D)}$	(72)	$1.05 \times 10^{-12} \times T^{0.5}$	[57]
$\mathbf{N(^4S) + O_2 \rightarrow NO + O(^3P)}$	(73)	$1.1 \times 10^{-14} \times T \times \exp(-3150/T)$	[98]
$\mathbf{N(^4S) + NO_2 \rightarrow N_2 + O(^3P) + O(^3P)}$	(74)	9.1×10^{-13}	[98]
$\mathbf{N(^4S) + NO_2 \rightarrow N_2O + O(^3P)}$	(75)	3×10^{-12}	[98]
$\mathbf{N(^4S) + NO_2 \rightarrow NO + NO}$	(76)	2.3×10^{-12}	[98]
$\mathbf{N(^4S) + NO_2 \rightarrow N_2 + O_2}$	(77)	7×10^{-13}	[98]
$\mathbf{N(^4S) + O_3 \rightarrow NO + O_2}$	(78)	2×10^{-16}	[98]
$\mathbf{O(^3P) + O(^3P) + N_2 \rightarrow N_2 + O_2(X,a,b)}$	(79)	$2.76 \times 10^{-34} \times \exp(720/T)$	[98]
$\mathbf{O(^3P) + O_2 + N_2 \rightarrow N_2 + O_3}$	(80)	$6.2 \times 10^{-34} \times (300/T)^2$	[98]

$O(^3P) + NO + N_2 \rightarrow NO_2 + N_2$	(81)	6.51×10^{-32} for T=300K	[98]
$O(^3P) + NO_2 + N_2 \rightarrow NO_3 + N_2$	(82)	8.49×10^{-32} for T=300K	[98]
$O(^3P) + NO_2 \rightarrow NO + O_2$	(83)	$1.13 \times 10^{-11} \times (T/1000)^{0.18}$	[98]
$O(^3P) + NO_3 \rightarrow O_2 + NO_2$	(84)	1×10^{-11}	[98]
$NO + O_3 \rightarrow O_2 + NO_2$	(85)	$4.3 \times 10^{-12} \times \exp(-1560/T)$	[98]
$NO + NO_3 \rightarrow NO_2 + NO_2$	(86)	1.7×10^{-11}	[98]
$NO_2 + O_3 \rightarrow O_2 + NO_3$	(87)	$1.2 \times 10^{-13} \times \exp(-2450/T)$	[98]
$NO_2 + NO_3 \rightarrow NO + O_2 + NO_2$	(88)	$2.3 \times 10^{-13} \times \exp(-1600/T)$	[98]
$NO_2 + NO_2 + N_2 \rightarrow N_2O_4 + N_2$	(89)	2.5×10^{-35}	[98]
$NO_2 + NO_3 + N_2 \rightarrow N_2O_5 + N_2$	(90)	2.31×10^{-33}	[98]
$NO_3 + NO_3 \rightarrow O_2 + NO_2 + NO_2$	(91)	$5 \times 10^{-12} \times \exp(-3000/T)$	[98]
Neutral reactions involving electronically excited particles			
$N_2(A) + O_2 \rightarrow N_2 + O(^3P) + O(^3P)$	(92)	1.7×10^{-12}	[57,98]
$N_2(A) + O_2 \rightarrow N_2 + O_2(b)$	(93)	7.5×10^{-13}	[57,98]
$N_2(A) + NO \rightarrow N_2 + NO$	(94)	6.4×10^{-11}	[57,98]
$N_2(A) + O(^3P) \rightarrow NO + N(^2D)$	(95)	7×10^{-12}	[98]
$N_2(A) + O(^3P) \rightarrow N_2 + O(^1S)$	(96)	3×10^{-11}	[57,98]
$N_2(A) + O_2 \rightarrow N_2O + O(^3P)$	(97)	7.8×10^{-14}	[98]
$N_2(A) + N_2O \rightarrow N_2 + N(^4S) + NO$	(98)	1×10^{-11}	[98]
$N_2(A) + NO_2 \rightarrow N_2 + NO + O(^3P)$	(99)	1.3×10^{-11}	[98]
$N_2(B) + NO \rightarrow N_2(A) + NO$	(100)	2.4×10^{-10}	[98]
$N_2(B) + O_2 \rightarrow N_2 + O(^3P) + O(^3P)$	(101)	3×10^{-10}	[57,98]
$N_2(a) + NO \rightarrow N_2 + N(^4S) + O(^3P)$	(102)	3.6×10^{-10}	[98]
$N_2(a) + O_2 \rightarrow N_2 + O(^3P) + O(^1D)$	(103)	2.8×10^{-11}	[57]
$N_2(C) + O_2 \rightarrow N_2 + O(^3P) + O(^1S)$	(104)	3×10^{-10}	[98]
$N(^2P) + O(^3P) \rightarrow N(^2D) + O(^3P)$	(105)	1×10^{-12}	[57]
$N(^2P) + O_2 \rightarrow O(^3P,^1D) + NO$	(106)	2.5×10^{-12}	[57]
$N(^2P) + NO \rightarrow O(^3P,^1D) + N_2$	(107)	2.9×10^{-11}	[57]
$N(^2D) + NO \rightarrow O(^3P,^1D,^1S) + NO$	(108)	6×10^{-11}	[57]
$N(^2D) + O_2 \rightarrow O(^3P) + NO$	(109)	$2.4 \times 10^{-12} \times \exp(-185/T)$	[57]
$N(^2D) + O_2 \rightarrow O(^1D) + NO$	(110)	$7.3 \times 10^{-12} \times \exp(-185/T)$	[57]
$N(^2D) + O(^3P) \rightarrow N(^4S) + O(^3P)$	(111)	1.4×10^{-12}	[57]
$N(^2D) + NO \rightarrow N_2O$	(112)	6×10^{-11}	[98]
$N(^2D) + NO \rightarrow O(^3P,^1D,^1S) + N_2$	(113)	6×10^{-11}	[57]
$N(^2D) + N_2O \rightarrow NO + N_2$	(114)	3×10^{-12}	[98]
$O(^1S) + N(^4S) \rightarrow O(^3P) + N(^2P)$	(115)	1×10^{-12}	[57]
$O(^1S) + NO \rightarrow O(^3P,^1D) + NO$	(116)	5×10^{-10}	[98]
$O(^1S) + N_2 \rightarrow O(^1D) + N_2$	(117)	5×10^{-17}	[57]
$O(^1D) + N_2 \rightarrow O(^3P) + N_2$	(118)	$1.8 \times 10^{-11} \times \exp(107/T)$	[57]
$O(^1D) + N_2O \rightarrow NO + NO$	(119)	7.2×10^{-11}	[98]
$O(^1D) + N_2O \rightarrow N_2 + O_2$	(120)	4.4×10^{-11}	[98]
$O(^1D) + NO \rightarrow N(^4S) + O_2$	(121)	1.7×10^{-10}	[98]
$O(^1D) + N_2O \rightarrow O(^3P,^1D) + N_2O$	(122)	9.4×10^{-12}	[98]
$O_2(a) + N(^4S) \rightarrow NO + O(^3P)$	(123)	$2 \times 10^{-14} \times \exp(-600/T)$	[98]
$O_2(a) + N_2 \rightarrow O_2 + N_2$	(124)	3×10^{-21}	[98]
$O_2(a) + NO \rightarrow O_2 + NO$	(125)	2.5×10^{-11}	[98]
$O_2(b) + N_2 \rightarrow O_2(a) + N_2$	(126)	$4.9 \times 10^{-15} \times \exp(-253/T)$	[98]
$O_2(b) + NO \rightarrow O_2(a) + NO$	(127)	4×10^{-14}	[98]
$O_2(A) + N_2 \rightarrow O_2(b) + N_2$	(128)	3×10^{-13}	[98]
Associative ionization			
$N(^2P) + O(^3P) \rightarrow NO^+ + e^-$	(129)	1.5×10^{-11}	[57,98]

Table A- 9 Reactions involved in the production/destruction of radiative species

Reaction		Rate constant (s^{-1}, cm^3s^{-1}, cm^6s^{-1})	Reference
Production and destruction of NO(A) responsible for the emission of the NOγ system			
$\mathbf{NO(X) + N_2(A) \rightarrow NO(A) + N_2}$		6.4×10^{-11}	[57,98]
$\mathbf{NO(A) \rightarrow NO(X) + h\nu}$		5×10^{6}	[113]
$\mathbf{NO(A) + N_2 \rightarrow NO(X) + N_2}$		1×10^{-13}	[113]
$\mathbf{NO(A) + O_2 \rightarrow NO(X) + O_2}$		1.5×10^{-10}	[113]
$\mathbf{NO(A) + NO \rightarrow NO(X) + NO}$		2×10^{-10}	[113]
Production and destruction of $N_2(C''^5\Pi_u)$ responsible for the emission of the HIR system			
$\mathbf{N_2(A) + N_2(A) \rightarrow N_2(C''^5\Pi_u) + N_2}$		$(8.1 - 9.9) \times 10^{-11}$	[111]
$\mathbf{N_2(C''^5\Pi_u) \rightarrow N_2(A'^5\Sigma_u^+) + h\nu}$		$2.3 \times 10^{5} - 2.5 \times 10^{7}$	[111]
Production and destruction of $O(^1S)N_2$ responsible for the emission of the HIR system			
$\mathbf{O(^1S) + N_2 + N_2 \rightarrow O(^1S)N_2 + N_2}$		2×10^{-36}	[55]
$\mathbf{O(^1S)N_2 \rightarrow O(^1D) + N_2 + h\nu}$		1×10^{7}	[55]
Production and destruction of $N_2(C)$ responsible for the emission of the second positive system (SPS)			
$\mathbf{e^- + N_2 \rightarrow e^- + N_2(C)}$		from EEDF	[83]
$\mathbf{N_2(C) \rightarrow N_2(B) + h\nu}$		2.5×10^{7}	[83]

APPENDIX 2

Before performing the measurements, a careful attention was paid to optimize the discharge cell. Indeed, with the originating setup, a small displacement of the electrodes was observed during the discharge displacement, which results in two drawbacks. First, even a small horizontal or vertical displacement of one electrode compared to the other modifies the discharge behavior, which can be directly observed on the discharge power. Second, a small displacement of the dielectrics in the vertical direction can change the position of the laser beam inside the gas gap, which can deviate from the center. To solve this problem, a new design was implemented as shown in Figure A- 15(a) and (b). The main components of this design consists in:

- two electrodes with two holes for each one,

- two plastic holders both with two holes at the same position of holes in the electrodes,

- two glass sticks put at the edges of the electrodes used to guide the gas flow and to ensure a gap of 2mm between the electrodes

- two metal sticks passing through the holes of the plastic holders and electrodes allowing maintaining the two electrodes face-to-face and to avoid the horizontal displacement,

- two plastic pieces with a form of “E” fixing at the end of the electrodes used to avoid the vertical displacement.

The final design has a sandwich form. The “sandwich” is connected to the displacement system by the fastening device.

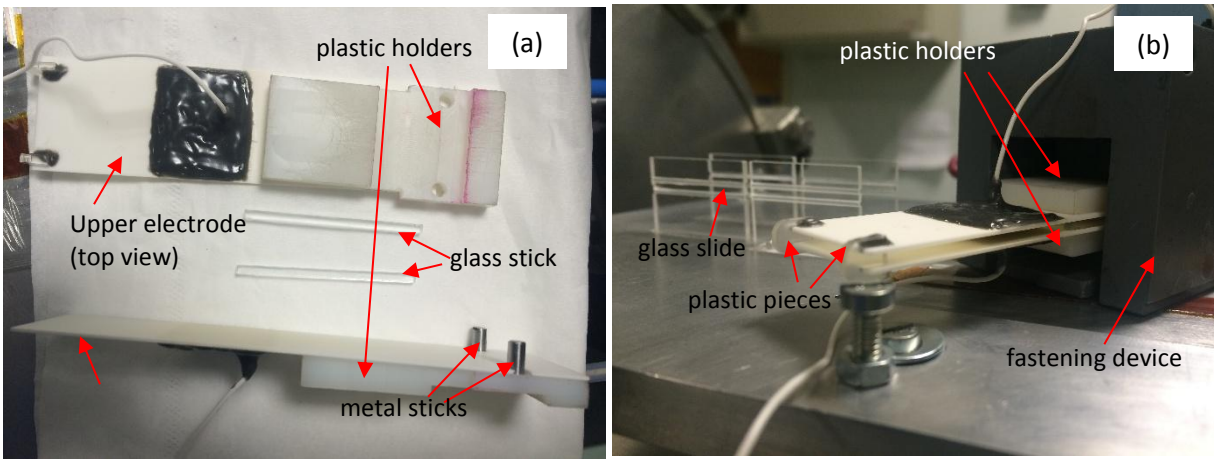

Figure A- 15 New design for the fixation of two electrodes

References

[1] Moisan M and Pelletier J 2012 *Physics of collisional plasmas: introduction to high-frequency discharges* (Springer Science & Business Media)

[2] Fridman A, Chirokov A and Gutsol A 2005 Non-thermal atmospheric pressure *J. Phys. D. Appl. Phys.* **38** 1–24

[3] Massines F, Sarra-Bournet C, Fanelli F, Naudé N and Gherardi N 2012 Atmospheric pressure low temperature direct plasma technology: Status and challenges for thin film deposition *Plasma Process. Polym.* **9** 1041–73

[4] Pankaj S K and Keener K M 2017 Cold plasma: background, applications and current trends *Curr. Opin. Food Sci.* **16** 49–52

[5] Montie T C, Kelly-Wintenberg K and Reece Roth J 2000 An overview of research using the one atmosphere uniform glow discharge plasma (OAUGDP) for sterilization of surfaces and materials *IEEE Trans. Plasma Sci.* **28** 41–50

[6] Ben Gadri R, Roth J R, Montie T C, Kelly-Wintenberg K, Peter P.-Y. Tsai, Dennis J. Helfritch, Paul Feldman, Sherman D M, Karakaya F and Zhiyu Chen 2000 Sterilization and plasma processing of room temperature surfaces with a one atmosphere uniform glow discharge plasma (OAUGDP) *Surf. Coatings Technol.* **131** 528–41

[7] Niemira B A 2012 Cold plasma decontamination of foods *Annu. Rev. Food Sci. Technol.* **3** 125–42

[8] Van Durme J, Dewulf J, Leys C and Van Langenhove H 2008 Combining non-thermal plasma with heterogeneous catalysis in waste gas treatment: A review *Appl. Catal. B Environ.* **78** 324–33

[9] Morent R, De Geyter N, Verschuren J, De Clerck K, Kiekens P and Leys C 2008 Non-thermal plasma treatment of textiles *Surf. Coatings Technol.* **202** 3427–49

[10] Roth J R 2001 *Industrial plasma engineering: Volume 2: Applications to nonthermal plasma processing* (CRC press)

[11] Massines F, Gherardi N, Fornelli A and Martin S 2005 Atmospheric pressure plasma deposition of thin films by Townsend dielectric barrier discharge *Surf. Coatings Technol.* **200** 1855–61

[12] Levasseur O, Stafford L, Gherardi N, Naudé N, Blanchard V, Blanchet P, Riedl B and Sarkissian A 2012 Deposition of hydrophobic functional groups on wood surfaces using atmospheric-pressure dielectric barrier discharge in helium-hexamethyldisiloxane gas mixtures *Plasma Process. Polym.* **9** 1168–75

[13] Starostin S A, Premkumar P A, Creatore M, Van Veldhuizen E M, De Vries H, Paffen R M J and Van De Sanden M C M 2009 On the formation mechanisms of the diffuse atmospheric pressure dielectric barrier discharge in CVD processes of thin silica-like films *Plasma Sources Sci. Technol.* **18**

[14] P. Raizer Y 1991 *Gas Discharge Physics*

[15] Raether H 1964 *Electron avalanches and breakdown in gases* (London : Butterworths)

[16] Nijdam S, Van De Wetering F M J H, Blanc R, Van Veldhuizen E M and Ebert U 2010 Probing photo-ionization: Experiments on positive streamers in pure gases and mixtures *J. Phys. D. Appl. Phys.* **43**

[17] Wormeester G, Pancheshnyi S, Luque A, Nijdam S and Ebert U 2010 Probing photo-ionization: Simulations of positive streamers in varying N2: O2-mixtures *J. Phys. D. Appl. Phys.* **43**

[18] Schoenbach K H, Verhappen R, Tessnow T and Peterkin F E 2003 Microhollow cathode discharges *J. Vac. Sci. Technol. A Vacuum, Surfaces, Film.* **21** 1260–5

[19] Deconinck T and Raja L L 2009 Modeling of mode transition behavior in argon microhollow cathode discharges *Plasma Process. Polym.* **6** 335–46

[20] Lukes P, Clupek M, Babicky V, Janda V and Sunka P 2005 Generation of ozone by pulsed corona discharge over water surface in hybrid gas-liquid electrical discharge reactor *J. Phys. D. Appl. Phys.* **38** 409–16

[21] Masuda S and Nakao H 1990 Control of NO/sub x/ by positive and negative pulsed corona discharges *IEEE Trans. Ind. Appl.* **26** 374–83

[22] Lee Y H, Jung W S, Choi Y R, Oh J S, Jang S D, Son Y G, Cho M H, Namkung W, Koh D J, Mok Y S and Chung J W 2003 Application of pulsed corona induced plasma chemical process to an industrial incinerator *Environ. Sci. Technol.* **37** 2563–7

[23] Joshi A A, Locke B R, Arce P and Finney W C 1995 Formation of hydroxyl radicals, hydrogen peroxide and aqueous electrons by pulsed streamer corona discharge in aqueous solution *J. Hazard. Mater.* **41** 3–30

[24] Plaks N, Ramsey G H, Ensor D S and Newsome J R 1992 Control of Volatile Organic Compounds by an ac Energized Ferroelectric Pellet Reactor and a Pulsed Corona Reactor *IEEE Trans. Ind. Appl.* **28** 528–34

[25] Kogelschatz U, Eliasson B and Egli W 1997 Dielectric-barrier discharges. Principle and applications *Le J. Phys. IV* **7** C4-47

[26] Siemens W 1857 Ueber die elektrostatische Induction und die Verzögerung des Stroms in Flaschendrähten *Ann. Phys.* **178** 66–122

[27] Buss K 1932 Die elektrodenlose Entladung nach Messung mit dem Kathodenoszillographen *Archiv fur Elektrotechnik* vol 26pp 261–5

[28] Klemenc A, Hintenberger H and Hofer H 1937 UBER DEN ENTLADUNSVORGANG IN EINER SIEMENS-OZONROHRE. *Ztschr. Elektrochem* **43** 708–12

[29] Kogelschatz U 2003 Dielectric-barrier Discharges : Their History, Discharge Physics, and Industrial Applications *Plasma Chem. Plasma Process.* **23** 1–46

[30] Bartnikas R 1969 Note on ac discharges between metallic-dielectric electrodes in helium *J. Appl. Phys.* **40** 1974–6

[31] Massines F, Gherardi N, Naudé N and Ségur P 2005 Glow and Townsend dielectric barrier discharge in various atmosphere *Plasma Phys. Control. Fusion* **47**

[32] Kanazawa S, Kogoma M, Moriwaki T and Okazaki S 1988 Stable glow plasma at atmospheric pressure *J. Phys. D. Appl. Phys.* **21** 838–40

[33] Okazaki S, Kogoma M, Uehara M and Kimura Y 1993 Appearance of stable glow discharge in air, oxygen and nitrogen at atmospheric pressure using a 50 Hz source *J. Phys. D Appl. Phys.*

26 889–92

[34] Massines F, Mayoux C, Messaoudi R, Rabehi A and Ségur P 1992 Experimental study of an atmospheric pressure glow discharge. Application to polymers surface treatment, *International Conference on Gas Discharges and their Applications, Swansea, U. K., 13–18 September 1992* pp 730–3

[35] Massines F, Rabehi A, Decomps P, Gadri R Ben, Ségur P and Mayoux C 1998 Experimental and theoretical study of a glow discharge at atmospheric pressure controlled by dielectric barrier *J. Appl. Phys.* **83** 2950–7

[36] Roth J R, Laroussi M and Liu C 1993 Experimental generation of a steady-state glow discharge at atmospheric pressure *Proc. IEEE International Conference on Plasma* pp 170–1

[37] Liu C and Roth J R 1993 Plasma-Related Characteristics of a Steady-State Glow Discharge At Atmospheric Pressure *IEEE Conference Record - Abstracts 1993 IEEE International Conference on Plasma* p 129

[38] Massines F, Gherardi N, Naudé N and Ségur P 2009 Recent advances in the understanding of homogeneous dielectric barrier discharges *Eur. Phys. J. Appl. Phys.* **47** 22805

[39] Palmer A J 1974 A physical model on the initiation of atmospheric-pressure glow discharges *Appl. Phys. Lett.* **25** 138–40

[40] Enache I, Naudé N, Cambronne J P, Gherardi N and Massines F 2006 Electrical model of the atmospheric pressure glow discharge (APGD) in helium *Eur. Phys. Journal-Applied Phys.* **33** 15–21

[41] Tu X, Verheyde B, Corthals S, Paulussen S and Sels B F 2011 Effect of packing solid material on characteristics of helium dielectric barrier discharge at atmospheric pressure *Phys. Plasmas* **18** 1–5

[42] Massines F, Segur P, Gherardi N, Khamphan C and Ricard A 2003 Physics and chemistry in a glow dielectric barrier discharge at atmospheric pressure: diagnostics and modelling *Surf. Coatings Technol.* **174–175** 720–4

[43] Osawa N and Yoshioka Y 2012 Generation of low-frequency homogeneous dielectric barrier discharge at atmospheric pressure *IEEE Trans. Plasma Sci.* **40** 2–8

[44] Naudé N, Belinger A, Dap S and Gherardi N 2015 Memory effects in Atmospheric Pressure Townsend Discharges in N2 and air *The International Conference on Phenomena in Ionized Gases (ICPIG) (Iași - Romania, July 26-31, 2015)*

[45] Laurent C, Tyl C, Dap S, Gherardi N and Naudé N 2018 ATR-FTIR Study of Low-Temperature Atmospheric Pressure Plasma Treated Aspergillus Mycelia *The 16th International Symposium on High Pressure Low Temperature Plasma Chemistry(Beijing- China, Semptember 02-07, 2018)*

[46] Massines F, Ségur P, Gherardi N, Kamphan C, Jimenez C, Bordage M C, Camrome J P and Naude N 2003 Dielectric barrier glow discharges: Science and applications *Proc. 16th Int. Symp. Plasma Chemistry* pp 22–7

[47] Gherardi N and Massines F 2001 Mechanisms controlling the transition from glow silent discharge to streamer discharge in nitrogen *IEEE Trans. Plasma Sci.* **29** 536–44

[48] Tyl C, Lin X, Bouzidi M C, Dap S, Caquineau H, Ségur P, Gherardi N and Naudé N 2018 Investigation of memory effect in atmospheric pressure dielectric barrier discharge in nitrogen with small oxygen or nitric oxide addition *J. Phys. D. Appl. Phys.* **51**

[49] Kamphan C, Ségur P, Massines F, Bordage M C, Gherardi N and Cesses Y 2003 Secondary electron emission by nitrogen metastable states in athospheric-pressure glow discharge *Proc. of The 16th International Symposium on Plasma Chemistry., Taormina,Italy,2003*

[50] Popov N A 2013 Vibrational kinetics of electronically-excited $N_2(A^3\Sigma^+_u,v)$ molecules in nitrogen discharge plasma *J. Phys. D. Appl. Phys.* **46**

[51] Bosan D A, Jovanovic T V and Krmpotic D M 1997 The role of neutral metastable N2(A) molecules in the breakdown probability and glow discharge in nitrogen *J. Phys. D. Appl. Phys.* **30** 3096–8

[52] Khamphan C 2004 *Modélisation numérique de décharges contrôlées par barrières diélectriques à la pression atmosphérique (Université Paul Sabatier PhD thesis)*

[53] Cardinaud C, Marcos G, Clergereaux R and Mottin S 2012 *Plasma et son environnement. Plasmas Froids en France et au Québec* ed S Mottin and G Lelièvre (MRCT-CNRS)

[54] Golubovskii Y B, Maiorov V A, Behnke J and Behnke J F 2002 Influence of interaction between charged particles and dielectric surface over a homogeneous barrier discharge in nitrogen *J. Phys. D. Appl. Phys.* **35** 751–61

[55] Brandenburg R, Maiorov V A, Golubovskii Y B, Wagner H E, Behnke J and Behnke J F 2005 Diffuse barrier discharges in nitrogen with small admixtures of oxygen: discharge mechanism and transition to the filamentary regime *J. Phys. D. Appl. Phys.* **38** 2187–97

[56] Bouzidi C 2014 *Etude d'une Décharge à Barrière Diélectrique (DBD) homogène dans l'azote à pression atmosphérique : Effet mémoire et Optimisation du transfert de Puissance (Université Paul Sabatier PhD thesis)*

[57] Popov N A 2009 Associative Ionization Reactions Involving Excited Atoms in Nitrogen Plasma *Plasma Phys. Reports* **35** 436–49

[58] Dilecce G, Ambrico P F and De Benedictis S 2007 $N_2(A^3\Sigma^+_u)$ density measurement in a dielectric barrier discharge in N_2 and N_2 with small O_2 admixtures *Plasma Sources Sci. Technol.* **16** 511–22

[59] ES-Sebbar E 2007 *Étude électrique et analyse par fluorescence induite par laser des décharges de Townsend à la pression atmosphérique dans N_2, N_2/N_2O et N_2/O_2 (Université Paul Sabatier PhD thesis)*

[60] Es-Sebbar E, Sarra-Bournet C, Naudé N, Massines F and Gherardi N 2009 Absolute nitrogen atom density measurements by two-photon laser-induced fluorescence spectroscopy in atmospheric pressure dielectric barrier discharges of pure nitrogen *J. Appl. Phys.* **106**

[61] Es-Sebbar E, Gherardi N and Massines F 2013 Effects of N_2O and O_2 addition to nitrogen Townsend dielectric barrier discharges at atmospheric pressure on the absolute ground-state atomic nitrogen density *J. Phys. D. Appl. Phys.* **46**

[62] Naudé N, Cambronne J P, Gherardi N and Massines F 2005 Electrical model and analysis of the transition from an atmospheric pressure Townsend discharge to a filamentary discharge *J. Phys. D. Appl. Phys.* **38** 530–8

[63] Uddi M, Jiang N, Adamovich I V and Lempert W R 2009 Nitric oxide density measurements in air and air/fuel nanosecond pulse discharges by laser induced fluorescence *J. Phys. D Appl. Phys. J. Phys. D Appl. Phys* **42** 75205–18

[64] Klochko A V., Lemainque J, Booth J P and Starikovskaia S M 2015 TALIF measurements of

oxygen atom density in the afterglow of a capillary nanosecond discharge *Plasma Sources Sci. Technol.* **24**

[65] Dilecce G, Vigliotti M and DeBenedictis S 2000 A TALIF calibration method for quantitative oxygen atom density measurement in plasma jets *J. Phys. D* **33** 53

[66] Koochesfahani M and Dimotakis P E 1985 Laser-induced fluorescence measurements of mixed fluid concentrationin a liquid plane shear layer *AIAA J.* **23** 1700–7

[67] Yin Z, Adamovich I V. and Lempert W R 2013 OH radical and temperature measurements during ignition of H 2-air mixtures excited by a repetitively pulsed nanosecond discharge *Proc. Combust. Inst.* **34** 3249–58

[68] Dilecce G, Martini L M, Tosi P, Scotoni M and De Benedictis S 2015 Laser induced fluorescence in atmospheric pressure discharges *Plasma Sources Sci. Technol.* **24**

[69] Amorim J, Baravian G and Jolly J 2000 Laser-induced resonance fluorescence as a diagnostic technique in non-thermal equilibrium plasmas *J. Phys. D. Appl. Phys.* **33**

[70] Lee M P, Mc Millin B K and Hanson R K 1993 Temperature Measurements in Gases by use of planar laser-induced fluorescence imaging of NO *Appl. Opt.* **32** 5379–96

[71] Niemi K, Schulz-von der Gathen V and Dobele H F 2001 Absolute calibration of atomic density measurements by laser-induced fluorescence spectroscopy with two-photon excitation *J. Phys. D. Appl. Phys.* **34** 2330–5

[72] Loudon R 1983 *The Quantum Theory of Light 2nd edn*

[73] Czarnetzki U, Miyazaki K, Kajiwara T and Muraoka K 1994 Comparison of various two-photon excitation **11**

[74] Van Gessel A F H, Van Grootel S C and Bruggeman P J 2013 Atomic oxygen TALIF measurements in an atmospheric-pressure microwave plasma jet with in situ xenon calibration *Plasma Sci. Technol.* **22**

[75] Niemi K, Schulz-Von Der Gathen V and Döbele H F 2005 Absolute atomic oxygen density measurements by two-photon absorption laser-induced fluorescence spectroscopy in an RF-excited atmospheric pressure plasma jet *Plasma Sources Sci. Technol.* **14** 375–86

[76] Goehlich A, Kawetzki T and Döbele H F 1998 On absolute calibration with xenon of laser diagnostic methods based on two-photon absorption *J. Chem. Phys.* **108** 9362–70

[77] http://www.sirah.com/

[78] Tachiev G I and Froese Fischer C 2001 Breit-Pauli energy levels and transition rates for nitrogen-like and oxygen-like sequences *Astronomy&Astrophysics* **10** 716–23

[79] Chang R S F, Horiguchi H and Setser D W 1980 Radiative lifetimes and two-body collisional deactivation rate constants in argon for Kr(4p ^{5}5p) and Kr(4p ^{5}5p ') states *J. Chem. Phys.* **73** 778–90

[80] Builder S T M D 2012 *specair User manual*

[81] Schröder D, Burhenn S, Kirchheim D and Gathen V S Von Der 2013 Enhanced oxygen dissociation in a propagating constricted discharge formed in a self-pulsing atmospheric pressure microplasma jet *J. Phys. D. Appl. Phys.* **46** 14

[82] Naudé N 2005 Etude Electrique de la Physique d'une Décharge de Townsend à la Pression

Atmosphérique et de son Interaction avec un Générateur : Modèle et Expérience (Université Paul Sabatier PhD thesis)

[83] Tsyganov D and Pancheshnyi S 2012 Simulation of N-atom production in dielectric-barrier discharge in nitrogen at atmospheric pressure *Plasma Sources Sci. Technol.* **21**

[84] Teramoto Y, Ono R and Oda T 2012 Production mechanism of atomic nitrogen in atmospheric pressure pulsed corona discharge measured using two-photon absorption laser-induced fluorescence *J. Appl. Phys.* **111**

[85] Popov N A 2013 Dissociation of nitrogen in a pulse-periodic dielectric barrier discharge at atmospheric pressure *Plasma Phys. Reports* **39** 420–4

[86] Stancu G D, Kaddouri F, Lacoste D A and Laux C O 2010 Atmospheric pressure plasma diagnostics by OES, CRDS and TALIF *J. Phys. D. Appl. Phys.* **43**

[87] A Hibber, E Biemont, M Godefroid N V 1991 E1 transitions of astrophysical interest in neutral oxygen *J. Phys. B At. Mol. Opt. Phys.* **24** 3943–58

[88] Horiguchi H, Chang R S F and Setser D W 1981 Radiative lifetimes and two-body collisional deactivation rate constants in Ar for Xe(5p ^{5}6p),Xe(5p ^{5}6p), and Xe(5p ^{5}7p) states *J. Chem. Phys.* **75** 1207–18

[89] Bruce M R, Layne W B, Whitehead C A and Keto J W 1990 Radiative lifetimes and collisional deactivation of two-photon excited xenon in argon and xenon *J. Chem. Phys.* **92** 2917–26

[90] Saxon R and Eichler J 1986 Theoretical calculation of two-photon absorption cross sections in atomic oxygen *Phys. Rev. A* **34** 199–206

[91] Popov N A 2016 Pulsed nanosecond discharge in air at high specific deposited energy: Fast gas heating and active particle production *Plasma Sources Sci. Technol.* **25** 44003

[92] Luque J and Crosley D R 1999 *LIFBASE (version 1.5)* vol 19

[93] De Benedictis S, Ambrico P F and Dilecce G 2010 LIF investigations of O and NO products in air like RF plasma jet *J. Phys. Conf. Ser.* **227**

[94] Van Gessel A F H, Hrycak B, Jasiński M, Mizeraczyk J, Van Der Mullen J J A M and Bruggeman P J 2013 Temperature and NO density measurements by LIF and OES on an atmospheric pressure plasma jet *J. Phys. D. Appl. Phys.* **46** 12

[95] Reisel J R, Carter C D and Laurendeau N M 1992 REISEL, Engineering, **47** 43–54

[96] Herron J T 1999 Evaluated Chemical Kinetics Data for Reactions of N (^{2}D), N (^{2}P), and N ($A^3\Sigma^+_u$) in the Gas Phase *J. Phys. Chem. Ref. Data* **28** 1453–83

[97] Dorai R and Kushner M J 2003 A model for plasma modification of polypropylene using atmospheric pressure discharges *J. Phys. D-Applied Phys.* **36** 666–85

[98] Kossyi I A, Kostinsky A Y, Matveyev A A and Silakov V P 1992 Kinetic scheme of the non-equlibrium discharge jn nitrogen-oxygen mixtures *Plasma Sources Sci. Technol.* **1** 207–20

[99] Greaves J C and Linnett J W 1958 The recombination of oxygen atoms at surfaces *Trans. Faraday Soc.* **54** 1323–30

[100] UNAM database, www.lxcat.net, retrieved on November 24, 2017

[101] Viehland L A and Fahey D W 1983 The mobilities of NO^-_3 , NO^-_2 , NO^+ , and Cl^- in N_2 : A measure of inelastic energy loss *J. Chem. Phys.* **78** 435–41

[102] Viehland database, www.lxcat.net, retrieved on September 1, 2017

[103] Salmon A, Popov N A, Stancu G D and Laux C O 2018 Quenching rate of N(^{2}P) atoms in a nitrogen afterglow at atmospheric pressure *J. Phys. D. Appl. Phys.* **51**

[104] IST-Lisbon database, www.lxcat.net, retrieved on August 14, 2017

[105] Hagelaar G J M and Pitchford L C 2005 Solving the Boltzmann equation to obtain electron transport coefficients and rate coefficients for fluid models *Plasma Sources Sci. Technol.* **14** 722–33

[106] Biagi database, www.lxcat.net, retrieved on August 14, 2017

[107] Morgan database, www.lxcat.net, retrieved on August 14, 2017

[108] Kozlov K V, Brandenburg R, Wagner H-E, Morozov A M and Michel P 2005 Investigation of the filamentary and diffuse mode of barrier discharges in N_2 /O_2 mixtures at atmospheric pressure by cross-correlation spectroscopy *J. Phys. D. Appl. Phys.* **38** 518–29

[109] Cosby P C 1993 Electron-impact dissociation of nitrogen *J. Chem. Phys.* **98** 9544–53

[110] Herron J T and Green D S 2001 Chemical kinetics database and predictive schemes for nonthermal humid air plasma chemistry. Part II. Neutral species reactions *Plasma Chem. Plasma Process.* **21** 459–81

[111] Šimek M 2003 Determination of $N_2(A^3\Sigma^+_u)$ metastable density produced in nitrogen streamers by pulsed positive corona discharge at atmospheric pressure. Experimental verification *Plasma Sources Sci. Technol.* **12** 454–463

[112] Thomas J M and Kaufman F 1996 An Upper Limit on the Formation of $NO(X^2\Pi_r)$ in the Reactions $N_2(A^3\Sigma^+_u)$ + O(^{3}P) and $N_2(A^3\Sigma^+_u)$+ $O_2(X^3\Sigma^-_g)$ at 298 K *J. Phys. Chem.* **100** 8901–6

[113] Pintassilgo C D, Loureiro J and Guerra V 2005 Modelling of a N_2-O_2 flowing afterglow for plasma sterilization *J. Phys. D-Applied Phys.* **38** 417–30